

Engineering of bacteriochlorophyll pigments and quantum dots for the production of novel photonic materials

Amanda Louise McDonnell

Submitted in accordance with the requirements for the degree of
Doctor of Philosophy

The University of Leeds
School of Molecular and Cellular Biology
and
School of Physics and Astronomy

September 2016

The candidate confirms that the work submitted is his/her own and that appropriate credit has been given where reference has been made to the work of others.

This copy has been supplied on the understanding that it is copyright material and that no quotation from the thesis may be published without proper acknowledgement.

The right of Amanda Louise McDonnell to be identified as Author of this work has been asserted by her in accordance with the Copyright, Designs and Patents Act 1988.

© 2016 The University of Leeds and Amanda Louise McDonnell

Acknowledgements

I would like to acknowledge the BBSRC for funding. I would also like to thank the following people for their invaluable contributions to this thesis.

First and foremost, I would like to thank my two supervisors, Roman Tuma and Kevin Critchley who have provided amazing support and shown great patience over the course of the last four years.

I would also like to thank Jakub Psencik and Radek Litvin for initial batches of *Chlorobaculum tepidum* cells and assistance with their growth. I would like to thank Ben Johnson for help with X-ray photoelectron spectroscopy on pigment samples and for general life advice and support in moments of stress. I am extremely grateful to Sarah Harris for all her help with simulation aspects of this thesis (including provision of initial simulation scripts) and numerous highly entertaining chats. I would like to thank Matt Booth for initial help in the synthesis of quantum dots. I am grateful to Jan Alster for provision of the original optimised structures for simulation and the global analysis script used for analysis of photoluminescence lifetime and transient absorption data. The photoluminescence lifetime and transient absorption studies on quantum dots would not have been possible without the amazing help of Jakub Psencik and Petro Khoroshy. I would like to acknowledge Michael Greben who helped with the quantum yield measurements on quantum dots.

On a personal note, I would like to thank members of the Stockley-Tuma Lab (Alex, Amit, Amy, Becca, Emma, Jack, Nikesh, Ruiyang and Simon) for providing an enjoyable, if often projectile-filled, working environment. I credit the “Physics coffee group”, Chris, Freya, Joe, Matt and Rachel, for helping to keep me sane or at least providing company in insanity. I would like to thank my parents, Theresa and David, for their unwavering support and for always taking an interest in my work.

Last, but by no means least, I would like to thank my amazing fiancé Adam for all his support and for putting up with everything over the last four years. I am certain I could not have completed any of this without you.

‘So Long, and Thanks for All the Fish’ – Douglas Adams

Abstract

Due to their small size, and consequent quantum confinement, quantum dots (QDs) exhibit electronic properties intermediate between those of bulk semiconductors and individual molecules. The electronic and optical properties of these semiconductor nanocrystals are tuneable by nanocrystal size and composition. Consequently, they offer a range of attractive photophysical properties with a wide range of possible applications. Copper indium sulphide (CIS) QDs are attracting increasing attention due to lower toxicity, significant quantum confinement, and a bulk direct band-gap of $\sim 1.5\text{eV}$ making them ideal for solar energy applications.

Bacteriochlorophylls (BChls) *c/d* and *e* are photosynthetic pigments found in green photosynthetic bacteria. Due to their structure, they are able to self-assemble into densely packed aggregates exhibiting strong excitonic coupling between individual pigments as well as optical spectra substantially different to those of monomeric BChls. The self-aggregating nature of these molecules and the resulting strong coupling results in impressive light harvesting ability and rapid energy transfer, thus providing exciting opportunities for use in nanomaterials.

Coupling BChl aggregates with QDs should lead to strong interaction between energy levels and efficient energy transfer, yielding new hybrid nanostructures with novel electronic and optical properties.

In this thesis, BChl pigments and QDs are investigated with a focus on how they might be combined to produce novel photonic materials. This thesis outlines a new method for the production of zinc containing BChl analogues as well as presenting the first molecular dynamics simulations on BChl *c* pigment assemblies investigating the origin of intrinsic curvature. In addition, a new method for the direct synthesis of hydrophilic CIS QD is presented, along with the first quantitative data on size dependent photoluminescent quantum yield for CIS QDs. Furthermore photoluminescent decay studies presented in this thesis shed new light on the role of size and composition on the relative contribution of key recombination pathways within CIS quantum dots.

Table of Contents

Acknowledgements	iii
Abstract	iv
Table of Contents	v
List of Tables	x
List of Figures	xi
Chapter 1 Introduction	1
1.1 BChls c, d, and e	1
1.1.1 Chlorosomes	2
1.1.2 Structure of Chlorosomes	3
1.1.3 Molecular organisation of BChl molecules	6
1.1.4 Long range ordering of BChl aggregates	10
1.1.5 Spectroscopic properties of chlorosomes	14
1.1.6 Excitation energy transfer in chlorosomes	19
1.1.7 In vitro BChl aggregates	20
1.1.8 Theoretical description of BChls and their aggregates	22
1.2 QDs	27
1.2.1 Semiconductors	27
1.2.2 Quantum confinement	34
1.2.3 Appeal and applications	39
1.2.4 Quantum dot materials and synthesis routes	39
1.2.5 Properties and size dependence	49
1.2.5.1 Band-gap	49
1.2.5.2 Absorption	51
1.2.5.3 Emission	52
1.3 Combining Bacteriochlorophylls and Quantum dots	54
1.4 Summary of key aims and results	58
1.4.1 I. Chemical modification of pigments	58
1.4.2 II. Simulation of BChl pigments to better understand aggregation	59
1.4.3 III. Synthesis and characterisation of CIS QDs	59
Chapter 2 Materials and Methods	61
2.1 Introduction	61
2.1.1 Materials	61
2.2 Bacteriochlorophylls (BChls) and chlorophylls (Chls)	62

2.2.1	Purification of BChls and Chls	62
2.2.1.1	Source and growth of cells	62
2.2.1.2	Extraction of BChl c from <i>Chlorobaculum tepidum</i> cells	63
2.2.1.3	Extraction of BChl e from chlorosomes	64
2.2.1.4	Extraction of chlorosomes from <i>Chlorobaculum tepidum</i> cells	64
2.2.1.5	Extraction of pigments from spinach.....	64
2.2.1.6	Absorbance measurements and concentration determination.....	65
2.2.1.7	HPLC purification of BChl c pigments.....	66
2.2.1.8	HPLC purification of chlorophyll a and b.....	66
2.2.2	Chemical modification of pigments	67
2.2.2.1	Zinc-(Bacterio)Pheophytin (Zn-(B)Phe) production.....	67
2.2.2.2	Pre-purification and HPLC purification and analysis of Zn-(B)Phees	68
2.2.2.3	Incorporation of an thiol group	68
2.2.2.4	X-ray photoelectron spectroscopy (XPS) analysis of pigments	68
2.3	MD simulation of BChl aggregation	69
2.3.1	Theoretical basis of molecular dynamics	69
2.3.2	Construction of pigment systems.....	79
2.3.2.1	Dimer arrangements	79
2.3.2.2	Single and triple layer sheets.....	80
2.3.3	Simulation details and setup.....	82
2.3.3.1	Minimisation, heating, and equilibration steps	82
2.3.3.2	Production dynamics	84
2.3.4	Computational resources.....	84
2.3.5	Analysis of MD results	85
2.3.5.1	Structures	85
2.3.5.2	Energy of simulated systems.....	86
2.3.5.3	X-ray scattering predictions	86
2.4	Quantum dots	86
2.4.1	Quantum dot synthesis	86
2.4.2	Quantum dot cleaning	87

2.4.3 Absorbance measurements, determination of E_1 , E_x and concentration	88
2.4.4 TEM measurements.....	89
2.4.5 X-ray diffraction (XRD) measurements	89
2.4.6 Energy dispersive analysis of X-rays (EDX).....	89
2.4.7 XPS analysis of quantum dots	90
2.4.8 Photoluminescence (PL) emission and excitation spectra	90
2.4.9 Photoluminescence quantum yield (PLQY) measurements	90
2.4.10 PL lifetime measurements.....	91
2.4.11 Transient absorption measurements.....	91
Chapter 3 Results and Discussion: Bacteriochlorophyll and Zinc-(Bacterio)Pheophytin Preparation and Chemical Modification.....	93
3.1 Introduction	93
3.2 Purification of BChls and Chls.....	93
3.2.1 Growth of <i>Chlorobaculum tepidum</i> cells.....	93
3.2.2 Extraction of BChl c from cells	94
3.2.3 Extraction of BChl e from chlorosomes	96
3.2.4 Extraction of chlorosomes from <i>Chlorobaculum tepidum</i> cells	97
3.2.5 Extraction of pigments from spinach	98
3.2.6 High Pressure Liquid Chromatography (HPLC) purification of BChl c pigments.....	99
3.2.7 HPLC purification of chlorophyll a and b	102
3.2.8 XPS analysis of native pigments.....	104
3.3 Chemical modification of pigments.....	109
3.3.1 Zn-(B)Phe production and purification.....	109
3.3.1.1 Transmetallation of pigments	109
3.3.1.2 Spectroscopic properties of transmetallated pigments	110
3.3.1.3 Pre-purification and HPLC purification and analysis of Zn-(B)Phes.....	112
3.3.1.4 XPS analysis of zinc modified pigments.....	118
3.3.1.5 Aggregation of Zn-BPhes and BChls	122
3.3.2 Incorporation of a thiol group	123
3.3.2.1 XPS analysis of Cysteamine treated pigments.	124

3.4 Conclusions	130
Chapter 4 Results and Discussion: Simulations of bacteriochlorophyll pigment assemblies	131
4.1 Introduction.....	131
4.2 Single sheets.....	131
4.2.1 Structures from simulation.....	132
4.2.2 Energy of simulated systems.....	145
4.2.3 X-ray scattering predictions.....	150
4.3 Multilamellar systems	153
4.3.1 Structures from simulation.....	153
4.3.2 Energy of simulated systems	166
4.4 Conclusions and future directions.....	171
Chapter 5 Results and Discussion: Synthesis and characterisation of copper indium sulphide quantum dots	175
5.1 Introduction.....	175
5.2 Structure and composition	175
5.2.1 Quantum dot synthesis and cleaning.....	175
5.2.2 Transmission electron microscopy	177
5.2.3 Lattice spacings from high resolution TEM.....	180
5.2.4 X-ray diffraction	181
5.2.5 Energy dispersive X-ray analysis.....	183
5.2.6 X-ray photoelectron spectroscopy	183
5.3 Optical properties	188
5.3.1 Absorbance measurements, determination of E_1 , E_x	188
5.3.2 PL emission	196
5.3.3 PLQY	200
5.3.3 Fluorescence lifetime measurements	202
5.3.4 Transient absorption measurements	207
5.4 Conclusion.....	209
Chapter 6 Conclusions and future perspectives	210
6.1 Conclusions	210
6.1.1 BChl and Zinc-(Bacterio)Pheophytin (Zn-(B)Phe) Preparation and Chemical Modification	210
6.1.2 Simulations of BChl pigment assemblies.....	211
6.1.3 Synthesis and characterisation of CIS QDs.....	212
6.2 Future work.....	213

6.2.1 Pigment modification and production of hybrid systems ..	213
6.2.2 Simulations on pigment assemblies	213
6.2.3 Quantum dots	215
List of Abbreviations	216
List of References	219
Appendix A Summary of “heat up” synthesis methods	239
Appendix B Preparation of triple layer pigment systems for simulation	242
Appendix C Amber simulation scripts	246
C.1 equil.sh	246
C.2 min1.in.....	248
C.3 min2.in.....	248
C.4 min3.in.....	249
C.5 min4.in.....	249
C.6 md1.in.....	249
C.7 md2.in.....	250
C.8 md3.in.....	250
C.9 md4.in.....	251
C.10 md5.in.....	251
C.11 md6.in.....	251
C.12 md7.in.....	252
C.13 md8.in.....	252
C.14 md9.in.....	253
Appendix D Molecular dynamics (MD) analysis scripts	254
D.1 Root-mean-squared (RMS) pair-wise separation	254
D.2 System energy analysis.....	256
D.3 Dipole moment plots.....	257
D.4 Parallelised Brute force X-ray scattering code.....	258
Appendix E Dipole moment plots from Chapter 4.....	264

List of Tables

Table 1.1 Comparison of band-gap data for CIS quantum dots of different sizes as reported by Zhong et al.¹⁵⁴	50
Table 2.1 Modified Pennings' medium.²²⁰	62
Table 2.2 Mineral supplement for Modified Pennings' medium.²²⁰	63
Table 2.3 Positions of Q_y peaks and values used for concentration determinations of BChl c, BChl e, Chl a, and Chl b.	65
Table 2.4 Gradient conditions for separation of chlorophylls, their derivatives, and carotenoids.	67
Table 2.5 List of simulations performed.	82
Table 2.6 Conditions for system minimisation, heating, and equilibration.	84
Table 3.1 Summary of Soret and Q_y positions for natural pigments, their free bases, and zinc analogues.	111
Table 5.1 NP size as determined using TEM for each synthesis time.	179
Table 5.2 Copper to indium ratio as determined using XPS for quantum dots of each size. Quantum dots were found to be increasingly copper deficient with increasing size.	184
Table 5.3 Stokes shifts calculated for nanoparticles of various sizes.	200
Table 5.4 PLQY for nanoparticles between 1.8 ± 0.2 and 2.6 ± 0.4 nm at a range of excitation energies.	202
Table 5.5 Stokes shift for each of the three fitted PL decay components. No significant dependence on nanoparticle size was observed.	206
Table A.1 Overview of experimental procedures for 'heating up' methods	239

List of Figures

Figure 1.1 Schematic showing shape and basic structure of a chlorosome.....	3
Figure 1.2 Cryo-Electron microscopy (Cryo-EM) images of chlorosomes.....	4
Figure 1.3 Basic structures of chlorins, bacteriochlorins and porhins.....	6
Figure 1.4 Structure of different bacteriochlorophylls.	7
Figure 1.5 Schematic representation of structural models proposed for BChl aggregates.	8
Figure 1.6 The curved lamellar system in chlorosomes.....	11
Figure 1.7 Q_y transition dipole moment.	13
Figure 1.8 Absorption spectra for chlorosomes and monomeric BChl c in methanol.....	16
Figure 1.9 Structural motifs investigated in Alster et al.. ²⁶	25
Figure 1.10 Insulators, semiconductors, and conductors.....	28
Figure 1.11 Intrinsic, n-type, and p-type semiconductors.....	29
Figure 1.12 Excitation of a direct band-gap semiconductor.	31
Figure 1.13 Photoluminescence recombination of the electron hole pair in a direct band-gap semiconductor.	32
Figure 1.14 Electronic properties of quantum dots c.f. bulk semiconductors and molecules.	35
Figure 1.15 Quantum confinement.	35
Figure 1.16 Change in free energy as a function of radius in NC growth.....	41
Figure 1.17 Nanoparticle growth: broadening vs. focusing.	44
Figure 1.18 Relationship between energy levels in CIS quantum dots (orange) and zinc containing BChl pigments (green).	57
Figure 1.19 Project scheme showing the key stages of composite material production.....	58
Figure 2.1 Summary of bonded interactions.	74
Figure 2.2 Summary of non-bonded interactions.....	75
Figure 2.3 Verlet algorithm timeline.	79
Figure 2.4 Classification of structural motifs used in molecular dynamics simulations.....	80
Figure 2.5 Construction of multilayer system from initial dimers.	81
Figure 2.6 KrosFlo diafiltration setup used for purification.	88

Figure 3.1 Extraction of BChl c pigments from <i>Chlorobaculum tepidum</i>	95
Figure 3.2 Extraction of BChl e pigments from <i>Chlorobaculum phaeobacteroides</i> chlorosomes.....	96
Figure 3.3 Absorbance spectrum of chlorosomes from <i>Chlorobaculum tepidum</i> purified using a sucrose density gradient.	97
Figure 3.4 Spectrum of crude pigment extract from spinach.....	99
Figure 3.5 HPLC Purification of BChl c from <i>Chlorobaculum tepidum</i>	100
Figure 3.6 HPLC 3-dimensional field chromatogram for purification of BChl c.	101
Figure 3.7 HPLC purification of chlorophylls a and b.	103
Figure 3.8 HPLC 3-dimensional field chromatogram for purification of Chls.....	104
Figure 3.9 XPS survey spectrum for unmodified Chl a.	105
Figure 3.10 XPS survey spectrum for unmodified Chl b.....	105
Figure 3.11 XPS survey spectrum for unmodified BChl c.....	106
Figure 3.12 Detailed XPS spectra for Chl a.	107
Figure 3.13 Detailed XPS spectra for Chl b.	108
Figure 3.14 Detailed XPS spectra used for BChl c.	109
Figure 3.15 Spectral changes during transmetallation of pigments. ..	111
Figure 3.16 Energy levels of transmetallated pigments.....	112
Figure 3.17 Successful HPLC purification of Zn-BPhe c (after pre-purification using phase separation method).	114
Figure 3.18 3-dimensional field chromatogram for purification of Zn-BPhe c.....	115
Figure 3.19 HPLC purification of Zn-BPhe c without pre-purification using phase separation method.	116
Figure 3.20 HPLC purification of Zn-pheophytin a.	117
Figure 3.21 3-dimensional field chromatogram for purification of Zn-Phe a.	117
Figure 3.22 XPS survey spectrum for Zn-Phe a.....	118
Figure 3.23 XPS survey spectrum for Zn-BPhe c.	119
Figure 3.24 Detailed XPS spectra used for composition determinations of Zn-Phe a.	120
Figure 3.25 Detailed XPS spectra used for composition determinations of Zn-BPhe c.....	121

Figure 3.26 Spectra of aggregates and monomers of BChl c and Zn-BPhe c.	123
Figure 3.27 Reaction vial used for attempted incorporation of an SH group in Chl a.	124
Figure 3.28 XPS survey spectrum for cysteamine-treated Chl a.	125
Figure 3.29 XPS survey spectrum for cysteamine-treated Chl b.	125
Figure 3.30 Detailed XPS spectra for cysteamine-treated Chl a.	126
Figure 3.31 Detailed XPS spectra used for cysteamine-treated Chl b.	127
Figure 3.32 Difference spectra for C 1s peaks of cysteamine-treated Chl a and Chl b.	129
Figure 4.1 RMS pair-wise separation of Mg atoms for single layer pigment systems.	132
Figure 4.2 Initial and final structures for simulations on sheets formed using the $\alpha A\alpha A$ dimer arrangement.	134
Figure 4.3 Q_y dipole moments for sheets formed using the $\alpha A\alpha A$ dimer arrangement.	134
Figure 4.4 Initial and final structures for simulations on sheets formed using the $\alpha S\alpha S$ dimer arrangement.	135
Figure 4.5 Q_y dipole moments for sheets formed using the $\alpha S\alpha S$ dimer arrangement.	135
Figure 4.6 Initial and final configurations for simulations on sheets formed using the $\alpha S\beta A$ dimer arrangement.	137
Figure 4.7 Q_y dipole moments for sheets formed using the $\alpha S\beta A$ dimer arrangement.	138
Figure 4.8 Initial and final structures for simulations on sheets formed using the $\alpha S\beta Ad$ dimer arrangement.	139
Figure 4.9 Q_y dipole moments for sheets formed using the $\alpha S\beta Ad$ dimer arrangement.	139
Figure 4.10 Initial and final structures for simulations on sheets formed using the $\beta A\beta A$ dimer arrangement.	140
Figure 4.11 Q_y dipole moments for sheets formed using the $\beta A\beta A$ dimer arrangement.	140
Figure 4.12 Initial and final structures for simulations on sheets formed using the $\beta S\alpha A$ dimer arrangement.	141
Figure 4.13 Q_y dipole moments for sheets formed using the $\beta S\alpha A$ dimer arrangement.	142
Figure 4.14 Initial and final structures for simulations on sheets formed using the $\beta S\alpha Ag$ dimer arrangement.	142

Figure 4.15 Q_y dipole moments for sheets formed using the $\beta S\alpha Ag$ dimer arrangement.	143
Figure 4.16 Initial and final structures for simulations on sheets formed using the $\beta S\alpha Au$ dimer arrangement.	143
Figure 4.17 Q_y dipole moments for sheets formed using the $\beta S\alpha Au$ dimer arrangement.	144
Figure 4.18 Initial and final structures for simulations on sheets formed using the $\beta S\beta S$ dimer arrangement.	144
Figure 4.19 Q_y dipole moments for sheets formed using the $\beta S\alpha Au$ dimer arrangement.	145
Figure 4.20 Energy evolution for single layer pigment systems.	146
Figure 4.21 Final energy per dimer of single sheet systems.	149
Figure 4.22 X-ray scattering predictions for single sheet systems.	150
Figure 4.23 RMS pair-wise separation of Mg atoms for single layer pigment systems.	154
Figure 4.24 Initial and final structures for simulations on triple layer systems formed using the $\alpha A\alpha A$ dimer arrangement.	155
Figure 4.25 Q_y dipole moments for sheets formed using the $\alpha A\alpha A$ dimer arrangement.	156
Figure 4.26 Initial and final structures for simulations on triple layer systems formed using the $\alpha S\alpha S$ dimer arrangement.	156
Figure 4.27 Q_y dipole moments for sheets formed using the $\alpha S\alpha S$ dimer arrangement.	157
Figure 4.28 Initial and final structures for simulations on triple layer systems formed using the $\alpha S\beta A$ dimer arrangement.	158
Figure 4.29 Q_y dipole moments for sheets formed using the $\alpha S\beta A$ dimer arrangement.	158
Figure 4.30 Initial and final structures for simulations on triple layer systems formed using the $\alpha S\beta Ad$ dimer arrangement.	159
Figure 4.31 Q_y dipole moments for sheets formed using the $\alpha S\beta Ad$ dimer arrangement.	160
Figure 4.32 Initial and final structures for simulations on triple layer systems formed using the $\beta A\beta A$ dimer arrangement.	161
Figure 4.33 Q_y dipole moments for sheets formed using the $\beta A\beta A$ dimer arrangement.	161
Figure 4.34 Initial and final structures for simulations on triple layer systems formed using the $\beta S\alpha A$ dimer arrangement.	162
Figure 4.35 Q_y dipole moments for sheets formed using the $\beta S\alpha A$ dimer arrangement.	162

Figure 4.36 Initial and final structures for simulations on triple layer systems formed using the β S α Ag dimer arrangement.	163
Figure 4.37 Q_y dipole moments for sheets formed using the β S α Ag dimer arrangement.....	163
Figure 4.38 Initial and final structures for simulations on triple layer systems formed using the β S α Au dimer arrangement.	164
Figure 4.39 Q_y dipole moments for sheets formed using the β S α Au dimer arrangement.....	164
Figure 4.40 Initial and final structures for simulations on triple layer systems formed using the β S β S dimer arrangement.....	165
Figure 4.41 Q_y dipole moments for sheets formed using the β S β S dimer arrangement.....	165
Figure 4.42 Energy evolution for the simulation of triple layer pigment systems.....	168
Figure 4.43 Final energy per dimer of triple layer systems.	169
Figure 4.44 Energy stabilisation for triple layer systems.	170
Figure 5.1 Aliquots of quantum dots taken at various synthesis times.....	176
Figure 5.2 TEM images of CIS quantum dots (220 000x magnification).	177
Figure 5.3 Size distribution histograms of quantum dots from TEM images.....	178
Figure 5.4 Dependence of quantum dot size on synthesis time.....	180
Figure 5.5 Lattice spacings from HR-TEM (690 000x magnification).	181
Figure 5.6 Powder XRD pattern of CIS nanoparticles.....	182
Figure 5.7 Dependence Cu:In ratio on nanoparticle size as determined by EDX analysis.	183
Figure 5.8 XPS survey spectra for CIS nanoparticles of various sizes.	185
Figure 5.9 Detailed XPS spectra used for the determination of elemental ratios of Cu:In for various sizes of nanoparticles.	187
Figure 5.10 Composition: Dependence of copper-indium ratio on nanoparticle size as determined by XPS.	188
Figure 5.11 UV-Vis absorbance of quantum dots with various synthesis times.....	189
Figure 5.12 Tauc plots for determination of band-gap.	191
Figure 5.13 Band-gap of quantum dots as a function of size.	191
Figure 5.14 Second derivative of absorbance used for the determination of E_1	193

Figure 5.15 Position of first excitation of quantum dots as a function of size.	194
Figure 5.16 Reproducibility of E_x and E_1 between batches (different colours).....	195
Figure 5.17 PL emission spectra for quantum dots with various synthesis times.....	197
Figure 5.18 Dependence of PL peak position on NP synthesis time.	198
Figure 5.19 Reproducibility of PL emission between batches (different colours).....	199
Figure 5.20 UV-vis and PL showing the Stokes shift for 1.9 ± 0.3 nm diameter nanoparticles.....	200
Figure 5.21 Dependence of PLQY on nanoparticle size and excitation energy.	201
Figure 5.22 Contour plot of representative PL decay spectrum.....	203
Figure 5.23 Decay associated spectra (DAS) obtained from global analysis fitting.	204
Figure 5.24 Size dependence of fitted peak positions and area fractions.	205
Figure 5.25 Effect of nanoparticle size on energy levels.	207
Figure 5.26 Transient absorption spectroscopy.....	208
Figure E.1 Q_y dipole moments for sheets formed using the $\alpha A\alpha A$ dimer arrangement.	264
Figure E.2 Q_y dipole moments for sheets formed using the $\alpha S\alpha S$ dimer arrangement.	265
Figure E.3 Q_y dipole moments for sheets formed using the $\alpha S\beta A$ dimer arrangement (first repeat).	266
Figure E.4 Q_y dipole moments for sheets formed using the $\alpha S\beta A$ dimer arrangement (third repeat).	267
Figure E.5 Q_y dipole moments for sheets formed using the $\alpha S\beta A$ dimer arrangement (first repeat).	268
Figure E.6 Q_y dipole moments for sheets formed using the $\alpha S\beta Ad$ dimer arrangement.	269
Figure E.7 Q_y dipole moments for sheets formed using the $\beta A\beta A$ dimer arrangement.	270
Figure E.8 Q_y dipole moments for sheets formed using the $\beta S\alpha A$ dimer arrangement.	271
Figure E.9 Q_y dipole moments for sheets formed using the $\beta S\alpha Ag$ dimer arrangement.	272

Figure E.10 Q_y dipole moments for sheets formed using the $\beta S\alpha Au$ dimer arrangement.....	273
Figure E.11 Q_y dipole moments for sheets formed using the $\beta S\beta S$ dimer arrangement.....	274
Figure E.12 Q_y dipole moments for triple layer sheets formed using the $\alpha A\alpha A$ dimer arrangement.	275
Figure E.13 Q_y dipole moments for triple layer sheets formed using the $\alpha S\alpha S$ dimer arrangement.....	276
Figure E.14 Q_y dipole moments for triple layer sheets formed using the $\alpha S\beta A$ dimer arrangement.	277
Figure E.15 Q_y dipole moments for triple layer sheets formed using the $\alpha S\beta Ad$ dimer arrangement.	278
Figure E.16 Q_y dipole moments for triple layer sheets formed using the $\beta A\beta A$ dimer arrangement.	279
Figure E.17 Q_y dipole moments for triple layer sheets formed using the $\beta S\alpha A$ dimer arrangement.	280
Figure E.18 Q_y dipole moments for triple layer sheets formed using the $\beta S\alpha Ag$ dimer arrangement.	281
Figure E.19 Q_y dipole moments for triple layer sheets formed using the $\beta S\alpha Au$ dimer arrangement.	282
Figure E.20 Q_y dipole moments for triple layer sheets formed using the $\beta S\beta S$ dimer arrangement.....	283

Chapter 1

Introduction

This thesis seeks to investigate bacteriochlorophyll (BChl) pigments and quantum dots (QDs) with the view to ultimately produce a novel photonic material.

As a result of their small size, QDs exhibit electronic properties intermediate between those of bulk semiconductors and individual molecules. The electronic and optical properties of these semiconductor nanocrystals may be tuned through the careful control of nanocrystal size and composition. Consequently, they offer a range of attractive photophysical properties with a wide range of possible applications.

Photosynthetic BChls c/d and e pigments self-assemble into densely packed aggregates exhibiting strong excitonic coupling between individual pigments as well as optical spectra substantially different to those of monomeric BChls. These aggregates exhibit impressive light harvesting properties with rapid and efficient energy transfer. Consequently, these pigments provide exciting opportunities for use in nanomaterials.

Coupling BChl aggregates with QDs should lead to strong interaction between energy levels and efficient energy transfer, yielding new hybrid nanostructures with novel electronic and optical properties.

A brief overview of both BChls and QDs is presented in this chapter along with a discussion of how they might be combined to produce such a material. Finally, the key aims and results of this work are summarised.

1.1 BChls c, d, and e

BChl c, d, and e are photosynthetic pigments found exclusively within light harvesting antenna systems called chlorosomes. Bacteriochlorophyll pigments, due to their unique chemical structures self-assemble into higher order structures with dense packing and tight excitonic coupling enabling their host organisms to live in extremely low light environments. Therefore, these

pigments have tremendous potential to be used as building blocks for nanotechnology and optical application including solar energy and sensing. This section gives an overview of the relevant key properties of these pigments as well as providing background on their biological function.

1.1.1 Chlorosomes

Chlorosomes (Figure 1.1) are extramembranous organelles which function as peripheral antenna systems. They are the largest supramolecular antenna system observed to date. They were first discovered in thin sections of cells from *Chlorobi* species by Cohen-bazire et al..¹ They have since been found to be the main light harvesting apparatus in three phyla of green photosynthetic bacteria – a group of anoxygenic phototrophs. These include the green sulphur bacteria phylum *Chlorobi* and some filamentous anoxygenic phototrophs of the phylum *Chloroflexi* (formerly green non-sulfur bacteria). Additionally, chlorosomes have more recently been identified in the bacterium “*Candidatus Chloracidobacterium thermophilum*” – a member of the poorly characterised *Acidobacteria* phylum.² *Chlorobaculum tepidum* and *Chloroflexus aurantiacus* have emerged as model species of the *Chlorobi* and *Chloroflexi* phyla, respectively, with *Chlorobaculum tepidum* being the most studied species of chlorosome containing photosynthetic bacteria and the first chlorosome containing bacterium to have its full genome sequenced.³ Chlorosomes from the three phyla are similar, despite significant differences in the rest of their photosynthetic apparatus, suggesting that a horizontal gene transfer may have been responsible for their presence in three unrelated phyla.⁴

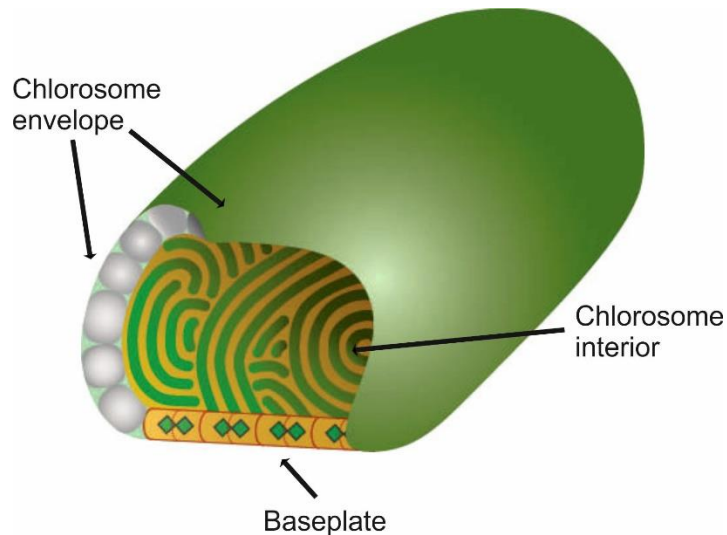


Figure 1.1 Schematic showing shape and basic structure of a chlorosome.

The chlorosome envelope, whilst originally believed to be a lipid monolayer is now thought to consist primarily of proteins with a small number lipid molecules filling in the gaps between. The chlorosome is bound on one side by a BChl a and CsmA containing baseplate which is responsible for transferring energy from the chlorosome onwards towards the reaction centre. Within the chlorosome core, BChl c/d/e molecules aggregate to form lamellar layers (Image taken from Psencik et al.).⁵

1.1.2 Structure of Chlorosomes

The size and shape of chlorosomes have been widely studied using transmission electron microscopy (TEM) demonstrating that both size and shape vary widely between species as well as depending sensitively on growth conditions (Figure 1.2). An ellipsoidal form, with typical dimensions of 150 – 200 x 50 x 25 nm, was reported for chlorosomes from *Chlorobaculum tepidum*. Chlorosomes from other species may differ in size by up to a factor of five. Irregularly shaped chlorosomes with an undulating surface were observed for “*Candidatus Chloracidobacterium thermophilum*”. Rough surface features have also been observed using atomic force microscopy (AFM) for both *Chlorobaculum phaeobacteroides* and *Chlorobaculum vibrioforme*.⁶

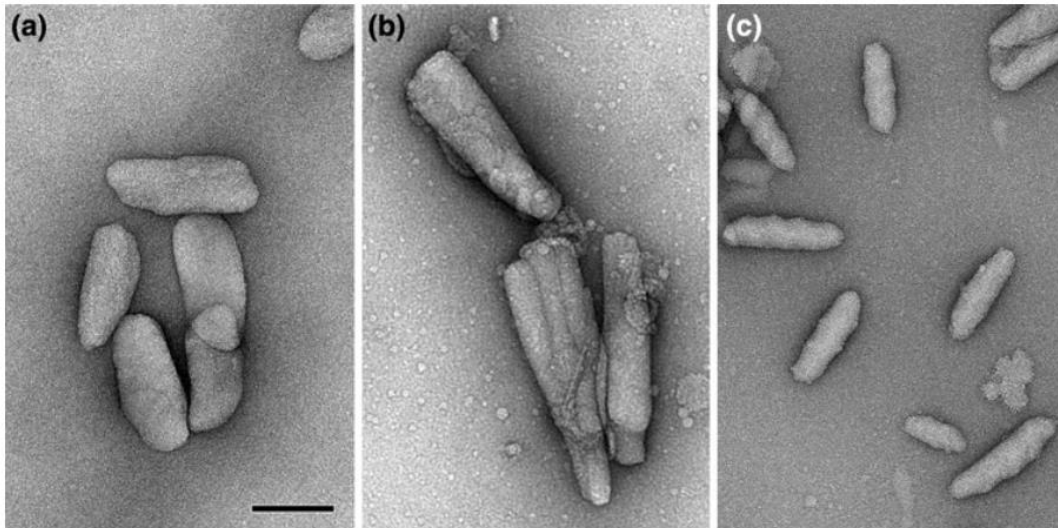


Figure 1.2 Cryo-Electron microscopy (Cryo-EM) images of chlorosomes.

(a) ellipsoidal chlorosomes from *Chlorobaculum tepidum* wild type, (b) conical chlorosomes from the *Chlorobaculum tepidum* triple mutant bchQRU, and (c) irregular chlorosomes from “*Candidatus Chloracidobacterium thermophilum*”. Scale bar = 100 nm. (Image taken from Oostergetel et al.).⁷

Additionally, with approximately 200 000 – 250 000 BChl c/d/e molecules residing in the chlorosome core,⁸ the supposed pigment content in chlorosomes far exceeds estimates for other photosynthetic complexes. By dry weight, chlorosomes are approximately 50% BChl c, d or e, 30% protein 10% lipids. The remaining fraction consists of carotenoids, quinines, and BChl a.⁹ Estimates for the number of BChl c/d/e molecules vary widely due to batch to batch ($50 - 500 \times 10^3$) variations in chlorosome dimensions as well as various assumptions used in methods to determine the volume and BChl fraction within chlorosomes.

Early freeze-fracture work by Staehelin et al.^{10,11} indicated that the chlorosome core was bound by a lipid layer which was approximately 3 nm thick. This was later confirmed by cryo-EM.⁷ The thickness and the absence of an observed regular structure is suggestive of a lipid monolayer rather than a lipid bilayer. However, estimates of the lipid content of chlorosomes suggest that there are

sufficient lipid molecules to cover only 5% of the envelope surface. The remaining portion of the surface likely consists of proteins with a small number of polar lipid molecules filling in the space in between¹² with their polar heads oriented towards the cytoplasm.¹³

Chlorosomes also contain a baseplate (Figure 1.1), located on one side of the chlorosome which plays a vital role in the transfer of excitonic energy from the chlorosome downstream towards the bacterial reaction centres located in the plasma membrane.¹⁴ It has been proposed that the highly ordered baseplate may be responsible for the long range order observed for BChl aggregates within the chlorosome core.^{15,16} The baseplate is formed by multiple copies of the BChl a coordinating protein CsmA which accounts for up to 50% of all protein mass in chlorosomes⁴ and has been shown to be the only protein necessary for chlorosome formation.⁴ Pedersen et al.¹⁷ described a baseplate model constructed from nuclear magnetic resonance (NMR) structural data for CsmA, with circular dichroism, and simulations of optical spectra for the CsmA–BChl a complex, in which CsmA dimers were used as the basic unit. In this model, two BChl a molecules are coordinated at the dimer interface by histidine side chains. Additionally, it is anticipated that a fraction of chlorosomal carotenoids resides in close proximity to the BChl a molecules to enable the molecular overlap required for the protective quenching of BChl a triplet state.¹⁸

The photosynthetic BChl c/d/e pigments, essential for the function of the chlorosome, are contained within the chlorosome interior. Unlike all other known antenna systems, these pigments self-organise into higher order structures; they maintain distances and mutual orientations without forming protein complexes. The chlorosome interior also contains carotenoids, quinines, and, in the case of thermophilic species, non-polar lipids.

The self-organisation of BChls within chlorosomes may be divided into two distinct levels: the molecular level organisation of pigments into aggregates and the long range organisation of these into larger structures.

1.1.3 Molecular organisation of BChl molecules

Bacteriochlorophyll c, d, and e are found exclusively in chlorosomes. Despite their name, they are not bacteriochlorophylls (Figure 1.3) like the BChl a molecules found in the baseplate. However, these pigments were isolated from bacteria and named before knowledge of their chemical structure.

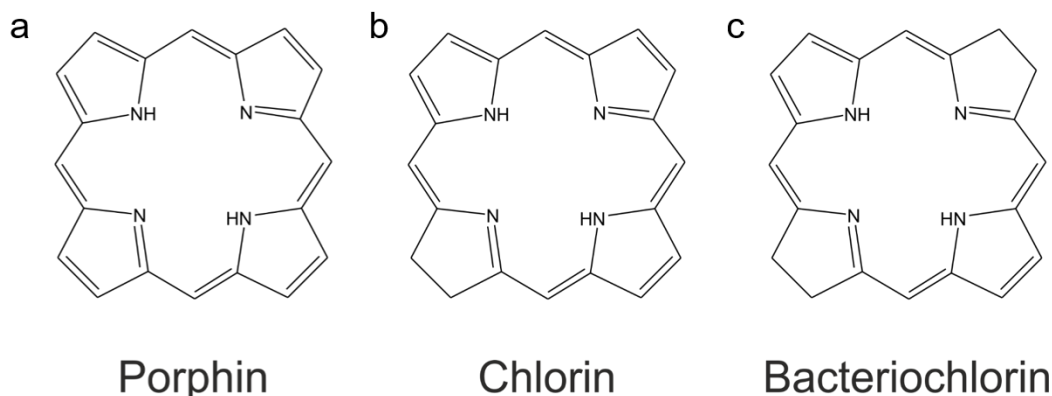


Figure 1.3 Basic structures of chlorins, bacteriochlorins and porphins.

Bacteriochlorophyll a is a true bacteriochlorophyll with a structure based on bacteriochlorin. Bacteriochlorophylls c, d, and e, in common with chlorophylls are based on a chlorin ring.

Instead their chemical structure is based on a chlorin ring as commonly found in plant chlorophylls. Chlorins differ from bacteriochlorins by the presence of a double bond between C7 and C8. Also, spectrally, Bacteriochlorophylls c, d, and e are similar to their chlorophyll counterparts. BChl c has peaks at 436 and 668 nm in CCl₄. Consequently, BChl c has an absorption spectrum nearly identical to that of Chl a.¹⁹ BChl e has a spectrum similar to that observed for Chl b.

BChl c, d, and e differ from each other in modifications at the C20 position (Figure 1.4) – where BChls c and e have methyl – and the C7 where BChl e has an aldehyde group. The fourth possible combination, BChl f, which harbours an aldehyde at C7 and hydrogen at C20 has been synthesised and characterised.²⁰ In addition, a BChl f accumulating mutant of *Chlorobaculum*

limnaeu, which usually produces BChl e, was recently produced by knocking out the *bchU* gene encoding C20 methyltransferase.²¹

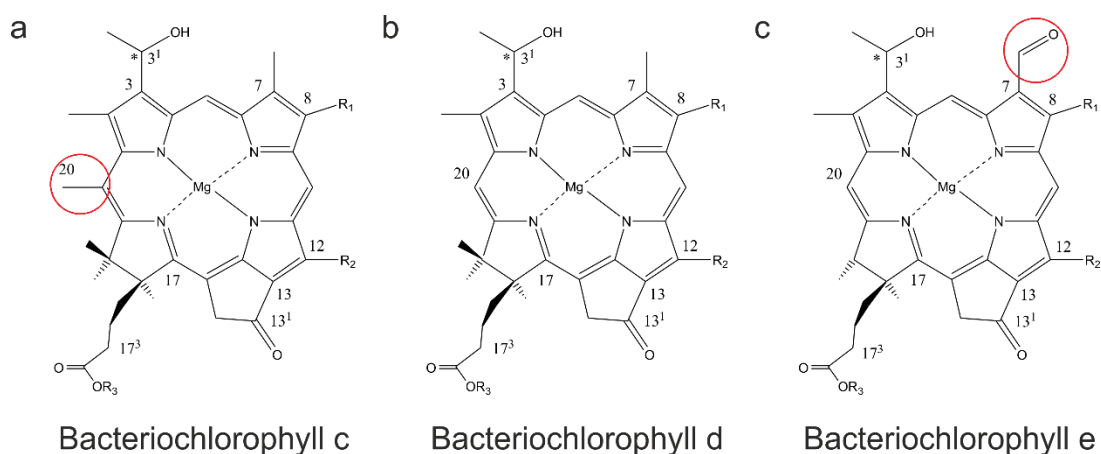


Figure 1.4 Structure of different bacteriochlorophylls.

Bacteriochlorophyll c, d, and e differ at the C20 and C7 positions. BChls c and e have methyl at C20 and BChl e has an aldehyde group at C7.

Naturally occurring BChls exist as a mixture of homologues in chlorosomes of *Chlorobi* species. These homologues are divided into two classes, namely primary homologues, which differ in substituents of the chlorin ring (carbons C8 and C12) and secondary homologues that harbour different esterifying alcohols at the C17³ propionic acid. The presence of various primary and secondary homologues have also been confirmed for *Acidobacteria*.²² *Chloroflexi* only possess a single primary homologue (ethyl at C8 and methyl at C12) together with multiple secondary homologues.

BChl c, d, and e pigments are able to self-assemble into aggregates due to the presence of a hydroxyl group at asymmetric C3¹ and the absence of a bulky carboxymethyl group at C13² (Figure 1.4).²³

The chemical groups involved in aggregation have been identified largely by vibrational spectroscopies.^{9,14} The key interaction leading to aggregation is thought to be the intermolecular coordination of the central Mg ion of one BChl molecule to the hydroxyl group at C3¹ of a second BChl. Additionally, an H-

bond may form between the hydroxyl at C3¹ of the second BChl and keto group at C13¹ of the third BChl molecule²⁴ (Figure 1.4). However, this has recently been questioned and an alternative model, in which the C13¹ keto group of the second BChl is weakly coordinated to the central Mg ion of yet another BChl within the aggregate, has been proposed.²⁵ These interactions are in principle compatible with a number of molecular arrangements,²⁶ of which three categories have received the most attention (Figure 1.5). These are the parallel monomer model,^{25,27,28} the anti-parallel piggy-back dimer,^{29–31} and the syn-anti parallel dimer model.³² The parallel monomer model would appear unlikely given the need for the hydrophobic esterifying alcohol chains that stabilise the system to point in opposite directions³³ (Figure 1.3). This requirement is met by both the anti-parallel piggy-back dimer model and the syn-anti parallel dimer model.

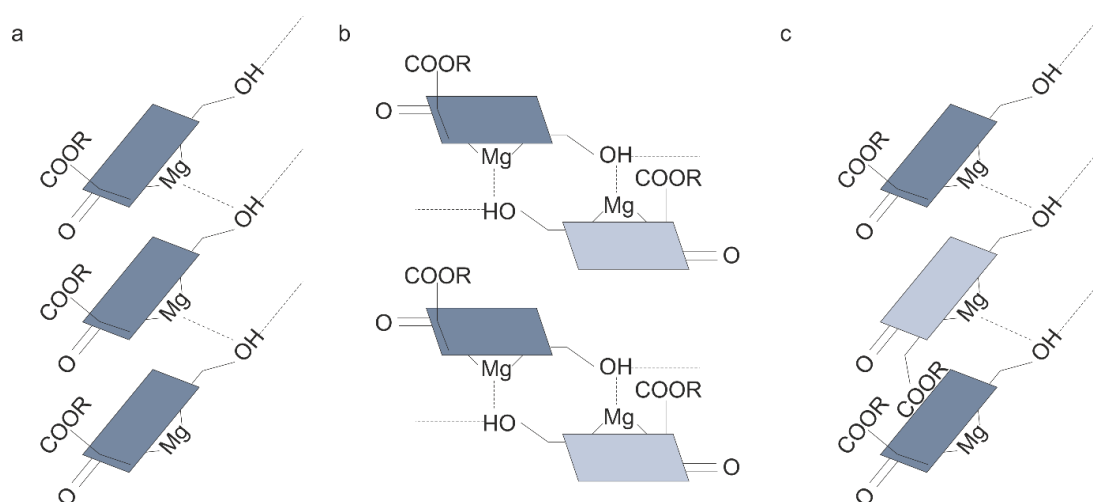


Figure 1.5 Schematic representation of structural models proposed for BChl aggregates.

(a) Parallel-stack model, (b) Piggy-back dimer model, and (c) Syn-anti dimer model. (Image adapted from Ganapathy et al.).³²

Higher resolution cryo-Em images of *Chlorobaculum tepidum* chlorosomes and their calculated diffraction patterns indicate the presence of a smaller spaced regular structure in the direction of the long axis in addition to long range lamellar ordering. In wild-type chlorosomes, a weak periodicity of 1.25 nm is present whereas, in the bchQRU mutant a strong periodicity of 0.83 nm is evident from the diffraction pattern and also directly visible in the electron

micrograph images. The smaller spacing in the bchQRU triple mutant is ascribed to the absence of side chain heterogeneity at C8 and C12, the limited stereochemical heterogeneity at C3¹ and the absence of a methyl group at C20.

X-ray diffraction studies on partially oriented chlorosomes and BChl aggregates have yielded information on the size of the asymmetric unit as well as the approximate orientation of the lattice with respect to the long axis of the chlorosome.³⁴ Both the anti-parallel piggy-back dimer model and the syn-anti parallel dimer models fulfil the limits implied by X-ray experiments. In addition to the most intense lamellar peak (spacing about 2.1 nm), the X-ray scattering patterns of *Chlorobaculum tepidum* exhibit two peaks (Bragg spacing ~0.94 and ~1.17 nm) that have been assigned to the chlorin ring lattice within individual lamellar layers.³⁵ These three values define a monoclinic unit cell which is too large to contain just a single BChl molecule but can accommodate two BChl molecules.

High resolution magic angle spinning solid state NMR measurements were performed on chlorosomes from the *Chlorobaculum tepidum* triple mutant bchQRU. Both the alternating syn-anti ligated BChl stack and the antiparallel monomer are consistent with the inter-stack distances derived from NMR data.³² However, when these stacks are combined into sheets, several inter-stack distance for the anti-parallel monomer stacking configuration are larger than those derived from NMR measurements. Syn-anti monomer stacks are, however, consistent with the observed distance constraints.

Ring current shift calculations were performed for the syn-anti monomer stacks, the anti-parallel monomer model and two earlier structural models that were proposed for BChl c in chlorosomes: the monomer-based parallel stack model)²⁸ and the piggy-back dimer model.²⁹ Calculations on the syn-anti monomer stack and the parallel stack reproduced the experimentally observed shifts. As only the syn-anti monomer stack satisfies the NMR distance constraints. This model is consistent with both theoretical, NMR, X-ray, and EM observations.³²

1.1.4 Long range ordering of BChl aggregates

The organisation of BChl aggregates into higher order structures has been the subject of much debate. Early freeze-fracture electron microscopy (EM) work on unstained chlorosomes by Staehelin et al.^{10,11} indicated the presence of rod-shaped structures with diameters of approx. 5 and 10 nm in *Chloroflexus aurantiacus* and *Chlorobium limicola*, respectively. In addition, a striation pattern usually parallel to the long axis was observed.^{10,11} The calculated diffraction pattern indicated a strong diffraction spot equivalent to a spacing of ~2.1 nm. Further EM studies observed a striation pattern with a spacing of ~2 nm for chlorosomes from *Chlorobaculum tepidum*^{34,36} and a larger 2.6 – 4 nm spacing for species of *Chloroflexus aurantiacus*.³⁷ Similar features were also observed in the micrographs of Cohen-bazire et al.¹ who were the first to observe chlorosomes.

Comparable spacings (2.1 nm for *Chlorobaculum tepidum*, 3.3 nm for *Chloroflexus aurantiacus*) were obtained from solution X-ray scattering.³⁷ The observed scattering pattern was consistent with the lamellar phase observed in the case of other amphipathic molecules such as lipids and block copolymers.

The ~2 nm spacing seen in electron micrographs and evident from X-ray scattering appears at first to be inconsistent with the observation of 5 – 10 nm rods. However, Psencik et al.³⁵ interpreted the 2.1 nm spacing as the distance between lamellae oriented parallel to the long axis and, based on the extent of the striations, appear to persist over the entire length of the chlorosome (Figure 1.6). Cryo-EM tilt series experiments indicated that this lamellar system could not be planar, but must in fact be curved. This led to the proposal of a model of undulating lamellar arrangements of pigment aggregates for three different *Chlorobi* species.³⁵

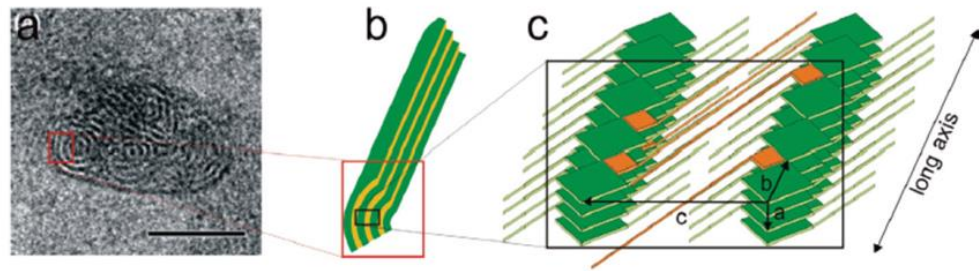


Figure 1.6 The curved lamellar system in chlorosomes.

(a) End on views of chlorosomes from EM, (b) schematic interpretation, and (c) schematic of Bchl stacking (green = BChl c, orange = carotenoids). (Image taken from Psencík et al.).⁵

An important insight into the lamellar arrangement of BChl aggregates was provided by cryo-EM performed on intact chlorosomes of both the *Chlorobaculum tepidum* wild type and bchQRU mutant.³⁶ End-on views of these chlorosomes, fixed vertically and embedded in a thicker layer of ice, helped elucidate the arrangement of BChl sheets and their packing. Images of chlorosomes from the wild type indicated the presence of disordered multi-lamellar tubular structures of variable diameter (10 – 30 nm) with some non-tubular locally curved lamellae in between. In the case of the bchQRU mutant, chlorosomes had two tubular domains. For both types of chlorosomes, cryo-EM shows that these multi-lamellar tubular domains extend over most of the length of the chlorosome, and are embedded in a matrix of less well ordered smaller curved lamellar domains. This model is consistent with both the early freeze fracture experiments, X-ray scattering studies, and the more recent cryo-EM observations.

Images from the above cryo-EM experiments have been used to produce an idealized internal structural model consisting of lamellar cylinders.³² However, completely closed cylindrical features are unlikely to be prevalent among wild type chlorosomes. Hexane-wash experiments showed that inter-lamellar spacing decreases on removal of carotenoids and other lipophilic molecules – a transition unlikely to be possible for the closed concentric cylinders proposed. Additionally, anisotropy in X-ray scattering results³⁴ and the extent

of the observed intrinsic disorder³⁸ in wild type chlorosomes do not support a model consisting entirely of closed cylinders.

The observed variability in higher order arrangements between wild type and mutant chlorosomes notwithstanding, BChl aggregate organisation is always in the form of repeating layers and is found to differ only in the extent of the long range order. The existence of a lamellar structure is believed to be a consequence of hydrophobic interaction due to the alternation of the relatively polar stacked chlorin rings and the interdigitating hydrophobic esterifying alcohol chains. The interdigitating esterifying alcohols protrude in both directions from the layer containing stacked chlorin rings, most likely due to alternating orientations of chlorin rings within BChl stacks, allowing interactions between esterifying alcohols from adjacent layers.

The tilt-series experiments and end-on-views revealed significant fragmentation in the lamellar system perpendicular to the chlorosome long axis, as well as the existence of distinct domains with different orientations with respect to this axis. Such domains, whilst occasionally present in *Chlorobaculum tepidum* were particularly pronounced in chlorosomes from *Chlorobaculum phaeobacteroides* which have BChl e as the primary pigment.³⁸ Physiologically, such fragmentation and the existence of domains may confer an advantage for light harvesting. The largest transition dipole moment (Figure 1.7) of BChl molecules is oriented in a direction parallel to the lamellar layers, consequently the orientation disorder afforded by the existence of these domains, allows chlorosomes to capture photons with different polarisations more effectively. This is advantageous for chlorosome containing bacteria that are found in extremely low light conditions. Additionally, the existence of these domains provides an explanation for the rough surface features of chlorosomes as observed by both EM and atomic force microscopy (AFM).^{6,38}

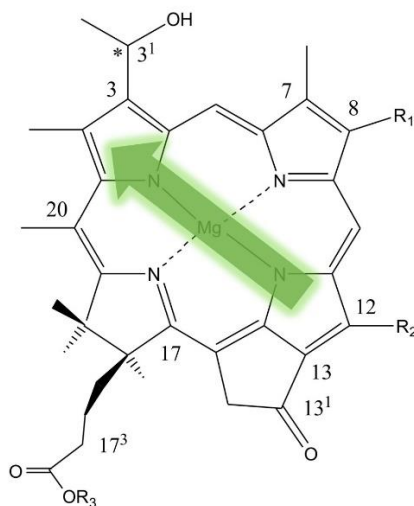


Figure 1.7 Q_y transition dipole moment.

The transition dipole moment is shown for BChl c. In lamellar sheets, the transition dipole moments are orientated parallel to the layers.

The effect of the length of the esterifying alcohol harboured at the C17 position of the BChl molecule has been investigated in in vitro assembled BChl c analogues.³⁴ A linear dependence between chain length and lamellar spacing was observed which, extrapolated to zero, yielded an inter-lamellar spacing of 1.1 nm – the approximate diameter of the chlorin ring. The experimental spacing of 2.1 nm observed for *Chlorobaculum tepidum* is in good agreement with this prediction. The observed increase in spacing of 0.08 nm per carbon corresponds to the projection of the chain in the direction of the spacing. Based on comparison with the projection of the C-C bond length in the direction of the chain, which gives an increment per carbon twice the observed value, the esterifying alcohol chains are believed to be either extensively twisted (gauche conformers) and/or to have their average direction at an angle to the spacing.

Experimentally observed spacing for both brown coloured species, *Chlorobaculum phaeobacteroides* and *Chloroflexus aurantiacus*, are far higher than those predicted. Both species contain longer esterifying alcohols e.g., BChls harbouring octadecanol in *Chloroflexus aurantiacus* and a higher proportion of secondary homologues in brown-coloured species which are longer than farnesyl. The existence of longer esterifying alcohol chains is

thought to be necessary to increase the inter-lamellar space to allow the inclusion of the greater numbers of carotenoids found in these species within the hydrophobic space. BChl e containing species exhibit both longer alcohol chains and higher carotenoid levels. This is likely to be important for light harvesting as these species typically inhabit deep water low light environments where the spectrum of available light overlaps with the spectral region of carotenoid absorption. Additionally, a link has been identified between an increase in inter-lamellar spacing and disorder within the lamellar system^{37,38} as manifested by a greater spread in the distribution of inter-lamellar spacing and the existence of distinct domains.

Brune et al.³⁹ showed that washing intact chlorosomes with hexane effectively removed carotenoids without otherwise disrupting chlorosomes. When the inter-lamellar spacings of native and hexane washed chlorosomes from *Chlorobaculum phaeobacteroides* were compared, a decrease was observed in the case of hexane washing³⁸ and the resulting inter-lamellar spacing was close to the value predicted on the basis of the esterifying alcohol chain length.

1.1.5 Spectroscopic properties of chlorosomes

BChls are known to have two transition bands in the visible region.⁴⁰ For BChl c these are the peaks mentioned above at 436 and 668 nm in CCl₄. These bands are referred to as the Soret (*B*) and *Q* bands respectively. The lower wavelength Soret band consists of two overlapping bands, *B_x* and *B_y*. The *Q* band can also be decomposed into two bands, *Q_x* and *Q_y*. Of these, the *Q_y* band has the higher cross section and contributes more to the absorbance spectrum. The *Q_x* band, which has a higher transition energy, only has a minor absorbance intensity. The *Q_x* and *Q_y* transition dipoles are nearly parallel to the vectors from the central Mg to the nitrogen atom as shown above in Figure 1.7.

The optical spectra of chlorosomes are remarkably different from those of the monomeric BChls they contain (Figure 1.8). On aggregation of BChl molecules, a pronounced red shift in the position of the *Q_y* absorption band is

observed (Figure 1.8). The peak shifts from 668 to 745 nm, from 655 to 730 nm and from 654 to 715 nm for BChl c, d, and e respectively. Changes in the Soret band within the blue region of the spectrum are observed on aggregation though these are usually far more subtle than those observed for the Q_y band with the exception of BChl e. On aggregation of BChl e, splitting of the Soret band and a bathochromic shift in the B_y band is observed due to the strong coupling between the B transition dipole moment.⁴⁰ As discussed previously, BChl e containing species inhabit some of the lowest light environments and there is a significant physiological advantage to the enhanced spectral coverage in the 500 – 600 nm spectral region afforded by these changes.

These changes are due to the dense packing of BChl molecules afforded by their ability to self-assemble into aggregates. This dense packing and the alignment of the Q_y transition dipole moments of the molecules (due to the hydrogen bonding network within lamellar planes) leads to strong excitonic coupling (estimated coupling energy -750 to -550 cm^{-1})⁷ between BChl molecules that is similar to J-aggregates, in which molecules are arranged in linear stacks with a head-to-tail transition dipole moment orientation. The strong excitonic coupling leads to excitation delocalisation over BChl pigments and splitting of the energy levels into a number of exciton states and redistribution of the oscillator strength.

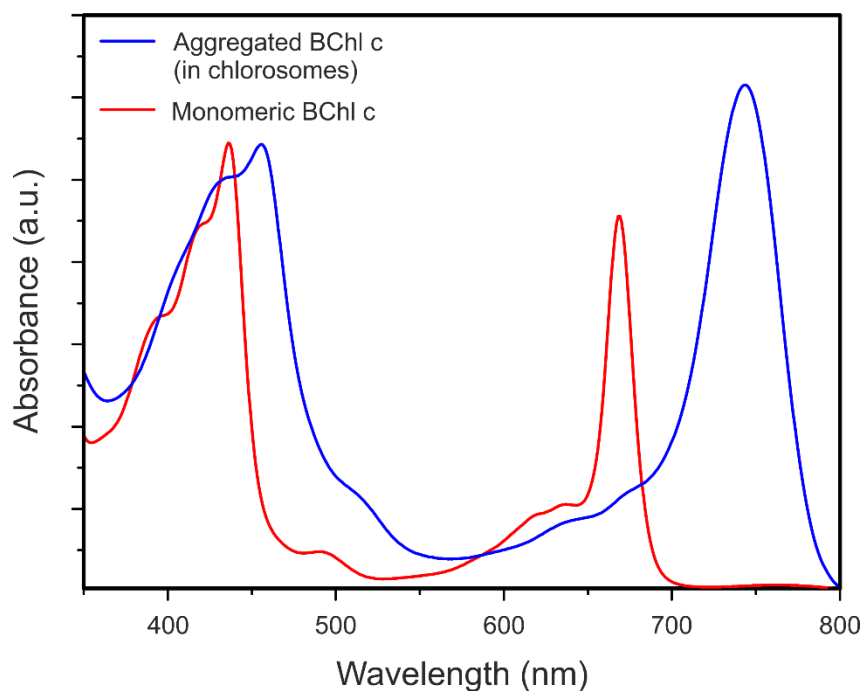


Figure 1.8 Absorption spectra for chlorosomes and monomeric BChl c in methanol.

On aggregation of BChl c, the dense packing and alignment of the Q_y dipole moments leads to strong excitonic coupling. Excitation is delocalised over BChl pigments and energy levels are split into a number of exciton states with redistribution of the oscillator strength. (Own data).

Whilst the spectra of BChl aggregates are similar to those of J-aggregates, there are notable differences; most significantly is the absence of exchange line narrowing.⁷ Such narrowing would reduce the spectral coverage of the chlorosomes and be detrimental to light harvesting. Line narrowing is absent even when aggregates of BChl are produced *in vitro* using single isomers.⁴¹ A further increase in band-width is observed for BChl aggregates in chlorosomes that contain epimers and homologues as can be seen by comparing spectra of chlorosomes extracted from *Chlorobaculum tepidum* and *Chloroflexus aurantiacus*. In *Chlorobaculum tepidum* BChl c is found as a mixture of several primary (and a number of secondary homologues) and has a Q_y band with a full-width-half-maximum (FWHM) of ~50 nm compared to chlorosomes of *Chloroflexus aurantiacus*, which harbour only a single

primary homologue of BChl c which has a Q_y band FWHM of ~30 nm. However, more recent results for "*Candidatus Chloracidobacterium thermophilum*" do not follow this trend.⁴² The Q_y absorption band for chlorosomes from this species was much narrower than that of chlorosomes from *Chlorobaculum tepidum* and was blue-shifted by about 10 nm relative to that of *Chlorobaculum tepidum*. However, the absorption spectrum was similar to that of chlorosomes of *Chloroflexus aurantiacus* – despite previous studies using reverse phase high pressure liquid chromatography (HPLC) and mass spectrometry, which indicated the existence of a complex mixture of BChl c homologs.²²

Linearly polarized light can be used to obtain information on the orientations of the main exciton transitions. These are dependent on pigment orientation as well as the organization of the BChl molecules within chlorosomes. The hydrogen bonding pattern within BChl aggregates acts to keep the Q_y transition dipole moment of the BChl molecules parallel to the lamellar system, which is itself generally parallel to the long axis of the chlorosome. Consequently, it is expected that the strongest exciton transitions of this band should be approximately oriented parallel to the chlorosome long axis. In the case of perfect cylinders, theoretical models predict that this would correspond to the strongest transition being polarized parallel to the long axis of the cylinder.⁴³ Linear dichroism measurements have been performed on chlorosomes from *Chloroflexus aurantiacus*^{44–48} and various *Chlorobi* species.^{49,50} Values ranging from 15° to 27° were obtained for the angle between the transition dipole moment of the Q_y band and the long axis of the chlorosomes for chlorosomes from *Chloroflexus aurantiacus*.

In addition to ensemble LD measurements, single molecule spectroscopy studies have been carried out on individual chlorosomes (for a review see e.g. Saga et al.).⁵¹ Significant disorder at a single chlorosome level manifests itself in relatively broad absorption spectra which are observed for individual chlorosomes. Furthermore, polarisation measurements suggest that the observed single chlorosome fluorescence at low temperatures is due to the existence of multiple transition dipoles with different orientations.^{52,53}

Fluorescence-detected three-dimensional LD combined with absorption LD on individual isolated chlorosomes also revealed a significant amount of disorder on the single-chlorosome level.⁵⁴ These measurements showed that the Q_y exciton transition dipoles have a larger angle to the chlorosome axis when monitored from the top than from the side. This is consistent with polarization anisotropy of fluorescence spectra obtained from single chlorosomes isolated from *Chlorobaculum tepidum* which showed that whilst the dominant component of the Q_y transition is parallel to the long axis of the chlorosome, the components in the direction of the chlorosome height and width are not equal.⁵³ The component of the Q_y transition in the direction of the width is larger than that in the direction of the chlorosome's height. This anisotropic distribution of emitting transition dipoles within a single chlorosome is proposed to be due to the lack of rotational symmetry in the pigment arrangement and the asymmetric orientation of the curved lamellar system. The triple mutant bchQRU exhibited a more symmetric distribution of emitting transition dipoles,⁵⁴ consistent with the previously observed highly ordered internal structure that consists of closed lamellar cylinders.³⁶

Strong circular dichroism (CD) has been observed for chlorosomes, however, a large degree of variation has been observed for different growth conditions and preparations of chlorosomes from the same species. The long range ordering of BChl aggregates into curved lamellar structures effectively creates helices from the linear chlorin stacks. The strong dichroism is a consequence of the resulting local helicity in the transition dipoles. Theoretical models indicate that the curvature is necessary as planar structures lead to only weak CD.⁵⁵ It has however been proposed that continuous regions exhibiting alternating curvature would cause the observed CD signal to vanish. End-on-views of chlorosomes have shown that this is avoided by the separation of such regions by fragmentation.³⁶ The large variability in CD spectra may be explained by the fact that circular dichroism has been predicted to depend on the length of aggregate in both closed, helical cylindrical aggregates⁴³ and in certain open curved structures.⁵⁵

1.1.6 Excitation energy transfer in chlorosomes

Fast photophysical processes in chlorosomes have been studied by several groups. Femtosecond transient absorption spectroscopy studies^{56,57} and two-colour absorption difference profiles⁵⁸ revealed that Q_y band excitation of BChl aggregates in *Chloroflexus aurantiacus* and *Chlorobaculum phaeobacteroides* is followed by a rapid exciton relaxation, within 1 ps. Subsequently, long-range energy transfer processes within aggregates led to excitation equilibration over the whole chlorosome.⁵⁶ From BChl c/d/e aggregates energy is transferred to BChl a molecules within the baseplate. Excitation energy transfer (EET) from bulk BChl aggregates to baseplate BChl a has been studied for a number of species with large differences observed for the speed of such transfer. For example, transfer times of 10 ps have been observed in *Chloroflexus aurantiacus*^{57,58} whilst far longer times were observed for the major component of EET (timescale of 120 – 130 ps) for chlorosomes from *Chlorobium phaeobacterioides*.⁵⁶ As EET within chlorosomes is sensitively dependent on pigment organisation, it is not surprising that there should be such variations between species.

Dostál et al.⁵⁹ used two-dimensional electronic spectroscopy to investigate the first 200 fs after excitation by monitoring the evolution of the 2-dimensional spectral line-shape. The excitation dynamics were explained by proposing a model of effective diffusion-like behaviour of the excitons. For perfectly periodic aggregates, it is expected that strong resonant coupling will result in energy eigenstates delocalised over the whole system. This is not the case for significantly disordered systems where a distribution of transition frequencies and couplings between molecules are observed. The observation of these distributions implies the existence of a number of regions or domains, which are separated by high local energetic or structural dislocation. It is not possible, in such cases, for the wave function of the aggregate's excited state to be fully delocalised over the whole system. However, delocalisation should remain over individual "coherent domains". Energy diffuses rapidly among and within coherent domains of the chlorosome after an initial excitation event. Due to the intrinsic static disorder within chlorosomes, it was impossible to

rule out the existence of coherent transfer on a shorter time scale. The model implies rapid dephasing between coherent domains due to energy diffusion. As a result, the electronic phase relationship between different domains is lost suggesting that overall energy transfer within chlorosomes cannot be mediated by coherent processes.

1.1.7 In vitro BChl aggregates

Aggregates of both chlorosomal BChls and their synthetic analogues have been prepared *in vitro* in non-polar and polar environments and have been found to produce similar spectra to chlorosomes.

Self-aggregates of chlorosomal BChl c were first reported by Bystrova et al.⁶⁰ who observed that the self-aggregates, formed in hexane with small amounts of carbon tetrachloride. These exhibited similar absorption bands to those of chlorosomes with a large red shift compared with those of monomeric BChls in diethyl ether. Aggregates with a long wavelength maximum were later observed for BChls c, d, and e in 0.5% (v/v) dichloromethane-hexane.⁶¹ Subsequently, self-aggregates of natural BChls have been reported by a number of groups and are commonly used for investigating properties of chlorosomal aggregates.^{39,62-70}

In chlorosomes, the BChl self-aggregates exist within a microheterogeneous hydrophobic environment provided by the lipid monolayer. In aqueous environments BChl molecules are hardly soluble and are found to form dimers. By mimicking the microheterogeneous hydrophobic condition of the chlorosome interior, BChl aggregates have also been prepared *in vitro* in aqueous environments.⁷¹⁻⁷⁴ Monogalactosyldiacylglycerol (MGDG), the primary lipid constituent of the chlorosome envelope, has been used to prepare a number of BChl aggregates *in vitro*. In these studies, BChl aggregates formed in the stable hydrophobic environment provided by the MGDG. Chlorosome components (BChl c, carotenoids, lipids, and BChl a) extracted using either chloroform or chloroform/methanol mixtures have also been shown to effectively reassemble into chlorosome-like entities in aqueous environments.^{73,75,76} These assemblies, not only share similar absorption and

CD spectra to chlorosomes, but were revealed by electron microscopy and X-ray scattering³⁴ to have similar structures. Concentrated solutions of BChl c in polar solvents also form aggregates similar to those found in chlorosomes when diluted with a large volume of water.⁷⁵ Individual epimers of BChl c homologs formed aggregates in dichloromethane and in a 1:1 solvent mixture for dimethylsulfoxide and water. This approach overcomes both the solubility problem encountered for BChls in aqueous environment and the difficulty experienced in dispersing them.

A number of semi-synthetic and fully synthetic BChl analogues have been produced (for a review see Balaban et al.).⁷⁷ Such compounds are useful as they overcome the instability and heterogeneity (stereoisomers and homologues) of natural pigments. The majority of these analogues contain zinc as the central atom rather than magnesium and thus are less prone to demetallation and opening of the macro-ring. They are readily prepared by treating free base versions of naturally derived complexes with zinc acetate under relatively mild conditions. Self-aggregates of zinc BChl analogues have been widely reported (see for example Tamiaki et al., Tamiaki et al., and Cheng et al.)⁷⁸⁻⁸⁰ both in polar and non-polar environments. The first of these showed that homolog mixtures of zinc methyl bacteriopheophytins c and d self-aggregated in 0.5% (v/v) dichloromethane-hexane to produce oligomers with significantly blue shifted Q_y absorption maxima of 728 and 716 nm, respectively – similar to magnesium containing aggregates.⁸⁰ Due to their similar properties to chlorosomal aggregates, zinc aggregates have since been used as a model for chlorosomes. As zinc containing chlorins are found to occur naturally in the acidophilic bacterium *Acidiphilium rubrum*⁸¹ it is not surprising that they provide a good model for chlorosomal aggregates.

In addition to zinc-bacteriopheophyrins, both semi-synthetic and fully synthetic pigments have been produced featuring a range of central metal atoms including Mn, Fe, Co, Ni, Cu, Pd, Ag, and Cd (see for example Tamiaki et al.).⁸² The aggregation properties of chlorins containing a variety of metals have been extensively studied. Neither Ni, Ag, Cu nor Pd containing chlorins have been shown to self-aggregate in hexane.^{61,82} However, Co containing chlorins were found to self-aggregate in 1% tetrahydrofuran : hexane and Mn

and Fe containing chlorins were found to fully and partially dimerize respectively. Cd chlorins were observed to self-aggregate in dried thin film as well as in non-polar solvents.^{83,84}

1.1.8 Theoretical description of BChls and their aggregates

Theoretical studies on bacteriochlorophylls seeking to elucidate interactions between key groups and the nature of aggregation have been limited to quantum mechanical (QM) studies and molecular mechanics (MM) simulations on a relatively small number of pigments.

³¹R-[E,M] BChlide d aggregation was explored by Holzwarth and Schaffner²⁸ who sought to explain the rod model of BChls in chlorosomes. Using monomer, trimer, pentamer, and decamer stacks with the Mg-hydroxyl coordination as the basic interaction element, strong interactions were observed for extended stacking of chlorins in van der Waals contact. In addition, large energy stabilisation was found to arise from the extended hydrogen bonding network brought about by OH...O=C bonding and electrostatic interactions. Structural features of large aggregates were found to agree well with both spectroscopic and low-resolution structural information from chlorosomes and *in vitro* BChl aggregates. The authors extrapolated the determined structural parameters including the rotation angle between stacks and a stack-stack distance to produce tubular structures with diameters corresponding to those proposed for the rod model of BChl aggregation in *Chloroflexus* species.

A subsequent study by Ganapathy et al.³² investigated the properties of a syn-anti structure by performing MM optimisation of six stacks of 12 interacting BChl d molecules. A single syn-anti pair was taken from this structure and used to construct a larger tubular structure. The electron density of this structure was calculated and projected down the central axis to produce side views that could be compared with cryo-EM data. These simulated images and their Fourier transforms were found to reproduce the 0.83 nm periodicity and striped appearance revealed for the concentric cylinders of the BChl d triple mutant bchQRU.

Simulations on artificially curved single, double, and multiple concentric rod structures as well as lamella and Archimedean spirals formed from 3¹R-[E,M] BChl c have been performed. The effects of length, width, diameter, curvature and orientation of dipole moments⁵⁵ were investigated. MM calculations were used to produce stable optimised aggregates with a number of structural motifs divided into rods built from homogeneous arrays where BChls bind via a hydroxyl group and an Mg atom (m-rods); rods built from piggy-back dimers (d-rods);²⁹ lamellar structures with the same binding pattern as m-rods (t-sheets); and lamellar structures where hydroxyl and keto groups kept the structure intact (l-sheets). Archimedean spiral models were created using the same pigment binding motifs as lamellar sheets. Exciton theory was used to predict optical properties of aggregates based on these optimised structures. Whilst absorption, linear dichroism, and polarisation dependent fluorescence-excitation spectra of the long structures were found to be practically identical for different architectures, circular dichroism predictions turned out to be highly sensitive to geometry and monomeric transition dipole moments within the structures. Long multiple rod and spiral structures, similar to those observed in high resolution EM studies,³⁶ successfully reproduced the CD profile seen experimentally for chlorosomes. Calculations suggested that the broad nature of the Q_y line observed for chlorosomes could be due to either different orientations of the transition moment vectors within multi-lamellar structures or the presence of a variety of different types of BChl aggregates within chlorosomes. The possibility of broadening due to the presence of a fractured domain structure as observed for BChl e containing species was not considered.

Alster et al.²⁶ used MM and QM methods to more extensively explore the short range structural parameters of a wider range of structural motifs. In addition, powder diffraction, and optical property predictions allowed comparison with experimental data. Eight structures based on dimers of 3¹R-[E,M] BChl-_{CF} homologue with their esterifying alcohol chains protruding in opposite directions were explored. This homologue is one of four homologues found in the model organism *Chlorobaculum tepidum*. It differs from the homologue found in *Chloroflexus aurantiacus* only in its esterifying alcohol. Furthermore, it

differs only in the methyl at C20 from the 3¹R-[E,M] BChl d_F homologue found in the bchQRU triple mutant found to produce highly ordered lamellar structures. Figure 1.9 shows the structural motifs used to create the aggregate systems. Structures were named according to IUPAC rules for tetrapyrroles:⁸⁵ S, used to denote “Syn” refers to the arrangement where the hydroxy group at C3¹ is on the same side of the chlorin ring as the C17-propionic acid moiety. Conversely, A, used to denote “Anti” is used when it is on the opposite side. The orientation of the Mg cation with respect to the C17 is denoted using α and β . Consistent with the notation proposed by Balaban et al.,⁸⁵ the configuration with the magnesium cation on the opposite face to the C17-propionic acid moiety is designated as the α -configuration with the β -configuration having the magnesium cation on the same side. Using this nomenclature, specifying the positions of both entities for both molecules within the basic dimer unit gives a four-letter code denoting stereochemistry of each motif e.g. A α A α or S β A α . In addition, the suffixes of -d and -dd were used to denote displaced and doubly displaced systems. The structural models can be divided into two groups: sheet and chain structures. In sheet structures, Mg atoms coordinate to C3¹ hydroxyl groups throughout the whole layer whereas, in chain structures they are formed from paired rows of BChl pigments. Structural models can also be divided by considering the mutual orientation of dipole moments within dimers into parallel and antiparallel motifs. Combining these, we obtain a system where structural motifs maybe divided into four groups (Figure 1.9):

- 1) Parallel chains (e.g. α A α S, β S β S)
- 2) Antiparallel chains (e.g. β S α A)
- 3) Parallel sheets (e.g. α S β A, α S β A-d, α S β A-dd)
- 4) Antiparallel sheets (e.g. α S α S, β A β A)

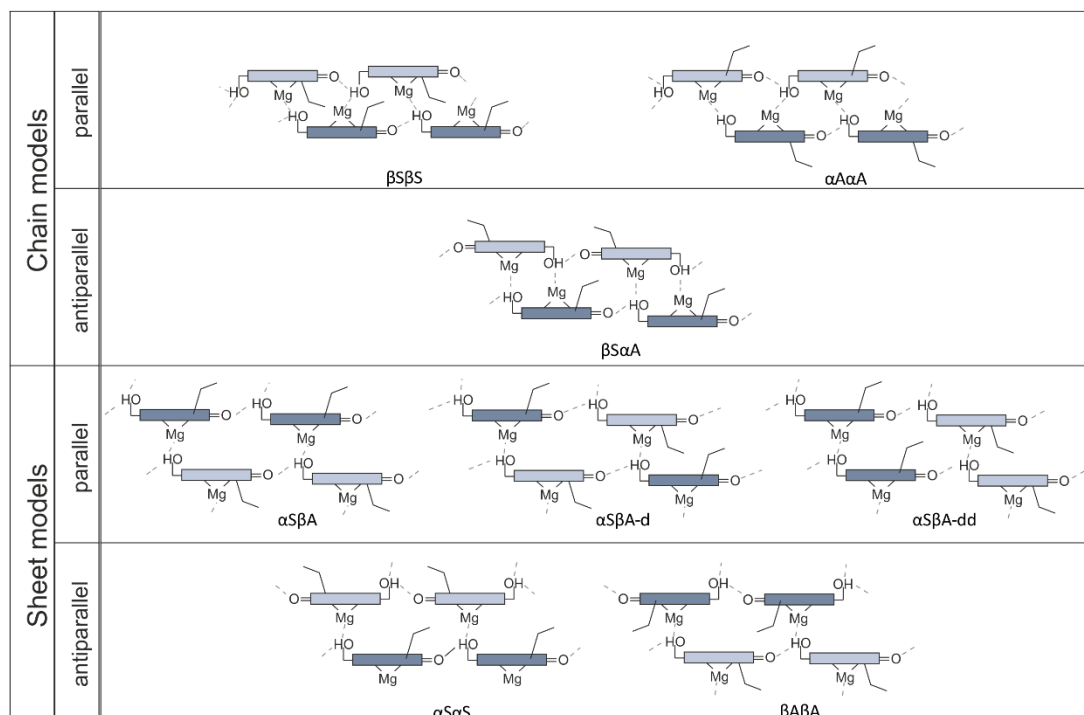


Figure 1.9 Structural motifs investigated in Alster et al..²⁶

The structural motifs may be divided into four categories: parallel chains, antiparallel chains, parallel sheets, and antiparallel sheets. Figure adapted from Alster et al..²⁶

Structural models of aggregates formed from a single layer of 8 x 10 dimers were optimised using a modified General Amber Force Field (GAFF). When compared to the pre-optimized monomer and a significant displacement of Mg atom out of the plane of the chlorin ring was observed. However, there was little change in the arrangement of the esterifying alcohol tails. An investigation of key chemical groups revealed that the Mg hydroxyl separation always corresponded to the value expected for coordination, whilst the H-bond (= O...H-O) distances were sometimes larger than that expected for a typical H-bond. Pigment densities of the most energetically favourable structure after MM optimisation were found to be in good agreement with estimates for chlorosomes with the discrepancy ascribed to the presence of increased disorder – and therefore lower density in real chlorosomes.

The electronic structure of the central tetramer of each of the MM structure was investigated using three QM methods. These calculations suggested the

most favourable structure was the antiparallel chain model corresponding to the antiparallel piggy-back dimer ($\beta\text{S}\alpha\text{A}$) with one of the antiparallel sheet models and one of the parallel sheet arrangements coming second and third respectively. These had energies about 10 – 20 kcal/mol lower than other structures. Using energy decomposition, it was possible to determine the contribution of individual interactions to the structural stabilisation. Of the three key interactions, the $\pi - \pi$ stacking was found to have the largest contribution to stabilisation (40 kcal/mol for the completely stacked chlorin ring) followed by Mg-hydroxyl coordination (20 kcal/mol) with the H-bond having the smallest stabilisation effect (8 kcal/mol).

Deformation energies were also determined for the tetramer structures. These values are consistent with significant deformation of the monomeric building blocks in the MM optimized structures relative to isolated monomers due to the packing effects in aggregates.

The structures modelled in the work of Alster et al. all remained planar despite the curvature observed in EM of chlorosomes, with the authors noting: “it will be necessary to use molecular dynamics on a larger, multilayer assembly to solve this problem.” Despite this, they were able to demonstrate the importance of curvature by “wrapping” the layers around a central x-axis. The resulting scattering predictions were found to reproduce the observed X-ray scattering data.

Electronic absorption spectra for each of the structural motifs were determined and the tetramer-monomer energy levels of the Q_y and Soret band were compared to expected shifts for monomeric, dimeric, and aggregated BChl c. The largest Q_y spectral line shift was observed for the $\alpha\text{S}\beta\text{A}$ -dd structural motif. The spectrum of $\alpha\text{A}\alpha\text{A}$ displayed the second largest shift. The experimental spectral shift of the Soret band was relatively well reproduced by structures $\alpha\text{A}\alpha\text{A}$, $\beta\text{A}\beta\text{A}$, and $\alpha\text{S}\beta\text{A}$ -dd. The ability to closely reproduce the experimentally observed spectra further supports the proposal that the energetically preferred structures may correspond to structures found within chlorosomes.

Whilst Alster et al. provided a solid basis for further exploration, it did not allow decisive conclusions to be drawn. Investigation of larger systems with better sampling of phase space using molecular dynamics simulations should allow a more comprehensive understanding of aggregate structure with in chlorosomes including the existence and origin of lamellar curvature.

1.2 QDs

QDs are semiconductor nanoparticles (NPs), which due to quantum confinement have size tuneable properties intermediate between those of bulk semiconductors and individual atoms. Since their discovery by Brus in 1984,⁸⁶ quantum dots have been the focus of intensive interdisciplinary study drawing on expertise from amongst others chemistry, physics, biology, engineering, and materials science due to their unique size tuneable properties, and the vast array of applications they afford. This section gives a brief overview of semiconductor physics, quantum confinement, and quantum dot properties as well as current and potential applications.

1.2.1 Semiconductors

Solid state materials can be broadly divided into three categories: conductors, insulators, and semiconductors. According to band theory, when individual atoms come together to form a molecule, their atomic orbitals combine to form molecular orbitals resulting in new discrete energy levels. In the case of bulk materials, as more and more molecular orbitals come together, energy levels will be close together or even completely degenerate in energy forming continuous bands of accessible energy levels which are dispersed over momentum space.

A 'forbidden' energy region called the band-gap (E_g) may exist between the valence band (the lowest band of occupied levels) and the conduction band (where orbitals are completely unoccupied at absolute zero temperature). The size of this band-gap determines the electronic properties of a material and allows them to be classified as either insulators, conductors or semiconductors (Figure 1.10). In the case of insulators, the band-gap is large

> 4eV with few to no electrons residing within the conduction band at room temperature. Conversely, conductors exhibit band-gaps below the thermal energy at room temperature < 0 to 0.1 eV.

For a semiconductor, at zero Kelvin, the ground state consists of a valence band with set of fully occupied levels and a conduction band with a set of unoccupied electronic energy levels separated by a small forbidden energy band-gap (between 0.1 and 4 eV). Rather than think of the absence of electrons in the conduction band, it is conventional to discuss the conduction band in terms of being occupied by 'holes'. These holes can be treated as positively charged particles with mass – equivalent to electrons in the valence band.

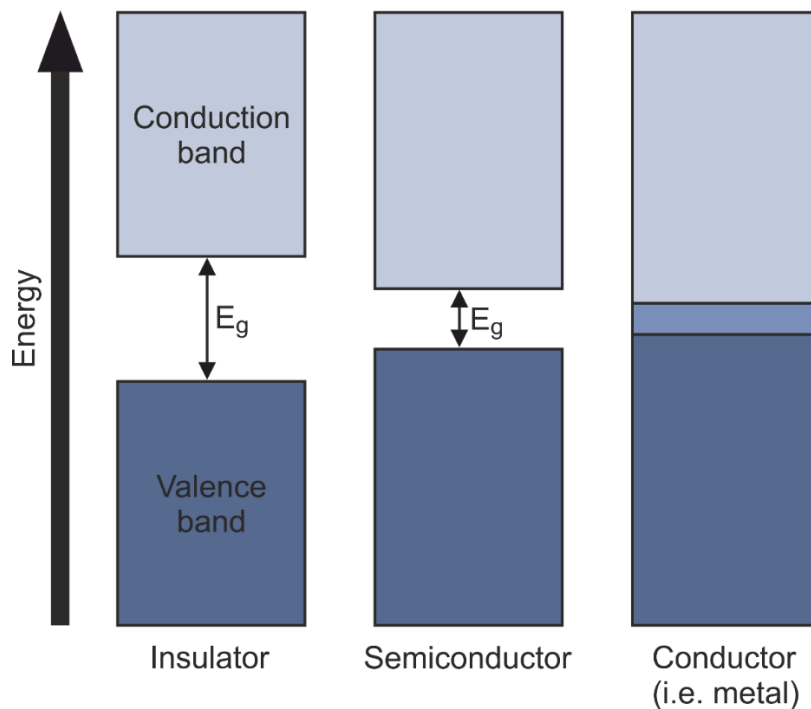


Figure 1.10 Insulators, semiconductors, and conductors.

Materials may be divided into insulators, semiconductors, and conductors based on the magnitude of the band-gap. In insulators, the gap between the valence and conduction band is large (>4 eV) where as in conductors the band-gap is small, less than the thermal energy at room temperature (<0.1 eV). Semi-conductors represent an intermediate case where the band-gap lies between 0.1 and 4.0 eV.

Excitation occurs when an electron is promoted from the valence band to an unoccupied site in the conduction. This is equivalent to a hole being promoted from the conduction band to the valence band. The result is the generation of an electron-hole pair. The relative abundance of electrons and holes allows semiconductors to be further classified into intrinsic – where there are an equal number of holes and electrons, n-type – where there are more electrons than holes and p-type – where there are more holes than electrons (Figure 1.11).

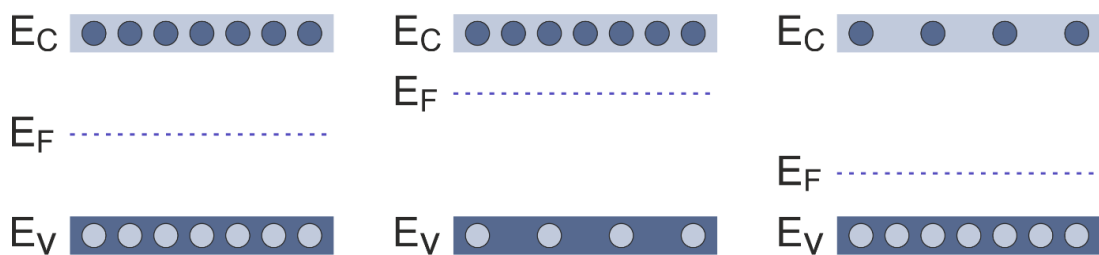


Figure 1.11 Intrinsic, n-type, and p-type semiconductors.

(a) Intrinsic semiconductor with equal population of electrons and holes, with fermi level E_F in the middle of the band-gap; (b) n-type semiconductor with majority of electrons; (c) p-type semiconductor.

A key parameter in band theory is the Fermi level, which is a virtual energy level corresponding to the energy where the probability of being occupied is one half. The position of the Fermi level in the relation to the conduction and valence bands plays a critical role in determining electrical properties. The probability that an electron is in a state with energy E_i is given by

$$P(E_i) = \frac{1}{1 + e^{\frac{E_i - E_F}{k_B T}}}$$

(1. 1)

Where k_B is Boltzman’s constant and T is absolute temperature. For intrinsic semiconductors, with their equal numbers of electrons and holes, this level lies exactly halfway between the valence and conduction bands. For n-type

semiconductors, E_F lies closer to the conduction band, whereas for p-type semiconductors it lies closer to the valence band.

The lowest energy state of the conduction band and the highest energy state of the valence band are each characterized by a certain crystal momentum (\mathbf{k}). The crystal momentum may either be the same for both states or different. This allows semiconductors to be divided into direct (\mathbf{k} the same) and indirect (\mathbf{k} different) band-gap semiconductors. In direct band-gap semiconductors an electron can be promoted from the highest-energy state in the valence band to the lowest-energy state in the conduction band without a change in crystal momentum. Similarly, an electron can move from the conduction band to the valence band without a change in momentum. In the case of indirect band-gap semiconductor, a momentum exchange with the lattice in the form of a phonon is needed to account for the momentum change on moving an electron between bands. CIS is a direct band-gap semiconductor. Figure 1.12 illustrates how an electron can be promoted from the valence band to the conduction band on absorption of a photon. For semiconductors with E_g in the range 1.4 – 2.5 eV, such transitions may be invoked by absorption of a photon of visible light. Consequently, the details concerning the electronic band structure of the semiconductor crystal determine its optical response.

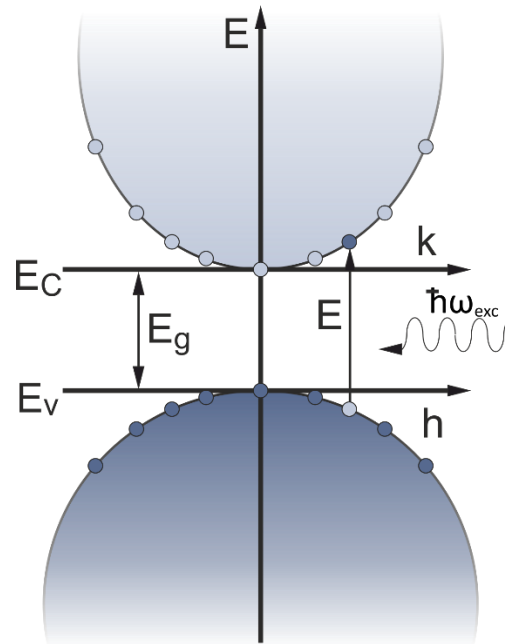


Figure 1.12 Excitation of a direct band-gap semiconductor.

The momentum conserving promotion of an electron from the valence band into the conduction band may take place on absorption of a photon with $E > E_g$.

After excitation of a semiconductor, the created electron-hole pair may undergo momentum-conserving recombination by emission of a photon (Figure 1.13) with energy equal to the difference between the initial electron and hole energies. This process is called photoluminescence (PL). It should be noted that if intra-gap states exist the energy of the emitted photon may not necessary be equal to the band-gap energy.

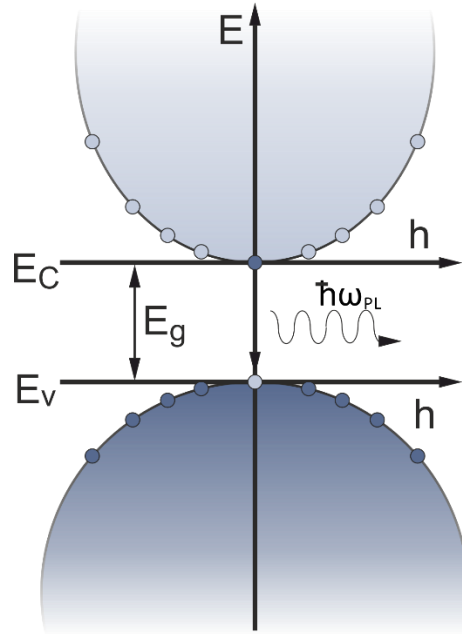


Figure 1.13 Photoluminescence recombination of the electron hole pair in a direct band-gap semiconductor.

Recombination of an electron hole pair results in the emission of corresponding energy.

Direct band-gap semiconductors are more efficient emitters than their indirect band-gap semiconductors because no change in momentum is required.

Photoluminescence decay is a first order kinetic process described by:

$$I_t = I_0 e^{-\Gamma_r t}$$

(1. 2)

where Γ_r is a characteristic radiative decay constant. An important property of semiconductor photoluminescence is quantum yield (PLQY). The PLQY describes the conversion efficiency of absorbed energy into photons. It is defined as the ratio of absorbed to emitted photons:

$$\phi = \frac{\# \text{ photons emitted}}{\# \text{ photons absorbed}} = \frac{\Gamma_r}{\Gamma_r + \Gamma_{nr}}$$

(1. 3)

where Γ_{nr} is a characteristic non-radiative decay constant.

During thermal excitation or photoexcitation, an electron is promoted from the valence band to the conduction band creating a bound electron-hole pair. This pair may be considered as a quasi-particle called an exciton which is free to move within the atomic lattice. If the effective masses of the electron and hole are m_e^* and m_h^* , respectively, the combined reduced mass, μ_{eff} , of the exciton quasi-particle is given by:

$$\frac{1}{\mu_{eff}} = \frac{1}{m_e^*} + \frac{1}{m_h^*}$$

(1. 4)

Excitons may broadly be divided into two classes: Wannier-Mott excitons⁸⁷ and Frenkel excitons.⁸⁸ Wannier-Mott excitons are typically found in semiconductors, where due to the high dielectric constant and subsequent electric field screening the Coulomb binding energies are reduced. Wannier-Mott exciton radii are typically larger than the lattice spacing. Conversely, in materials with a small dielectric constant, the Coulomb interaction between electrons and holes are stronger with smaller radii approximately the same size as the unit cell, leading to Frenkel excitations.

Wannier-Mott excitations, due to their large hydrogen-like wavefunctions and small binding energies may be treated using the Bohr model. In the Bohr

model, the radius may be found by equating the potential energy due to Coulomb attraction and the kinetic energy:

$$\mu_{eff}v^2 = \frac{1}{4\pi\epsilon_0} \frac{e^2}{r} \quad (1.5)$$

where r is the electron-hole separation, v is the velocity and ϵ_0 is the permittivity of free space. Due to quantisation of momentum,

$$L = \mu_{eff}vr \quad (1.6)$$

with $L \geq \hbar$, Equation (1.5) can be rearrange to yield the Bohr exciton radius:

$$a_B = \frac{4\pi\epsilon_0\hbar^2}{\mu_{eff}e^2}. \quad (1.7)$$

The Bohr exciton radius is typically ~10 nm for semiconductors.

1.2.2 Quantum confinement

For systems with one or more dimension below the Bohr exciton radius, quantum confinement of wavefunctions in crystals leads to changes in the corresponding eigenvalues from continuous bands to discrete levels as predicted for a particle in a box model.⁸⁹ The appearance of discrete levels introduces structure into the absorption spectra of the quantum dots and means the entities have properties intermediate between those of bulk semiconductors and individual molecules⁹⁰ (Figure 1.14). Suppression of wavefunction delocalisation leads to compression of the upper and lower energy limits of each band as well as introducing a finite number of states within these bands. These effects increase with decreasing particle size, shifting the upper valence orbital to a lower energy and the lower conduction orbital to a higher energy, this increasing the band-gap. The effect of decreasing system size on the ground state wavefunction, along with the changes in energy levels and the increase in E_g , is shown in Figure 1.15.

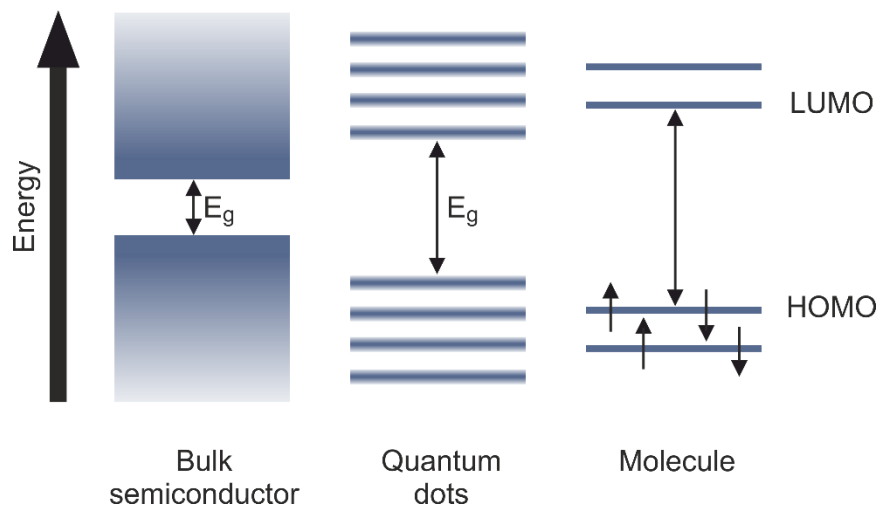


Figure 1.14 Electronic properties of quantum dots c.f. bulk semiconductors and molecules.

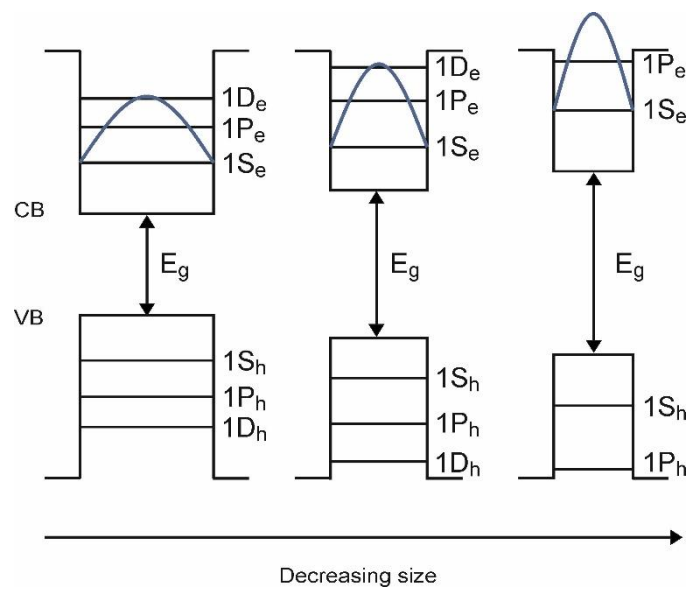


Figure 1.15 Quantum confinement.

Below the Bohr exciton radius, as the system size decreases, the upper valence orbital is shifted to a lower energy and the lower conduction orbital to a higher energy, thus increasing the band-gap energy.

The energy of such spatially confined systems may be modelled by the “particle in a box” model. For QDs, which are confined in three dimensions, spherical coordinates are most convenient. In this coordinate system, the potential function for a spherically symmetrical confinement system where the potential inside is zero and the potential outside is infinite is given by:

$$V(r, \varphi, \theta) = \begin{cases} 0, & r < d \\ \infty, & r \geq d \end{cases} \quad (1.8)$$

where d is the size of the system i.e. the quantum dot.

The Schrodinger equation for such a system is given by:

$$\begin{aligned} \left[\frac{-\hbar^2}{2\mu} \nabla^2 V(r, \varphi, \theta) \right] \psi(r, \varphi, \theta) &= \left[\frac{-\hbar^2}{2\mu_{eff}} \left(\nabla_r^2 + \frac{1}{r^2} \nabla_{\varphi, \theta}^2 \right) + V(r, \varphi, \theta) \right] \psi(r, \varphi, \theta) \\ &= i\hbar \frac{\partial \psi(r, \varphi, \theta)}{\partial t} \end{aligned} \quad (1.9)$$

where $\psi(r, \varphi, \theta)$ is the wavefunction of the exciton. Separating the angular $Y(\varphi, \theta)$ and radial components $X(r)$ and using the eigenvalue L of the angular momentum operator \hat{L} :

$$L^2 = -\hbar^2 \nabla_{\varphi, \theta}^2 = l(l+1)\hbar^2 \quad (1.10)$$

Gives the expression

$$\begin{aligned} & \left[\nabla_r^2 - \frac{l(l+1)}{r^2} + \frac{2\mu_{eff}}{\hbar^2} (E - V(r)) \right] X(r) \\ & = \left[\nabla_r^2 - \frac{l(l+1)}{r^2} + \kappa^2 + \frac{2\mu_{eff}}{\hbar^2} V(r) \right] X(r) = 0 \end{aligned} \tag{1.11}$$

where

$$\kappa^2 = \frac{2\mu_{eff}E}{\hbar^2} \tag{1.12}$$

For the simplest case of purely radial motion, $l = 0$ and thus Equation (1.11) becomes.

$$\left[\nabla_r^2 + \kappa^2 + \frac{2\mu_{eff}}{\hbar^2} V(r) \right] X(r) = 0 \tag{1.13}$$

Additionally, within the quantum dot, $V(r) = 0$, yielding:

$$[\nabla_r^2 + \kappa^2]X(r) = 0 \tag{1.14}$$

The general solution for Equation (1.14) is given by:

$$X_0(r) = A_0 \sin(\kappa r) + B_0 \cos(\kappa r) \tag{1.15}$$

The specific solution requires a spherical Bessel function whose amplitude at the edge of the quantum dot matches the zero amplitude of the wavefunction outside. This is achieved by setting the boundary conditions $X(0) = X(> r) = 0$. At the centre of the quantum dot, these conditions require that $B_0 = 0$.

$$\begin{aligned} X_0(0) &= A_0 \sin(0) + B_0 \cos(0) = 0 \\ \Rightarrow B_0 &= 0 \end{aligned}$$

(1. 16)

At the quantum dot boundary, for the wavefunction amplitude inside the quantum dot to match that outside, the product κd must be an integer of π .

$$\begin{aligned} X_0(> r) &= A_0 \sin(\kappa d) = 0 \\ \Rightarrow \kappa &= \frac{n\pi}{d} \end{aligned}$$

(1. 17)

The increase in energy due to confinement can be obtained by rearranging Equation (1. 12) and substituting $\kappa = \frac{n\pi}{d}$.

$$E_{conf} = \frac{\kappa^2 \hbar^2}{2\mu_{eff}} = \frac{\pi^2 \hbar^2 n^2}{2\mu_{eff} d^2}$$

(1. 18)

It can be seen from Equation (1. 18) the confinement energy scales with d^{-2} . Furthermore, the significance of the Bohr exciton radius can be seen from the μ_{eff} term. The effect of confinement on the wavefunction is illustrated in Figure 1.15.

The band-gap of a semiconductor nanoparticle, E_{gQD} , is a sum of three terms:

$$E_{gQD} = E_{gBulk} + E_{conf} + E_{exciton} ,$$

(1. 19)

where E_{gBulk} is the band-gap for a bulk system and the final term $E_{exciton}$ is the electrostatic energy due to the Coulombic attraction between the oppositely charged electron and hole. This term is given by:

$$E_{exciton} = -1.8 \frac{q^2}{2\pi\epsilon\epsilon_0 d}.$$

(1. 20)

The exciton energy scales with the inverse of the particle size, however this effect is usually only significant for materials with a small dielectric constant.

1.2.3 Appeal and applications

Quantum dots have attracted significant attention due to a host of attractive photophysical and photochemical properties including: broad size-dependent excitation bands, narrow size-tuneable symmetrical PL emission bands,^{86,91} high PLQY, good chemical stability, and high extinction coefficients. These properties combined with various available synthesis methods, has led to the development of many applications and fundamental studies.^{86,92,93}

These applications include lasers,^{94–96} light emitting devices,^{97–103} and solar cells.^{104–118} The potential for the use of quantum dots in biolabelling has also been explored extensively.^{119–128} Quantum dots are tuneable and have enhanced photostability compared with conventional organic dyes. Additionally, quantum dots are promising for applications in near infrared *in vivo* imaging.^{91,121–123,129–140} Further applications, include single photon sources for quantum cryptography,¹⁴¹ and visible range photocatalyst.^{142–144}

1.2.4 Quantum dot materials and synthesis routes

The synthesis of quantum dots can be broadly divided into two regimes: nucleation and growth. Nucleation occurs when monomers in a supersaturated solution overcome an energy barrier to form a thermodynamically stable structure. The energy barrier originates from the surface tension associated with the creation of a new phase. The difference in energy ΔG for a cluster of n atoms is given by

$$\Delta G = n(\mu_{crystal} - \mu_{solution}) + 4\pi r^2 \sigma \quad (1.21)$$

The first term gives the change due to the chemical potentials of the crystal $\mu_{crystal}$ and the solution $\mu_{solution}$. The second term represents the surface energy with σ the surface tension and r is the radius of the cluster.

The number of atoms in a cluster is given by $n = \frac{4\pi}{3}Nr^3$ where N is the number of atoms per unit volume. Equation (1.21) can be rewritten as:

$$\Delta G = \frac{4\pi}{3}Nr^3(\mu_{crystal} - \mu_{solution}) + 4\pi r^2 \sigma \quad (1.22)$$

Figure 1.16 shows the change in interfacial energy (blue line), volume free energy (red line), and overall free energy (green line) as a function of cluster size. For small clusters, the increase in energy due to the creation of a new interface between phases is greater than reduction in free energy due to the volume free energy. Consequently, the overall change in free energy is positive and the cluster is unstable. Once the cluster becomes large enough, the change in free energy becomes negative and the cluster becomes stable. This happens at the critical radius r_c .

The critical radius can be found by setting the derivative of ΔG with respect to r equal to zero.

$$\frac{d\Delta G}{dr} = 4\pi Nr^2(\mu_{crystal} - \mu_{solution}) + 8\pi r \sigma = 0 \quad (1.23)$$

Which leads to:

$$r_c = \frac{-2\sigma}{N(\mu_{crystal} - \mu_{solution})} \quad (1.24)$$

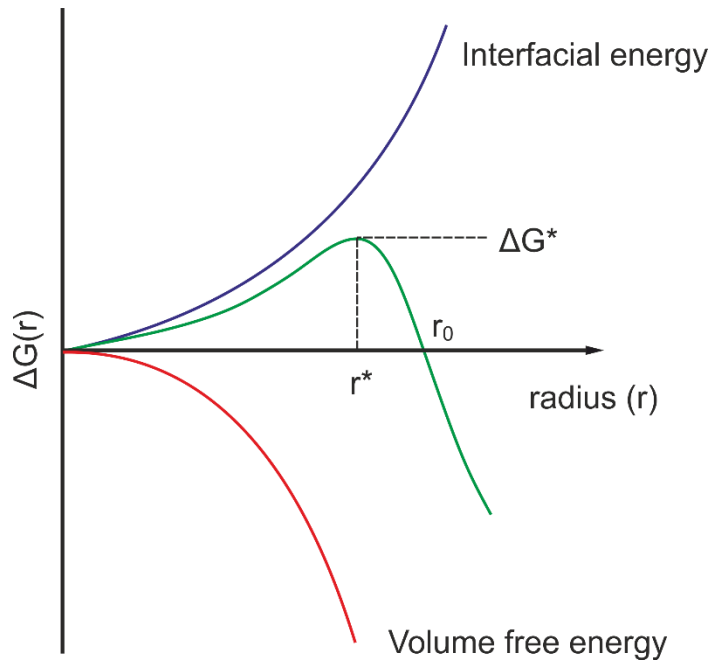


Figure 1.16 Change in free energy as a function of radius in NC growth.

The interfacial energy (blue) is the energy associated with the creation of a new interface. The volume free energy (red) is the energy released on the creation of a new phase. Above a critical radius, the change in sum of these (green) becomes negative and growth is energetically favourable.

The critical radius is the radius at which the cluster and the monomers in solution are in equilibrium. Once $r > r_c$, the addition of new molecules to the cluster leads to a reduction in free energy.

The growth of the nanocrystal beyond the critical radius is limited by the diffusion of monomers towards the cluster. This may be described by Fick's law:

$$J(x \gg r) = 4\pi x^2 \beta \frac{dC}{dx}$$

(1. 25)

Where J is the flux far away from the nanocrystal surface (i.e. $x \gg r$), β is the diffusion coefficient and the monomer concentration gradient is given by $\frac{dC}{dx}$.

At equilibrium the flux is independent of x which allows a second order differential equation to be formed.

$$\begin{aligned}\frac{dJ}{dx} &= 4\pi\beta \left(2x \frac{dC}{dx} + x^2 \frac{d^2C}{dx^2} \right) = 0 \\ \Rightarrow \frac{d^2C}{dx^2} &= -\frac{2}{x} \frac{dC}{dx}\end{aligned}$$

(1. 26)

If boundary conditions are selected such that the concentration of monomers at the crystal surface is C_r and bulk C_x at $x \gg r$, the solution to the above equation is:

$$C(x) = C_x - \frac{r(C_x - C_r)}{x}$$

(1. 27)

Taking the derivative of Equation (1. 27) and substituting into Fick's law we obtain:

$$J(x > r) = 4\pi\beta r(C_x - C_r)$$

(1. 28)

Giving a growth rate of

$$\frac{dr}{dt} = \frac{J}{4\pi r^2 N} = \frac{\beta(C_x - C_r)}{rN}$$

(1. 29)

The above treatment assumes both constant pressure and temperature. To take into account the effect of synthesis temperature it is necessary to use a formulation based on the general gas equation with the monomer concentrations treated as vapour pressures.

$$C_r = C_\infty \exp\left\{\frac{2\sigma}{rNk_B T}\right\} \approx C_\infty \left(1 + \frac{2\sigma}{rNk_B T}\right)$$

(1. 30)

$$C_x = C_\infty \exp\left\{\frac{2\sigma}{r_c N k_B T}\right\} \approx C_\infty \left(1 + \frac{2\sigma}{r_c N k_B T}\right)$$

(1. 31)

Where C_∞ is the vapour pressure of a flat surface. Substituting Equations (1. 30) and (1. 31) into the expression above for the growth rate we obtain:

$$\frac{dr}{dt} = \frac{2\sigma\beta C_\infty}{N^2 k_B T} \left(\frac{1}{r_c} - \frac{1}{r}\right)$$

(1. 32)

The sign of the bracketed term determines whether a crystal will grow ($r > r_c$) or shrink ($r_c > r$). For the case where $r = r_c$ the system is in equilibrium and the growth rate is zero. As a result, smaller crystals shrink and large crystals grow, leading to a broadening of the size distribution and a decrease in nanocrystal concentration in a process known as Ostwald ripening. A maximum growth rate is found at $r = 2r_c$. For cases where the entire size distribution lies above this value, smaller crystals grow faster than larger crystals and the size distribution becomes narrower (known as size focussing). Experimentally, this can be achieved via repeated injection of precursors to keep monomer concentration sufficiently high.

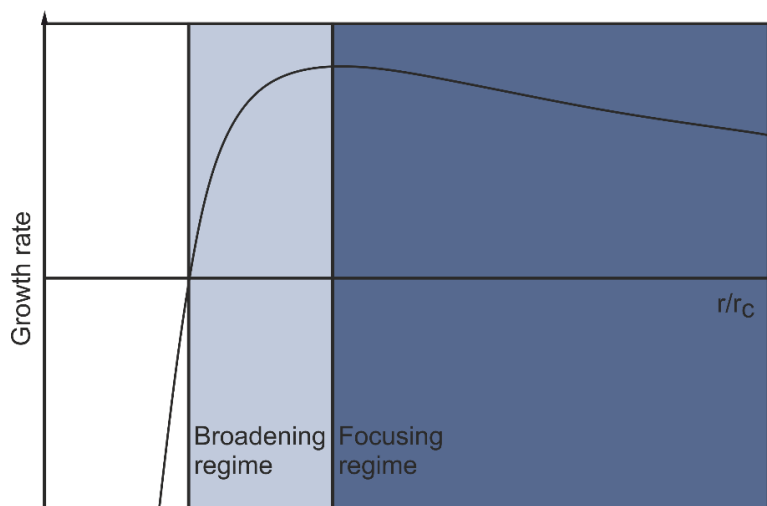


Figure 1.17 Nanoparticle growth: broadening vs. focusing.

Graphical representation of Equation (1. 32). For crystal radii in the range $r_c < r < 2r_c$ growth takes place in the broadening regime. For $r > 2r_c$, growth takes place in the focussing regime.

The degree to which a sample can be size focussed depends on a number of factors including: growth temperature, surface tension, and size distribution of nuclei. Ideally, nucleation should cease before the onset of the growth phase as nucleation taking place alongside growth reduces the concentration of available monomers and increases the critical radius and the potential for Ostwald ripening. The treatment here assumes spherical nanoparticles and does not deal with the different surface energies observed for different crystal facets. Nanoparticle morphology may be controlled by exploiting the preferential growth of certain crystal facets by diffusion limited reaction kinetics or the use of stabilising ligands which preferentially bind to specific facets.

A multitude of quantum dots of different composition with diameters ranging from 1 – 20 nm have been produced. The majority of work so far has focused on binary compound semiconductors such as CdSe, CdTe, CdS, PbS, and PbSe and great progress has been made towards the production and characterisation of high quality nanocrystals. However, despite their appealing optical properties, the potential environmental, and health risks posed by toxic heavy metals such as lead and cadmium are likely to limit their use particularly as fluorescent probes in biomedical imaging.^{135,138,145}

Whilst attempts to minimize these risks and improve quantum dot properties have been made using ZnS¹⁰¹ and SiO₂¹⁴⁶ shells, encapsulating toxic nanoparticles in less toxic shells cannot remove the risks entirely. As a consequence there has also been increasing interest in less toxic direct-transition semiconductor alternatives including Si,^{136,137} Ge,^{147,148} InP,^{131,149} transition metal doped ZnSe¹⁵⁰ as well as in ternary and quaternary semiconductor materials such as CuInSe,^{134,140,151} CuInS₂, and AgInS₂.^{152,153}

CuInS₂ (CIS) quantum dots in particular are a promising candidate for non-toxic quantum dots due to small size, large absorption coefficient ($\sim 10^5 \text{ cm}^{-1}$), high quantum yield and optical and colloidal stability. In addition, their PL emission is tuneable from the visible to the near infrared¹²¹ with a direct band-gap of $\sim 1.5 \text{ eV}$ ¹⁵⁴ making them especially promising for biomedical imaging and light harvesting applications, respectively. The large Stokes shift exhibited by CIS nanoparticles leads to lower self-reabsorption and consequently less loss further enhancing their suitability for energy applications. Whilst PLQY values for early CIS quantum dots were very low, more recent studies have reported values as high as 6 – 8%¹²³ for core nanoparticles and as high as 80%¹⁵⁵ for core shell systems. Additionally, studies also indicate that these quantum dot are less toxic than their Cd-based counterparts.^{121,123,130}

Synthesis of CIS nanocrystals presents a challenge due to the properties of the two cations. In³⁺ is a hard Lewis acid while Cu⁺ is a soft Lewis acid. As a result, they differ in their reactivity with sulphur compounds which are typically soft Lewis bases. It is therefore necessary to carefully balance the reactivity of both the cationic precursors to prevent the formation of copper sulphide binary compounds. The reactivity of Cu⁺ and In³⁺ may be modulated simultaneously through the use of multiple stabilisers. Xie et al.¹⁵⁶ achieved this using a thiol and a carboxylic acid to regulate the reactivity of Cu and In monomers respectively. Alternatively, a significant excess of a particular stabiliser can be used to reduce the reactivity of both cations to a similar level. This is a popular choice with thiols frequently being used as both the solvent and ligand.¹⁵⁷ Use of a single molecular precursors which decompose to release equal amounts of copper and indium also promoted the formation of CIS nanoparticles over copper sulphides.

Despite the inherent difficulty, several methods have been employed for the synthesis of CIS quantum dots with various morphologies and increasing research efforts are leading to a growing degree of control over composition, shape, size, and structure. Using a variety of metal salts and sulphur compounds, most of these methods involve organic solvents with only a few water-based procedures described to date.¹⁵⁷ Broadly, these methods include solvo/hydrothermal methods,^{104,107,115,152,158–165} hot injection techniques,^{106,121,129,156,166–176} “heating-up” methods,^{100,122,123,154,155,168,177–198} and photochemical decomposition,¹⁹⁹ microwave irradiation/heating.^{200–203} The best control over shape and size is observed for hot-injection and heat-up methods. The most common of these synthesis routes are heat-up methods, which provide a convenient route for the synthesis of quantum dots terminated by organic ligands which act to stabilize nanocrystal growth, maintain colloidal dispersion as well as partially isolating them from their environments. An overview of synthesis parameters and reagents/precursors used as well as details of the resulting nanoparticles can be found in Appendix A.

Crystallisation of bulk CIS at room temperature yields the chalcopyrite crystal phase. At higher temperatures a random distribution of cations is thermodynamically favourable, resulting in the formation of the zincblende phase for temperatures above 980°C and wurtzite for temperatures between 1045°C and 1090°C. Cation disordered polymorphs allow for more flexible stoichiometry. As the Fermi energy of these crystals depends sensitively on composition, this allows E_F to be tuned in a wide range, making them well suited to solar energy applications. Nanocrystalline CIS synthesised by different procedures have been shown to exhibit all three possible crystal phases at room temperature and a number of groups have reported control over crystal phase through varying synthesis conditions.

Pan et al.¹⁶⁹ were the first to describe tuneable zincblende and wurtzite structure for CIS nanoparticles. Using a mixed precursor hot-injection with oleylamine as the activation agent and oleic acid or dodecanthiol as the capping agent, they found that appropriate selection of the capping agent allows precise control of the crystalline structure from zincblende to wurtzite.

Nanoparticles synthesised using oleic acid as the capping agent exhibited the zincblende phase. Wurtzite nanocrystals were obtained by using dodecanethiol as the capping agent instead of oleic acid.

Using CuCl, In(acac)₃, di-tert-butyl disulfide, 1-dodecanethiol (DDT), and oleylamine (OLAM), Norako et al.¹⁶⁷ synthesised wurtzite nanopartiles. They attributed the formation of the crystal phase to the coordination of OLAM to the CuCl and In(acac)₃ and the slow release of sulphur from the di-tert-butyl disulfide.

Nose et al.¹⁷⁹ demonstrated phase controlled using the ligand species of the metallic monomers. When the metallic monomers were coordinated with trioctylphosphite (TOOP), the chalcopyrite or zincblende phase was observed. Coordinating with hexadecylamine (HDA) or OLAM led to the wurtzite phase. The observed crystal phase was found to be predominantly determined by the nanocrystal growth rate. This was influenced by both the bond strength between the metallic monomers and ligand molecules and steric size of the ligand molecules. In the case of TOOP complex of metallic monomers leading to the chalcopyrite or zincblende phase, crystal growth was slow. The wurtzite phase resulting from the OLAM or HDA complex of the metallic monomer was conversely proposed to be due to the very fast growth of crystals.

Batabyal et al.¹⁷⁷ demonstrated surfactant dependent phase control as well as providing the first report on the use of reaction temperature on crystal phase. In a synthesis using ((Ph₃P)CuIn(SC(O)Ph)₄) as a single source precursor in the presence of trioctylphosphine (TOPO) and DDT demonstrated that for moderate amounts of TOPO the wurtzite phase is formed below 250°C with the zincblende phase starting forming above 250°C with the pure phase observed above 300°C. For higher concentrations of TOPO the wurtzite phase could be formed even at 300°C. Kruszynska et al.¹⁷⁵, in contrast, reported the formation of zincblende particles from reaction of CuOAc and InOAc₃ with sulphur in OLAM at low temperatures and wurtzite at higher temperatures in the presence of thiols.

Chang and Waclawik¹⁸⁹ used the coordination properties of solvents and reaction temperatures to regulate crystallographic structure. Phase structure

was controlled by the coordination strength between solvent and metal precursors. Zincblende nanoparticles were obtained when CuI, InOAc, and DDT were heated at 220°C in 1 ODE or OA; however, replacing the solvent with OLAM or TOPO led to the wurtzite phase. The authors were able to produce the zincblende phase in OLAM solvent by injecting DDT into the reaction solution at 315°C. The CuInS₂ phase structure was found to be determined at the initial formation step of a CuIn(SR)_x intermediate, with a high crystallinity intermediate leading to the wurtzite structure and a low crystallinity intermediate to the zincblende phase. Furthermore, Chang and Waclawik were able to apply this phase control strategy to the synthesis of two other materials, namely, Cu₂SnS₃, and Cu₂ZnSn.

In a solvothermal synthesis, Huang et al.¹¹⁵ observed the formation of pure zincblende particles at 160°C using oleylamine as the solvent. Exchanging oleylamine for ethylenediamine yielded wurtzite CuInS₂ nanoparticles. When a mixture of these two solvents was used, mixed zincblende and wurtzite particles were observed.

An additional means of controlling CIS nanocrystal phase is afforded by using copper sulphide intermediates. Hexagonal copper sulphide and wurtzite CIS have similar anion lattices and copper sulphide has been shown to play the role of a template for the growth of wurtzite CIS nanoparticles.^{166,186,197}

A wide array of stabilising ligands have been employed in the synthesis of CIS nanoparticles. These include, amongst others, amines, thiols, carboxylic acids, phosphines or phosphonic acids, and mixtures of two or more ligands maybe used. Ligands used in nanoparticle synthesis feature a functional group able to bind surface metal atoms, in addition to at least one relatively long carbon chain. These carbon chains provide the nanoparticle with a hydrophobic shell, improving the colloidal stability in nonpolar solvents.

As well as core CIS particles, a significant effort has been focused on synthesis of core-shell systems where CIS nanoparticles are modified to incorporate a shell of a different material. Most work has focussed on ZnS encapsulated CIS quantum dots. This is typically achieved via addition of a zinc precursor to as synthesised quantum dots before additional heating. As

the unpurified CIS product typically contains high levels of unreacted sulphur it is often not necessary to add an additional sulphur source. Over-coating CIS nanoparticles in this way markedly improves the photoluminescence properties, including the PLQY, of the nanoparticles. Despite this advantage, this the work presented in this thesis deals with core CIS nanoparticles in order to reduce system complexity and maximise the probability of successful energy and charge transfer between bacteriochlorophyll ligands and quantum dots (see Section 1.3).

1.2.5 Properties and size dependence

The impact of ternary nanocrystal (NC) size, shape, composition and surface states on optical properties has been reported extensively (for a review see e.g. Kolny-Olesiak and Weller).¹⁵⁷ This section contains a brief overview of these properties focusing ternary CIS nanoparticles and on those properties most relevant to the work presented in this thesis.

1.2.5.1 Band-gap

Through varying nanoparticle size, the absorption of CIS quantum dots can be tuned to cover almost all of the visible spectrum. Theoretical predictions based on finite-depth-well effective mass calculations for the chalcopyrite CIS structure show that the band-gap can be tuned to 3.3 – 1.7 eV for nanoparticles in the size range 1 – 6 nm.²⁰⁴ This is in good agreement with experimentally observed values.

Zhong et al.¹⁵⁴ provided a thorough investigation of the size dependence of the optical (E_x) and electronic band-gap (E_g) energies of monodisperse chalcopyrite CuInS₂ quantum dots as well as the binding energies of their excitons. The size of these quantum dots, grown by thermal decomposition with reaction times ranging from 20 – 120 min were between 3 and 8 nm as determined by X-ray diffraction (XRD) and high resolution transmission electron microscopy (HRTEM). E_x was determined for each particle size from absorbance measurements using Tauc plots (a description of this can be found in Huxter et al.).²⁰⁵ Values for E_x were found to increase with decreasing particle size ranging from 1.668 eV for 7.2 nm particles to 1.945 eV for 3.5 nm. Cyclic voltammetry (CV) was used to determine the values of the lowest

conductive states and the highest valence states and consequently the band-gap (E_g) of the pyramidal nanocrystals. The size of the band-gap was found to increase with decreasing particle size ranging from 1.7 eV for 7.3 nm to 2.04 eV for 3.5 nm. Even for the largest nanoparticles investigated, the band-gap was well above that reported for bulk phase CuInS_2 (~1.5 eV).^{206,207} The electronic band-gap energy is the energy required to create a non-bound electron-hole pair whereas, the optical band-gap energy is that required to promote an electron from the valence band to the conduction band and create a bound electron-hole pair. Due to Coulombic attraction between the electron and hole, the optical band-gap energy is always lower than electronic band-gap energy. The exciton binding energy (E_b) due to the Coulombic interaction is therefore given by $E_b = E_g - E_x$. Values calculated using the E_g and E_x values determined for each particle size were found to be in the range 100 – 30 meV. The exciton binding energy was found to decrease with increasing nanocrystal size due to the size dependence of the electron-hole coulomb interaction. The values reported by Zhong et al.¹⁵⁴ for E_g , E_x , and E_b are shown in Table 1.1.

Table 1.1 Comparison of band-gap data for CIS quantum dots of different sizes as reported by Zhong et al..¹⁵⁴

Average sizes	3.5 nm	5.2 nm	5.6 nm	6.1 nm	7.3 nm
E_g (eV) (determined by CV)	2.04	1.88	1.80	1.78	1.70
E_x (eV) (determined by absorption)	1.945	1.798	1.757	1.719	1.668
E_b (meV) (determined from $E_g - E_x$)	~95	~82	~43	~61	~32

It should be noted that composition, as well as size, influences the band-gap.¹⁸³ Lowering of the valence band is observed in copper deficient nanoparticles leading to widening of the band-gap.^{183,184} Nevertheless, the band-gap in CIS has been demonstrated to be stable even against high degrees of off-stoichiometry,^{208–210} though the size dependence of this has not

been thoroughly investigated for materials specially confined in three dimensions.

The lowest energy transition E_1 for which a valid solution to the Schrodinger equation exists may be larger than the band-gap energy. In the case of CIS nanoparticles, this transition is not typically easy to distinguish in absorption spectra. Consequently, in order to determine the value of E_1 alternative methods must be used. One option is to use the local minimum of the second derivative of the absorption spectrum.²¹¹ Alternatively, Qin et al.²¹² employed a different method; taking the position of the intersection of two tangents in the absorption spectrum.

1.2.5.2 Absorption

In general CIS quantum dot absorbance spectra feature a broad absorption band together with an absorption tail at longer wavelengths. With increasing quantum dot size, the absorption edge shifts to longer wavelengths. Typically, no sharp absorption peak is observed for CIS quantum dots.^{154,156,182}

Several explanations have been presented for the absence of a sharp excitonic peak. One possibility is that this is an intrinsic property of CIS nanoparticles. Alternatively, this feature, or rather lack thereof, could stem from sample heterogeneity in either size, shape or composition. Despite recent progress in the controllable synthesis of CIS nanoparticles, size distributions for most methods remain large with a significant degree of variation in shape.¹⁵⁷

The tail observed at long wavelengths has been attributed to both participation of the electronic states of ligands in absorption and the contribution of intraband CIS states. However, work by Castro et al.¹⁸¹ looking at the effect of different ligands on CIS quantum dot absorption appeared to disprove the first hypothesis.

A key property associated with absorption of light is a material's extinction coefficient which allows the concentration of nanoparticles within a sample to be determined. For nanoparticles, this is a size dependent property and must be determined for different diameters of nanoparticles. Two groups have

investigated size dependent extinction coefficient determination for CIS core and CIS/ZnS core shell quantum dots.^{211,212} Booth et al.²¹¹ determined the extinction coefficient at two wavelengths, the first excitation E_1 and 3.1 eV. They determined the following relations:

$$\varepsilon_{CIS}(E_1) = (830 \pm 660)d^{3.7 \pm 0.6} \quad (1.33)$$

$$\varepsilon_{CIS}(3.1 \text{ eV}) = (2123 \pm 109)d^{3.8 \pm 0.3} \quad (1.34)$$

where d is the nanoparticle diameter. Due to the relatively high optical density, using the absorption at 3.1 eV offers greater sensitivity as well as removing the influence of ligands of a ZnS shell.

Qin et al.²¹² proposed an alternative equation for the extinction coefficient of CIS nanoparticles using the first excitonic transition:

$$\varepsilon_{CIS}(E_1) = 11430d^{2.147} \quad (1.35)$$

However, the values reported in this study are notably lower than those seen elsewhere. Furthermore, a different method was employed for the determination of the first excitonic transition. Extinction coefficient determinations using Equations (1.33) and (1.35) differ significantly despite showing similar size dependence. This can likely be traced to the broad size distributions observed for CIS nanoparticles as well as difficulty in accurately determining nanoparticle size for non-spherical particles. Whilst further progress is needed to accurately determine the size dependent nature of extinction coefficients, Equation (1.34) provided a reasonable means of estimating nanoparticle concentrations.

1.2.5.3 Emission

In contrast with quantum dots of other compounds, the PL emission band for CIS is broad in nature,^{154,156,182} with FWHMs of ~100 nm. Emission spectra consisting of multiple overlapping bands have also been reported.¹²³ In

addition, there is a large Stokes shift of between 130 and 170 nm indicating that defects likely play a significant role in emission. The large Stokes has the practical advantage of reducing self-reabsorption which is desirable for a number of applications including those in light harvesting. The wavelength of PL emission increases with particle size allowing tuneable emission in the red-near infrared (NIR) portion of the spectrum making them ideally suited to *in vivo* imaging.

Investigation of photoluminescence lifetimes of CIS¹⁸² were found to be significantly higher and more complex than more common quantum dot semiconductors such as CdS and CdSe. Different radiative lifetimes correspond to different electron hole recombination mechanisms and therefore offer an important insight into exciton behaviour in nanocrystals. Time resolved laser techniques have been used to probe the PL decay curves for CIS quantum dots at a range of wavelengths. PL decay curves were fitted using a sum of three exponential functions:

$$I(t) = A_1 \exp(-t/\tau_1) + A_2 \exp(-t/\tau_2) + A_3 \exp(-t/\tau_3) \quad (1. 36)$$

where τ_1, τ_2, τ_3 represent the decay times of the PL emission, $A_1, A_2,$ and A_3 are the amplitudes of the corresponding amplitudes. From fitting, $\tau_1, \tau_2,$ and τ_3 were determined to be 4 – 12 ns, 28 – 60 ns, and 140 – 300 ns respectively. The decay component with the longest time constant accounted for the 40 – 80% of the total PL emission spectra. This contrasts with earlier studies on the PL decay behaviour of CdSe quantum dots which revealed a universal biexponential decay.^{213,214} In this case, the shorter lifetime (several nanoseconds) is attributable to the intrinsic recombination of initially populated core states whereas the longer lifetime can be explained by the existence of surface states. For CIS quantum dots it is proposed that τ_1 and τ_2 correspond to intrinsic recombination and surface states respectively with the longer τ_3 attributed to donor-acceptor pair (DAP) recombination.

For DAP recombination to take place, coupling of the conduction band to an emitting donor state with either radiative or non-radiative energy transfer is

required. Whilst previous studies have shown that emission on excitation is instantaneous (at least on the nanosecond timescale) an ultrafast population transfer between the conduction band and "electron deficient" donor states is possible.²¹⁵ Studies of CIS and the similar CuInSe_2 (CISe) material indicate that due to the low energy of formation $\text{In}_{\text{Cu}} + 2\text{Cu}$ likely constitute the electron deficient domain.^{216–219} Such defects may exist either as isolated point defects, associated pairs or clusters depending on defect density.

Li et al.¹²³ also studied the time dependence of PL from CIS nanoparticles. They reported the presence of two long lived components with a red-shift with increasing delay time. The long lived nature of the PL means band edge recombination is unlikely. Furthermore, the observed red-shift is consistent with donor-acceptor transitions, with the shift to lower energies resulting from a decrease in the Coulomb energy with increasing charge separation.

In a later study, Li et al.¹⁵⁵ observed a faster decay channel which could be suppressed via surface treatment with a Zn or CdS overcoating. Combined with the concomitant increase in PLQY, this suggests recombination through surface defect states serving primarily as a centre for non-radiative decay.

The existence and extent of such a DAP recombination mechanism in CIS nanoparticles would also explain the broad nature of PL emission spectra compared to CdSe quantum dots, the large Stokes shift, as well as relatively low quantum efficiency.

Whilst PLQY values for early CIS quantum dots were very low, more recent studies have reported values as high as 6 – 8%¹²³ for core nanoparticles and as high as 80%¹⁵⁵ for core/shell systems. The increase in PLQY observed in the presence of a shell of higher band-gap material can be ascribed to a reduction in surface traps and consequent suppression of nonradiative recombination.

1.3 Combining Bacteriochlorophylls and Quantum dots

The energy levels associated with BChls and CIS QDs (Figure 1.18a) are ideal for the production of a composite material with excitonic coupling. Coupling of

individual zinc-containing BChl and Chl derivatives to the surface of quantum dots should lead to energy transfer between the two and provide a new material with interesting electronic and optical properties. This coupled system may exhibit either Förster Resonant Energy Transfer (FRET) or perhaps even a mixing of energy levels leading to radical changes in the band structure of the system.

Efficient energy transfer between pigments and quantum dots will require an appropriate relationship between the band-gap of the semiconductor nanocrystals and the energy levels of pigments and their aggregates. For illustrative purposes, Figure 1.18a shows the relationship between the band structure of CIS quantum dots and the energy levels corresponding to the Soret and Q_y transitions of zinc containing BChl c derivatives.

There exist two primary ways in which the levels of such a system may be modified to enhance energy coupling. The first of these involves size control of the synthesised quantum dots. By selecting quantum dots of an appropriate size, the energy levels of the quantum dots can be chosen to best match those of the bacteriochlorophyll pigments to ensure tight coupling and efficient energy transfer (Figure 1.18b)

Additionally, through appropriate selection of environmental conditions, it should be possible to drive pigment assembly at the quantum dot surface (Figure 1.18c). Due to the tight excitonic coupling observed in BChl aggregates and the remarkable changes in properties observed on aggregation, these systems should have properties different from both their constituent parts and quantum dot-monomer systems. Through carefully varying environmental conditions, control of assembly should allow further tuning of system properties (Figure 1.18).

Whilst transfer from quantum dot to the Q_y band of the pigment would require inordinately large particles, transfer between quantum dots and the Soret band, and vice versa, should be possible by tuning quantum dot size. Furthermore, transfer of energy from the Q_y band of the pigment to the quantum dot should be possible. It may also be possible to couple to defect levels within the quantum dot system.

As mentioned in Section 1.2.4, quantum dots are generally passivized with thiol containing ligands. These ligands offer a simple means of coupling BChls to quantum dot via ligand exchange. Ligand exchange has been used in a number of case to modify the nanoparticles and improve their suitability for potential applications. One such example is when nanoparticles are to be used in aqueous environments (as is typically required for biomedical imaging) for which synthesis ligands are typically insufficient. In addition, for some applications, such as those requiring charge transport a thinner ligand shell is necessary. Though modification of BChls to incorporate a short chain thiol or dithiol it should be possible to tightly couple pigments to quantum dots and thus allow energy transfer between the two.

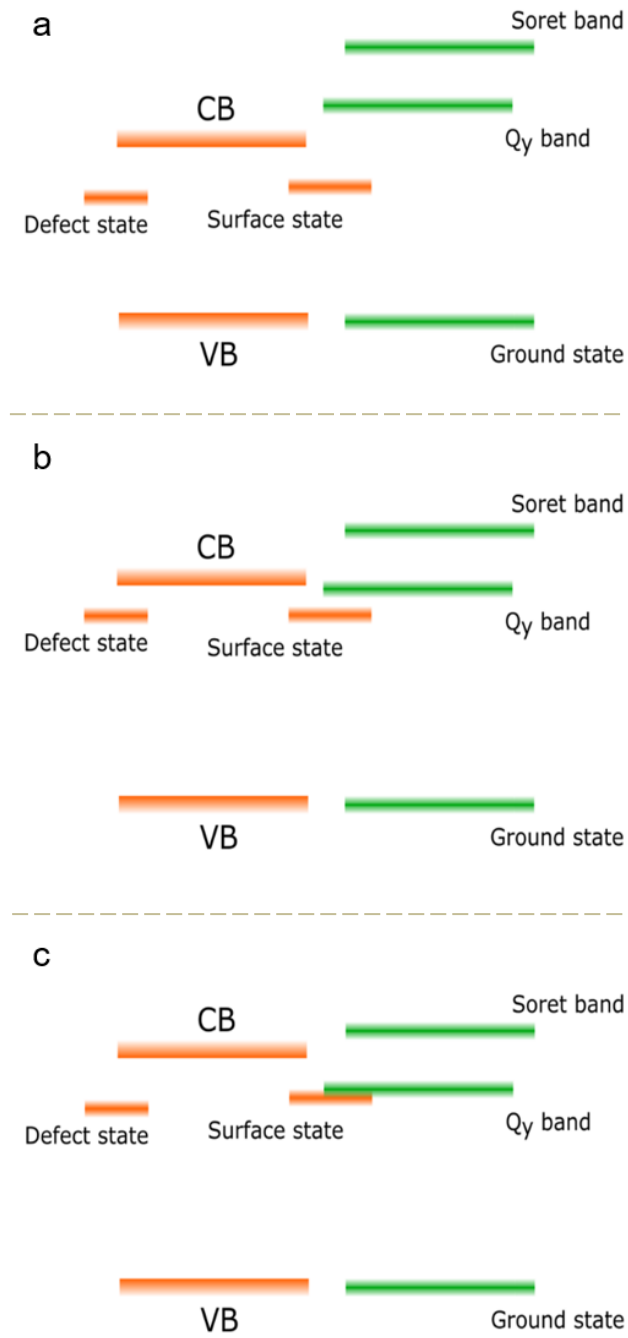


Figure 1.18 Relationship between energy levels in CIS quantum dots (orange) and zinc containing BChl pigments (green).

(a) The energy levels of CIS and zinc containing BChls are ideally suited for the production of a coupled hybrid system; (b) controlling the size of the CIS nanoparticles allows modulation of energy levels for CIS quantum dots; (c) further control is afforded by the shift in energy levels observed for aggregates of zinc containing BChl pigments.

1.4 Summary of key aims and results

Figure 1.19 provides an overview of the key steps involved in the production of a hybrid BChl-QD system. Briefly, pigments must first be modified to increase stability and provide a means of coupling. Then, using ligand exchange, pigments may be coupled to syntheses and well characterised quantum dots.

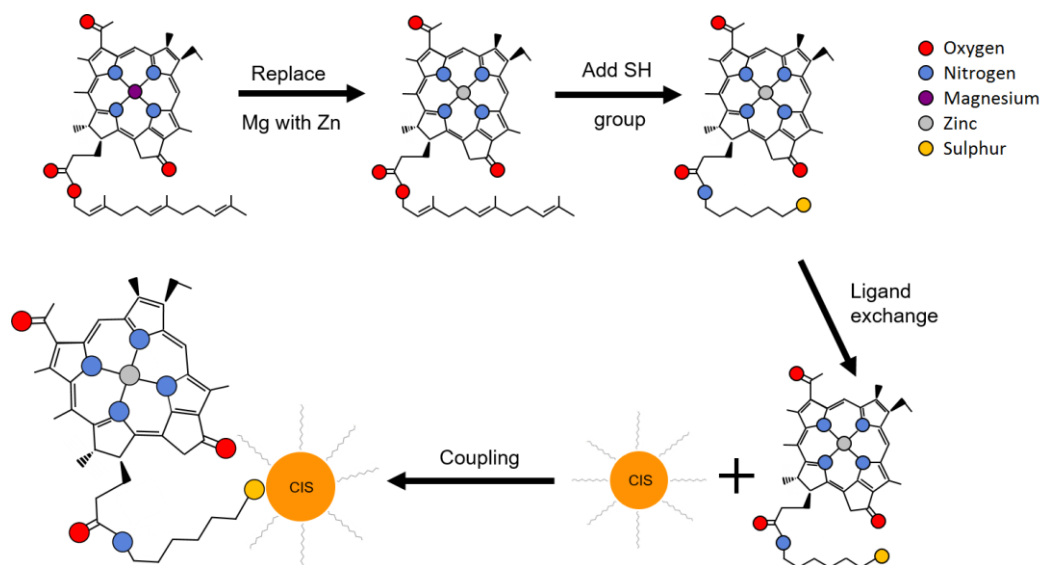


Figure 1.19 Project scheme showing the key stages of composite material production.

The work in this theses may be divided into three sections (I-III).

- I. Chemical modification of pigments
- II. Simulation of BChl pigments to better understand aggregation and intrinsic curvature.
- III. Synthesis and characterisation of Cu-deficient CIS QDs of different diameter (and consequently curvatures)

These are outlined below with a brief overview of the most significant findings.

1.4.1 I. Chemical modification of pigments

Key to the successful production of a novel photonic material combining BChls and QDs is the chemical modification of pigments to increase stability and to provide a means of chemical coupling to the QD surface. A new method for the conversion of BChls to Zn-Bacteriopheophytins was employed which

allowed the rapid production of large quantities of the later. Purification protocols were also developed for the production of pure samples of zinc modified BChl c and zinc modified Chl a. In addition, attempts were made to further modify pigments by replacing the long alcohol tail with a short chain thiol via transamidation. The goal of this was to provide SH functionalised BChls suitable for ligand exchange with thiol stabilised CIS QDs. X-ray photoelectron spectroscopy indicated successful modification albeit not conclusively. Chapter 3 deals with the modification of pigments.

1.4.2 II. Simulation of BChl pigments to better understand aggregation

With the vision of assembling BChls around highly curved QD surfaces, molecular dynamics (MD) simulations were performed on a number of pigment arrangements in order to study the mechanism of BChl pigment aggregation and in particular the origin of the curved lamellar system observed in electron micrographs of chlorosomes. These are the first MD simulation on pigment assemblies and through the investigation of a wide variety of pigment assemblies, new insight has been gained into the nature and energetic implications of sheet curvature. In addition, the exploitation of parallelised high performance computing methods has allowed the prediction of X-ray scattering patterns for simulated structures which may be compared to experimentally observed X-ray scattering.³⁵ Details of MD simulations on pigments and their analysis can be found in Chapter 4.

1.4.3 III. Synthesis and characterisation of CIS QDs

This thesis presents a novel method for the direct synthesis of high quality hydrophilic CIS nanoparticles with PLQY comparable to the best reported values for core CIS nanoparticles. The structure, composition and optical properties of these highly copper-deficient particles are investigated using a variety of methods. This allowed the exploration of quantum dot emission properties for both the steady state and the nanosecond time scale. The dependence of QD properties on size, composition, and defects is also

investigated. Consistent with previously published work, three key recombination pathways were identified, which contribute to PL emission; namely band-gap recombination, core defect, and surface defect emission. Additionally, an increase in the contribution of long-lived defect-related emission with increasing nanoparticle size was observed. This was attributed to an increase in the density of In_{Cu} antisites and copper vacancy defects with increasing synthesis time and resulting increasing copper deficiency. This provides an additional parameter for fine tuning of the energetic structure of CIS QDs and controlling energy flow in hybrid systems. The results of CIS quantum dot synthesis and characterisation are presented in Chapter 5.

Chapter 2

Materials and Methods

2.1 Introduction

This chapter contains details of materials and methods used in Chapters 3-5. Section 2.1.1 contains information on materials used and their sources. Section 2.2 provides details of methods used in the purification and chemical modification of pigments (Chapter 3). Section 2.3 covers methods for the Molecular Dynamics (MD) simulation of pigments and the analysis of these simulations (Chapter 4). Section 2.4 relates to the methods used in the synthesis and characterisation of copper indium sulphide (CIS) quantum dots (QDs) (Chapter 5).

2.1.1 Materials

The reagents were purchased from the following. Sigma Aldrich: Streptavidin, Ethyl acetate, Sucrose, 3-aminopropyltrimethoxysilane, Iron(III) chloride hexahydrate, Sodium molybdate dihydrate, Manganese(II) chloride tetrahydrate, Vanadium(IV) oxide sulfate heptahydrate, Sodium tungstate dihydrate, Monopotassium phosphate, Ammonium chloride, Calcium chloride dihydrate, Vitamin B-12, Sodium sulfide nonahydrate, Methanol (laboratory grade), Hexane, Indium acetate, Copper iodide, Mercaptoundecanol, Thiourea, Ethylene glycol. Fisher: Methanol (High pressure liquid chromatography (HPLC) grade), Acetic acid, Boric acid, Ammonium acetate, Sodium chloride, Magnesium sulfate heptahydrate, Methanol (laboratory grade), Acetone, Tris buffer, Methanol (analytical reagent grade). Lichrosolve: Tetrahydrofuran (THF) and Dichloromethane. Alfa aesar: Zinc acetate and Copper chloride dehydrate. Fluka: Sodium bicarbonate, Sodium selenite penta-hydrate, Cysteamine. Acros organics: Hydrochloric acid, Nickel(II) chloride hexahydrate, Chloroform, Potassium tert-butoxide. Gibco: Phosphate buffered saline (PBS) tablets. Thermo: Ethylenediaminetetraacetic acid. VWR: Sodium thiosulfate pentahydrate. Merk: Sodium thiocyanate. Nanocs: HS-Polyethylene glycol (PEG)(3400)-Biotin. Rapp Polymere: N-

hydroxysuccinimide (NHS) PEG 5000, NHS-PEG 5000-biotin. MP biomedical: Cobalt(II) chloride hexahydrate, Zinc sulfate heptahydrate. Fresh spinach was purchased from the supermarket. All chemicals were used as supplied.

2.2 Bacteriochlorophylls (BChls) and chlorophylls (Chls)

2.2.1 Purification of BChls and Chls

2.2.1.1 Source and growth of cells

Initial batches of *Chlorobaculum tepidum* cells were obtained from Jakub Psencik (Charles University, Prague) and Radek Litvin (University of South Bohemia, České Budějovice and Czech Academy of Sciences, České Budějovice). These were either stored in the dark at 5 °C or aliquoted and stored at -20 °C until use.

Additionally, a live culture of *Chlorobaculum tepidum* cells for growth was received. These cells were grown using a modified Pfenning's medium²²⁰ as described in Table 2.1.

Table 2.1 Modified Pennings' medium.²²⁰

Na ₂ S ₂ O ₃ x 5H ₂ O	1.0 g
KH ₂ PO ₄	500 mg
CH ₃ COONH ₄	500 mg
NH ₄ Cl	400 mg
NaCl	400 mg
MgSO ₄ x 7H ₂ O	200 mg
CaCl ₂ x 2H ₂ O	50 mg
Ethylenediaminetetraacetic acid (EDTA)	12.5 mg
NaHCO ₃	2 g
Mineral supplement (see Table 2.2)	1 ml
Vitamin B ₁₂	4 µg

*(quantities are per litre of medium).

Table 2.2 Mineral supplement for Modified Pennings' medium.²²⁰

The pH was adjusted to 8.0 using concentrated NaOH.

EDTA	6.7 g
FeCl ₃ x 6H ₂ O	2.0 g
CoCl ₂ x 6H ₂ O	190 mg
Na ₂ MoO ₄ x 2H ₂ O	190 mg
ZnSO ₄ x 7H ₂ O	150 mg
MnCl ₂ x 4H ₂ O	100 mg
VOSO ₄ x 2H ₂ O	30 mg
NiCl ₂ x 6H ₂ O	25 mg
CuCl ₂ x 2H ₂ O	17 mg
H ₃ BO ₃	6 mg
Na ₂ SeO ₃ x 5H ₂ O	3.2 mg
Na ₂ WO ₄ x 2H ₂ O	2 mg

*(quantities are per litre of supplement).

Before autoclaving, the pH of the media was adjusted to 6.7, using HCl, and gas exchange was performed by sparging with sterile N₂ gas for 40 min to remove O₂. NaS₂ was added and the lid fastened quickly to prevent O₂ entering. 800 ml of the medium was autoclaved (121 °C, 1-2 bar, 25 min) in 1 l bottles fitted with a resalable polytetrafluoroethylene (PTFE) septum. After autoclaving, the pH was readjusted by a needle and syringe through the PTFE septum to 6.7-6.9 using 10% HCl. The medium was inoculated with 20 - 40 ml of culture before flasks were left at room temperature in on a window sill in indirect sunlight and inverted daily to ensure cells remained in suspension and received sufficient light to grow. Once the flasks had become a dark green, the contents was aliquoted into falcon tubes and centrifuged at 4000 g for 10 min. The supernatant was removed and the pellet stored at -20 °C.

2.2.1.2 Extraction of BChl c from *Chlorobaculum tepidum* cells

Pigments were extracted from whole cells using a modified version the protocol outlined by Zhu et al.²²¹ Briefly, cells were dried under vacuum at 40 °C. A 1:1:2 (v/v/v) mixture of methanol : chloroform : H₂O was added. The

chloroform layer was washed with fresh deionised H₂O until clear. The chloroform subphase was removed and dried under nitrogen. Dried pigments were washed repeatedly with hexane to remove carotenoids until the hexane remained colourless. UV-Visible (UV-Vis) absorption spectra were taken of the extracted pigments before washing with hexane and after. UV-Vis absorption spectra were also obtained for the hexane used to wash the pigments. Pigments were then dried under nitrogen and stored as a thin film in the dark at -20 °C until purification by HPLC or further use.

2.2.1.3 Extraction of BChl e from chlorosomes

Bacteriochlorophyll e was extracted from chlorosomes of *Chlorobaculum phaeobacteroides* using the same protocol used for extraction of BChl c pigments from whole cells (section 2.1.1.2).

2.2.1.4 Extraction of chlorosomes from *Chlorobaculum tepidum* cells

Chlorosomes were extracted from *Chlorobaculum tepidum* cells by dilution in 50 mM Tris buffer (pH 8) containing 2 M NaSCN and lysed by three passage through a cold French pressure cell at 20 000 psi. Cell debris were removed by centrifugation at 10 000 rpm for 10min at 4 °C. The chlorosome containing supernatant was loaded onto a 10-50% sucrose density gradient and centrifuged for 24 h at 220 000 g at 5 °C (SW40Ti rotor). The chromosome containing band was recovered and concentrated by centrifugation (235 000 g, 45Ti, 2 h, 5 °C). Chlorosomes were stored at -20 °C as pellets until use.

2.2.1.5 Extraction of pigments from spinach

Pigments (Chlorophyll a, b, their derivatives, and carotenoids) were extracted from commercially obtained spinach. Leaves of fresh spinach were cut into small pieces, discarding stems and larger veins. 2 ml of ice cold acetone was added per 1 g of spinach and leaf fragments were homogenised using a Warring blender. The resulting mixture was centrifuged at 5000 g for 10 min. The supernatant was transferred to fresh tubes and equal amounts of hexane and water were added. After thorough shaking of tubes, the mixture was centrifuged again at 5000 g for 10 min to phase-separate the emulsion. The pigment containing hexane layer was removed, dried under nitrogen and

stored at -20 °C until HPLC purification. Extraction was performed in the dark at 5 °C.

2.2.1.6 Absorbance measurements and concentration determination

All UV-Vis absorbance spectra for native and modified pigments were obtained either using a Jasco V-560 spectrophotometer, a Genesys 6 spectrophotometer, or a DeNovix DS-11+ Spectrophotometer. Measurements made using both the Jasco and Genesys were typically made over the range 300-750 nm at a resolution of 1 nm. A scanning speed of 2000 nm min⁻¹ was used on the Jasco instrument and the fast scan setting on the Genesys. Measurements using the DeNovix were performed over the range 220-750 nm using default settings and a resolution of 1 nm.

All spectra of pigments were obtained in methanol with the exception of the spectra of aggregates which were taken in 200:1 (v/v) hexane : dichloromethane. Chlorosome spectra were measured in water. The values used in the determination of pigment concentrations in methanol and their sources are shown in Table 2.3.

Table 2.3 Positions of Q_y peaks and values used for concentration determinations of BChl c, BChl e, Chl a, and Chl b.

Pigment	Q_y position (nm)	Molar absorptivity at Q_y (mM ⁻¹ cm ⁻¹)
BChl c	669	70 ²²²
BChl e	660	35.5 ²²³
Chl a	665	88.8*
Chl b	652	42.9**

*calculated based on an absorption coefficient of 79.24 g⁻¹ cm⁻¹ and molar mass of 892 g mol⁻¹ (both values taken from Craft²²⁴) ** calculated based on an absorption coefficient of 38.87 g⁻¹ cm⁻¹ and molar mass of 906 g mol⁻¹ (both values taken from Craft).²²⁴

2.2.1.7 HPLC purification of BChl c pigments

BChl c was isolated from the pigment extract by reverse-phase HPLC using a Zorbax XDB-C18 Semi-preparative 9.4 x 250 mm (5 µm particle size) column. A modified version of the method employed by Klinger et al.³³ was used for separation of BChl c homologues, BChl derivatives, and remaining β-carotenes. Briefly, a three step isocratic gradient consisting of 100% solvent A (100% methanol) for the first 25 min followed by 100% solvent B (4:1 (v/v) methanol/hexane) for the next 10 min followed by 100% solvent A for a further 15 min. The flow rate throughout was 1.5ml/min. The column was equilibrated with the initial run conditions for > 15 min prior to each run. HPLC grade solvents were degassed and filtered through 0.2 µm filters prior to use. Chromatography was monitored at 669 nm and a 3-dimensional field detector allowed spectral identification of each peak across the range 250 to 750 nm. Saturated pigment solutions were prepared immediately before use by dissolving dried pigments in methanol. The autosampler was cooled to 5 °C and the column held at 20 °C to minimise sample degradation due to temperature. Injection volumes were selected based on concentration of sample but were typically in the range 75 -150 µl. The four main C8 and C12 homologs of BChl c esterified with farnesyl at C17³ were combined and dried immediately under N₂. Samples were dried in the dark and stored in dried films at -20 °C until use to minimise sample degradation.

2.2.1.8 HPLC purification of chlorophyll a and b

Individual pigment species were isolated using the same C18 Zorbax Semi-preparative column used for purification of BChl c. Solvents used and gradient conditions are given in Table 2.4. Chromatography was monitored at 658 nm. 3-dimensional full spectral chromatograms were also obtained to assist with assignment of peaks. All other parameters and sample preparation considerations were as described above for BChl c. HPLC purified pigments were dried under nitrogen and stored as a dried film in the dark at -20 °C until use.

Table 2.4 Gradient conditions for separation of chlorophylls, their derivatives, and carotenoids.

Solvent A: 15:65:20 (v/v/v) ethyl acetate/methanol/water. Solvent B: 60:30:10 (v/v/v) ethyl acetate/methanol/water. *method adapted from Craft²²⁴ to allow for larger column diameter.

Time (min)	Flow rate (ml min ⁻¹)	% Solvent A	% Solvent B
0.0	5.2	100.0	0.0
6.0	5.2	100.0	0.0
7.0	6.0	70.0	30.0
10.0	6.0	70.0	30.0
11.0	6.0	60.0	40.0
12.0	6.0	50.0	50.0
13.0	6.0	0.0	100.0
24.0	6.0	0.0	100.0
26.0	6.0	100.0	0.0

2.2.2 Chemical modification of pigments

2.2.2.1 Zinc-(Bacterio)Pheophytin (Zn-(B)Phe) production

Pigments were dried in a thin film and treated with 2 ml HCl (concentrations ranging from 1 – 5 M) to remove Mg. HCl was removed and residual HCl was evaporated under nitrogen. 2 ml sodium hydroxide (concentrations ranging from 1-5 M) was added and the vessel rotated for ~2 min to ensure thorough deprotonation of pheophytins. Sodium hydroxide was removed from the vessel and pigments were dried briefly under nitrogen. Pigments were dissolved in methanol. The solution was then saturated with zinc acetate and the container shaken vigorously for 5 mins or until colour change ceased. The reaction mixture was centrifuged for 10 min at 5000g to remove the insoluble fraction of zinc.

2.2.2.2 Pre-purification and HPLC purification and analysis of Zn-(B)Phe

To prevent precipitation of zinc on the column, an intermediate purification step was added to remove unreacted zinc and sodium hydroxide. After transmetallation, the supernatant was either mixed with an equivalent volume of chloroform and 2 equivalent volumes of H₂O or dried under N₂ and dissolved in a 1:3 (v/v) chloroform : H₂O mixture. In the case of the latter, the chloroform layer was removed and transferred to a new tube. The chloroform layer was washed a minimum of three times with H₂O or until the upper water phase was clear and the interface between layers was free from precipitant.

The method used for HPLC purification of BChl c was modified further to allow purification of the more polar Zn-BPhe c. The modified protocol consisted of three isocratic steps: 100% solvent A (100% methanol) for the first 35 min followed by 100% solvent B (4/1 (v/v) methanol hexane) for the next 10 min followed by 100% solvent A for a further 15 min leading to a total run time of 60 min. All other conditions and preparative steps were as used for BChl c.

2.2.2.3 Incorporation of an thiol group

(B)Chl and Zn-(B)Phe pigments were chemically modified to include an SH group at the C17³ position using cysteamine. 1 μmol of pigment was dried in a glass vial before being dissolved 1.2 ml THF. 1 μmol cysteamine in 400 μl ultrapure H₂O was added followed by 2 μmol potassium tert-butoxide in ultrapure H₂O. The reaction mixture was incubated overnight in the dark at 5°C on a rolling incubator. The reaction mixture was then dried and stored at -20°C.

2.2.2.4 X-ray photoelectron spectroscopy (XPS) analysis of pigments

XPS analysis of modified and native above was performed using a VG Escalab 250 with monochromated aluminum K-α X-ray source. The incident Xray beam had an energy of 1486.68 eV and the spot size was 500 μm. Measurements were made at a pressure of <1 × 10⁻⁹ mbar. Pigments were dried onto ozone cleaned fragments of microscope slides with evaporated gold layer. Samples were immobilised onto stainless steel sample holders by means of double sided carbon tape.

Low resolution survey spectra obtained using a pass energy of 150 eV over a binding energy range of -2 to 1400 eV with 1 eV increments were used to define regions for high resolution spectral scanning. Additional regions were also identified which corresponded to peaks expected for modified pigments.

For native and zinc modified Chl a and Chl b detailed scans of the Au 4f, C 1s, Mg 1s, N 1s, O 1s, Zn 2p, and S 2p regions were obtained. For BChl c and zinc modified BChl c, the Mg 2p region was used instead of the Mg 1s due to low signal strength. In addition, as no cysteamine-treated versions of BChl were prepared the S 2p peak regions were omitted for these pigments. For cysteamine-treated pigments, the regions were the same as those for native and zinc modified Chls with the addition of the K 2p region. These scans were obtained using a pass energy of 20 eV with 0.1 eV increments. Binding energies were calibrated by setting the 1s carbon peak to 285 eV.

2.3 MD simulation of BChl aggregation

Simulations of BChl aggregates were performed using molecular dynamics. Molecular dynamics is a computational technique, which, whilst originally developed for the modelling of liquids,²²⁵ has proved itself a useful tool for the modelling of complex biomolecules (see e.g. Schlick et al.).²²⁶ The wide applicability of MD owes itself, in large part to the technique's underlying simplicity.

2.3.1 Theoretical basis of molecular dynamics

Molecular dynamics is governed by Newton's second law (Equation (2. 1)). For a known starting configuration, it is possible to numerically integrate the equation of motion iteratively such that the positions of particles may be generated at each time step.

$$\mathbf{F} = m \frac{d^2 \mathbf{r}}{dt^2} = m\mathbf{a}$$

(2. 1)

Where \mathbf{F} is the force, m is the mass, $\frac{d^2 \mathbf{r}}{dt^2}$ the second derivative of the position, \mathbf{r} , with respect to time, t , and \mathbf{a} is the acceleration.

Such initial configurations may be determined from experimental techniques such as X-ray diffraction or nuclear magnetic resonance (NMR). Alternatively, models may be constructed from “best guesses” refined through computational techniques such as quantum mechanical (QM) modelling.

In order to compute future positions from an initial starting configuration, a potential energy function $U(\mathbf{r})_{total}$ is required. $U(\mathbf{r})_{total}$ is also referred to as the forcefield. The forces on each particle are given by the gradient of the forcefield i.e.

$$\mathbf{F} = \nabla U(\mathbf{r})_{total}$$

(2. 2)

The potential $U(\mathbf{r})_{Total}$ is an empirically derived function. A number of different biomolecular forcefields exist, differing either in their functional form or parameterisation, for example AMBER, CHARMM, GROMOS, and OPLS. Ubiquitous among these forcefields is the summation of the bonded and non-bonded interaction terms. The generic form of the potential energy function is given by:

$$U(\mathbf{r})_{total} = U_{Bond} + U_{Angle} + U_{Torsion} + U_{Improper} + U_{VDW} + U_{Electrostatic}$$

(2. 3)

where the first four terms represent contributions from bonded interactions between covalently linked atoms and the final two from non-bonded interactions. A summary of bonded and non-bonded interaction terms can be found in Figure 2.1 and Figure 2.2 respectively.

U_{Bond} is the potential energy due to bond stretching from an equilibrium separation (Figure 2.1a) summed over all bonds. This behaviour is treated as a simple harmonic oscillator and is given by:

$$U_{Bond} = \sum_{Bonds} \frac{1}{2} k_B (r - r_{eq})^2, \quad (2.4)$$

Where k_B is the force constant of the bond and r_{eq} is the equilibrium bond length.

However, harmonic potentials are only valid for small fluctuations from the equilibrium position. For larger fluctuations including those involved in bond breakage and formation events, the potential is more accurately described by the Morse potential given by:

$$U_{Bond} = D_e (1 - e^{-a(r-r_{eq})})^2 \quad (2.5)$$

where D_e is the dissociation energy, r_{eq} is the equilibrium bond length and a is constant which gives how quickly the potential changes with increasing separation. Due to its much higher computational cost and the need to parameterise D_e , r_{eq} and a for each bond, the Morse potential is rarely implemented.

The contribution due to angle bending, U_{Angles} away from an equilibrium bond angle is also described as a simple harmonic oscillator and given by:

$$U_{Angle} = \sum_{Angles} \frac{1}{2} k_A (\theta - \theta_{eq})^2, \quad (2.6)$$

where, k_A is the force constant for angle bending and θ_{eq} is the equilibrium bond length.

$U_{Torsion}$ is the contribution from torsional energy between a group of four atoms linked by three covalent bonds. This term is, given by:

$$U_{Torsion} = \sum_{dihedrals} \frac{V_n}{2} [1 + \cos(n\phi - \gamma)] \quad (2.7)$$

where, $\frac{V_n}{2}$ is the barrier height, n is the periodicity (the number of maxima and minima) and γ shifts the position of the maxima and minima.

$U_{Torsion}$ only takes into consecutively linked atoms i.e. proper dihedrals. An additional term, $U_{Improper}$, is needed to account for improper dihedrals and out-of-plane bending is given by:

$$U_{Improper} = \sum_{Improvers} \frac{1}{2} k_I (\omega - \omega_{eq})^2 \quad (2.8)$$

Where k_I is the associated force constant and ω_{eq} is the equilibrium angle between planes.

The non-bonded contributions come from van der Waals and electrostatic interactions given by:

$$U_{VDW} = \sum_{Non-bonded\ pairs} 4\varepsilon \left[\left(\frac{\sigma}{r} \right)^{12} - \left(\frac{\sigma}{r} \right)^6 \right] \quad (2.9)$$

where, ε is the depth of the potential well and σ is the finite distance at which the inter-particle potential is zero.

In vacuum, the electrostatic interaction term $U_{Electrostatic}$ is given by:

$$U_{Electrostatic} = \sum_{Non-bonded\ pairs} \frac{q_i q_j}{4\pi\varepsilon_0 r} \quad (2.10)$$

where, q_i and q_j are the charges on the two particles and ε_0 permittivity of free space.

The evaluation of the pairwise non-bonded interactions accounts for a large proportion of the computational cost. A number of methods and approximations are employed to reduce the computational cost. Van der Waals interactions are represented using the Lennard-Jones potential Equation (2. 9). As can be seen from Figure 2.2a atom pairs beyond the optimal inter-particle distance move closer to each other due to mutual attraction given by the r^{-6} term. Particles closer than the optimal distance will repel each other given by the r^{-12} term. Van der Waals interactions are typically short ranged and as such, distance cut-offs or switching functions may be used to reduce computational costs.

In the case of electrostatic reactions described by Equation (2. 10), the interaction scales with r^{-1} , indicating long ranged interactions for which cut-offs or switching functions are inappropriate. Fortunately, alternative methods for improving efficiency in calculating electrostatic interactions have been developed. One such method is the particle-mesh Ewald method (PME). The Ewald summation method, a special case of the Poisson summation formula, divides long range interactions into two parts, a short range contribution in real space and a long range contribution in reciprocal space. The method offers rapid convergence reducing the problem from $\mathcal{O}N^2$ to $\mathcal{O}N \log N$. This speed up is facilitated by the use of a fast Fourier transform requiring each atomic point charge to be distributed on a lattice grid.

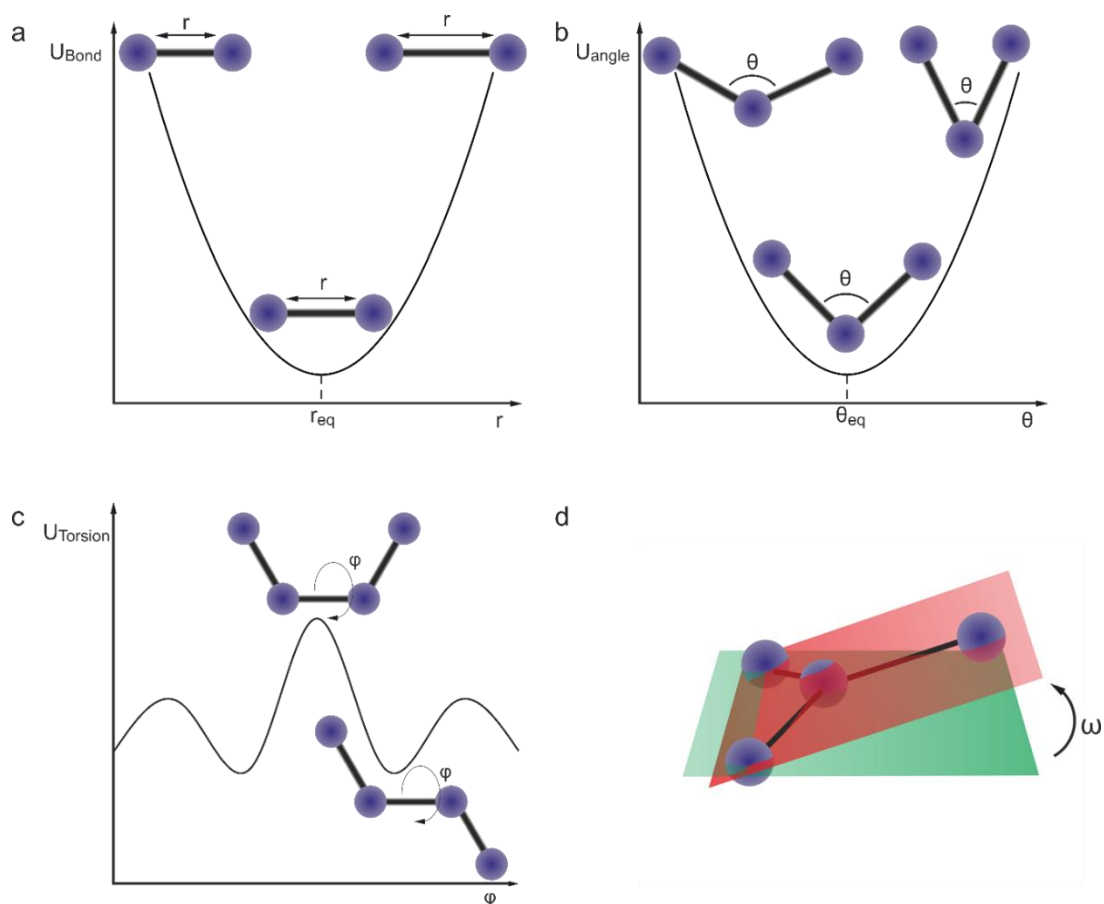


Figure 2.1 Summary of bonded interactions.

The potential from bonded interactions may be divided into contributions from (a) bond stretching, U_{Bond} ; (b) bond bending, U_{Angle} ; (c) bond torsion, $U_{Torsion}$; (d) improper dihedrals, $U_{Improper}$.

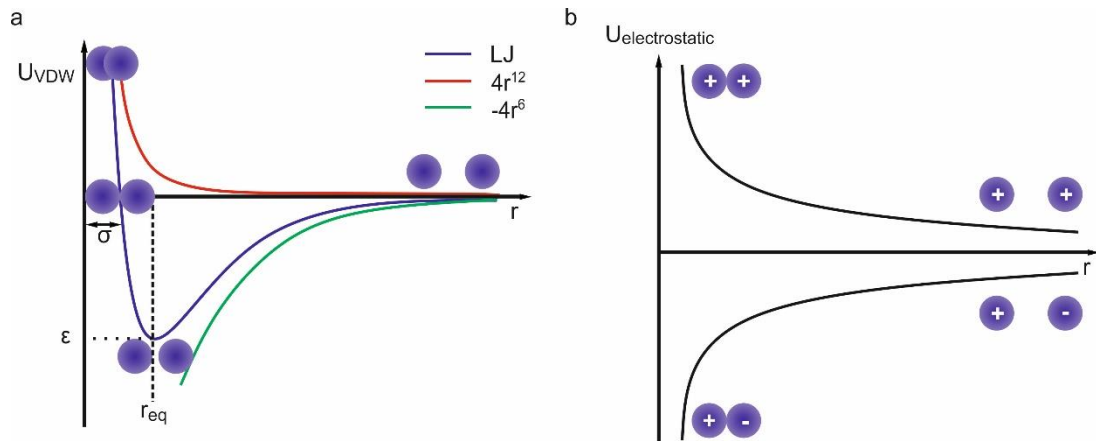


Figure 2.2 Summary of non-bonded interactions.

The non-bonded contributions to the potential energy function can be divided into those from (a) van der Waals interactions, U_{VDW} , and (b) electrostatic interactions, $U_{Electrostatic}$.

Once an appropriate forcefield has been selected Newton's equations of motion may be solved through numerical integration to yield particle trajectories.

The most common method uses the Verlet algorithm. In molecular dynamics simulations, the configuration is split in to a series of frames separated by a time τ the time step. Information from previous steps can be used to generate subsequent steps.

The Lagrangian of a system is defined as the difference between its kinetic and potential energy.

$$L = K(\dot{q}) - U(q)$$

(2. 11)

Here q is a general coordinate. In forcefield dynamics, the potential energy $U(q)$ depends only on position. The kinetic energy $K(\dot{q})$ depends only on the velocity, \dot{q} . A general property of the Lagrangian is that the time derivative of the momentum is equal to the derivative of the Lagrangian with respect to position i.e.

$$\frac{\partial}{\partial t} \left(\frac{\partial L}{\partial \dot{q}_i} \right) = \frac{\partial L}{\partial q_i}$$

(2. 12)

For a general system, the Lagrangian may be given by:

$$L(\vec{r}_i, \vec{v}_i) = \frac{1}{2} \sum_i^N m_i v_i^2 - \sum_i^{N-1} \sum_{j>1} U(r_{ij})$$

(2. 13)

With the first term giving the kinetic energy and the second giving the potential energy.

As $\dot{q}_i = \frac{\partial r_i}{\partial t} = v_i$ and the momentum is given by,

$$\frac{\partial L}{\partial v_i} = m_i v_i$$

(2. 14)

The left hand side of Equation (2. 12) can be rewritten as:

$$\frac{\partial}{\partial t} \left(\frac{\partial L}{\partial v_i} \right) = m_i \frac{\partial v_i}{\partial t}$$

(2. 15)

Similarly, the right hand side can be rewritten as:

$$\frac{\partial L}{\partial r_i} = - \frac{\partial V}{\partial r_i}$$

(2. 16)

This gives

$$- \frac{\partial V}{\partial r_i} = m_i \frac{\partial v_i}{\partial t}$$

(2. 17)

which simply states that force is the rate of change of momentum i.e. $f = ma$ for each particle.

$$f_i = m_i \frac{\partial v_i}{\partial t} \tag{2. 18}$$

The force on an atom i for any given configuration can be determined from the forcefield. The above equation can be rearranged to give:

$$\frac{\partial v_i}{\partial t} = \frac{f_i}{m_i} \tag{2. 19}$$

Meaning that for any given configuration we know the acceleration of each particle. This means given an initial velocity $v_i(0)$ we can determine the velocity of the particle some time later $v_i(\tau)$:

$$v_i(\tau) = v_i(0) + \int_0^\tau \frac{dv_i}{dt} dt \tag{2. 20}$$

Similarly, we can obtain the position of each particle at τ by integrating the particle's velocity:

$$r_i(\tau) = r_i(0) + \int_0^\tau v_i(t) dt \tag{2. 21}$$

Once particles move and the distances governing the potentials change, the forces acting on them also change. Molecular dynamics must therefore integrate these equations of motion such that trajectories may be obtained numerically.

There are a number of requirements for such an integration algorithm:

- 1) Computational speed
- 2) Low memory demand
- 3) Accuracy
- 4) Stability (i.e. energy is conserved and there is no drift)
- 5) Time reversibility

- 6) Symplectic (i.e. each step in the simulation constitutes the same volume of phase space)

A popular example of an algorithm which meets these requirements is the Verlet algorithm. Newton's law for the position of any atom at a time $t + \tau$ may be given as a Taylor expansion:

$$r_i(t + \tau) = r_i(t) + v_i(t)\tau + \frac{1}{2} \frac{f_i(t)}{m_i} \tau^2 + \frac{1}{6} \ddot{r}_i(t) \tau^3 \dots$$

(2. 22)

Similarly, for a negative time step $t - \tau$ we have:

$$r_i(t - \tau) = r_i(t) - v_i(t)\tau + \frac{1}{2} \frac{f_i(t)}{m_i} \tau^2 - \frac{1}{6} \ddot{r}_i(t) \tau^3 \dots$$

(2. 23)

Adding Equations (2. 22) and (2. 23) and approximating:

$$r_i(t + \tau) = 2r_i(t) - r_i(t - \tau) + a_i(t)\tau^2$$

(2. 24)

With:

$$a_i(t) = -\frac{1}{m_i} \nabla U(r_i)_{total}$$

(2. 25)

For a sufficiently small timestep, $\delta\tau$, Equation (2.24) converges to continuous trajectories gives the position of the atom at τ and removes the need to calculate the velocity at each time step. A 'timeline' for the Verlet algorithm is shown in Figure 2.3.

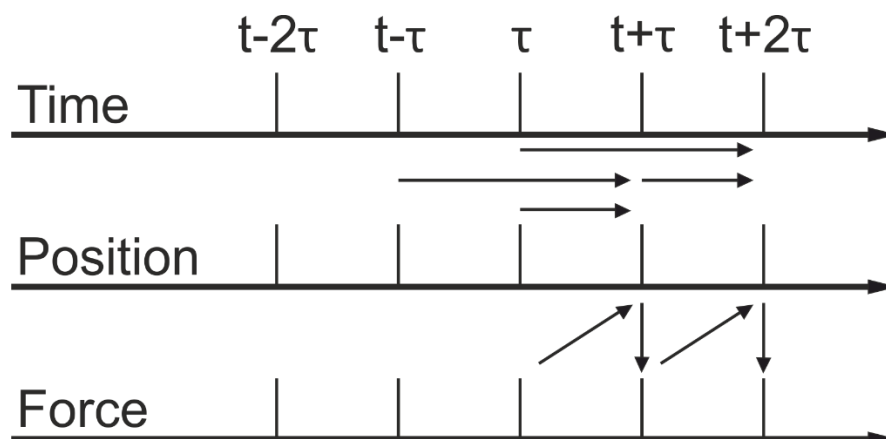


Figure 2.3 Verlet algorithm timeline.

The Verlet algorithm is a method which allows integration of the equations of motion such that continuous trajectories are obtained numerically.

2.3.2 Construction of pigment systems

2.3.2.1 Dimer arrangements

Pigment assemblies were constructed for various pigment dimer building block units (as shown in Figure 2.4). Structures were named according to IUPAC rules for tetrapyrroles: S, used to denote “Syn” refers to the arrangement where the hydroxy group at C3¹ is on the same side of the chlorin ring as the C17-propionic acid moiety. Conversely, A, used to denote “Anti” is used when it is on the opposite side. The orientation of the Mg cation with respect to the C17 is denoted using α and β . Consistent with the notation proposed by Balaban et al.,⁸⁵ the configuration with the magnesium cation on the opposite face to the C17-propionic acid moiety is designated as the α -configuration with the β -configuration having the magnesium cation on the same side. Using this nomenclature, specifying the configurations of both entities for both molecules within the dimer unit gives a four-letter code denoting stereochemistry of each motif e.g. $\alpha A\alpha A$ or $\beta S\alpha A$. In addition, a suffixes of d, g, and u are used to denote structures with special properties. For example $\alpha S\beta A-d$ is formed of displaced dimers whereas $\beta S\alpha A-g$ is a modified version of $\beta S\alpha A$ with intermolecular contacts according to Ganapathy et al..³² $\beta S\alpha A-u$ is an anti-parallel dimer, optimised to reproduce

experimentally observed X-ray diffraction. β S α A-g and β S α A-u are not shown in Figure 2.4 due to their stereochemistry being identical to β S α A.

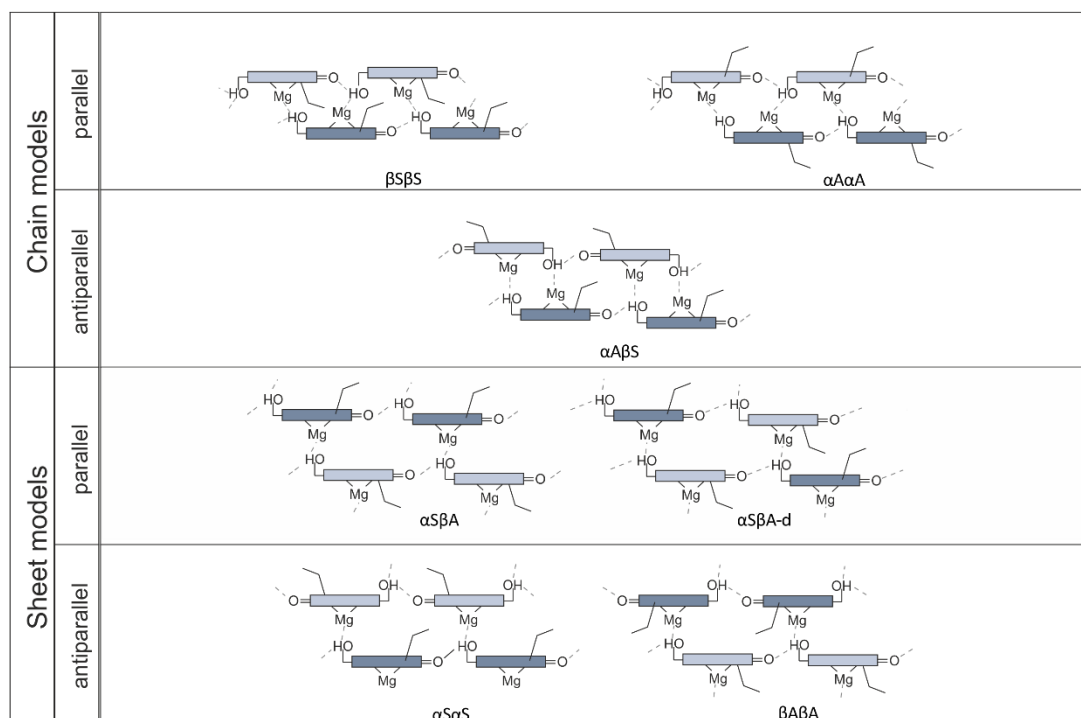


Figure 2.4 Classification of structural motifs used in molecular dynamics simulations.

The structural motifs used in this thesis may be divided into four categories: parallel chains, antiparallel chains, parallel sheets, and antiparallel sheets. Figure adapted from Alster et al.²⁶ Not shown β S α A-g and β S α A-u due to similarity to β S α A.

2.3.2.2 Single and triple layer sheets

The above dimers were arranged into (10 x 8) sheets of dimers with alcohol tails pointing perpendicular to the plane formed by the sheet. These sheets were optimised by Alster et al.²⁶ to satisfy known experimental constraints such as Mg coordination. These sheets were then repeated using the script in Appendix B to form a 3 lamellae system as shown in Figure 2.5.

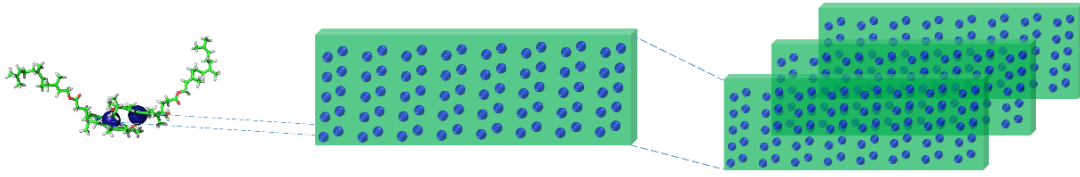


Figure 2.5 Construction of multilayer system from initial dimers.

The initial dimer (as described in Figure 2.4) is arranged on a regular lattice which is then repeated to form a 3 lamellae system.

For the simulations the first 4 (or 5 in the case of $\alpha S\beta A_d$, $\beta S\alpha A_g$, $\beta S\alpha A_u$) letters correspond to the dimer arrangement used to produce a sheet. The suffix 3 is used to denote a three layer system.

For each system, three repeats were performed, the first of these is simply labelled as described above, the second and third repeats are denoted by the suffixes $_1$ and $_2$. For example a single layer system performed on sheet based on the $\alpha A\alpha A$ dimer configuration is given by $\alpha A\alpha A$ and the first repeat of a triple layer system based on $\beta A\beta A$ is given by $\beta A\beta A_3_1$. A full list of simulations is presented below.

Table 2.5 List of simulations performed.

	First repeat	Second repeat	Third repeat
Single layer	$\alpha A\alpha A$	$\alpha A\alpha A_1$	$\alpha A\alpha A_2$
	$\alpha S\alpha S$	$\alpha S\alpha S_1$	$\alpha S\alpha S_2$
	$\alpha S\beta S$	$\alpha S\beta S_1$	$\alpha S\beta S_2$
	$\alpha S\beta Sd$	$\alpha S\beta Sd_1$	$\alpha S\beta Sd_2$
	$\beta A\beta A$	$\beta A\beta A_1$	$\beta A\beta A_2$
	$\beta S\alpha A$	$\beta S\alpha A_1$	$\beta S\alpha A_2$
	$\beta S\alpha Ag$	$\beta S\alpha Ag_1$	$\beta S\alpha Ag_2$
	$\beta S\alpha Au$	$\beta S\alpha Au_1$	$\beta S\alpha Ag_2$
	$\beta S\beta S$	$\beta S\beta S_1$	$\beta S\beta S_2$
Triple layer	$\alpha A\alpha A3$	$\alpha A\alpha A3_1$	$\alpha A\alpha A3_2$
	$\alpha S\alpha S3$	$\alpha S\alpha S3_1$	$\alpha S\alpha S3_2$
	$\alpha S\beta S3$	$\alpha S\beta S3_1$	$\alpha S\beta S3_2$
	$\alpha S\beta Sd3$	$\alpha S\beta Sd3_1$	$\alpha S\beta Sd3_2$
	$\beta A\beta A3$	$\beta A\beta A3_1$	$\beta A\beta A3_2$
	$\beta S\alpha A3$	$\beta S\alpha A3_1$	$\beta S\alpha A3_2$
	$\beta S\alpha Ag3$	$\beta S\alpha Ag3_1$	$\beta S\alpha Ag3_2$
	$\beta S\alpha Au3$	$\beta S\alpha Au3_1$	$\beta S\alpha Ag3_2$
	$\beta S\beta S3$	$\beta S\beta S3_1$	$\beta S\beta S3_2$

2.3.3 Simulation details and setup

The MD simulations discussed in this thesis were performed using the AMBER 10 suite of programs using the general AMBER force field (GAFF). In order to fully exploit available high performance computing facilities, PMEMD, the parallelised implementation of SANDER, was used. Simulations were subjected to minimisation, heating, and equilibration steps prior to unrestrained production MD runs.

2.3.3.1 Minimisation, heating, and equilibration steps

As the structures were not necessarily energetically optimised, it was necessary to perform energy minimisation and equilibration of each system before performing proper simulations of the system. This was performed in

four stages at constant volume with restraints decreasing for each stage. Minimisation was performed for 10000 cycles with the first 50 using the steepest descents method before switching to the conjugate gradients method. For the first three minimisation steps the convergence criterion (drms) was set to 0.5 kcal/mol-Å. For the final minimisation step this was reduced to 0.2 kcal/mol-Å. The restraints were decreased from an initial value of 50 to 0 over the course of the minimisation. The details of the initial minimisation steps can be found in Table 2.6 together with details of other steps.

After minimisation, one heating step (md1), and seven equilibration steps (md2 – md8) at constant pressure were performed. At the start of the heating step atoms were assigned velocities from a Maxwellian distribution corresponding to an initial temperature of 100 K. Over the course of this step the temperature was raised to 300 K, which served as the reference temperature for all subsequent steps including the final MD production run. The weak coupling temperature algorithm was used ensure the kinetic energy remained appropriate for the reference temperature. For all steps bond interactions involving hydrogen atoms were omitted in force evaluations and a non-bonded cut-off of 9 Å. For each step the SHAKE algorithm was used to constrain all bonds involving hydrogen atoms. As bond stretching represents the fastest motion, its elimination using the SHAKE algorithm allowed a longer time step of 0.002 ps to be used. Each of these steps lasted 10 ps with the system restraints being progressively removed. Details of these steps are summarised below in Table 2.6.

Table 2.6 Conditions for system minimisation, heating, and equilibration.

A multistage minimisation, heating, and equilibration protocol was employed prior to full scale production MD. k is the positional restraint in units of kcal/molÅ².

Stage	Type	Details	Duration
min1	Minimisation	Solute restrained, solvent frozen, $k = \text{default}$	10000 cycles
min2	Minimisation	Solute restrained, solvent frozen $k = 50$	10000 cycles
min3	Minimisation	Solute restrained, solvent frozen $k = 25$	10000 cycles
min4	Minimisation	All atoms free to move, $k = 0$	10000 cycles
md1	Heating	Solute restrained, $k = 100$	10 ps
md2	Equilibration	Solute restrained, $k = 100$	10 ps
md3	Equilibration	Solute restrained, $k = 50$	10 ps
md4	Equilibration	Solute restrained, $k = 25$	10 ps
md5	Equilibration	Solute restrained, $k = 10$	10 ps
md6	Equilibration	Solute restrained, $k = 5$	10 ps
md7	Equilibration	Solute restrained, $k = 2.5$	10 ps
md8	Equilibration	Solute restrained, $k = 1$	10 ps

2.3.3.2 Production dynamics

After md8, a longer unrestrained MD step (md9) lasting 30 ns or 48 hours computation time, whichever was the shorter, was performed with the same conditions set out above.

Simulation scripts can be found in Appendix C.

2.3.4 Computational resources

High performance computing resources were used to carry out the simulations and perform analysis. These were supplied through the University of Leeds Advanced Research Computer 1 (ARC1) and Advanced Research Computer 2 (ARC2) facilities. ARC1 is a shared batch system running the CentOS 5

Linux operating system consisting of 672 cores (Intel X5560 2.8GHz processors) of computing capacity with an additional 64 'large memory' cores (AMD 8384 2.7 GHz processors) serviced by over 100 TB of fast disk storage with a data transfer rate of around 3.2 GB per second.

ARC2 is a shared batch system based on the CentOS 6 Linux operating system with 3040 cores of computing capacity (8-core Intel E5-2670 2.6GHz processors) with 2 GB/core and is serviced by 170 TB of fast disk storage (giving a data transfer rate of around 4 GB per second). In the case of both ARC1 and ARC2, compute nodes are connected with 'Infiniband' interconnects.

ARC1 was used for running simulations and ARC2 was used for performing computationally demanding analysis including the X-ray scattering predictions.

2.3.5 Analysis of MD results

2.3.5.1 Structures

The root-mean-squared (RMS) pair-wise separation of Mg atoms were calculated for a series of approximately logarithmically spaced time points (~100 points) for each structure. In order to do this, pdb files were generated from simulation .x output files using ptraj. A Matlab script was then used to extract Mg atom positions from these pdb files and calculate the RMS pair-wise separations for each time point. The Matlab script used can be found in Appendix D. These values were plotted as a function of time for each simulation to allow system evolution to be studied.

Simulation trajectories were visualised using the Virtual Molecular Dynamics program (VMD). This allowed visual assessments to be made on the degree of curvature present in each system as well as its axis and direction. Visualising simulation trajectories in this way also allowed for any defects within simulation sheets to be identified.

Dipole moment plots were created using Matlab to extract the positions of the ND and NB nitrogen atoms from pdb files. Plots were then generated with arrows pointing in these directions, corresponding to the Q_y dipole moments. The Matlab script used to produce dipole plots can be found in Appendix D.

These plots allowed the dipole stacking and disorder within structures to be visualised more easily.

2.3.5.2 Energy of simulated systems

Total system energy, was extracted from simulation output files (see Appendix D for script). This was plotted as a function of simulation time for each simulation in order to investigate system energy evolution.

The energy for the last 1 ns (10 000 points) was averaged to provide a final equilibrated system energy. Structures were ranked according to their final equilibrated energies to determine the effect of dimer type and curvature on energy.

In order to determine whether a stabilising effect exists for multilamellar systems, average energies were determined for each dimer type, for both single and triple layers, by averaging over repeats. Single layer average energies were then compared to their triple layer

2.3.5.3 X-ray scattering predictions

X-ray scattering predictions from simulations were produced using a modified code supplied by Roman Tuma. This code was modified to produce an OpenMP parallelised version (Appendix D) to allow more time points to be analysed. X-ray scattering predictions were summed over the final 0.1 ns of simulation (100 frames) and compared to both previously published X-ray scattering data and X-ray scattering predictions corresponding to the start of the simulation.

2.4 Quantum dots

2.4.1 Quantum dot synthesis

Quantum dots were prepared via precursor thermal decomposition. Briefly, 24 mg (0.125 mmol) of copper iodide, 73 mg (0.25 mmol) indium acetate, 38.2 mg (0.5 mmol) thiourea, 200.4 mg mercaptoundecanol, 64.7 mg Biotin-PEG(4300)-SH (molar ratio of 50:1 thiol:biotin-thiol, corresponding to on average to approx. 3-4 biotin-thiols per quantum dot) were mixed in 5 ml ethylene glycol. After purging with argon, the flask was heated to 170 °C whilst stirring. Aliquots for analyses were taken using a glass syringe at 10, 15, 20, 25, 30, 40, 50, 60 min (timed from the start of heating) and quenched by

injecting into room temperature methanol, effectively stopping the reaction while keeping the products dispersed. Due to larger sample requirements, in the case of quantum dots prepared for X-ray diffraction, aliquots were not taken and instead the reaction quenched at 15 min by submerging the reaction vessel in cold water.

2.4.2 Quantum dot cleaning

Free thiol, biotin-thiol, unreacted compounds and residual ethylene glycol were removed using a 30 kDa KrosFlow modified Polyethersulfone (mPES) hollow fibre filter module in conjunction with a KrosFlo Research Ili Tangential Flow Filtration System (based on the setup outlined in Sweeney et al.)²²⁷ set at a flow rate of 60 ml min⁻¹. The pressure of the sample entering and leaving the membrane tube was 5.9 psi and 4.1 psi respectively. The pressure applied on the outside of the membrane was 0.1 psi providing a transmembrane pressure of 5.2 psi. Due to the negative transmembrane pressure, the dispersing solvent was able to pass through the membrane, removing with it reagents, unbound ligand and residual amounts of ethylene glycol. The volume of the sample within the system was allowed to reduce by half before being made up to its initial volume with fresh methanol. This was repeated 5 times leading to a >96% reduction in sample contamination. Quantum dots were stored in the dark at 4 °C until use.

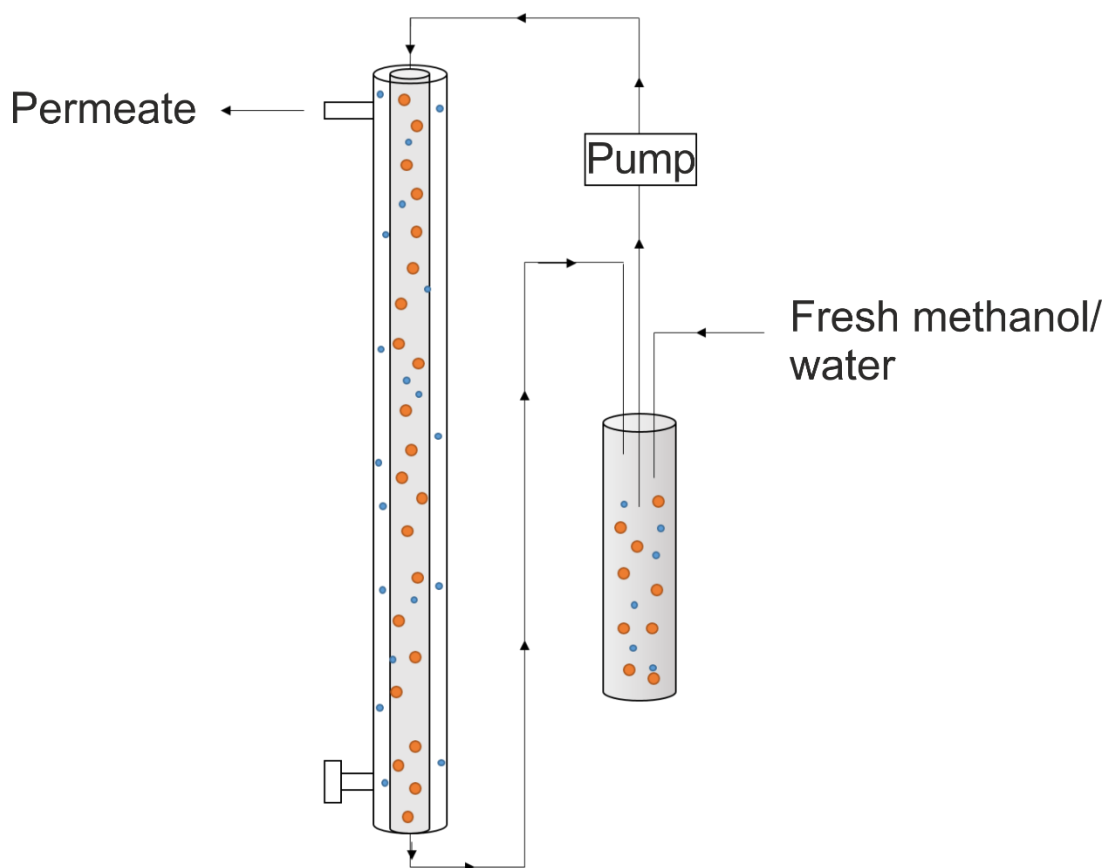


Figure 2.6 KrosFlo diafiltration setup used for purification.

Free thiols and unreacted reagents were removed using diafiltration.

2.4.3 Absorbance measurements, determination of E_1 , E_x , and concentration

UV-Vis absorption spectra were recorded using a Genesys 6 spectrophotometer. Samples used for UV-Vis absorption spectroscopy were diluted so the optical density at the first transition was ~ 0.1 . E_1 was determined from the minimum of the second derivative of the absorption spectrum. E_x was determined using Tauc plots (a description of this can be found in Huxter et al.).²⁰⁵ Where concentrations were estimated, this was done using the Beer-Lambert law with the extinction coefficient at 3.1 eV, $\epsilon_{CIS}(3.1 eV)$, determined according to the method of Booth et al.:²¹¹

$$\varepsilon_{ClS}(3.1 \text{ eV}) = (2123 \pm 109)d^{3.8 \pm 0.3}$$

(2. 26)

Where d is the size estimated here using transmission electron microscopy (TEM) data and synthesis time.

2.4.4 TEM measurements

Nanocrystal size and morphology was examined using High Resolution Transmission Electron Microscopy (HRTEM) with a FEI Tecnai TF20 field emission gun (FEG)-TEM operated at 200 kV and a Gatan Orius SC600A charge coupled device (CCD) camera. Quantum dots dispersed in methanol were deposited onto gold-coated carbon grids by drop casting. Regions of interest were determined using low magnification images (<120000x). Size distributions of quantum dots were determined using either 220000 or 390000 magnification images, based on a sample of at least 100 particles from each aliquot. Lattice spacings were determined from high magnification (690000x) images using 2-dimensional Fourier transform.

2.4.5 X-ray diffraction (XRD) measurements

Owing to larger sample requirements, an additional synthesis was performed as described above without aliquots. The synthesis was quenched at 15 min by immersing the reaction vessel in cold water. The entire reaction product (~100 mg) was used. Solvent exchange into pure (18.2 MΩ) H₂O was performed using the KrosFlo Research Ili Tangential Flow Filtration System under the conditions described above using H₂O instead of methanol to make up lost volume. Quantum dots in H₂O were frozen using liquid nitrogen and lyophilised to produce a fine powder. XRD pattern was obtained using a Panalytical Model X'Pert Pro MPD X-ray diffractometer with Cu Kα source ($\lambda = 0.154 \text{ nm}$) and a X'cellerator detector. A continuous scan over a 2θ range from 10° to 80° was performed with an acquisition time of 45 min.

2.4.6 Energy dispersive analysis of X-rays (EDX)

Elemental composition was established by energy dispersive X-ray analysis using an Oxford Instruments 80 mm X-Max silicon drift device (SDD) EDX detector on areas identified from low and medium magnification images as

having a high density of nanoparticles. A low background sample holder and gold TEM grids were used to minimise background copper signal.

2.4.7 XPS analysis of quantum dots

The elemental stoichiometry of quantum dots was determined using a Kratos Axis Ultra Delay-line detector (DLD) with monochromated aluminum K α X-ray source. The incident X-ray beam had an energy of 1486.69 eV with a rectangular illumination profile of \sim 300 by 700 μ m. Measurements were made under high vacuum ($p < 1 \times 10^{-9}$ mbar). Quantum dots in methanol were dropcast onto ozone cleaned fragments of microscope slides with a 50 nm evaporated gold layer on a 5 nm chromium. Samples were immobilised onto stainless steel sample holders by means of double sided carbon tape. Low resolution survey spectra were obtained using a pass energy of 160 eV over a binding energy range of -5 to 1200 eV with 0.5 eV increment. High resolution spectral scans were obtained using a pass energy of 20 eV with 0.05 eV increments. An acquisition time of 240 s was used for both survey and high resolution scans. Binding energies were calibrated by setting the 1s carbon peak to 285 eV. Copper to indium ratios were determined using the Cu2p 3/2 and In 3d 5/2 peaks.

2.4.8 Photoluminescence (PL) emission and excitation spectra

Photoluminescence spectra were obtained using a Shimadzu RF-301PC Spectrofluorophotometer. 450 nm excitation and emission slit widths of 5 nm were used. Samples used for steady state fluorescence measurements were diluted to fall within the linear response region of the spectrofluorimeter. Stokes shifts were calculated as the difference between the position of PL maximum intensity and the energy of the first transition determined above.

2.4.9 Photoluminescence quantum yield (PLQY) measurements

Absolute values for PLQY were determined using a spectroscope equipped with an 10 cm diameter integrating sphere (SphereOptics GmbH). Samples excitation was via indirect diffused light from light emitting diodes (LEDs) emitting in the range 2.4 to 3.1 eV. Light from the integrating sphere was

coupled to a silica fibre bundle, the output of which was imaged by a Acton SpectraPro SP2150i spectrometer with a Spec-10:400B back-illuminated CCD camera. PLQY was determined as the ratio of the number of emitted and the number of absorbed photons. A more detailed theoretical discussion and further details on the set-up can be found in Valenta.²²⁸

2.4.10 PL lifetime measurements

Time-domain nanosecond PL lifetime measurements were made using a set-up consisting of a gated PIMAX intensified CCD (ICCD) detector (Princeton Instruments) and iHR-320 monochromator (Horiba). An optical parametric oscillator (OPO) (PG-122, EXPLA, Vilnius, Lithuania), pumped by yttrium aluminium garnet (YAG) laser, was used as the excitation pulse source. Measurement frequency was 10 Hz. The pulse energy was measured to be 0.25 mJ at 450 nm with ~3.5 ns full width at half maximum. Spectra were measured over 503 to 897 nm range with delay times from 5 to 1580 ns, where zero time was taken to be the centre of the excitation pulse. Experiments were performed at 4 °C to minimise sample degradation. Steady-state absorption and PL spectra were measured before and after the experiments to ensure that no degradation occurred during acquisition. Global analysis fitting software^{229,230} (provided by Jan Alster) was used to extract lifetimes and decay associated spectra. Transition energies were determined from fitted PL peak positions and the relative contribution of each fitted component was estimated using fitted peak areas.

2.4.11 Transient absorption measurements

Nanosecond transient absorption spectroscopy was performed using the same set-up as PL measurement with the addition of a xenon flash lamp to generate probing white light pulse. White light was split into probe and reference beams, and were projected on to different parts of the ICCD detector. Measurement was running at 10 Hz frequency with halved (5 Hz) frequency of excitation laser. Changes in transient absorption over the range 364 to 743 nm were calculated as difference between measurements with and without excitation. Spectra were measured for delay times between -5 and 500 ns. Experiments were performed at 4 °C using glass cuvettes to minimise

degradation. Steady-state absorption and PL spectra were measured before and after to monitor sample degradation during data acquisition. Data was analysed using the same software used for PL lifetime analysis.

Chapter 3

Results and Discussion: Bacteriochlorophyll and Zinc-(Bacterio)Pheophytin Preparation and Chemical Modification

3.1 Introduction

This chapter covers the extraction, purification, and chemical modification of chlorophylls (Chls) and bacteriochlorophylls (BChls). Section 3.2 deals with the extraction of pigments from bacterial cells and plant matter and their purification. Section 3.3 deals with the chemical modification of pigments; including the production of zinc-(bacterio)chlorophyll derivatives to increase stability (Section 3.3.1) and attempts at incorporation of a thiol group to facilitate coupling to quantum dots (Section 3.3.2). These sections include details of UV-Visible (UV-Vis) absorbance spectroscopy and XPS analysis to determine whether modification was successful.

3.2 Purification of BChls and Chls

3.2.1 Growth of *Chlorobaculum tepidum* cells

Chlorobaculum tepidum were cultured in order to provide a supply of BChl c cells for modification and investigation. No bacterial growth was observed for attempts to grow cells in 38°C incubators under illumination. Initially, this was assumed to be due to incorrect selection of light bulbs. However, even after changing to the 60W incandescent bulbs used elsewhere,²³¹ no growth was observed. Nevertheless, growth, as indicated by the presence of a dark green matter, was observed for cells grown at room temperature in proximity to the laboratory window. Cells were allowed to grow until contents were visually so dense as to render additional growth unlikely. The dark green colour of the cultures, together with the high concentration of BChl c contained within lysed cell confirmed these cells were most likely *Chlorobaculum tepidum*.

3.2.2 Extraction of BChl c from cells

Extraction of BChl c cells from *Chlorobaculum tepidum* cells was performed using a modification of an established method.²²¹ On addition of the 1:1:2 (v/v/v) methanol/chloroform/water solvent mixture to the dried cells, a concentrated chloroform subphase formed below a cloudy white-green water-methanol layer. After repeated washing with water, the water layer became colourless and transparent and the turbidity of the chloroform layer disappeared. This is consistent with the successful removal of cell debris and other insoluble matter in the crude extract.

Figure 3.1a shows the spectrum of the resulting crude pigment extract from cells of *Chlorobaculum tepidum* before washing with hexane. Significant peaks are present at 416 nm, 434 nm, and 669 nm. A smaller peak is also present at 488nm. Pigments removed via hexane washing (dried and resuspended in methanol) are shown in Figure 3.1b. Spectra of removed pigments exhibited large peaks at 488 nm, 458 nm, and 431 nm, 414 nm, and a smaller peak at 669 nm. In the spectrum of the pigments remaining after multiple hexane washes is shown in Figure 3.1c. The carotenoid peaks previously present at 488nm and 416nm are absent. Peaks at 434 nm and 669 nm remain.

The largest peaks at 669 nm and 434 nm for pigments extracted from whole cells of *Chlorobaculum tepidum* observed both before and after washing with hexane correspond to the Q_y and Sorret peaks for monomeric BChl c pigments which is the most abundant constituent of the extract.

The significant absorption observed in the region 500-650 nm for pigment extracts before washing with hexane can be ascribed to the presence of a significant fraction of carotenoids. The decrease in absorption in this region on washing with hexane, together with the spectrum obtained for the hexane soluble component indicates the removal of the majority, though not all, of the carotenoids.

The increase in absorption observed at ~750 nm (not seen in BChl c) may be explained by the presence of a small amount of BChl a from the baseplate and reaction centre.

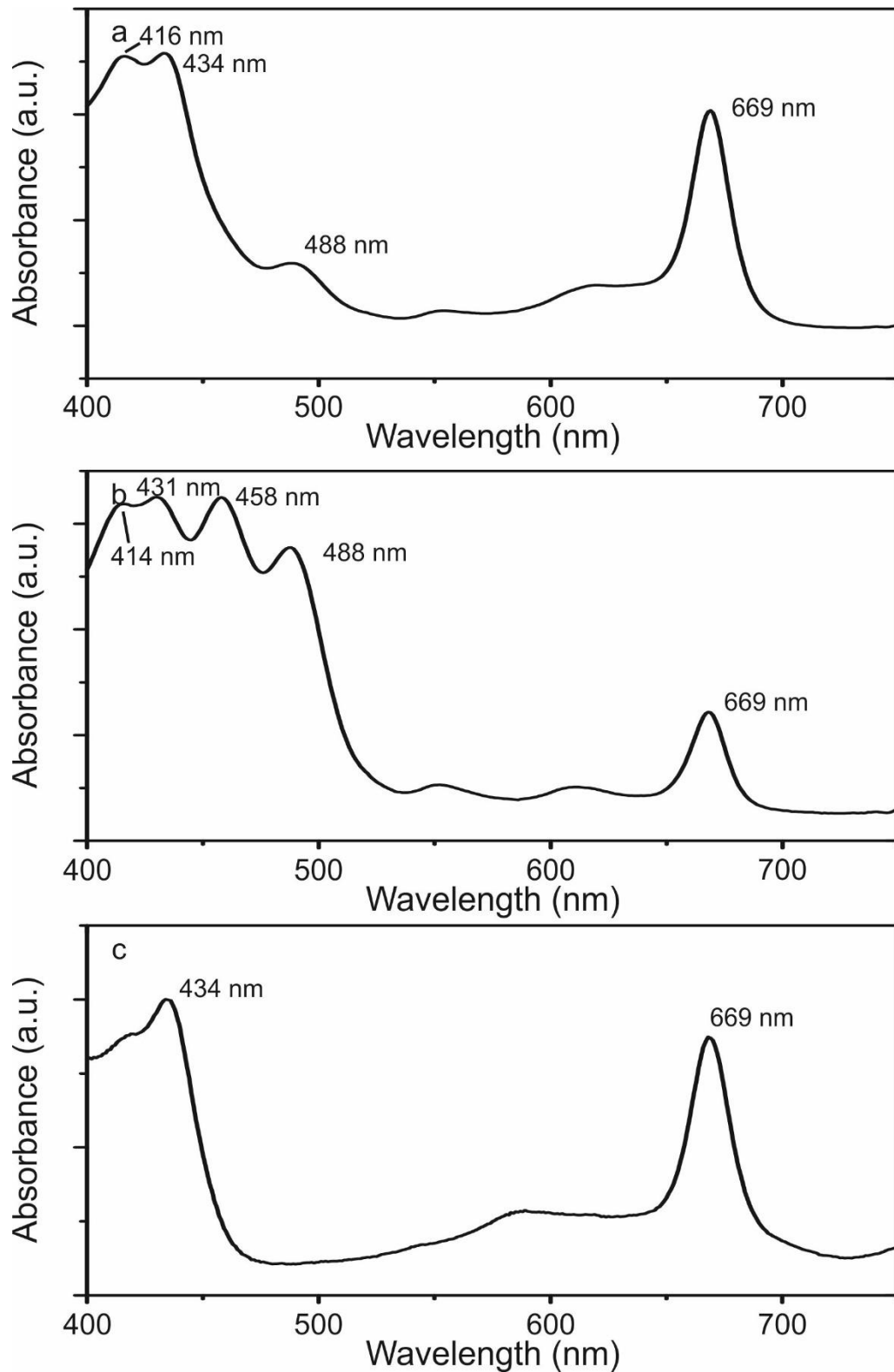


Figure 3.1 Extraction of BChl c pigments from *Chlorobaculum tepidum*.

Spectra of pigments extracted from whole cells of *Chlorobaculum tepidum*. (a) Pigment rich chloroform layer, (b) carotenoid rich hexane wash, and (c) after hexane washing.

3.2.3 Extraction of BChl e from chlorosomes

In order to provide a second bacteriochlorophyll pigment for modification and investigation, BChl e as extracted from chlorosomes of *Chlorobaculum phaeobacteroides*. Similar observations to those made for the extraction of BChl c from cells were made for BChl e pigments extracted from chlorosomes of *Chlorobaculum phaeobacteroides* (Figure 3.2). Figure 3.2a shows the absorbance spectra for whole *Chlorobaculum phaeobacteroides* chlorosomes with peaks at 457 nm, 521 nm, and 707 nm corresponding to the presence of aggregated BChl e as well as significant amounts of β -Carotene. After addition of methanol and rinsing with hexane, the two most prominent peaks were found at 472 nm and 656 nm, corresponding to BChl e monomers Figure 3.2b.

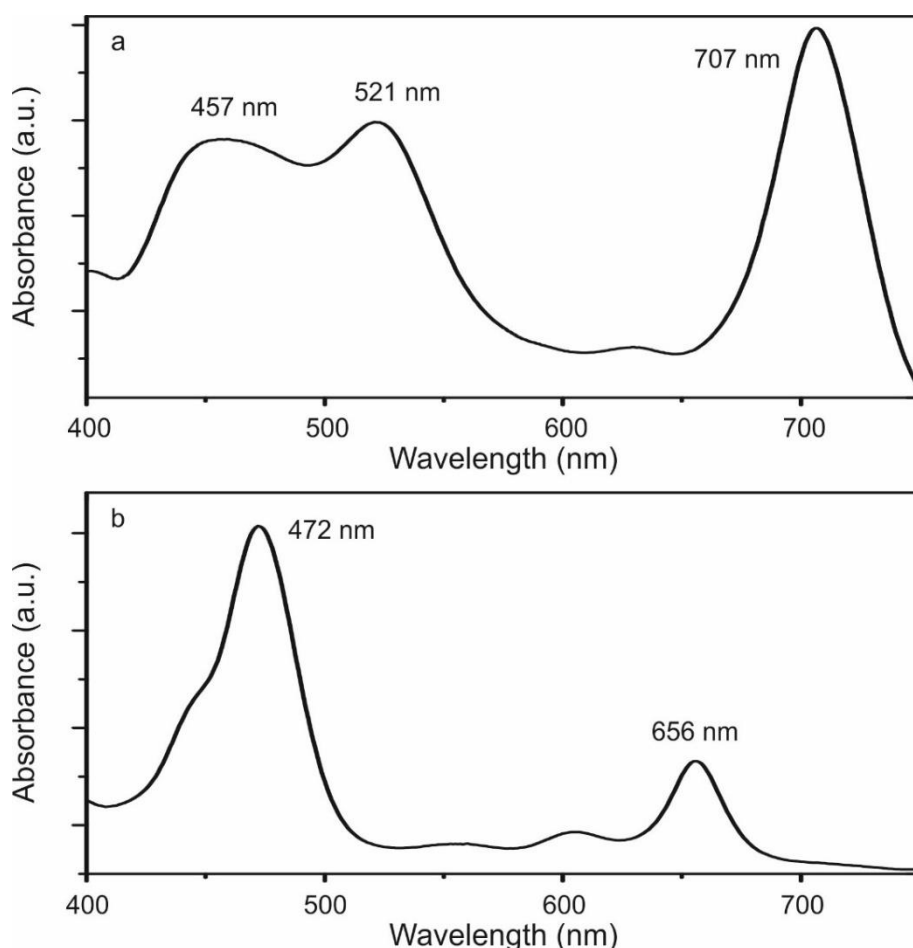


Figure 3.2 Extraction of BChl e pigments from *Chlorobaculum phaeobacteroides* chlorosomes.

- (a) spectrum of chlorosomes of *Chlorobaculum phaeobacteroides* and
- (b) after addition of methanol and hexane washing.

3.2.4 Extraction of chlorosomes from *Chlorobaculum tepidum* cells

Chlorosomes were extracted from *Chlorobaculum tepidum* cells as an alternative source of pure pigments and to provide a spectral comparison for aggregates of native pigments and their derivatives. Cell lysate was subjected to sucrose density gradient centrifugation. After sucrose density gradient centrifugation, a distinct well-defined green band was present approximately halfway up the tube. The absorption spectrum of this band after concentration and dilution in fresh milliQ-grade-H₂O is shown in Figure 3.3. Chlorosomes exhibited a Soret peak at 456 nm and a Q_y peak at 744 nm. The spectrum of chlorosomes purified using the 10-50% sucrose density gradient closely matches previously reported spectra for chlorosomes from this species with the peaks at 744 nm and 456 nm corresponding to aggregated BChl c.

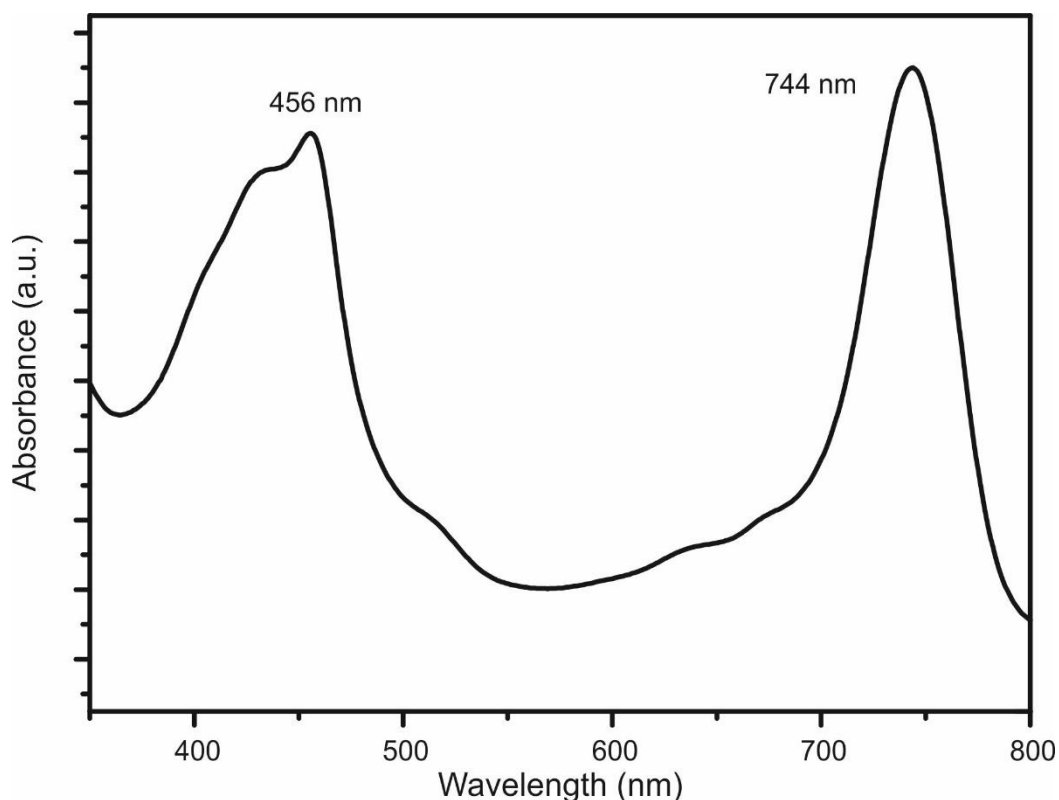


Figure 3.3 Absorbance spectrum of chlorosomes from *Chlorobaculum tepidum* purified using a sucrose density gradient.

3.2.5 Extraction of pigments from spinach

Chlorophyll pigments were extracted from spinach to provide a more abundant and easily obtained source of pigments. Whilst plant chlorophylls do not aggregate, their similarity to the aggregating bacteriochlorophylls means they provide a substitute for investigation of modification methods. Pigments were extracted using acetone and subjected to two rounds of centrifugation using different solvent mixes. After the second round of centrifugation, a green pigment-rich hexane layer and a colourless water-acetone subphase formed – indicating that the majority of the pigments were contained in the dark hexane layer. The spectrum of this layer dried and resuspended in methanol is shown in Figure 3.4. The two largest peaks are found at 438 nm and 663 nm. In addition, there is substantial absorbance in the 500-650 nm region as well as shoulders on the short wavelength side of the 438 nm peak and the short wavelength side of the 663 nm peak

The peaks at 663 nm and 438 nm as well as the pattern of peaks observed in the sub-438 nm region, correspond to Chlorophyll a – the most abundant pigment found in spinach. The asymmetry of the 663 nm peak and the peak at 467 nm are due to smaller amounts of Chlorophyll b present in the sample. The large absorbance in the 400-500 nm region compared to the peak at ~663 nm may also be explained by contributions from carotenoids.

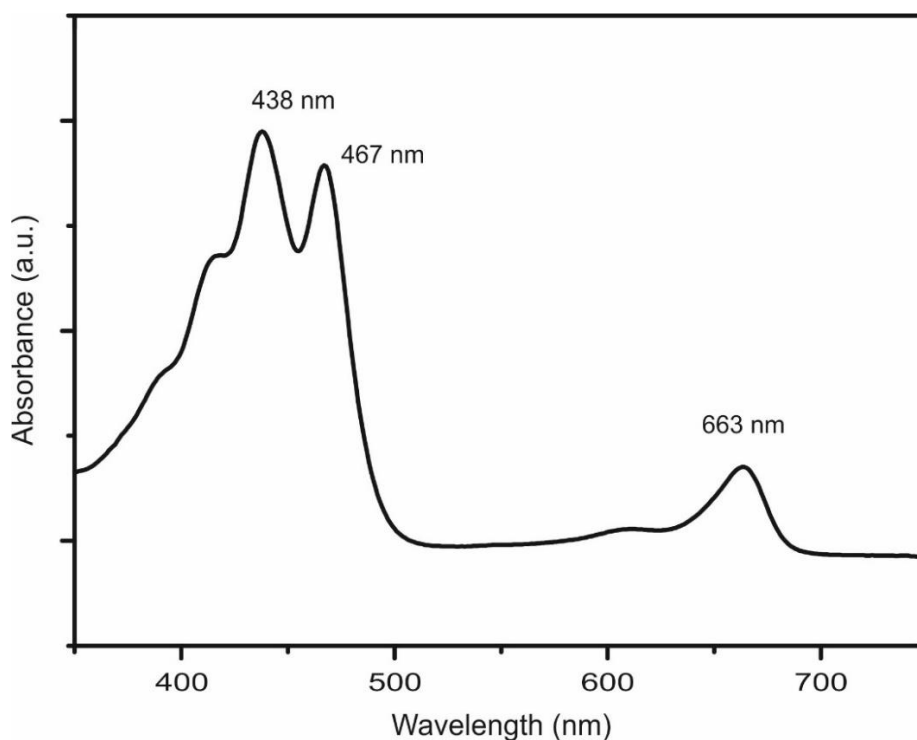


Figure 3.4 Spectrum of crude pigment extract from spinach.

The spectrum of crude spinach extract contains contributions from Chl a, Chl b as well as the carotenoids: Neoxanthin, Violaxanthin, Lutein, and β -Carotene.

3.2.6 High Pressure Liquid Chromatography (HPLC) purification of BChl c pigments

HPLC purification was used to separate BChl c homologues and carotenoids to provide a pure source of pigment for further modification and investigation. The chromatogram monitored at 669 nm is shown in Figure 3.5a. The four largest peaks eluted at times \sim 17.7, \sim 18.7, \sim 20.4, and \sim 22.5 min. The peaks were well separated and symmetrical in shape with the exception of the peak eluting at \sim 20.4 min which exhibited late eluting a shoulder. The components eluting at these times were present approximately in the ratio: 1.0:4.0:3.9:1.0. The spectra of the four largest peaks are shown in Figures 3.5(b – e). All exhibit maxima at 434 and 669 nm.

A small peak, not visible in Figure 3.5a, can be seen in chromatograms monitored at other wavelengths and in the 3D field chromatogram (Figure 3.6),

was present at ~42 min. The spectrum of this peak (Figure 3.5f) has maxima at 435 nm, 457 nm, and 487 nm.

A large peak was observed at ~38.4 min. The spectrum of the peak at ~38 min is shown in Figures 3.5g. The spectrum of this peak has peaks at 669nm, 416 nm, and 434 nm. The ratio of the peak intensities at 434 nm and 416 nm to each other and the component at 669 nm for this peak varied from run-to-run.

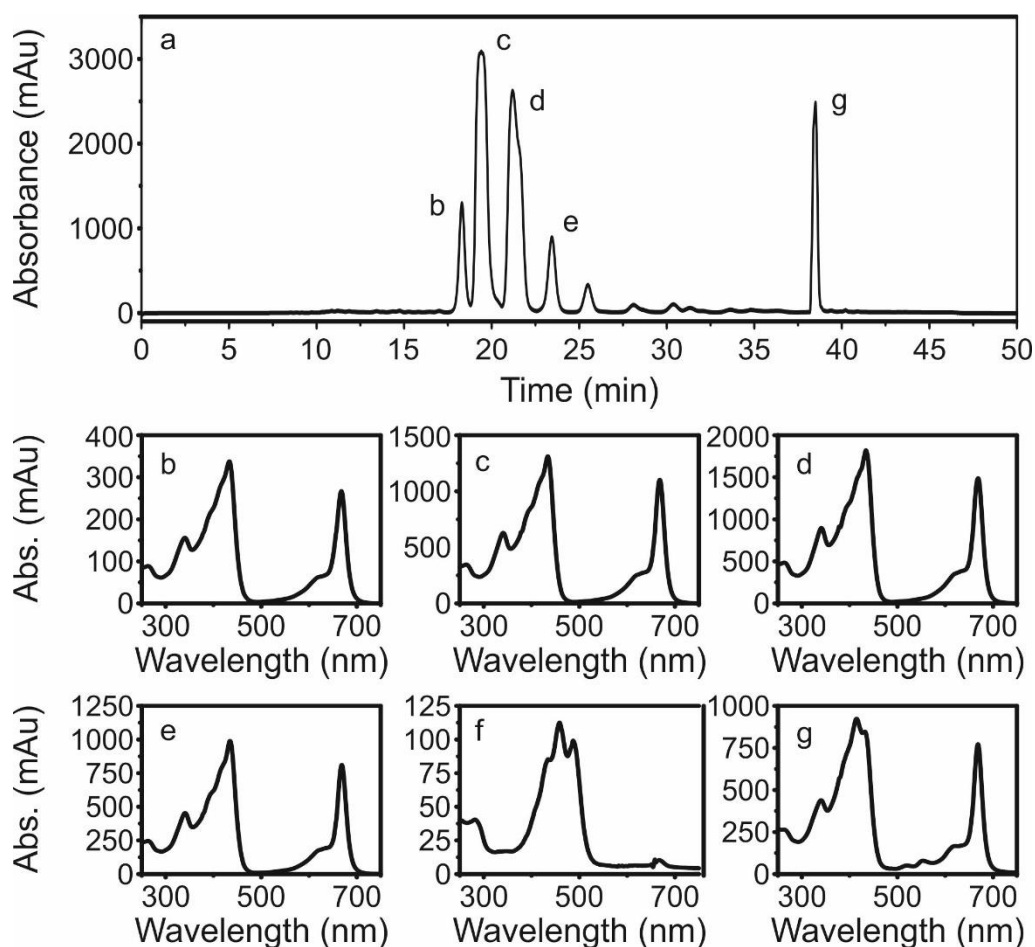


Figure 3.5 HPLC Purification of BChl c from *Chlorobaculum tepidum*.

(a) Chromatogram monitored at 669 nm. (b-e) Absorbance spectra for the four main homologues of BChl c (in order of elution), (f) spectrum of β -carotene, and (g) spectrum corresponding to late eluting pigments.

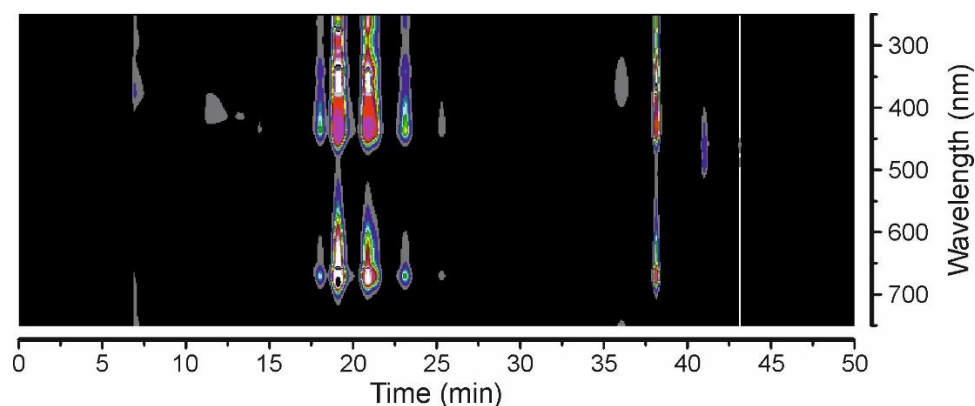


Figure 3.6 HPLC 3-dimensional field chromatogram for purification of BChl c.

Contour plot showing the spectra of pigments eluting at different times for pigments extracted from *Chlorobaculum tepidum* cells.

Based on the approximate elution time, spectra, and relative abundances, the peaks at ~17.7, ~18.7, ~20.4, and ~22.5 min may be ascribed to be the four main C8 and C12 homologs of BChl c esterified with farnesyl at C17^{3,232}. These are, in order of elution: 8-ethyl-12-methyl BChl c ([E,M]BChl c_F), 8-ethyl-12-ethyl BChl c ([E,E]BChl c_F), 8-propyl-12-ethyl BChl c ([P,E]BChl c_F), and 8isobutyl-12-ethyl BChl c ([I,E]BChl c_F) respectively. The existence of a slight shoulder to the 3rd peak may be explained by the existence of both R and S enantiomers of 8-propyl-12-ethyl BChl c ([P,E]BChl c_F) eluting close together. Typical relative abundances for these homologues are similar to those reported previously. However, it should be noted that these ratios have been found to vary depending on growth conditions.²³²

The small peak at ~42 min was determined, due to its spectrum and retention time to be residual β -carotene remaining after hexane washing.

The large peak was observed at ~38.4 min appears, based on the observation of peaks at 416 and 434 nm to be a mix of late eluting BChl c pigments and BPhe c. The run-to-run variation in the relative intensities of these peaks suggests batch-to-batch variations in the two pigments. This likely correspond to varying levels of sample degradation.

The lack of a significant peak corresponding to BChl a indicates that should BChl a be the reason for the small peak observed at ~750 nm observed above in the spectrum of extracted pigments (Figure 3.1), it is a minor component.

The method showed a high degree of reproducibility between runs and presents a reliable and efficient means of purifying BChl c. Additionally, it should be noted that whilst not attempted in this thesis due to lack of *Chlorobaculum phaeobacteroides* cells, based on their structural similarity and previously reported attempts, it should be possible to use the same method for the isolation of the four primary homologues of BChl e.

3.2.7 HPLC purification of chlorophyll a and b

Figure 3.7a shows the chromatogram monitored at 658 nm. The four largest peaks eluted at times ~16.4, ~16.8, ~17.8, and ~18.3 min. The spectra of the four largest peaks are shown in Figures 3.7(b – e). The spectra of peaks eluting at ~16.4, ~16.8 min (b and c) both exhibit maxima at ~460 and 649 nm. The spectra of peaks eluting at ~17.8 and ~18.3 min (d and e) both exhibit maxima at 432 and 664 nm.

In addition to those peaks observed in the chromatogram monitored at 658 nm, additional peaks were observed in chromatograms monitored at other wavelengths and in the 3D field chromatogram (Figure 3.8). The spectra of these peaks had multiple peaks in the 400-500 nm region but no peak in the 600-700 nm region as observed for the four peaks described above. These peaks do not overlap temporally with any of the four main peaks in Figure 3.7.

Based on the approximate elution time, spectra, and relative abundances, the peaks at ~17.6, ~18.0, ~19.3, and ~20.1 min may be ascribed chlorophyll b, chlorophyll b', chlorophyll a and chlorophyll a'.²²⁴ The relative abundances as determined by peak area are in good agreement with previously ratios for spinach.²²⁴ The additional peaks seen in the 3D field chromatogram correspond to the main carotenoids found in spinach, namely: Neoxanthin, Violaxanthin, Lutein, and β -Carotene.

Whilst closer inspection of some HPLC chromatograms revealed the presence of chlorophyllide (Chlide), in the 7-12 min region, and pheophytin (Phe), in the >30 min region, these were present at only a low level, suggesting that the method employed here allowed the extraction of chlorophyll a and b with only a minimal amount of sample degradation.

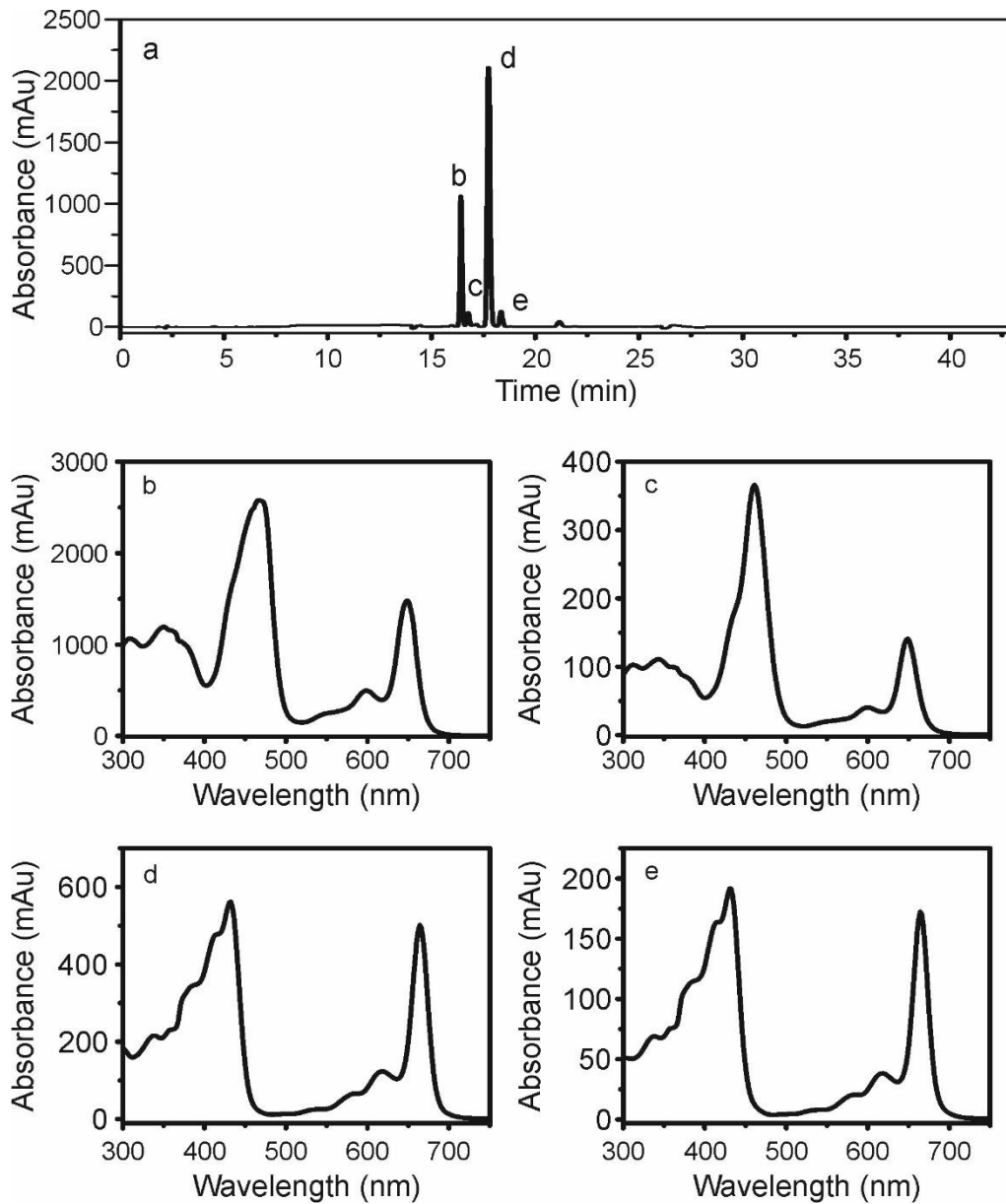


Figure 3.7 HPLC purification of chlorophylls a and b.

(a) Chromatogram monitored at 658nm. (b-e) Absorbance spectra of the four peaks (in order of elution) – Chl b, Chl b', Chl a, and Chl a'.

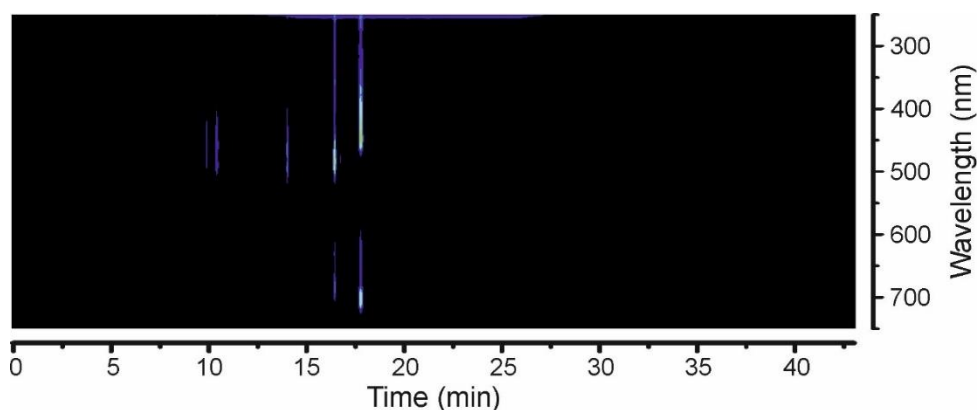


Figure 3.8 HPLC 3-dimensional field chromatogram for purification of Chls.

Contour plot showing the spectra of pigments eluting at different times for pigments extracted from spinach.

3.2.8 XPS analysis of native pigments

Figures 3.9, 3.10, and 3.11 show XPS survey spectra for HPLC purified Chl a, Chl b, and BChl c respectively. These spectra revealed the presence of significant amounts of Au, C, Mg, N, and O. The presence of Au is due to the gold coated substrate onto which samples were deposited. The C, Mg, N, and O detected are consistent with the composition expected for Chl a, b, and BChl c.

More detailed scans of the Au 4f, C 1s, Mg 1s, N 1s, O 1s, S 2p, and Zn 2p regions for Chl a and Chl b are shown in Figure 3.12 and 3.13. Scans for the Au 4f, C 1s, Mg 2p, N 1s, O 1s, and Zn 2p for BChl c are shown in Figure 3.14. The Mg 2p region was used for BChl instead of the Mg 1s region owing to low signal from this sample. Scans of the Zn 2p regions for all three pigments and the S 2p regions for Chl a and Chl b are presented to allow comparison with modified pigments in the subsequent sections. No indication of zinc was found for any of the three native pigments. A small peak at ~168 eV was observed in the S 2p regions of Chl a and Chl b. However, the small intensity of this peak indicates it is most likely from low level contamination.

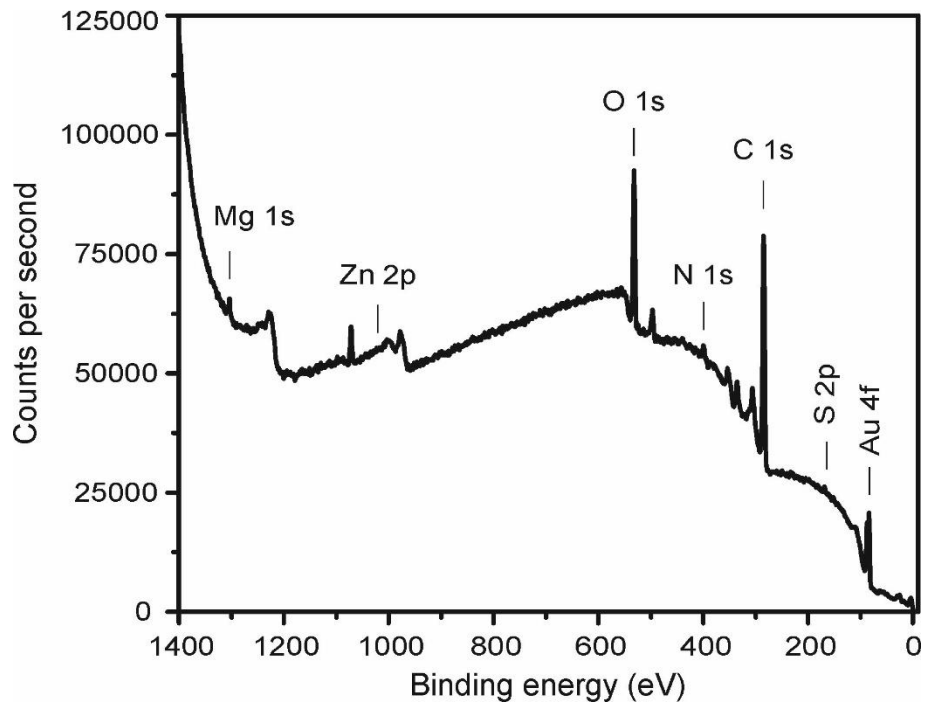


Figure 3.9 XPS survey spectrum for unmodified Chl a.

XPS survey spectrum for unmodified Chl a showing the presence of carbon, oxygen, nitrogen, and magnesium.

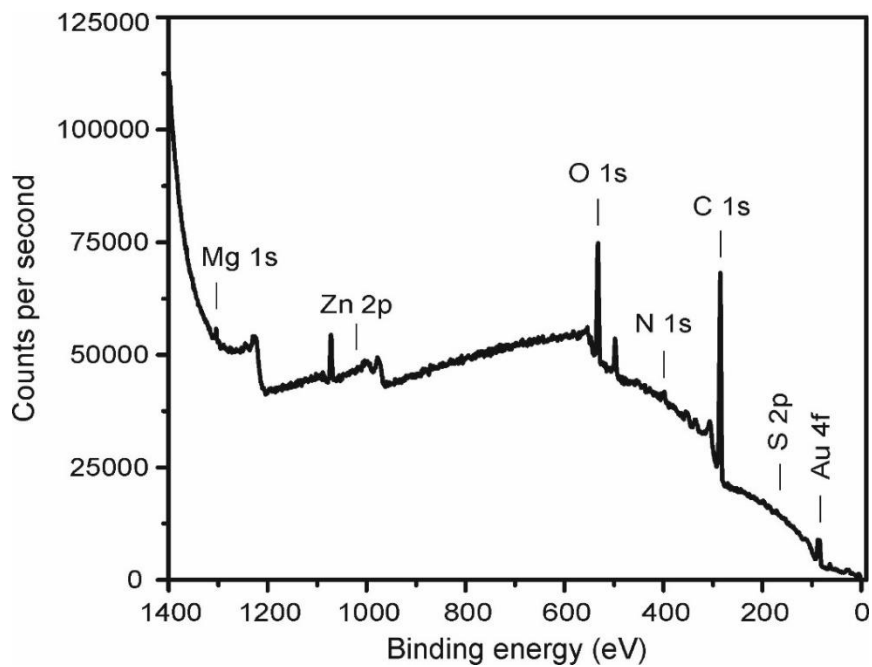


Figure 3.10 XPS survey spectrum for unmodified Chl b.

XPS survey spectrum for unmodified Chl b showing the presence of carbon, oxygen, nitrogen, and magnesium.

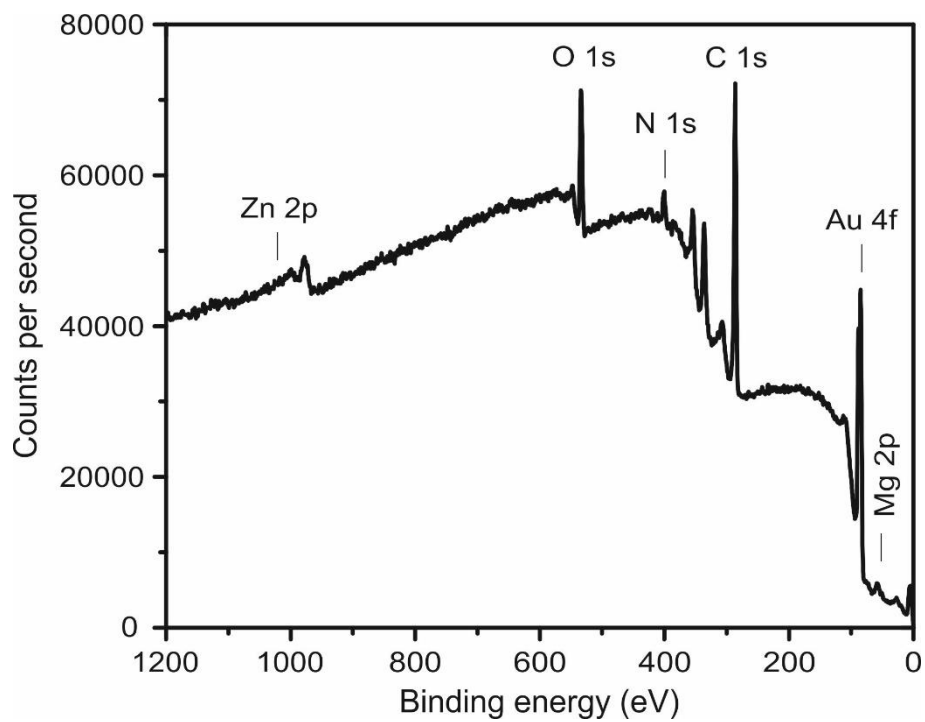


Figure 3.11 XPS survey spectrum for unmodified BChl c.

XPS survey spectrum for unmodified BChl c showing the presence of carbon, oxygen, nitrogen, and magnesium.

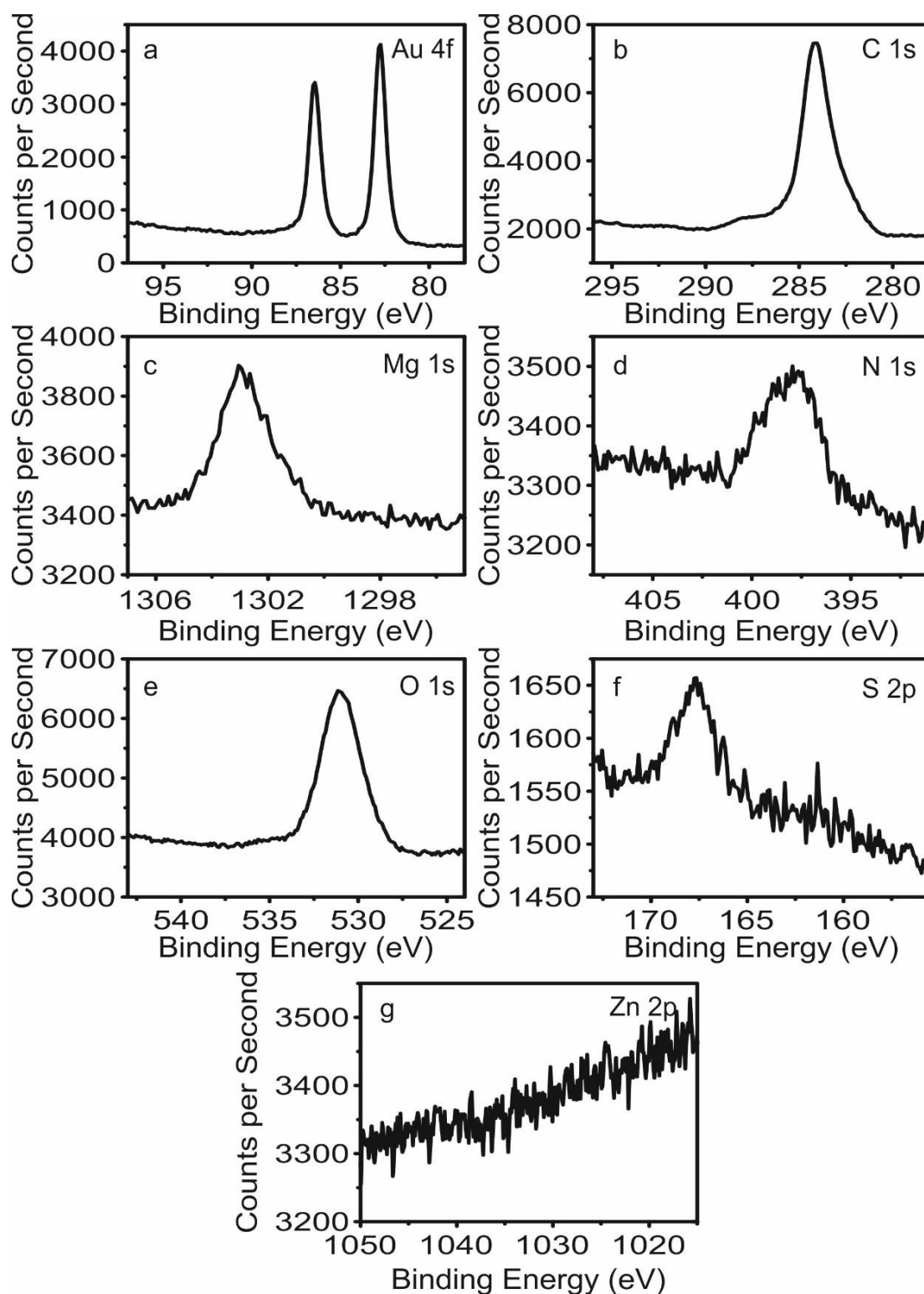


Figure 3.12 Detailed XPS spectra for Chl a.

Detailed XPS spectra of (a) Au 4f, (b) C 1s, (c) Mg 1s, (d) N 1s, (e) O 1s, (f) S 2p, and (g) Zn 2p peaks obtained for unmodified Chl a.

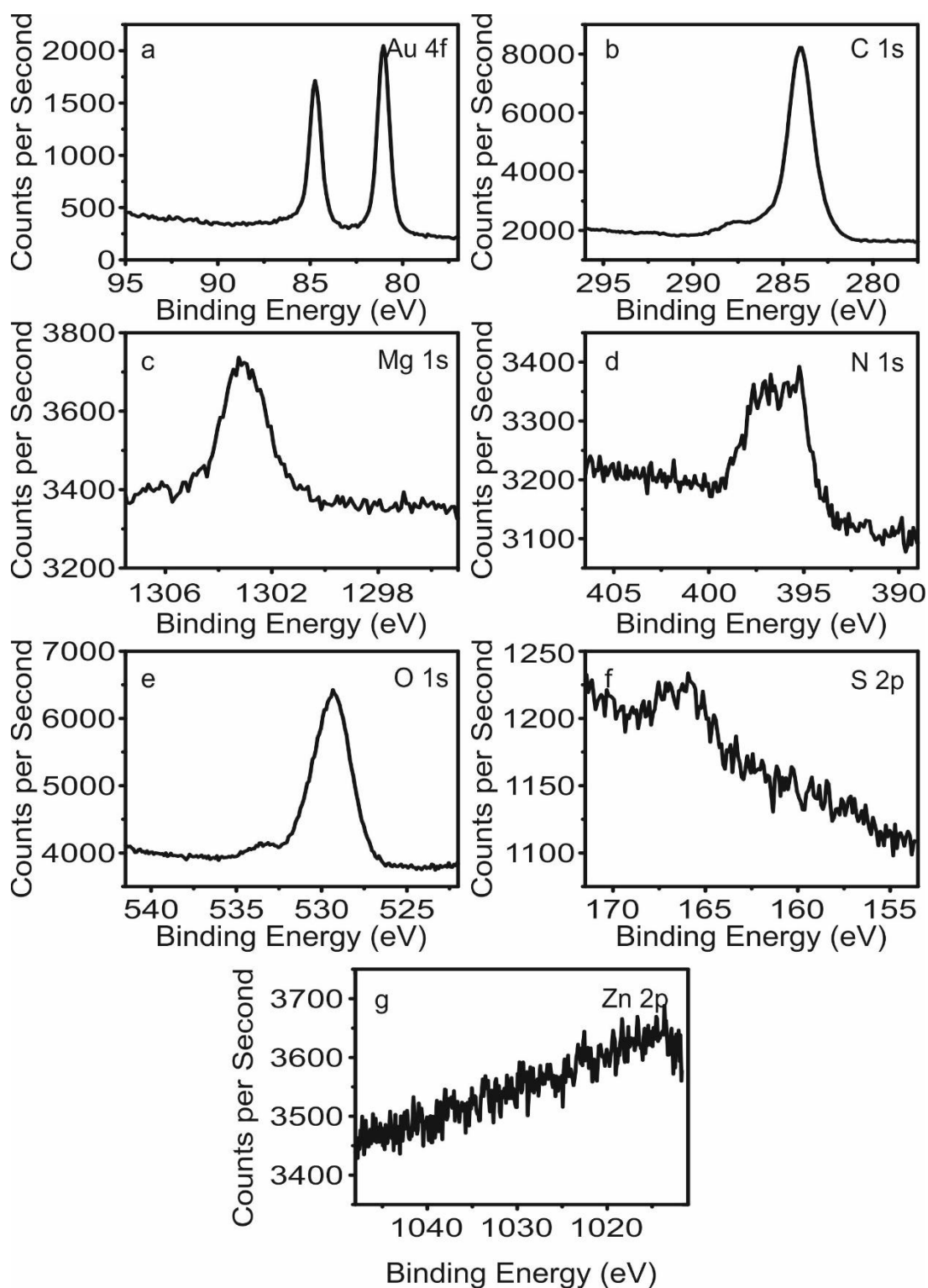


Figure 3.13 Detailed XPS spectra for Chl b.

Detailed XPS spectra of (a) Au 4f, (b) C 1s, (c) Mg 1s, (d) N 1s, (e) O 1s, (f) S 2p, and (g) Zn 2p peaks obtained for unmodified Chl b.

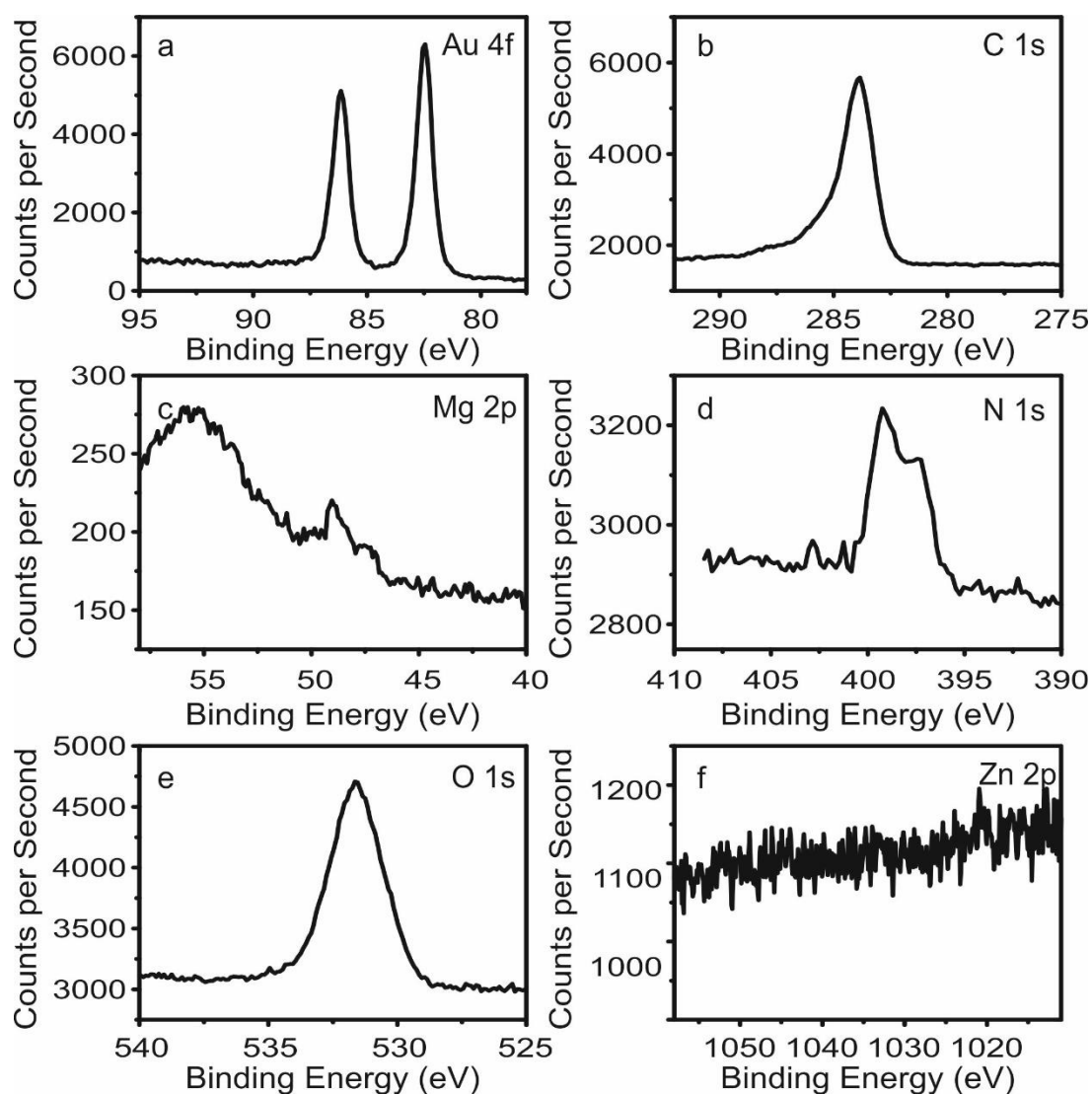


Figure 3.14 Detailed XPS spectra used for BChl c.

Detailed XPS spectra of (a) Au 4f, (b) C 1s, (c) Mg 2p, (d) N 1s, (e) O 1s, and (f) Zn 2p obtained for unmodified BChl c.

3.3 Chemical modification of pigments

3.3.1 Zn-(B)Phe production and purification

3.3.1.1 Transmetallation of pigments

Pigments were transmetallated to provide more stable and easier to work with zinc analogues. This was done using a novel method which provided a faster and more straightforward means of converting (B)Chls to Zn-(B)Phes. After treatment with HCl, the pigments changed from a green to brown colour with the extent of colour change increasing with increasing HCl concentration.

Should pigment be resuspended at this stage, a blue tint will be observed. Further treatment with NaOH resulted in a further change from green-brown to pink-brown with the extent of colour change dependent on NaOH concentration. On resuspension in zinc acetate saturated methanol and shaking, a further colour change from brown to vivid green was observed.

The changes in pigment colour observed on treatment with HCl are consistent with demetallation of the pigments and conversion to free-base analogues. The blue tint observed on drying and redispersal in methanol maybe explained by protonation of the ring. Conversely, the change in colour on treatment with NaOH may be explained by deprotonation of the ring. The rapid colour change seen on treatment with zinc acetate saturated methanol can be explained by the rapid incorporation of zinc in to deprotonated pheophytins.

3.3.1.2 Spectroscopic properties of transmetallated pigments

In order to monitor changes to pigments during treatment, UV-Vis absorbance spectra for Chl a, Chl b, BChl c, and BChl e taken before treatment, after treatment with HCl and after incubation with zinc acetate are shown in Figures 3.15(a-d). The positions of the Soret and Q_y peaks at each stage for each pigment are shown in Table 3.1. Spectra of Chl a and Chl b before treatment were similar to BChl c and BChl e respectively in terms of both peak positions and shape as reported previously.¹⁹ In all cases, treatment with HCl led to a blue-shift in the position of the Soret band whilst the position of the Q_y band remained largely unchanged. After treatment with the zinc acetate solution, the Q_y band was blue-shifted from the position of the untreated and HCl pigments by between 6 and 19 nm. In addition, with the exception of Chl b, the position of the Soret band was red-shifted but did not reach the position of the untreated pigments. An apparent splitting of the Soret band in the case of BChl e was observed after treatment with a large peak at 440 nm and a smaller component at 460 nm.

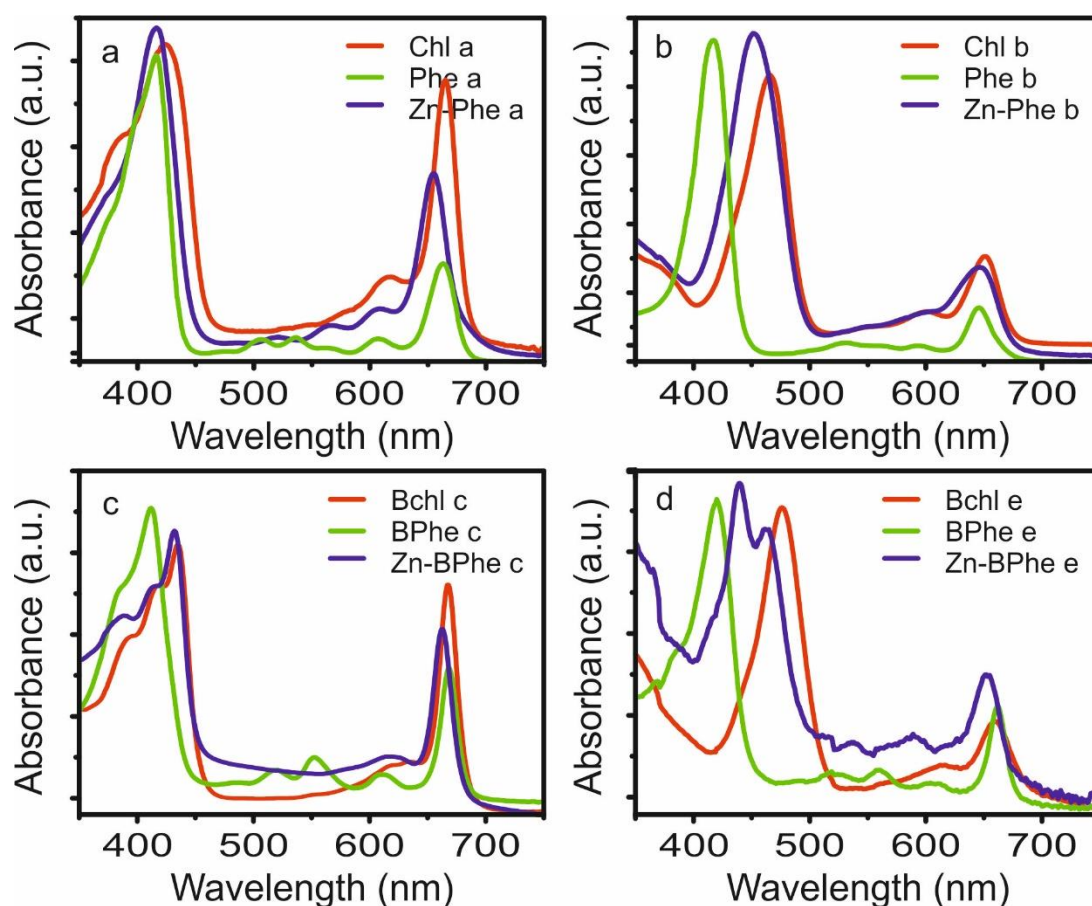


Figure 3.15 Spectral changes during transmetallation of pigments.

UV-Vis spectra of native, de-metallated and transmetallated (a) Chl a, (b) Chl b, (c) BChl c, and (d) BChl e.

Table 3.1 Summary of Soret and Q_y positions for natural pigments, their free bases, and zinc analogues.

Pigment	Soret and Q_y position of native pigments (nm)	Soret and Q_y position of demetallated pigments (nm)	Soret and Q_y position of transmetallated pigment (nm)
BChl c	435, 669	412, 669	432, 663
BChl e	476, 660	420, 662	429 and 451, 641
Chl a	423, 665	416, 663	416, 655
Chl b	466, 651	417, 646	452, 646

The above changes in colour and absorption spectra were found for all concentrations of HCl and NaOH used in the range 1-5 M.

Energy levels for the two allowed transitions with a significant cross-section are shown in Figure 3.16 for each of the final products.

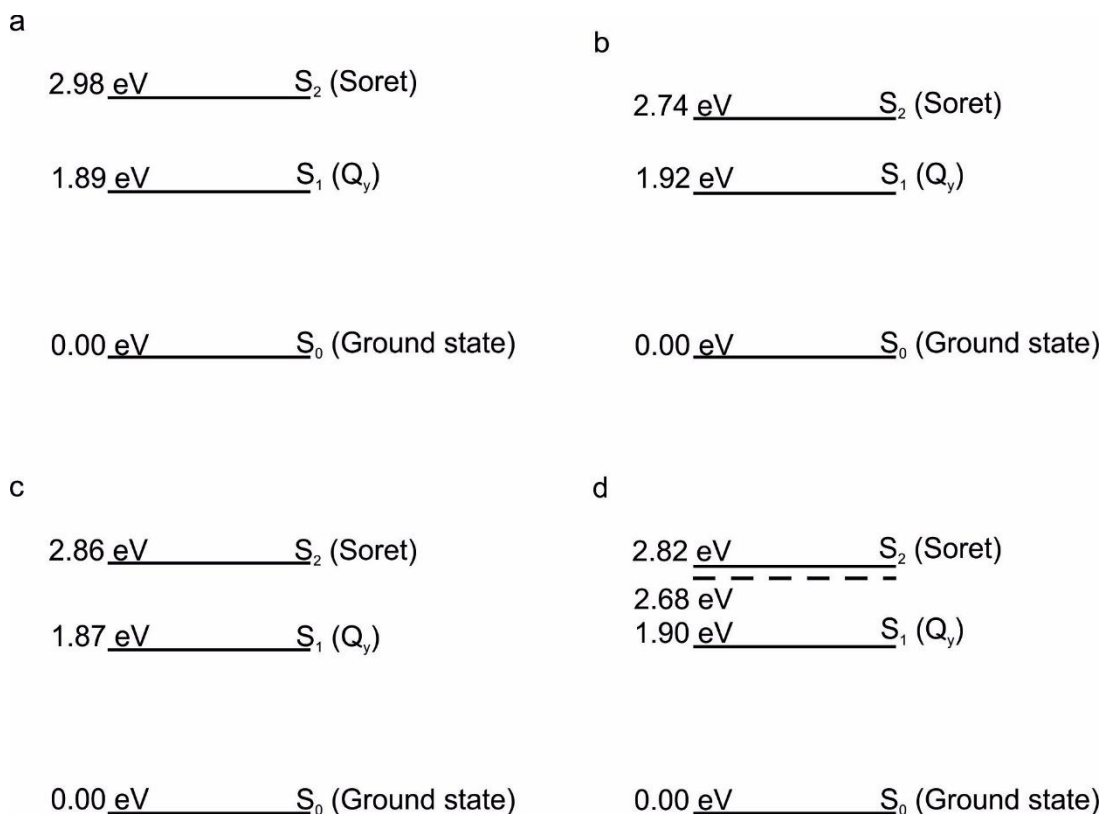


Figure 3.16 Energy levels of transmetallated pigments.

Energy levels showing the modified positions of the Soret and Q_y for (a) Zn-Phe a, (b) Zn-Phe b, (c) Zn-BPhe c, and (d) Zn-BPhe e.

The successful implementation of the method for four different pigments (two chlorophylls and two bacteriochlorophylls) illustrates the wide applicability of the method. In addition, when compared with other reported methods, the method offers a faster and easier means of converting (B)Chls to Zn-(B)Phes.

3.3.1.3 Pre-purification and HPLC purification and analysis of Zn-(B)Phes

Initial attempts to purify Zn-BPhe c by HPLC without first removing unreacted zinc led to the adhesion of zinc to the HPLC column. To avoid zinc precipitation on the HPLC column, a pre-purification step was therefore necessary. When the methanol containing reaction mixture was added to chloroform and water added, a white gel like phase formed throughout the

mixture. On centrifugation of this mixture two distinct phases formed with a white precipitate at the interface. After successive washing this interface became clear of precipitant and the pigment containing chloroform subphase was dried. The dried pigment layer was green with no visible trace of white contaminant.

Figure 3.17a shows the HPLC chromatogram of the pigment phase monitored at 663 nm (chosen to correspond to the Q_y maximum of Zn-BPhe c). Four peaks are eluted at 25.5, 27.5, 30.7, and 32 min in a similar pattern to those observed for the four main homologues of BChl c above, albeit eluting later. The spectra of these four peaks are shown, in order of elution, in Figures 3.17(b-e). All spectra exhibit peaks at 432 and 663 nm.

In addition, a similar cluster of much lower intensity peaks were observed in the chromatogram in the 10-12 min region. The shape of this cluster and the relative intensities of the peaks are almost identical to those observed for the four main peaks above. These peaks also have spectra with peaks at 432 and 663 nm. Finally, a large peak is observed at ~48 min. Again, the spectra of this peak has maxima at 432 and 663 nm.

Due to the spectra of the peaks eluting between 25.5 and 32 min, and their similar elution pattern and relative abundancies to those observed for BChl c, these peaks may be assigned to Zn-containing derivatives of the four BChl c homologues: 8-ethyl-12-methyl Zn-BPhe c ([E,M]Zn-BPhe_{CF}), 8-ethyl-12-ethyl Zn-BPhe c ([E,E]Zn-BPhe_{CF}), 8-propyl-12-ethyl Zn-BPhe c ([P,E]Zn-BPhe_{CF}), and 8-isobutyl-12-ethyl Zn-Phe c ([I,E]Zn-BPhe_{CF}). Based on the similarity to the peaks of the BChl c counterparts it may be assumed that pigments eluting in this region have undergone no additional change beyond replacement of the central metal atom. The later elution of these pigments compared to BChls indicate that the pigments have been made more apolar by the addition of zinc.

The early eluting peaks in the 10-12 min region, which are present to a lesser extent, can be assigned to Zn-BPheides which are more polar than their Zn-BPhe counterparts due to the loss of the alcohol chain at C17³. This is consistent with previously reported behaviour for Chl pigments (see e.g. Craft

et al.).²²⁴ In order of elution these peaks are 8-ethyl-12-methyl Zn-BPheide c ([E,M]Zn-BPheide c), 8-ethyl-12-ethyl Zn-BPheide c ([E,E]Zn-BPheide c), 8-propyl-12-ethyl Zn-BPheide c ([P,E]Zn-BPheide c), and 8-isobutyl-12-ethyl Zn-BPheide c ([I,E]Zn-BPheide c). The final peak corresponds to late eluting Zn-BPhe c like pigments which have bound more tightly to the column.

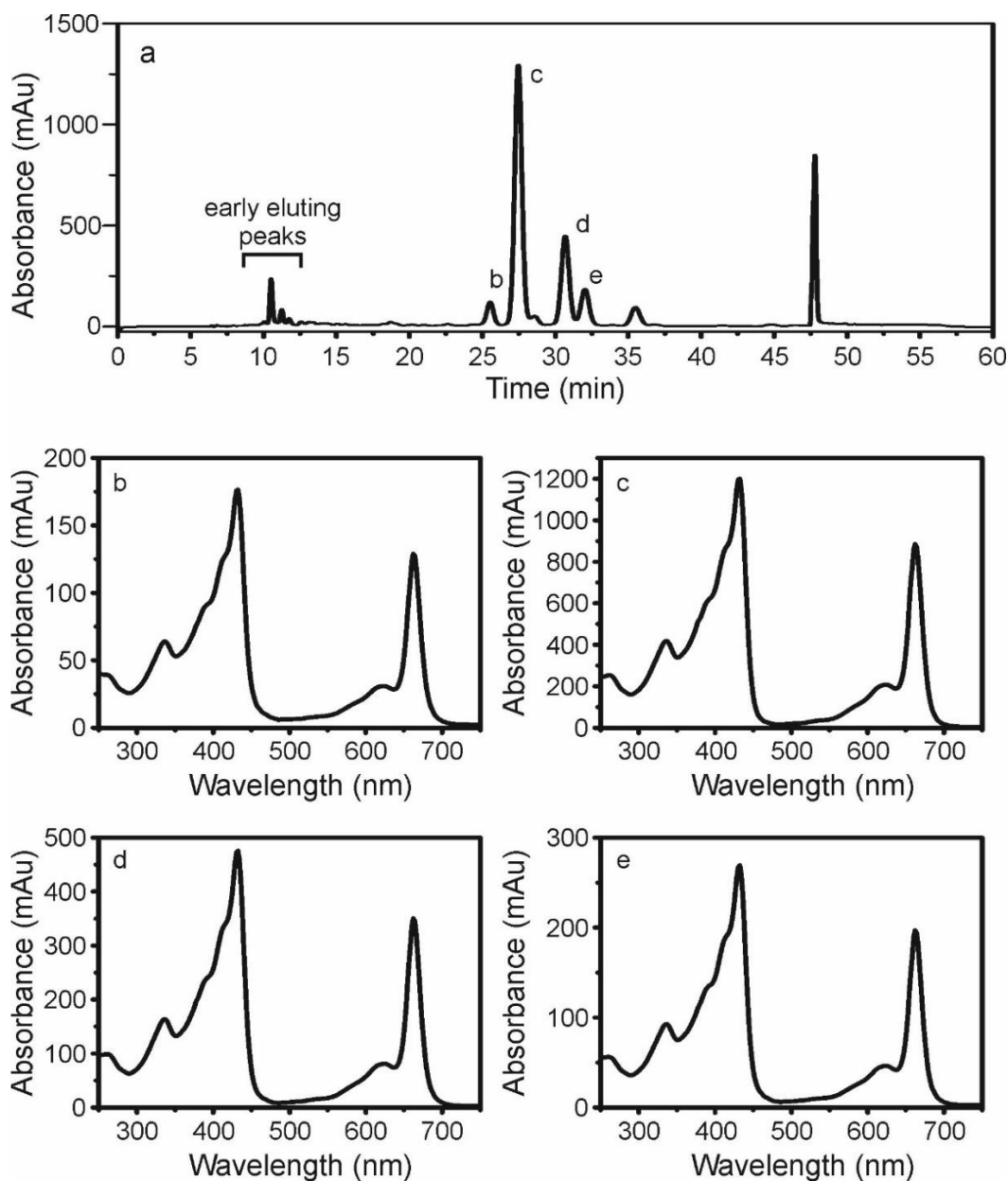


Figure 3.17 Successful HPLC purification of Zn-BPheide c (after pre-purification using phase separation method).

(a) Chromatogram monitored at 663 nm. (b-e) Absorbance spectra of the four main Zn-Pheide c peaks (in order of elution).

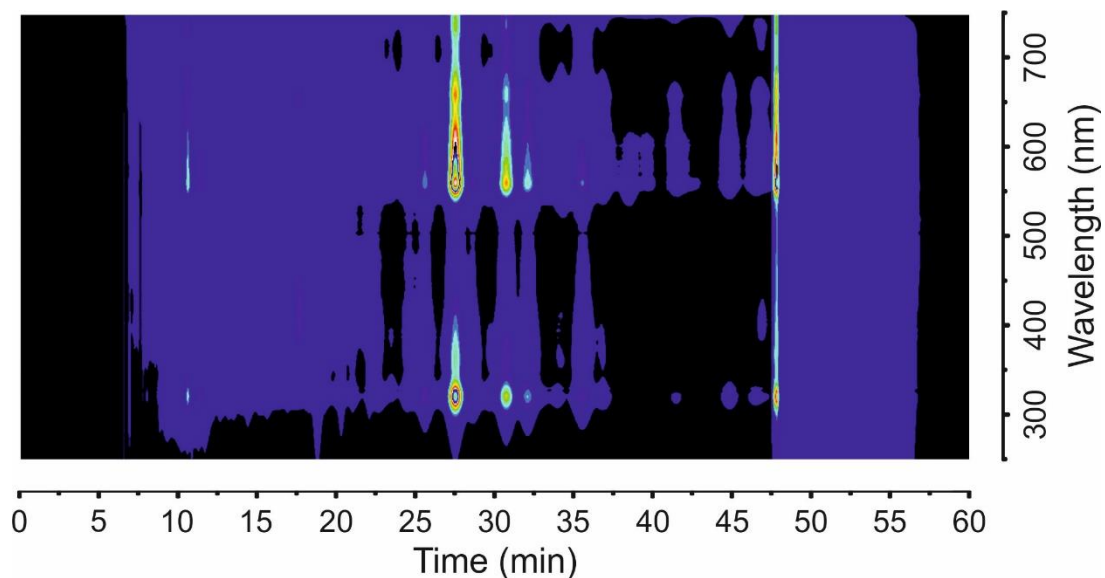


Figure 3.18 3-dimensional field chromatogram for purification of Zn-BPhe c.

Contour plot showing the spectra of pigments eluting at different times for zinc modified BChl pigments.

For comparison, Figure 3.19 shows an HPLC chromatogram monitored at 663 nm for Zn-BPhe c pigments which have not undergone prepurification. This chromatogram shows a greater proportion of hydrolysed pigments elution in the 10-12 min region. Only three peaks are clearly resolved in this case, likely due to loss of resolution due to an increased amount of sample eluting in this period. A greater proportion of hydrolysed pigments for the same concentration of HCl/NaOH suggests that in addition to zinc, the prepurification process also removed Zn-BPheides. This can be explained by the fact that Zn-BPheides, unlike Zn-BPhees, are water-soluble. Consequently, these pigments may preferentially partition into the water phase and be removed during successive washing steps.

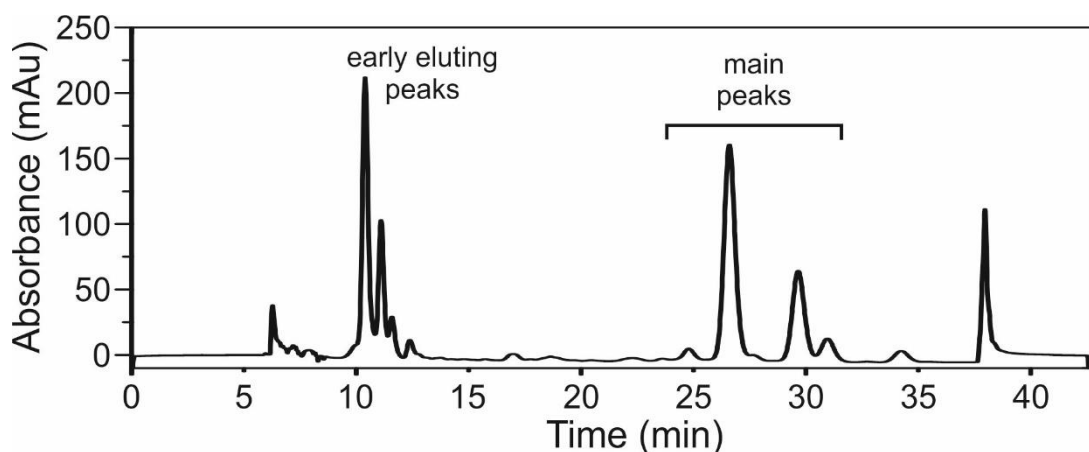


Figure 3.19 HPLC purification of Zn-BPhe c without pre-purification using phase separation method.

Figure 3.20a shows a chromatogram monitored at 658 nm for the purification of Zn-Phe a produced from HPLC purified Chl a. The two largest peaks elute at 18.2 and 19 min. The absorbance spectra of these peaks are shown in Figure 3.20(b and c). These peaks both exhibit absorbance maxima at 420 and 656 nm. Two additional peaks are present in the chromatogram either side of these peaks at 17.5 and 19.5 min. The spectra of these peaks have maxima at 428 and 660 nm.

The Soret maximum of the two central peaks is red-shifted from that observed above for transmetallated pigments. This can be explained by the different solvent environment of the pigments during HPLC (ethyl acetate/methanol/water mixture versus pure methanol). The absorbance properties of chlorophyll and chlorophyll-like pigments have previously been shown to be highly sensitive to different solvent environments. Based on their absorbance spectra, elution positions, and peak ratios, these two peaks were determined to be Zn-Phe a and Zn-Phe b respectively. As observed above for BChl c and Zn-BPhe c and as reported previously,²²⁴ the zinc containing analogues elute later than those containing magnesium. Only the Zn-Phe a peak was collected and used for further analysis. The two additional peaks on either side, based on spectra and retention times, are most likely Mg containing Chl a or Chl a derivatives.

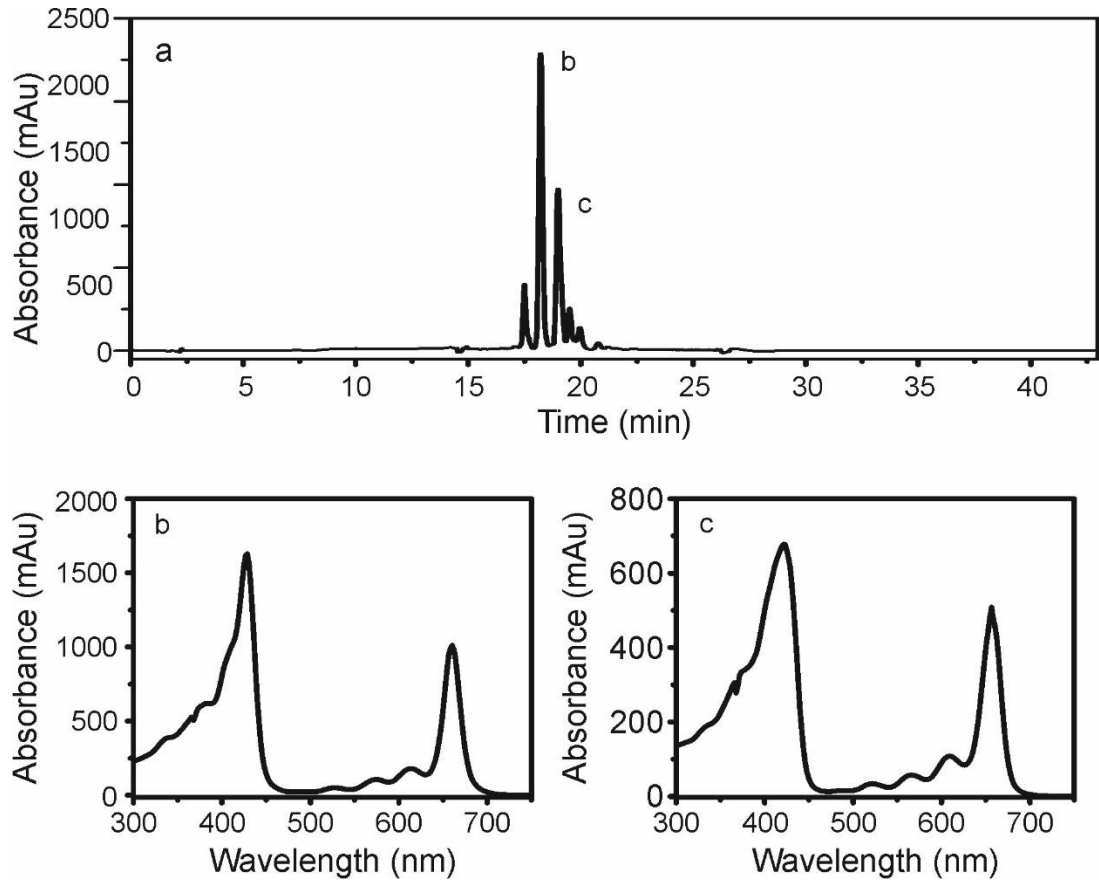


Figure 3.20 HPLC purification of Zn-pheophytin a.

(a) Chromatogram monitored at 658nm. (b-c) Absorbance spectra of the two peaks (in order of elution).

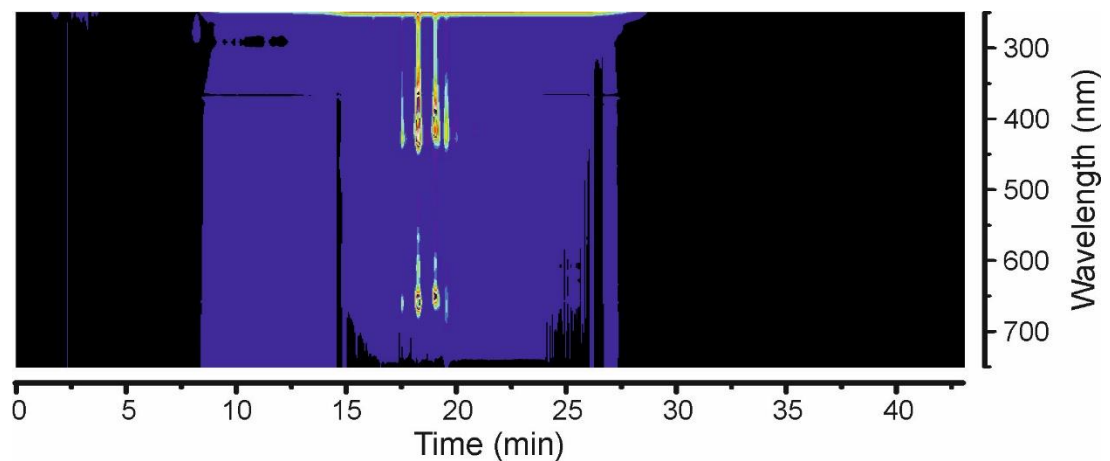


Figure 3.21 3-dimensional field chromatogram for purification of Zn-Phe a.

Contour plot showing the spectra of pigments eluting at different times for zinc modified Chl a pigments.

3.3.1.4 XPS analysis of zinc modified pigments

XPS was used to help confirm successful incorporation of a zinc into Chl a and BChl c pigments. Figures 3.22 and 3.23 show XPS survey spectra for these zinc modified pigments. The key elements detected were gold, carbon, oxygen, nitrogen, and zinc. The absence of magnesium as a component and presence of zinc is consistent with the successful transmetallation of pigments. Figures 3.24 and 3.25 detailed XPS spectra for the Au 4f, C 1s, N 1s, O 1s, and Zn 2p regions are shown for Zn-Phe a and Zn-BPhe c. In addition, Mg 1s and Mg 2p are shown for Zn-Phe a and Zn-BPhe c respectively.

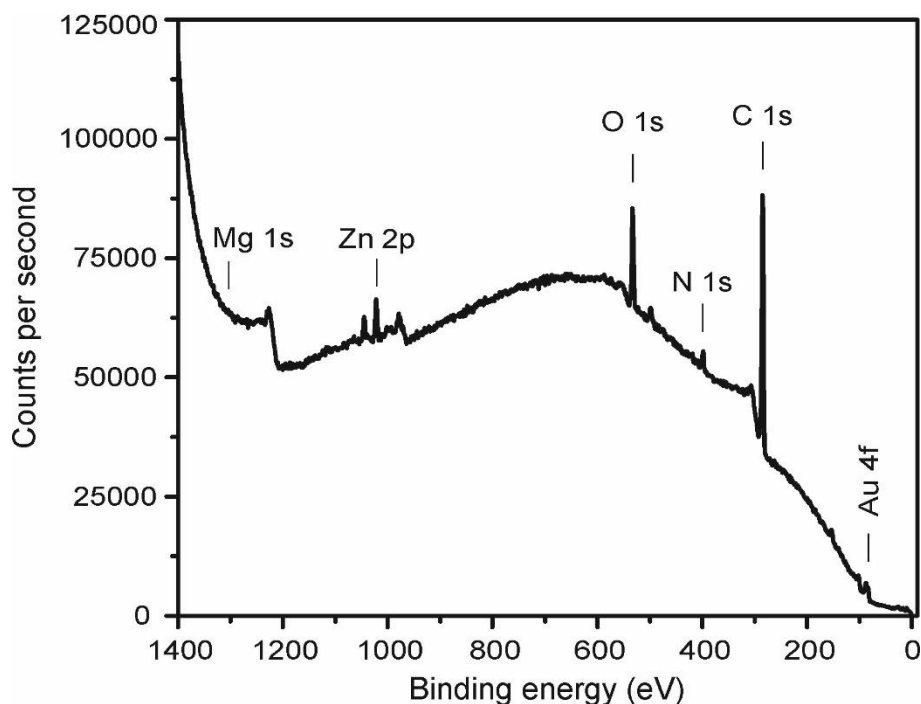


Figure 3.22 XPS survey spectrum for Zn-Phe a.

XPS survey spectrum for Zn-Phe a showing the presence of carbon, oxygen, nitrogen, and zinc.

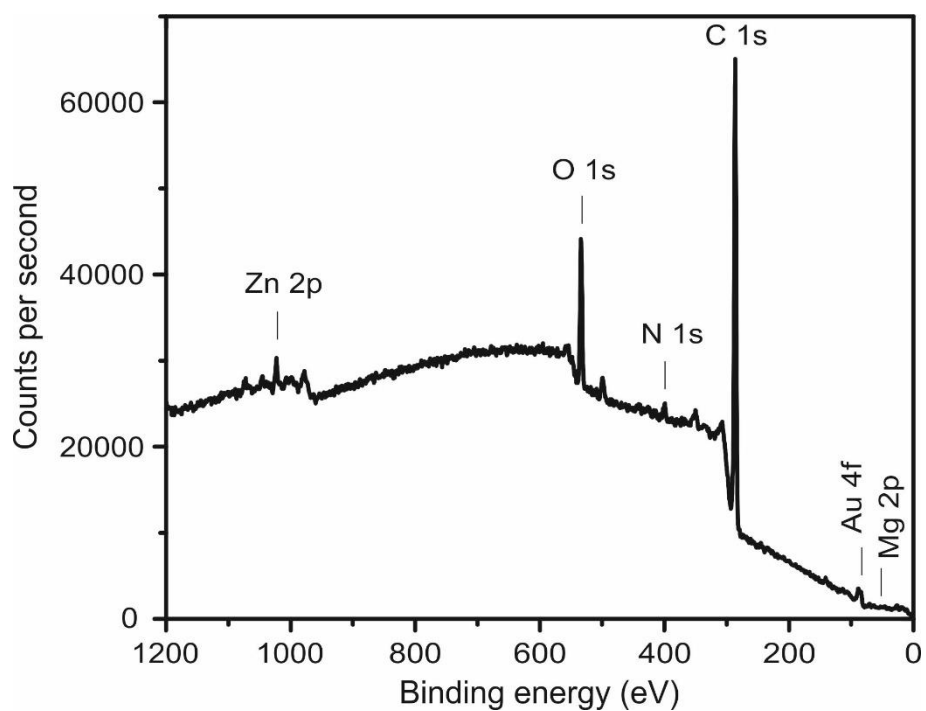


Figure 3.23 XPS survey spectrum for Zn-BPhe c.

XPS survey spectrum for Zn-BPhe b showing the presence of carbon, oxygen, nitrogen, and zinc.

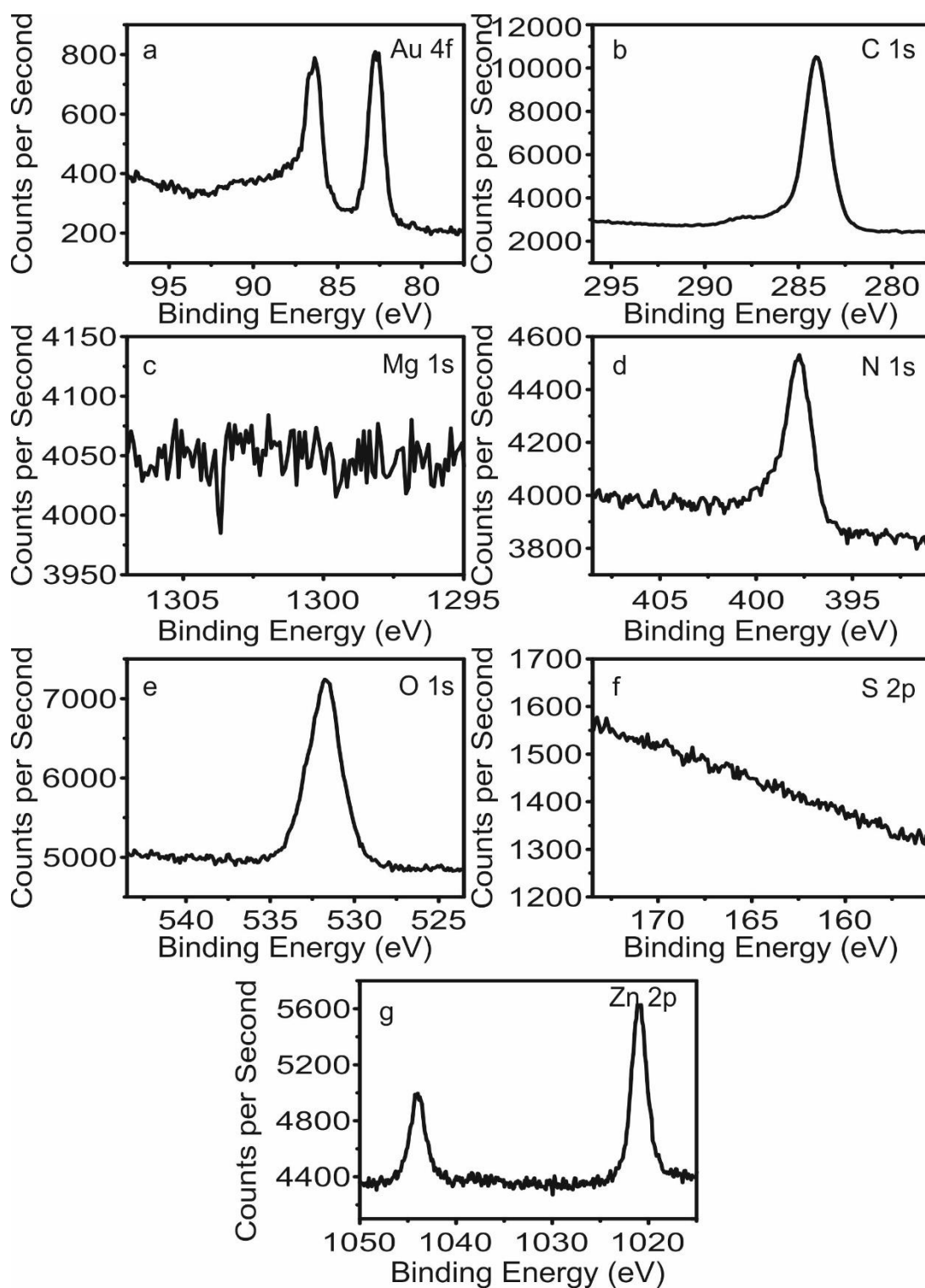


Figure 3.24 Detailed XPS spectra used for composition determinations of Zn-Phe a.

Detailed XPS spectra of (a) Au 4f, (b) C 1s, (c) Mg 1s, (d) N 1s, (e) O 1s, (f) S 2p, and (g) Zn 2p peaks obtained for Zn-Phe a.

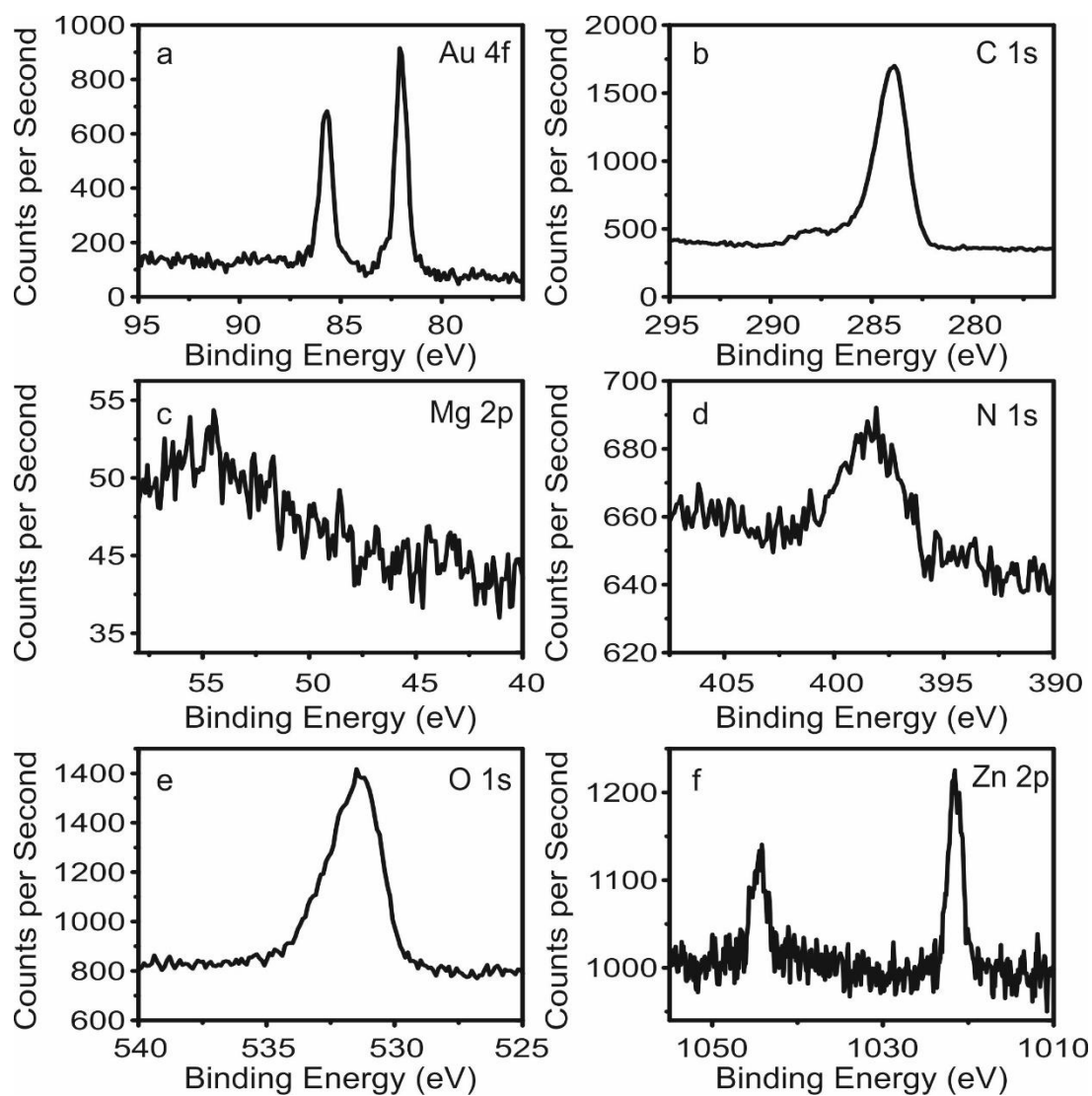


Figure 3.25 Detailed XPS spectra used for composition determinations of Zn-BPhe c.

Detailed XPS spectra of (a) Au 4f, (b) C 1s, (c) Mg 2p, (d) N 1s, (e) O 1s, and (f) Zn 2p peaks obtained for Zn-BPhe c.

3.3.1.5 Aggregation of Zn-BPhes and BChls

On injection of a saturated solution of BChl c into vigorously mixed hexane, a shift in the absorption maxima at 435 and 669 nm to 440 and 718 nm, respectively, was observed. A significant shoulder was observed at ~670 nm. Similarly, on injection of a saturated solution of HPLC purified Zn-BPhe c the peaks at 434 and 663 nm shifted to 427 and 703 nm, respectively, with a smaller peak appearing at ~660 nm. These spectral changes for BChl c and Zn-BPhe c are shown in Figures 3.26(a and b) respectively.

The spectral changes observed on injection of BChl c and Zn-BPhe c into vigorously mixed hexane can be explained by aggregation of pigment monomers. The relatively small shift in peak positions compared to the spectra observed for chlorosomes and for previously published aggregates of BChl c along with the shoulder at ~670 nm observed in the case of BChl c and the smaller peak at ~660 nm observed for Zn-BPhe c can be explained by the presence of a significant quantity of pigment monomers.

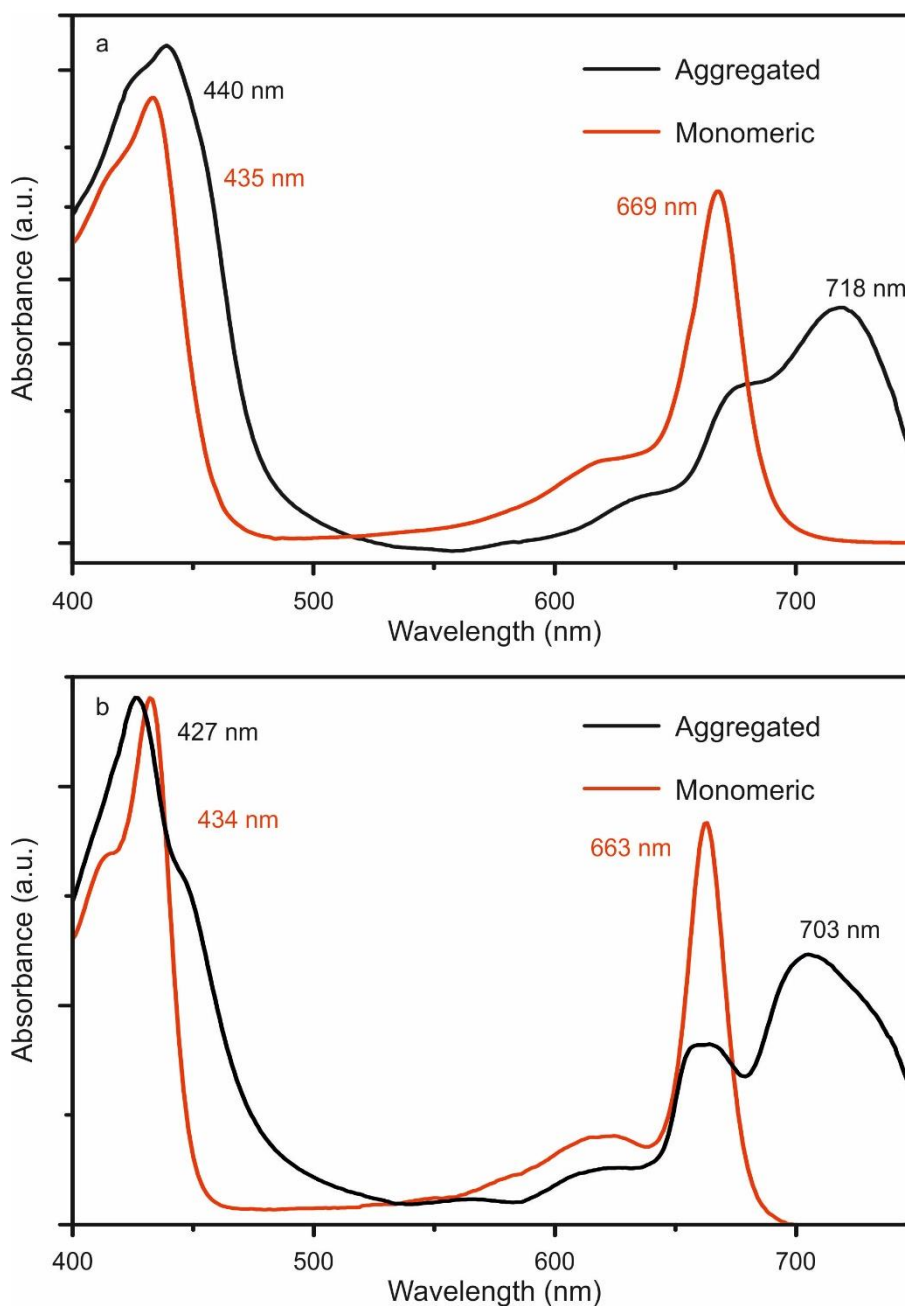


Figure 3.26 Spectra of aggregates and monomers of BChl c and Zn-BPhe c.

(a) Spectra for monomeric (red) and aggregated (black) BChl c. (b) Spectra for monomeric (red) and aggregated (black) Zn-BPhe c.

3.3.2 Incorporation of a thiol group

No visual change was observed directly after mixing of reagents used for incorporation of a thiol group at the C17³ position. However, during the course of incubation an oily less optically dense, subphase formed (Figure 3.27). The

formation of such a phase may be consistent with the removal of the long alcohol tails from pigments.

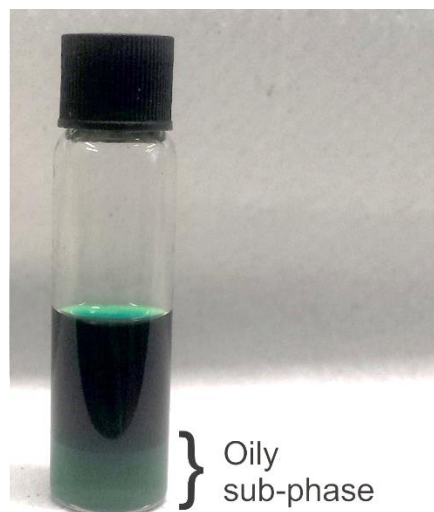


Figure 3.27 Reaction vial used for attempted incorporation of an SH group in Chl a.

The photograph shows the oily sub-phase which forms during incubation of Chl a, cysteamine, and potassium tert-butoxide.

3.3.2.1 XPS analysis of Cysteamine treated pigments.

Figures 3.28 and 3.29 show XPS survey spectra for cysteamine-treated Chl a and Chl b respectively. As with native pigments carbon, nitrogen, oxygen, and magnesium were detected. In addition, for cysteamine treated pigments, sulphur and trace amounts of potassium were detected. Figures 3.30 and 3.31 show detailed XPS spectra for the Au 4f, C 1s, Mg 1s, N 1s, O 1s, S 2p, Zn 2p, and K 2p for treated Chl a and Chl b respectively.

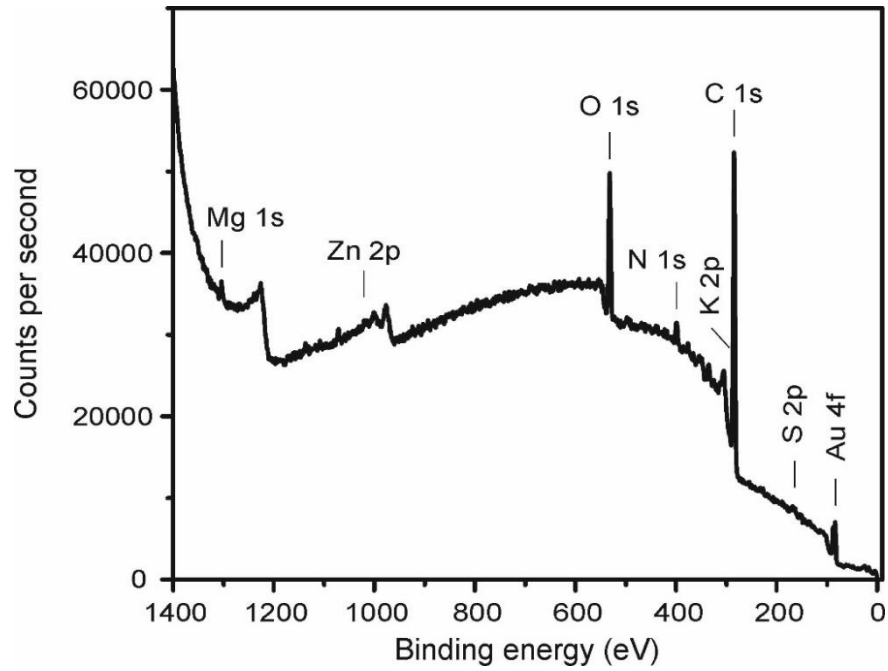


Figure 3.28 XPS survey spectrum for cysteamine-treated Chl a.

XPS survey spectrum for cysteamine-treated Chl a showing the presence of carbon, oxygen, nitrogen, magnesium, and sulphur.

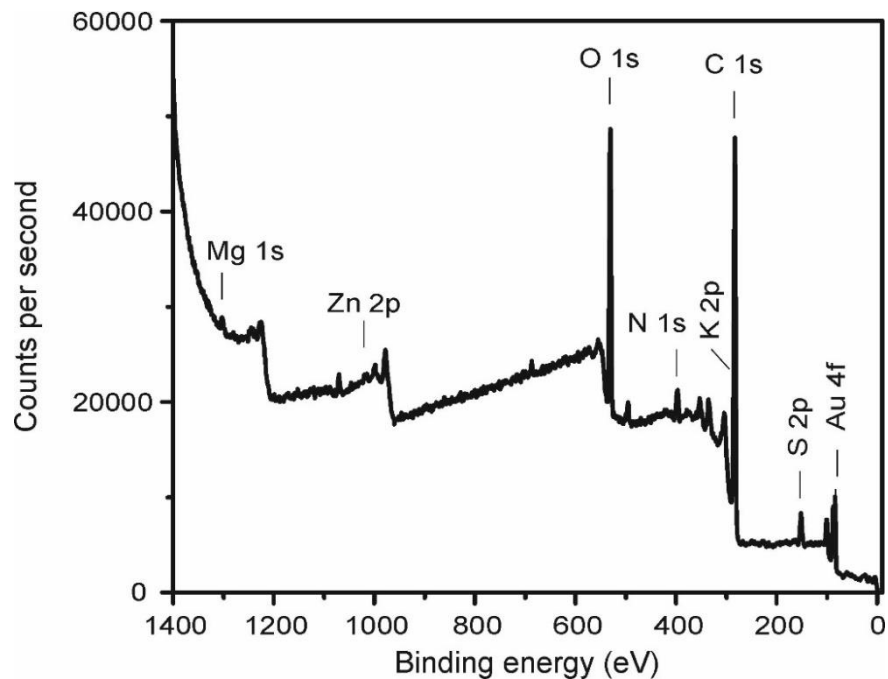


Figure 3.29 XPS survey spectrum for cysteamine-treated Chl b.

XPS survey spectrum for cysteamine-treated Chl b showing the presence of carbon, oxygen, nitrogen, magnesium, and sulphur.

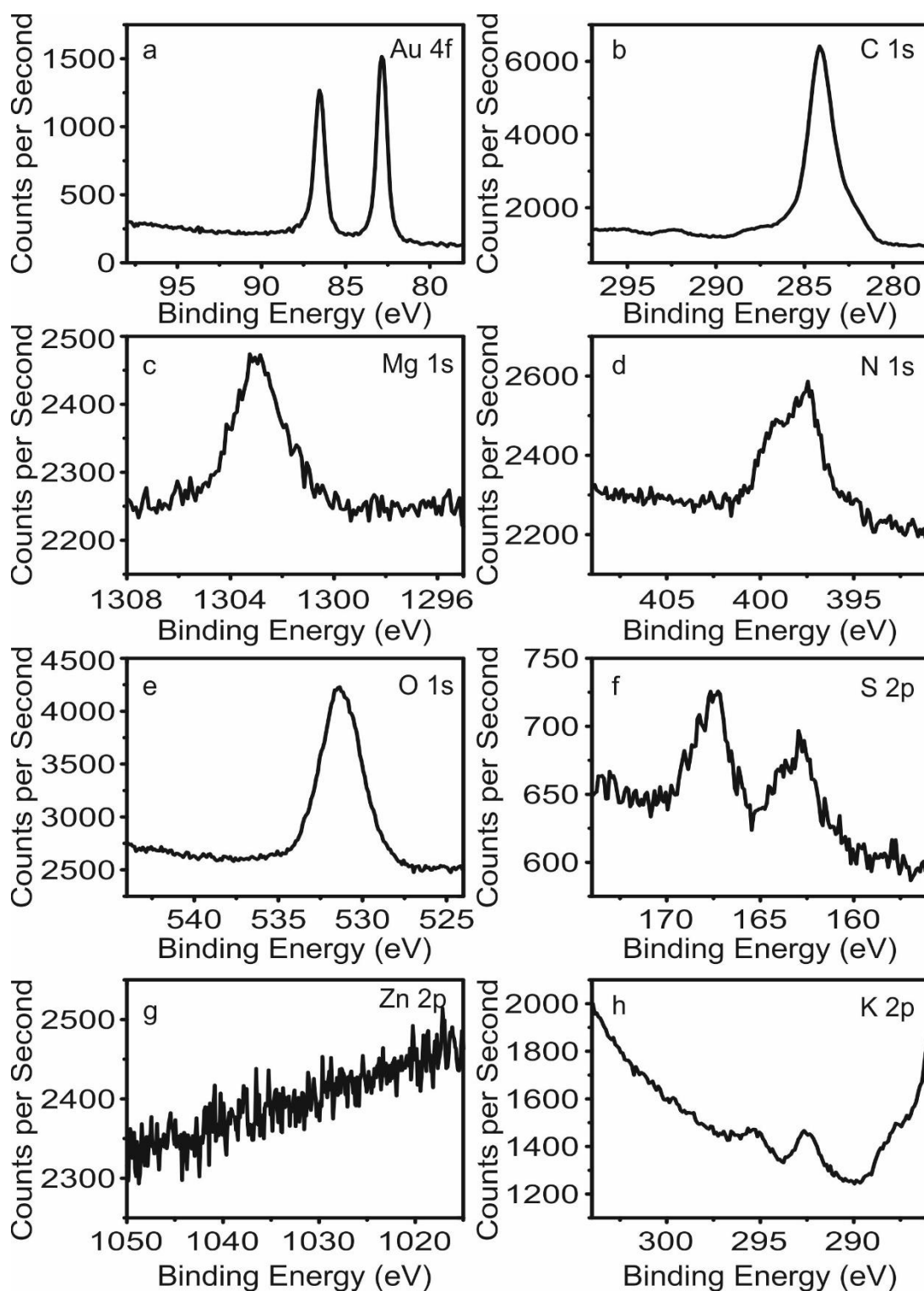


Figure 3.30 Detailed XPS spectra for cysteamine-treated Chl a.

Detailed XPS spectra of (a) Au 4f, (b) C 1s, (c) Mg 1s, (d) N 1s, (e) O 1s, (f) S 2p, (g) Zn 2p, and (h) K 2p peaks obtained for cysteamine-treated Chl a.

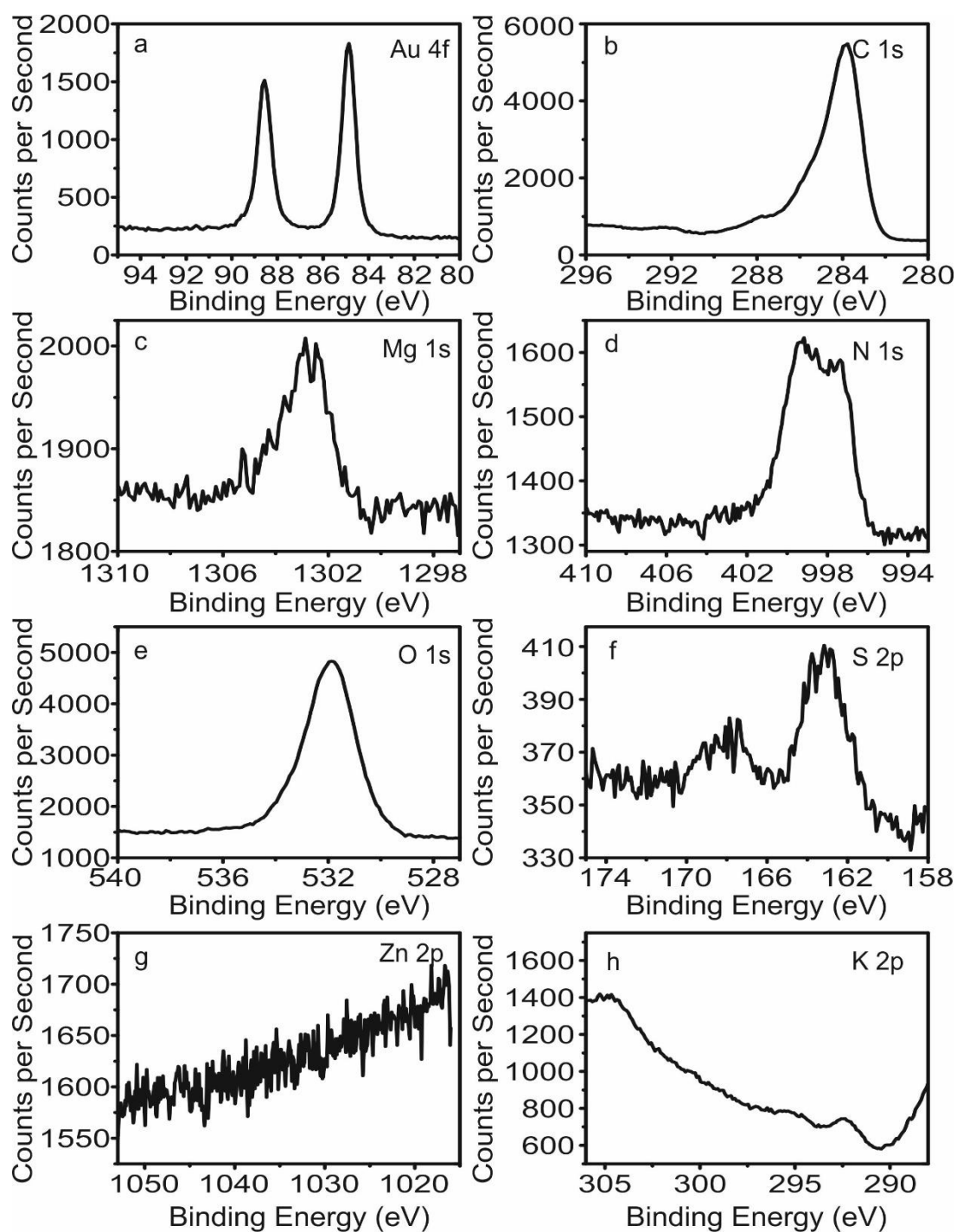


Figure 3.31 Detailed XPS spectra used for cysteamine-treated Chl b.

Detailed XPS spectra of (a) Au 4f, (b) C 1s, (c) Mg 1s, (d) N 1s, (e) O 1s, (f) S 2p, (g) Zn 2p, and (h) K 2p peaks obtained for cysteamine-treated Chl b.

As these pigments were not purified after treatment due to the lack of a suitable method, simple examination of the component elements is insufficient to determine whether the reaction was successful. Instead it is necessary to examine whether a change in the proportion of element species exists. Figure 3.32 shows C 1s spectra for treated Chl a and Chl b which have been normalised and had the normalised C 1s spectra of their Chl a and Chl b counterparts subtracted. In both cases two troughs can be seen. This corresponds to the absence of components which were present in the native pigments in the spectra for treated components. Due to the binding energies of these troughs, the first higher binding energy trough may be tentatively assigned to missing contributions from carbon double bonds and CH₃ carbon species.²³³ Similarly, the second lower energy peak most likely corresponds to missing CH₂ species of carbon.²³³ This is consistent with the removal of hydrolysed hydrocarbon tails from the treated pigments. Combined with the visual observations described above, it can be concluded that during treatment, alcohol tails are lost and may evaporate during pigment drying. It was however, not possible to determine whether these tails were simply lost or were replaced with an SH terminated amine as intended, though no chemistry is known between the reagents used which would account for simple hydrolysis. Additional techniques will be required to assess the success of modification. Nonetheless, XPS results presented here are by no means incompatible with successful incorporation of a thiol group.

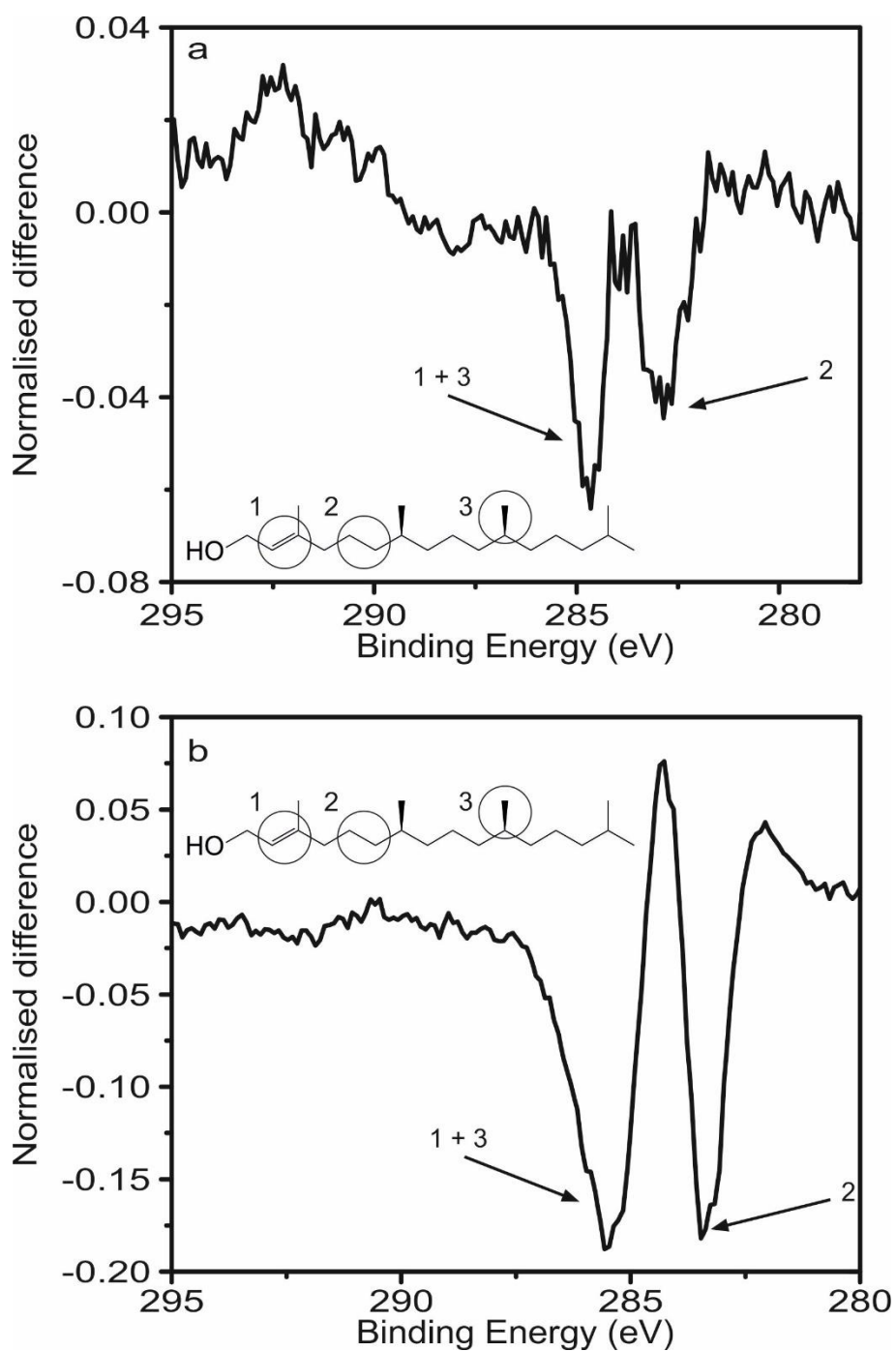


Figure 3.32 Difference spectra for C 1s peaks of cysteamine-treated Chl a and Chl b.

C 1s carbon spectra for (a) treated Chl a and (b) treated Chl minus their untreated counterparts. The insert shows the hydrolysed tail with key groups indicated.

3.4 Conclusions

This chapter demonstrates the successful extraction and purification of native chlorophylls and bacteriochlorophylls. Bacteriochlorophylls were successfully extracted from whole cells and chlorosomes using a modified method with minimal degradation. Similarly, chlorophyll a and b have been successfully extracted from spinach also with minimal sample degradation. HPLC methods for purification of as extracted pigments were implemented for BChl c as well as Chl a and Chl b allowing the production of pure pigment samples for further characterisation and modification. Elemental analysis of these pigments were consistent with native chlorophylls and bacteriochlorophylls.

A facile and versatile method for conversion of (B)Chls to Zn-(B)Phe has also been found and applied to Chl a, Chl b, BChl c, and BChl e, to produce Zn-Phe a, Zn-Phe b, Zn-BPhe c, and Zn-BPhe e. These pigments have been spectrally characterised and a protocol for the purification of Zn-Phe a and Zn-BPhe c developed. Crucially, it has been shown here that bacteriochlorophyll pigments modified in this way retain their ability to aggregate. As aggregation appears to be key to high efficiency energy transfer in bacteriochlorophyll containing systems, the ability of modified forms to aggregate is likely vital for their use in light harvesting or other photonic applications.

Unfortunately, whilst evidence presented here is not conclusive, it is consistent with the successful incorporation of a thiol group. The identification of a suitable purification method and the further analysis of the reaction products are therefore needed to determine whether or not this was successful.

Chapter 4

Results and Discussion: Simulations of bacteriochlorophyll pigment assemblies

4.1 Introduction

This chapter details results from the first all-atom molecular dynamics simulations of bacteriochlorophyll pigment assemblies. This work is exploratory in nature and seeks to shed light on whether there is a preferred dimer arrangement, the origin of lamellar curvature and how chemical structure influences final structure. To this end, this chapter examines nine different previously proposed dimer configurations arranged in single (Section 4.2) and triple layer (Section 4.3) assemblies. Initial and final structures of these simulations are examined and related to system energy. For single layer systems, X-ray scattering is predicted for stationary structures and compared to previously reported experimental results.

4.2 Single sheets

As a starting point, single sheet simulations were performed on optimised dimer arrangements of $\alpha A\alpha A$, $\alpha S\alpha S$, $\alpha S\beta A$, $\alpha S\beta Ad$, $\beta A\beta A$, $\beta S\alpha A$, $\beta S\alpha Ag$, $\beta S\alpha Au$, and $\beta S\beta S$ (see Figure 1.9). Three repeats with identical initial configurations and conditions were performed. Simulations were performed *in vacuo* in order to more closely mimic the hydrophobic environment found within chlorosomes.

4.2.1 Structures from simulation

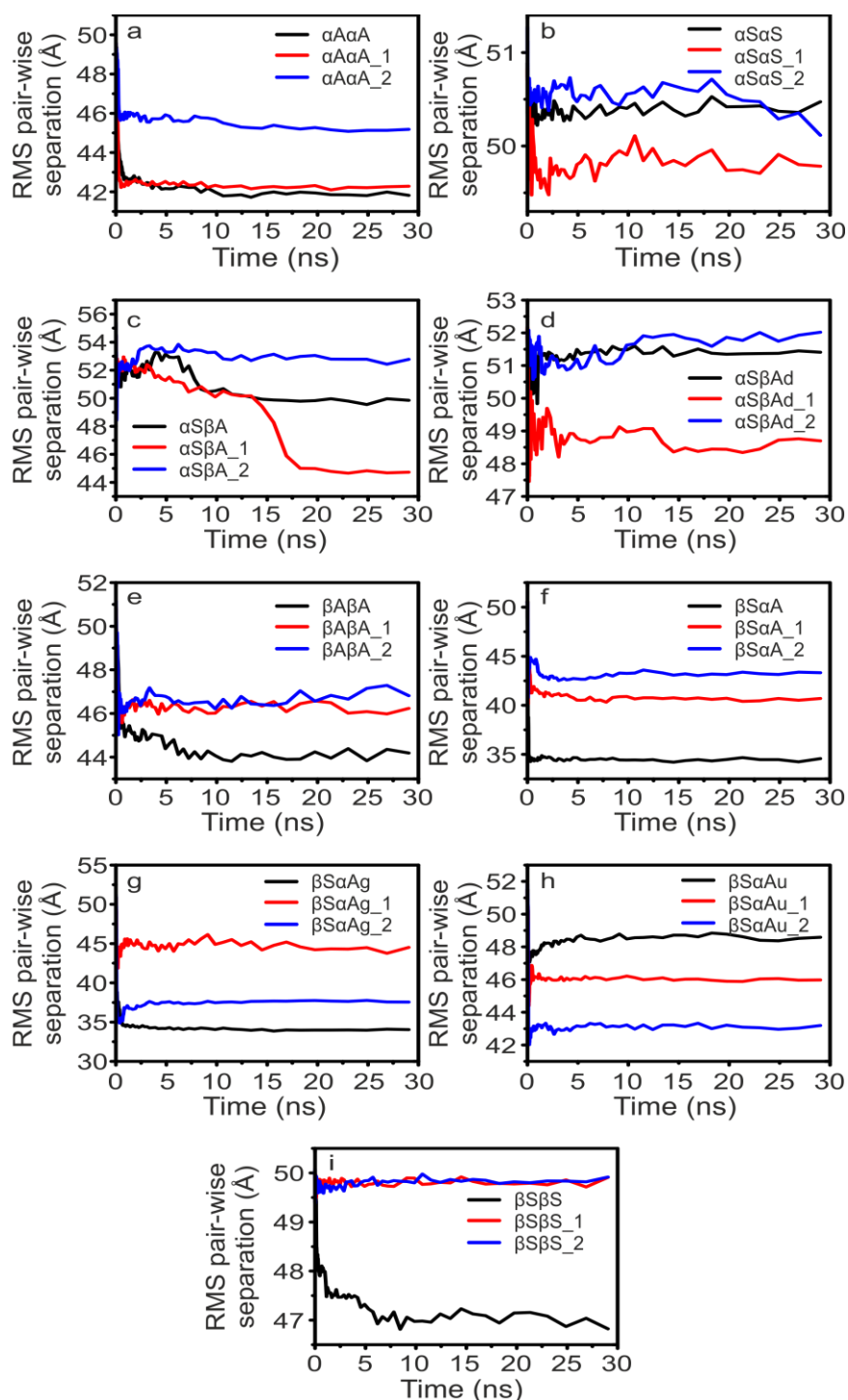


Figure 4.1 RMS pair-wise separation of Mg atoms for single layer pigment systems.

Change in RMS separation of Mg atoms with time for simulations based on (a) $\alpha A\alpha A$, (b) αSaS , (c) $\alpha S\beta A$, (d) $\alpha S\beta Ad$, (e) $\beta A\beta A$, (f) βSaA , (g) $\beta SaAg$, (h) $\beta SaAu$, and (i) $\beta S\beta S$ dimer configurations and their repeats.

Root-mean-squared (RMS) pair-wise separation plots for magnesium atoms within each of the single sheet simulations are shown in Figure 4.1. In all cases, except for $\alpha S\beta A_1$, values were found to stabilise quickly after a rapid initial decrease due to contraction of the sheets. In the case of $\alpha S\beta A_1$ a rapid change was observed at the beginning of the simulation, followed by a second rapid decrease at ~ 15 ns. This is consistent with the existence of a rapidly formed, relatively long lived, initial state which later transitions to a second more stable state. In a number of cases, repeats for identically prepared starting configurations (dimer motifs) lead to very different equilibrium separations for Mg atoms. This suggests the formation of slightly different structures despite the same initial dimer configuration.

Detailed discussion of simulation results for individual dimer configurations are presented in the following section. Dipole moment plots are provided both to show how dipole orientation differs between different dimer arrangements (e.g. parallel and anti-parallel arrangements) and also the extent to which initial dimer orientation is lost or maintained. Furthermore, whilst not calculated in this thesis, the arrangement of dipole moments within a structure determines its optical absorbance and circular dichroism properties. Consequently, significantly different dipole arrangements should lead to different optical properties.

$\alpha A\alpha A$: For the $\alpha A\alpha A$ dimer configuration, curvature was observed for two of the three repeats (Figure 4.2). In the case of the $\alpha A\alpha A$ and $\alpha A\alpha A_2$ curvature was observed about a single axis with curvature taking place in the same direction in each repeat. In the case of $\alpha A\alpha A_1$ curvature was minimal with slight bending only observed at the sheet edges. Dipole moment plots (Figure 4.3)¹ suggest that significant disorder is present for this dimer arrangement.

¹ Larger versions of all dipole moment plots can be found in Appendix E.

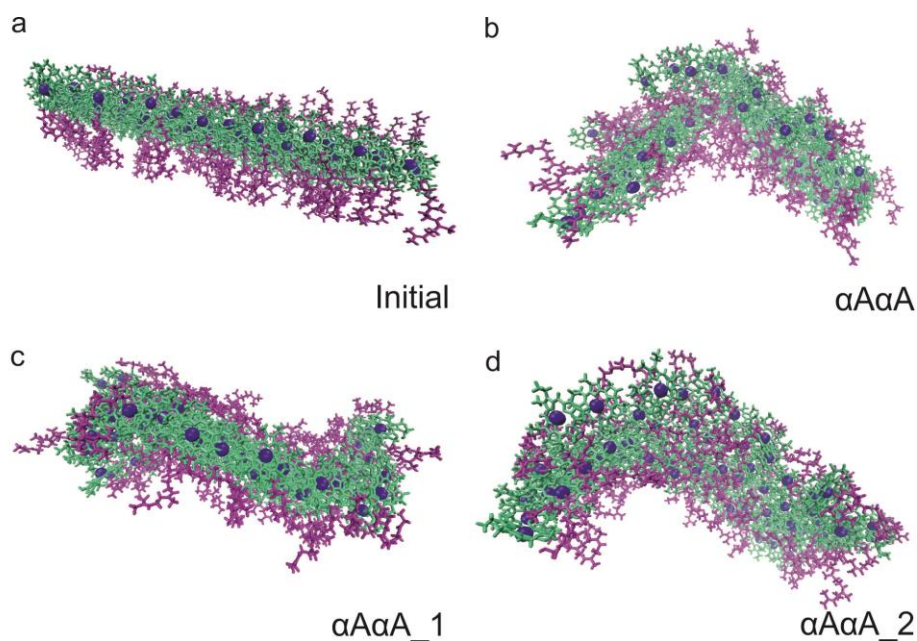


Figure 4.2 Initial and final structures for simulations on sheets formed using the $\alpha A\alpha A$ dimer arrangement.

Edge-on views of (a) the initial starting structure along with the three simulation repeats (b) $\alpha A\alpha A$, (c) $\alpha A\alpha A_1$, and (d) $\alpha A\alpha A_2$.

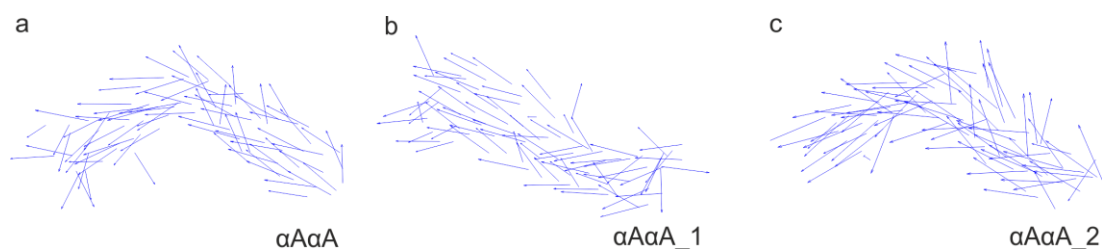


Figure 4.3 Q_y dipole moments for sheets formed using the $\alpha A\alpha A$ dimer arrangement.

Q_y dipole moments, shown as arrows, for the final structures of simulations (a) $\alpha A\alpha A$, (b) $\alpha A\alpha A_1$, and (c) $\alpha A\alpha A_2$. The direction of the arrow indicates the direction of the dipole moment.

α S α S: No curvature was observed for single sheets constructed based on the α S α S dimer motif (Figure 4.4), however, some twisting of the sheets was observed. This twisting can most easily be seen in the dipole moment plots (Figure 4.5). These plots also indicated that sheets formed of the α S α S dimer arrangement retain a high degree of order.

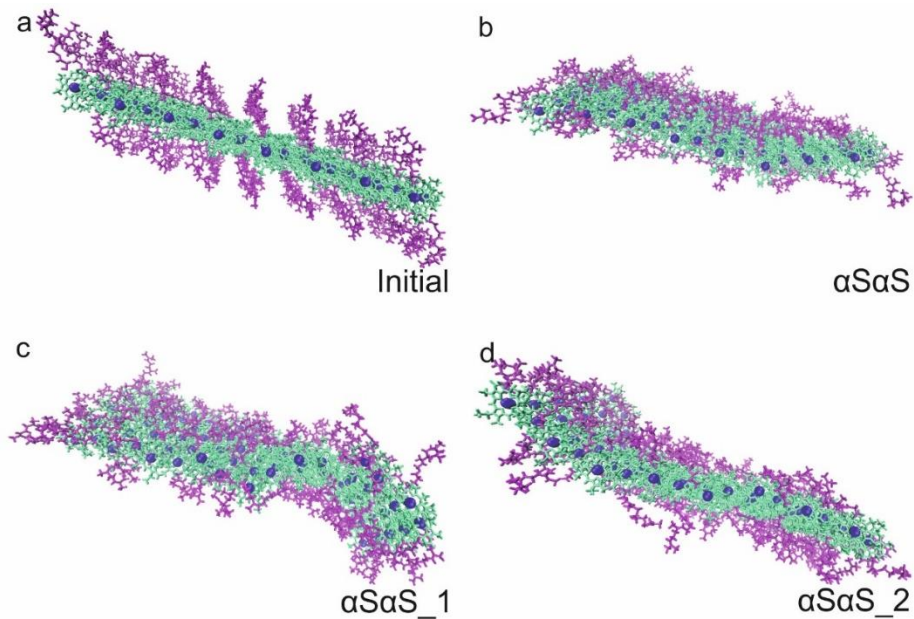


Figure 4.4 Initial and final structures for simulations on sheets formed using the α S α S dimer arrangement.

Edge-on views of (a) the initial starting structure along with the three simulation repeats (b) α S α S, (c) α S α S_1, and (d) α S α S_2.

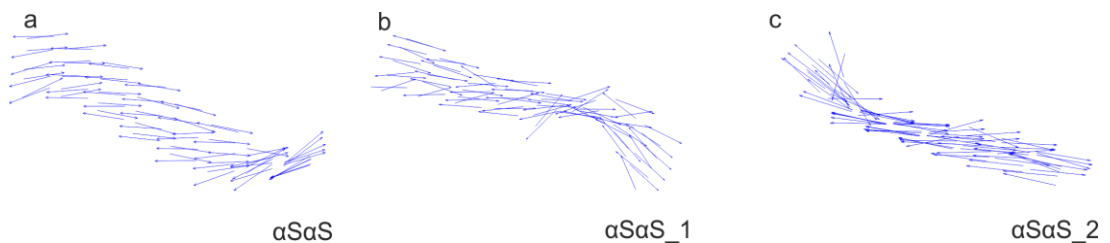


Figure 4.5 Q_y dipole moments for sheets formed using the α S α S dimer arrangement.

Edge-on views of the arrangement of the Q_y dipole moments, shown as arrows, for the final structures of simulations (a) α S α S, (b) α S α S_1, and (c) α S α S_2. The direction of the arrow indicates the direction of the dipole moment.

α S β A: In the case of the α S β A dimer sheets (Figure 4.6), two repeats, α S β A and α S β A_1, showed strong curvature shortly after the beginning of unrestrained simulation. However, sheets were later observed to straighten before finally curving again. The third repeat, α S β A_2, did not regain curvature. It can be seen from the dipole moment plots in Figure 4.7, that the third repeat is more disordered during the straightened phase, than its two counterparts. Consequently, one possible explanation for the failure of this repeat to either retain or regain curvature could be found in the increased disorder effectively blocking the transition.

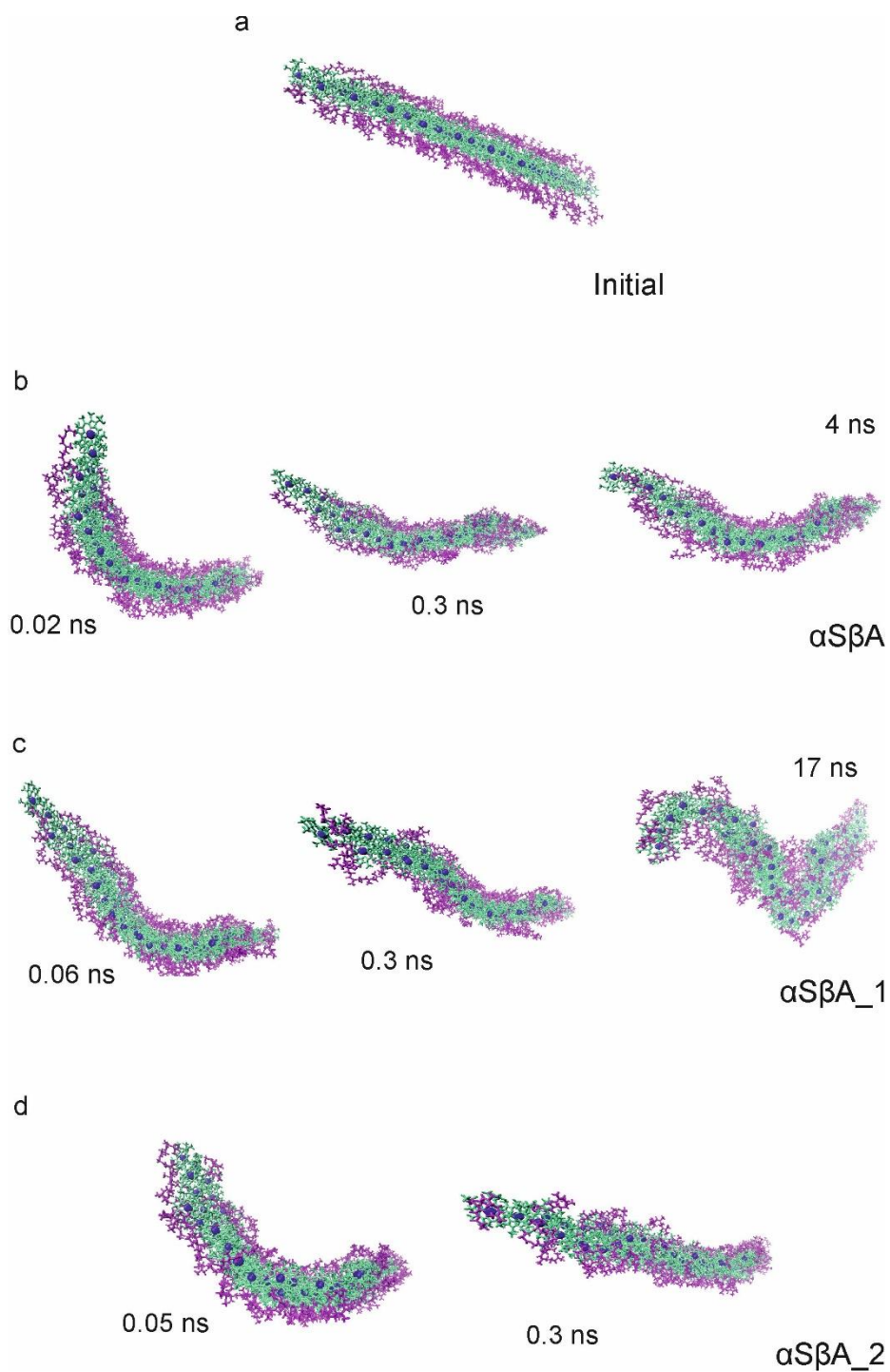


Figure 4.6 Initial and final configurations for simulations on sheets formed using the $\alpha S\beta A$ dimer arrangement.

Edge-on views of (a) the initial starting structures key states observed during the three simulation repeats (b) $\alpha S\beta A$, (c) $\alpha S\beta A_1$, and (d) $\alpha S\beta A_2$. States shown for $\alpha S\beta A$ and $\alpha S\beta A_1$ are representative of the three observed states.

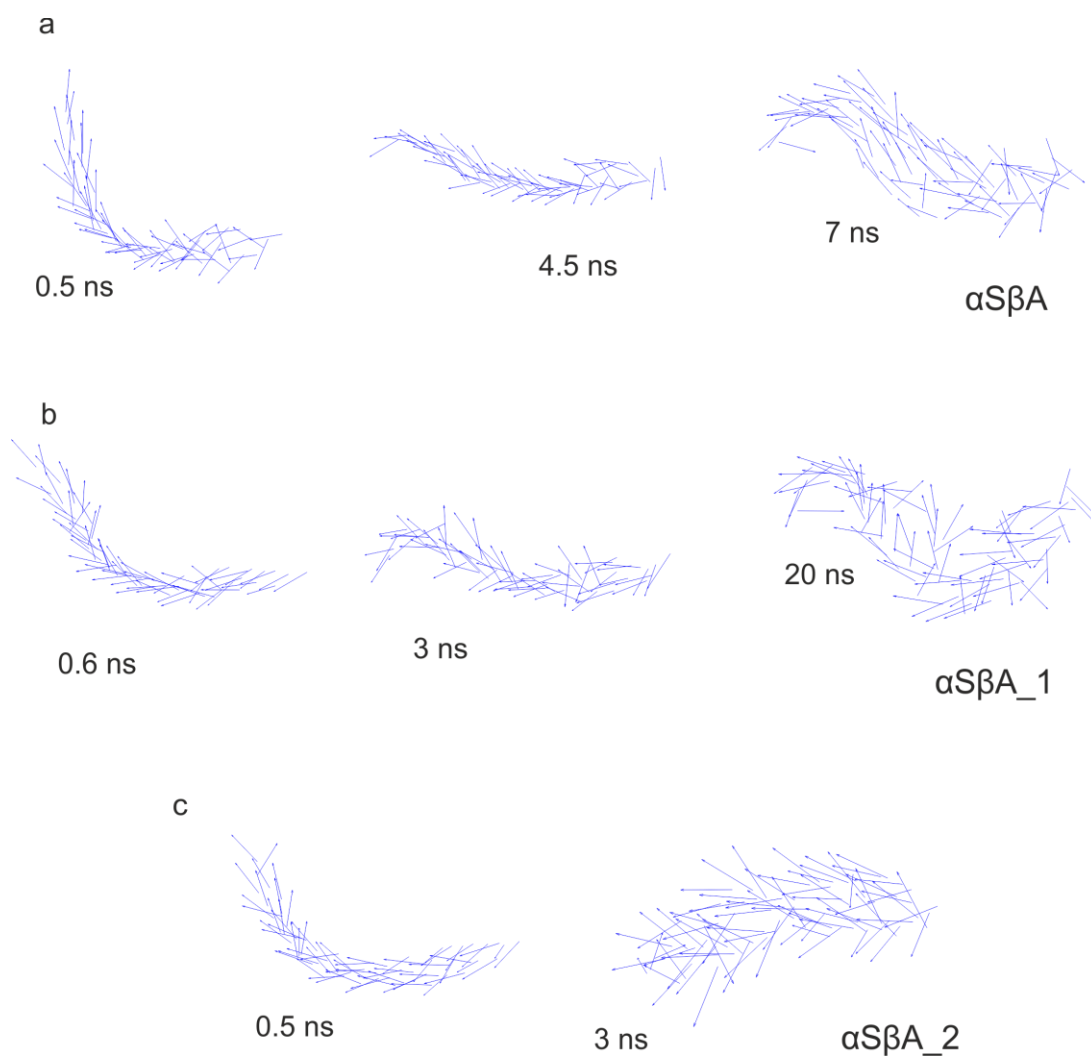


Figure 4.7 Q_y dipole moments for sheets formed using the $\alpha S\beta A$ dimer arrangement.

Edge-on views of the arrangement of the Q_y dipole moments, shown as arrows, for the final structures of simulations (a) $\alpha S\beta A$, (b) $\alpha S\beta A_1$, and (c) $\alpha S\beta A_2$. The direction of the arrow indicates the direction of the dipole moment.

$\alpha\text{S}\beta\text{Ad}$: None of the $\alpha\text{S}\beta\text{Ad}$ dimer simulations exhibited significant curvature (Figure 4.8). The slight curvature observed for simulation $\alpha\text{S}\beta\text{Ad}_1$ appears, on closer inspection, to be due to defect formation. This is consistent with the slight splintering of the sheet observed in the dipole moment plots (Figure 4.9b).

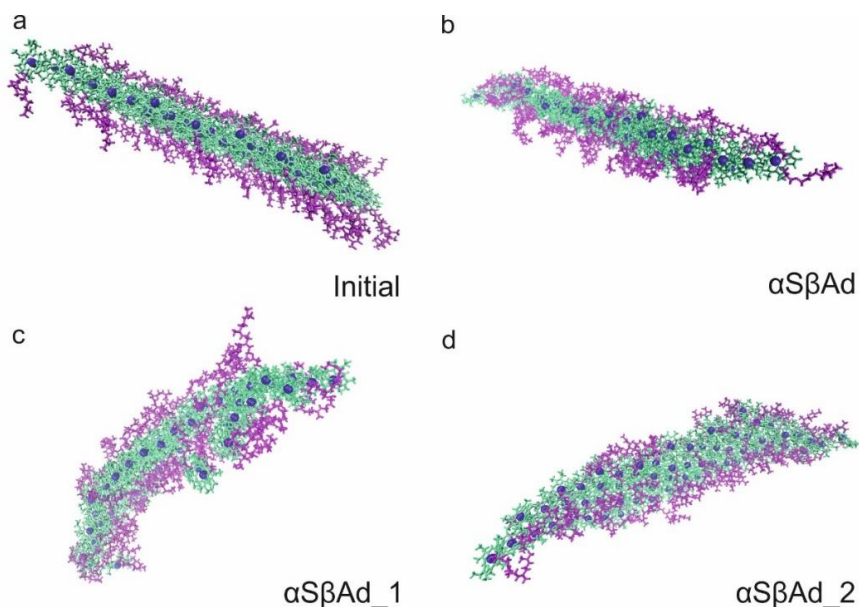


Figure 4.8 Initial and final structures for simulations on sheets formed using the $\alpha\text{S}\beta\text{Ad}$ dimer arrangement.

Edge-on views of (a) the initial starting structure along with the three simulation repeats (b) $\alpha\text{S}\beta\text{Ad}$, (c) $\alpha\text{S}\beta\text{Ad}_1$, and (d) $\alpha\text{S}\beta\text{Ad}_2$.

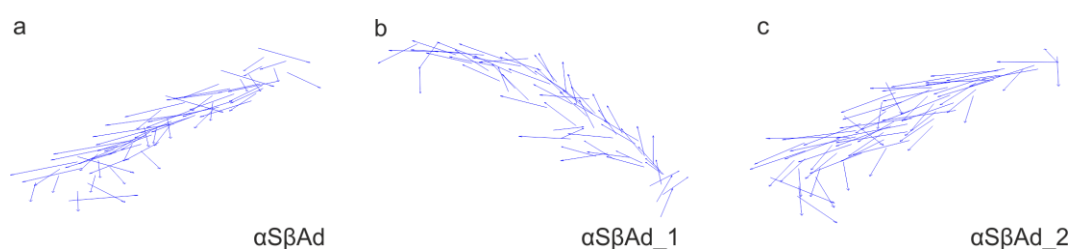


Figure 4.9 Q_y dipole moments for sheets formed using the $\alpha\text{S}\beta\text{Ad}$ dimer arrangement.

Edge-on views of the arrangement of the Q_y dipole moments, shown as arrows, for the final structures of simulations (a) $\alpha\text{S}\beta\text{Ad}$, (b) $\alpha\text{S}\beta\text{Ad}_1$, and (c) $\alpha\text{S}\beta\text{Ad}_2$. The direction of the arrow indicates the direction of the dipole moment.

$\beta A \beta A$: All three repeats of single sheets composed of the $\beta A \beta A$ motif curved strongly about a single axis in the same direction (Figure 4.10). The dipole moment plots for this dimer arrangement also look substantially different to those observed for other dimer configurations with dimers appearing to remain stacked and twist together as columns to provide curvature (Figure 4.11).

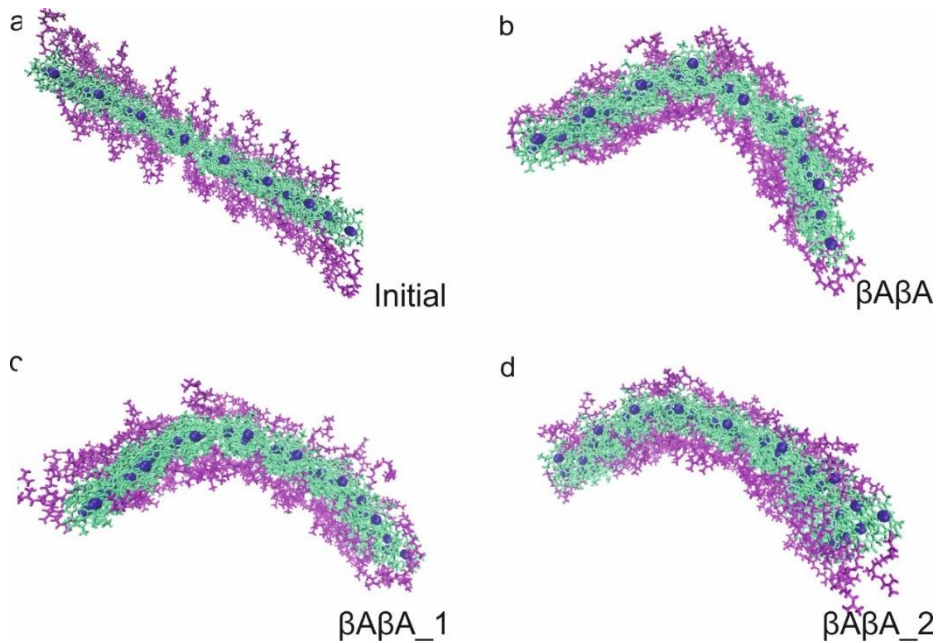


Figure 4.10 Initial and final structures for simulations on sheets formed using the $\beta A \beta A$ dimer arrangement.

Edge-on views of (a) the initial starting structure along with the three simulation repeats (b) $\beta A \beta A$, (c) $\beta A \beta A_1$, and (d) $\beta A \beta A_2$.

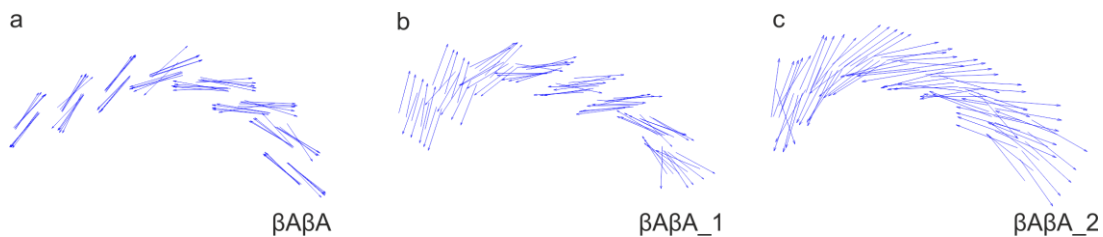


Figure 4.11 Q_y dipole moments for sheets formed using the $\beta A \beta A$ dimer arrangement.

Edge-on views of the arrangement of the Q_y dipole moments, shown as arrows, for the final structures of simulations (a) $\beta A \beta A$, (b) $\beta A \beta A_1$, and (c) $\beta A \beta A_2$. The direction of the arrow indicates the direction of the dipole moment.

β S α A: Together with the β S α Ag motif, this dimer arrangement led to some of the most curved structures (Figure 4.12). In all three repeats, curvature took place in the same direction. In addition, a significant degree of twisting was observed as manifested in dipole moments fanning out (Figure 4.13). In the β S α A repeat, the pigment sheet curves and twists sufficiently that the top right hand dimer appears to stack with the bottom left hand dimer forming a helically wrapped tube. An overlap in the Q_y dipole moment corresponding to these two dimers is observed (Figure 4.13a)

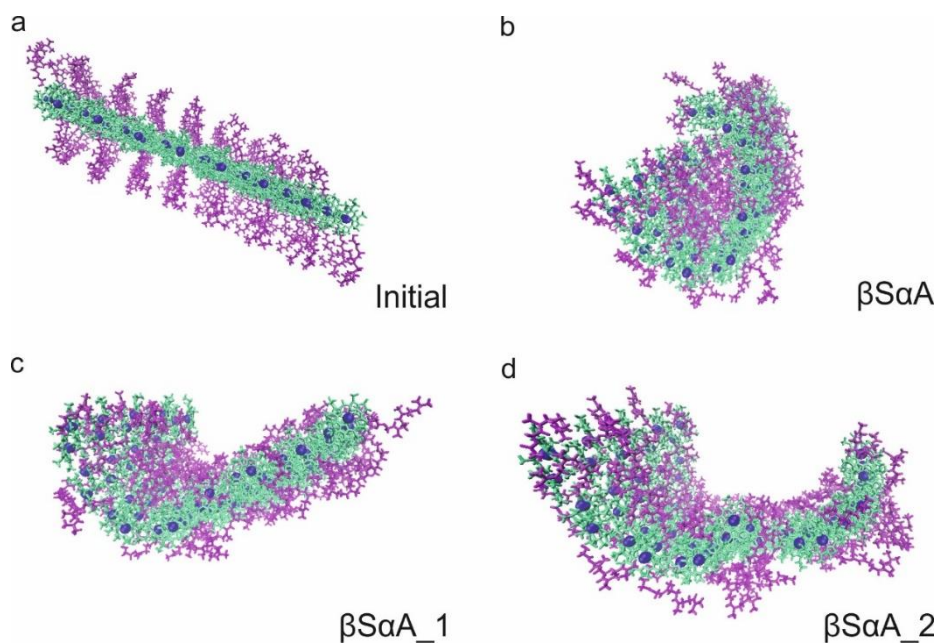


Figure 4.12 Initial and final structures for simulations on sheets formed using the β S α A dimer arrangement.

Edge-on views of (a) the initial starting structure along with the three simulation repeats (b) β S α A, (c) β S α A_1, and (d) β S α A_2.

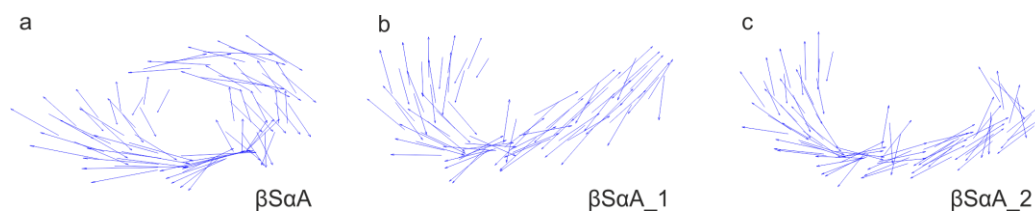


Figure 4.13 Q_y dipole moments for sheets formed using the β SaA dimer arrangement.

Edge-on views of the arrangement of the Q_y dipole moments, shown as arrows, for the final structures of simulations (a) β SaA, (b) β SaA_1, and (c) β SaA_2. Arrow indicates the direction of the dipole moment.

β SaAg: As with β SaA significant curvature and twisting is observed for the β SaAg dimer motif (Figure 4.14). Curvature takes place in the same direction for all repeats and in the same direction as that observed for β SaA dimer sheets. Two of the repeats, β SaAg and β SaAg_2, appear to form a helically wrapped tube, as described above. From the dipole moment plot, stacking of the dimers and dipole moments appears to take place along the interface where the tube forms (Figure 4.15 a and c).

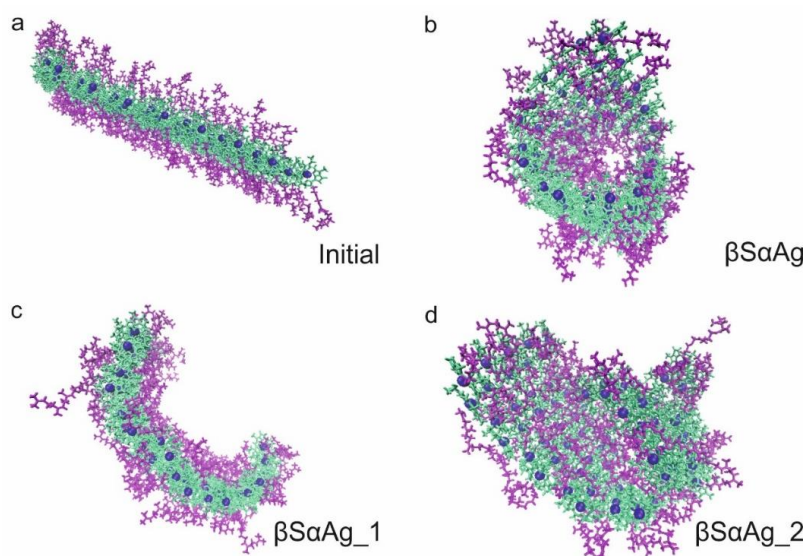


Figure 4.14 Initial and final structures for simulations on sheets formed using the β SaAg dimer arrangement.

Edge-on views of (a) the initial starting structures with the three simulation repeats (b) β SaAg, (c) β SaAg_1, and (d) β SaAg_2.

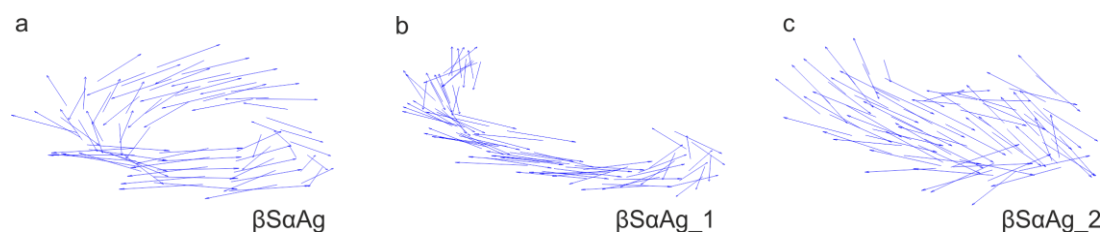


Figure 4.15 Q_y dipole moments for sheets formed using the $\beta\text{S}\alpha\text{Ag}$ dimer arrangement.

Edge-on views of the arrangement of the Q_y dipole moments, shown as arrows, for the final structures of simulations (a) $\beta\text{S}\alpha\text{Ag}$, (b) $\beta\text{S}\alpha\text{Ag}_1$, and (c) $\beta\text{S}\alpha\text{Ag}_2$. The direction of the arrow indicates the direction of the dipole moment.

$\beta\text{S}\alpha\text{Au}$: Strong curvature is observed in two of the three repeats ($\beta\text{S}\alpha\text{Au}_1$ and $\beta\text{S}\alpha\text{Au}_2$) (Figure 4.16). The remaining repeat did not curve but a degree of sheet twisting can be seen from the dipole moment plot (Figure 4.17a).

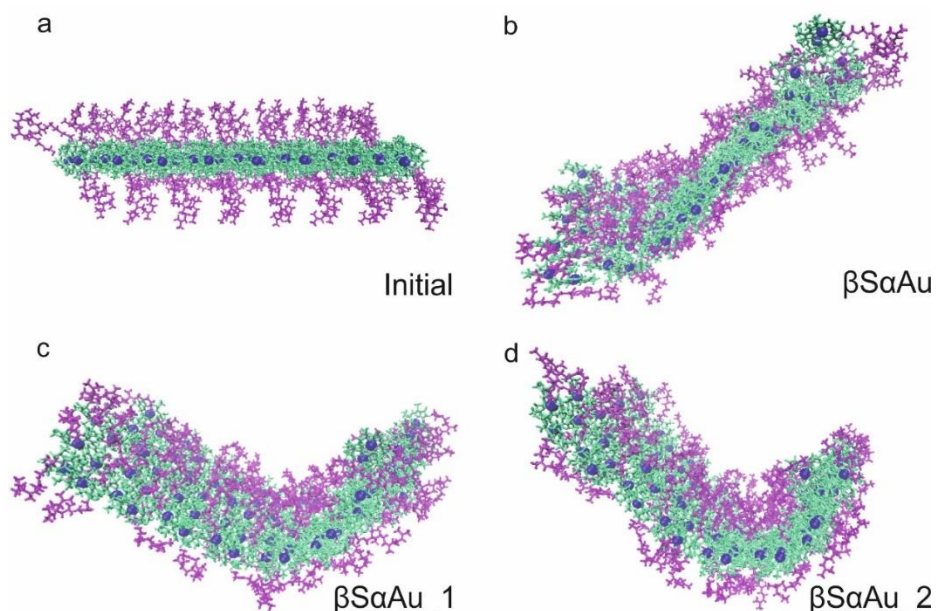


Figure 4.16 Initial and final structures for simulations on sheets formed using the $\beta\text{S}\alpha\text{Au}$ dimer arrangement.

Edge-on views of (a) the initial starting structures along with the three simulation repeats (b) $\beta\text{S}\alpha\text{Au}$, (c) $\beta\text{S}\alpha\text{Au}_1$, and (d) $\beta\text{S}\alpha\text{Au}_2$.

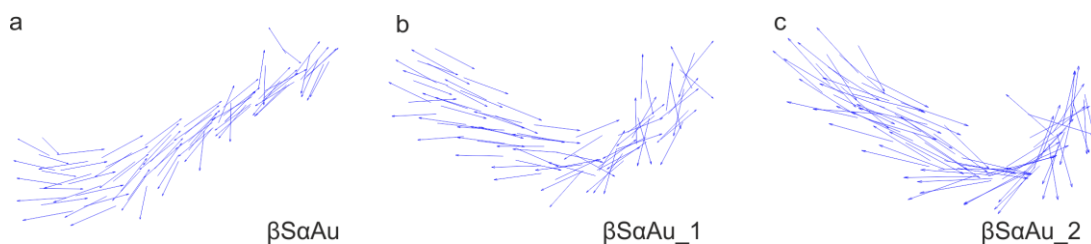


Figure 4.17 Q_y dipole moments for sheets formed using the $\beta S\alpha Au$ dimer arrangement.

Edge-on views of the arrangement of the Q_y dipole moments, shown as arrows, for the final structures of simulations (a) $\beta S\alpha Au$, (b) $\beta S\alpha Au_1$, and (c) $\beta S\alpha Au_2$. Arrow indicates the direction of the dipole moment.

$\beta S\beta S$: Whilst some slight curvature is apparent in the final structure of $\beta S\beta S$, $\beta S\beta S_1$ and $\beta S\beta S_2$ do not curve (Figure 4.18). Dipole moment plots (Figure 4.19) show the dipole moments for this structure are significantly different from those observed for other configurations. In the case of this configuration, the dipole moments do not simply point in alternating directions. Instead, there is a large angle between the moments.

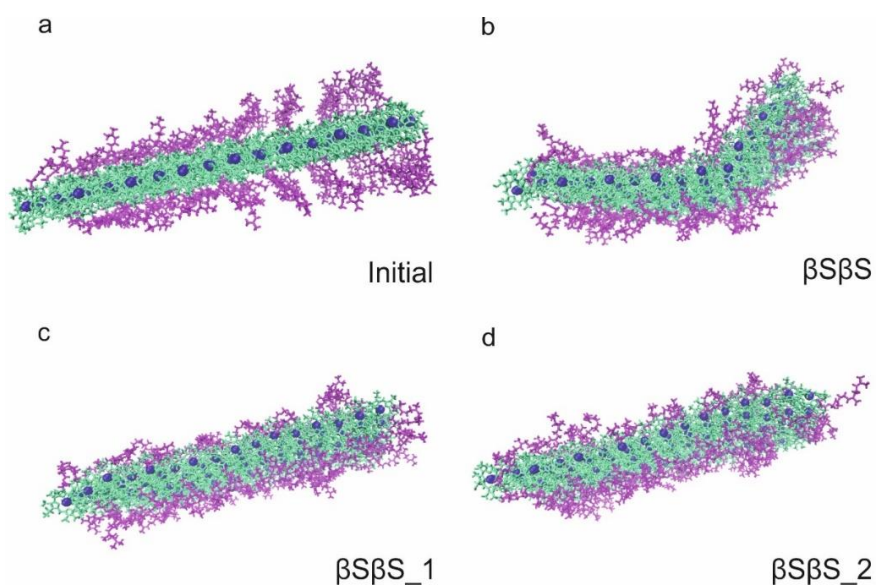


Figure 4.18 Initial and final structures for simulations on sheets formed using the $\beta S\beta S$ dimer arrangement.

Edge-on views of (a) the initial starting structure along with the three simulation repeats (b) $\beta S\beta S$, (c) $\beta S\beta S_1$, and (d) $\beta S\beta S_2$.

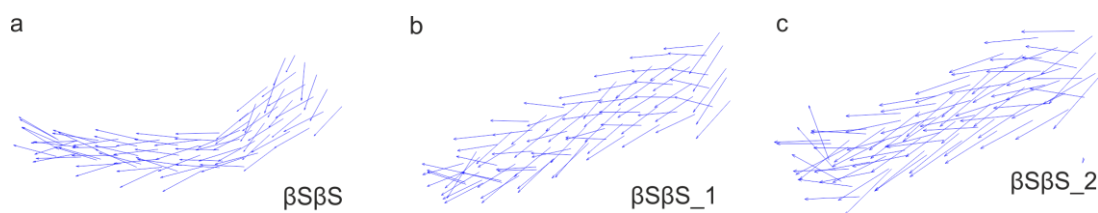


Figure 4.19 Q_y dipole moments for sheets formed using the $\beta S\alpha Au$ dimer arrangement.

Edge-on views of the arrangement of the Q_y dipole moments, shown as arrows, for the final structures of simulations (a) $\beta S\beta S$, (b) $\beta S\beta S_1$, and (c) $\beta S\beta S_2$. Arrow indicates the direction of the dipole moment.

Summary of physical structures:

A variety of structures were observed to form both within and between different dimer configurations. A number of systems exhibited significant curvature with the $\beta S\alpha A$ and $\beta S\alpha Au$ configurations curving most strongly. The formation of wrapped helical tube like structures together with overlapping and stacking of the dimers/dipole moment is of great interest given experimental observations of cylindrical forms within electron micrographs of chlorosomes.⁵ Significantly, it was observed that, should a particular dimer unit structure exhibit curvature, this always takes place in the same direction for all repeats. This suggests that curvature may be dictated by an asymmetry of the dimer unit since the composition is the same. Finally, the large variation in the appearance of dipole moment arrangement observed for different dimer configurations suggests that these systems will likely yield distinct absorbance and circular dichroism data. This may help further elucidate which structures are likely to be present in chlorosomes and *in vitro* aggregates.

4.2.2 Energy of simulated systems

Figure 4.20 shows the evolution of total system energy E_{Tot} for each simulation grouped by dimer type. For all simulations, E_{Tot} undergoes an initial rapid decrease. This rapid change mirrors the change seen in the pair-wise separation plots and consequently is likely due to the initial contraction of the system to a more favourable densely packed state. A more detailed analysis of system energy evolution is provided below for each dimer configuration.

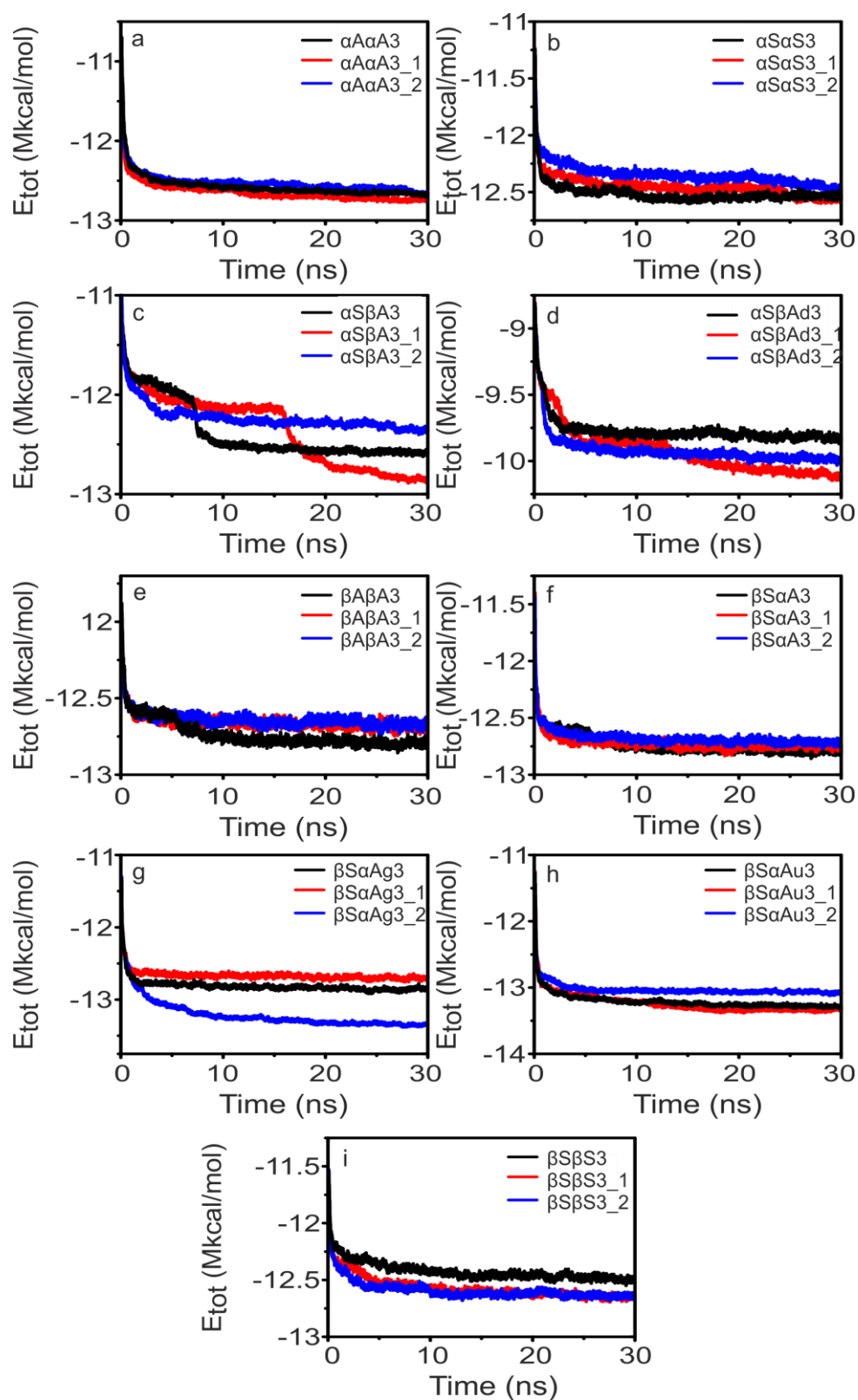


Figure 4.20 Energy evolution for single layer pigment systems.

Total system energy as a function of time for simulations based on (a) $\alpha A\alpha A$, (b) $\alpha S\alpha S$, (c) $\alpha S\beta A$, (d) $\alpha S\beta Ad$, (e) $\beta A\beta A$, (f) $\beta S\alpha A$, (g) $\beta S\alpha Ag$, (h) $\beta S\alpha Au$, and (i) $\beta S\beta S$ dimer configurations and their repeats.

$\alpha A\alpha A$: The evolution of total system energy during the simulation is very similar for all repeats despite two of the sheets exhibiting curvature. This suggests that for this dimer configuration the presence of curvature is neither more nor less energetically favourable.

$\alpha S\alpha S$: In all cases the change of energy during repeats of simulations of $\alpha S\alpha S$ followed the same trend however the energy for the $\alpha S\alpha S_2$ repeat decreases less than the other two repeats. This may be explained by the greater degree of twisting observed for this repeat preventing such close packing of pigments.

$\alpha S\beta A$: Of all the dimer motifs, the $\alpha S\beta A$ configuration showed the greatest variation in system energy between repeats. In addition, there also appeared to be a number of intermediate states. This correlates with visual observations of sheet morphology also indicating the existence of multiple states. The two simulation repeats with a final curved state were found to be of the lowest energy though there is insufficient evidence to conclusively state whether a causal link exists.

$\alpha S\beta Ad$: As with the corresponding non-displaced $\alpha S\beta A$ dimer arrangement, these simulations exhibited some variation in energies and existence of long lived intermediate states ($\alpha S\beta Ad_1$). The decrease in energy observed at ~12 ns for $\alpha S\beta Ad_1$ corresponds to a decrease in the RMS pair-wise separation at the same time. Despite this, no obvious structural transition could be discerned in the simulation movies.

$\beta A\beta A$: During simulations of $\beta A\beta A$ sheets, the system energy of the three repeats was similar however small differences in final equilibrium energy appear to be correlated to degree of curvature. More highly curved systems were found to have a lower final energy.

$\beta S\alpha A$: In the case of sheets composed of the $\beta S\alpha A$ dimer unit, the energy evolution of all three repeats were in good agreement with each other.

$\beta S\alpha Ag$: The energy of two repeats of simulations on sheets of this structure ($\beta S\alpha Ag$ and $\beta S\alpha Ag_1$) were very similar in energy. The third repeat, $\beta S\alpha Ag_2$ was markedly lower in energy, and was found to have the lowest energy of all

simulations. The reason why this repeat had an energy significantly lower than the other two $\beta\text{S}\alpha\text{Ag}$.

$\beta\text{S}\alpha\text{Au}$: In simulations of sheets based in the $\beta\text{S}\alpha\text{A}$ dimer motif, the total system energy evolved similarly in all three repeats. The energy of the $\beta\text{S}\alpha\text{A}$ **$\beta\text{S}\alpha\text{Au}_2$** is slightly higher than the other two repeats. The reason for this is not clear from examination of the three $\beta\text{S}\alpha\text{Au}$ repeats.

$\beta\text{S}\beta\text{S}$: Single sheet simulations based on this dimer structural unit were similar with the curved $\beta\text{S}\beta\text{S}$ repeat having a slightly higher energy than its two flatter counterparts.

The final system energy averaged over the final 1 ns is shown in Figure 4.21a. The antiparallel dimer arrangement appears to be the energetically favourable arrangement. It can be seen that of the majority lowest energy states, correspond to the $\beta\text{S}\alpha\text{A}$, $\beta\text{S}\alpha\text{Ag}$, and $\beta\text{S}\alpha\text{Au}$ dimer arrangements. The $\beta\text{S}\alpha\text{Ag}_2$ simulation had the lowest energy for any simulation, however, the other two repeats ($\beta\text{S}\alpha\text{Ag}$ and $\beta\text{S}\alpha\text{Au}_2$) had higher energy. After $\beta\text{S}\alpha\text{Ag}_2$ the next three lowest energy structures corresponded to the $\beta\text{S}\alpha\text{Au}$ configuration.

Figure 4.21b shows the average final system energy colour coded according to curvature. Here, energy is presented per dimer to allow comparison with the $\alpha\text{S}\beta\text{Ad}$ sheets which contain a smaller number of dimers. The lowest energy states generally exhibit curvature. The two exceptions to this are the $\beta\text{S}\alpha\text{Au}$ and $\alpha\text{A}\alpha\text{A}_1$ simulations. It is however, worth noting that other repeats of this dimer structures do exhibit curvature.

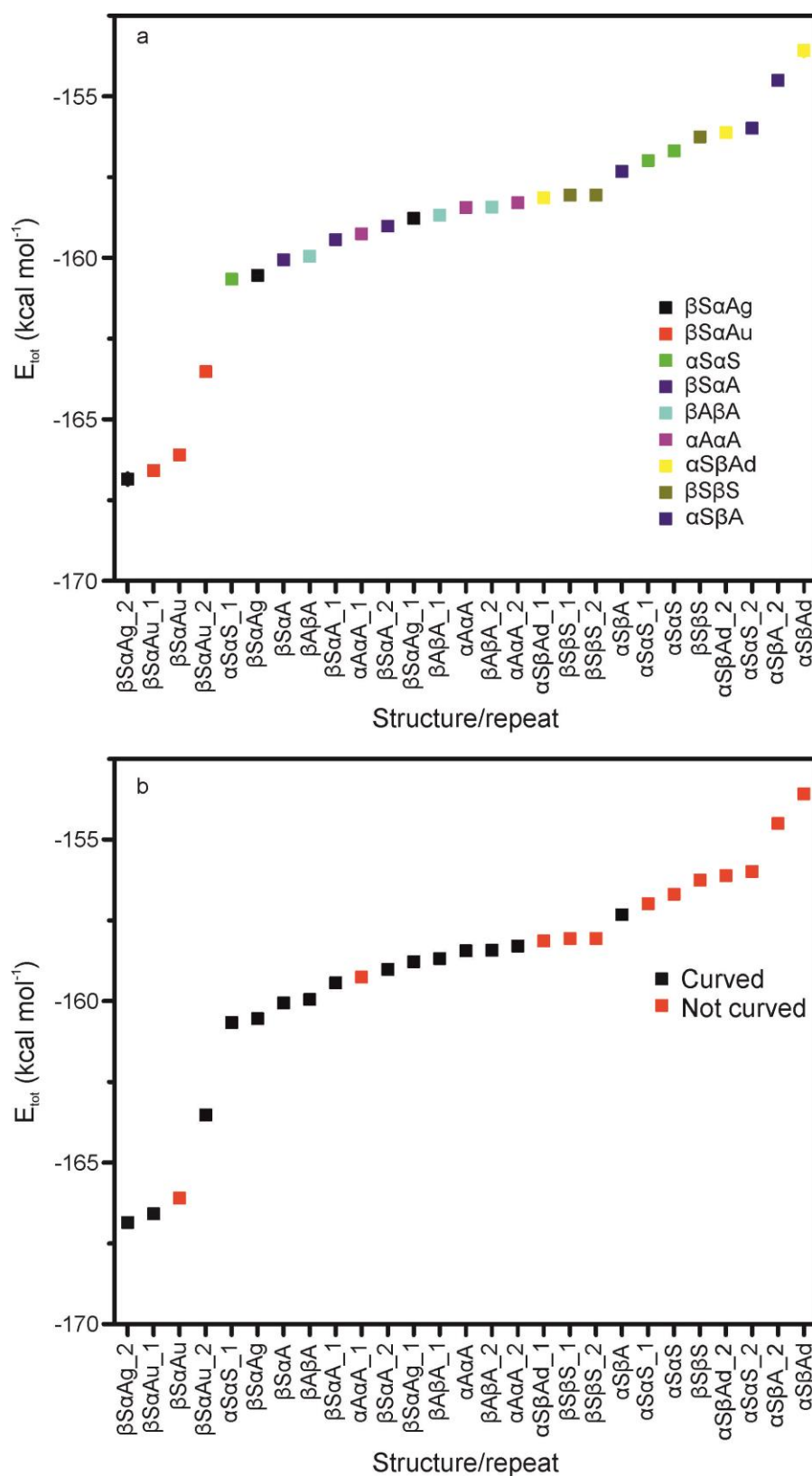


Figure 4.21 Final energy per dimer of single sheet systems.

Final E_{Tot} of single layer systems averaged over the last 1 ns and colour coded according to (a) dimer arrangement and (b) curvature.

4.2.3 X-ray scattering predictions

Figure 4.22. shows X-ray scattering predictions for each simulated sheet.

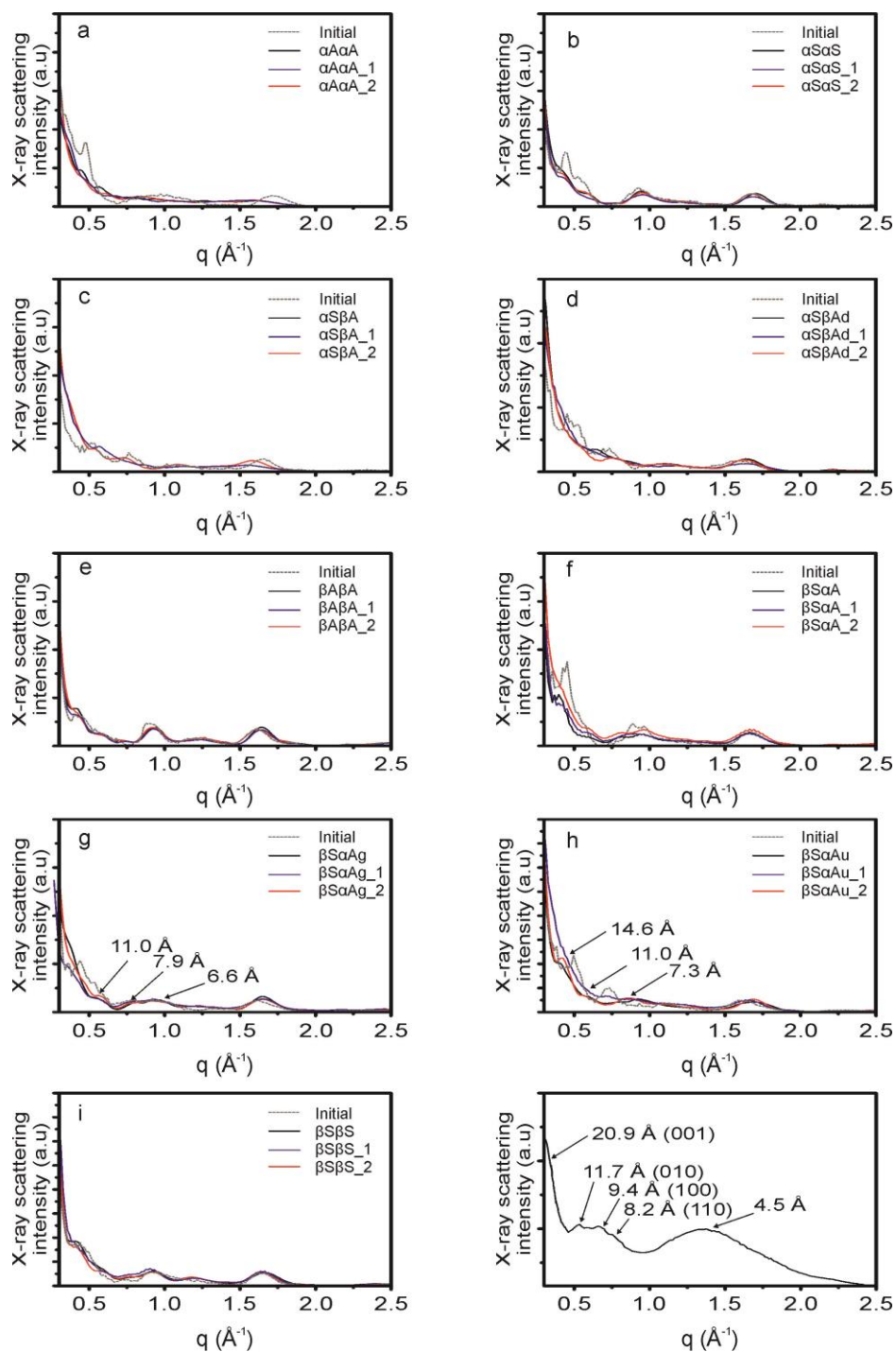


Figure 4.22 X-ray scattering predictions for single sheet systems.

X-ray scattering predictions for (a) $\alpha A\alpha A$, (b) αSaS , (c) $\alpha S\beta A$, (d) $\alpha S\beta Ad$, (e) $\beta A\beta A$, (f) βSaA , (g) $\beta SaAg$, (h) $\beta SaAu$, and (i) $\beta S\beta S$ dimer configurations, and repeats. (j) Experimental X-ray scattering data³⁵ for comparison.

X-ray scattering data is shown as the average of 100 frames (0.1 ns) in order to provide a more realistic basis for comparison with experimental results. With the exception of simulations for sheets based on the $\alpha A\alpha A$ dimer configuration (Figure 4.22a), significant peaks were observed in the predicted X-ray scattering curves for all simulations. A number of strong peaks were observed in the predicted X-ray scattering curve for the initial configuration of $\alpha A\alpha A$. These peaks however are largely absent in the curves obtained for the final configurations. The lack of structure observed in X-ray scattering for this repeat is consistent with the high degree of disorder observed in the dipole moment plot (Figure 4.3). In general, X-ray scattering patterns for a particular dimer configuration are similar across all repeats. The exception to this is for the $\alpha S\beta A$ dimer configuration for which one of the repeats exhibits significantly reduced X-ray scattering. The reason for this is not clear and the dipole moment plot for this simulation does not show any more or less disorder than the other two repeats.

Figure 4.22j shows experimental X-ray scattering data for dried chlorosomes. The key features of the X-ray scattering curve are shown. A significant peak at 0.3 \AA^{-1} corresponds to a lattice spacing of 20.9 \AA and the (001) lattice plane. Psencik et al.³⁵ attribute this peak to the inter-lamellar spacing. Three peaks are present in the $0.5 - 0.8 \text{ \AA}^{-1}$ region at 0.54 , 0.67 , and 0.76 \AA^{-1} . These peaks correspond to lattice spacings and planes of 11.7 \AA (010), 9.4 \AA (100), and 8.2 \AA (110). A final broad peak at 1.4 \AA^{-1} is present. This peak is attributed to short range interactions including chlorin ring stacking.

The lamellar peak at 0.3 \AA^{-1} is absent in all cases for predicted X-ray scattering curves. This can be explained by the presence of only a single layer of pigments in the simulations.

The two lowest energy systems $\beta S\alpha Ag$ and $\beta S\alpha Au$ do not exhibit the expected peaks in the $0.5-0.8 \text{ \AA}^{-1}$ region. $\beta S\alpha Ag$ and its two repeats exhibited peaks at ~ 0.57 , ~ 0.80 , and $\sim 0.95 \text{ \AA}^{-1}$. These peaks correspond to ~ 11.0 , ~ 7.9 , and $\sim 6.6 \text{ \AA}^{-1}$, indicating denser packing than that observed experimentally. $\beta S\alpha Au$ and $\beta S\alpha Au_2$ exhibit peaks at ~ 0.43 , ~ 0.57 , and $\sim 0.86 \text{ \AA}^{-1}$, corresponding to spacings of ~ 14.6 , ~ 11.0 , and $\sim 7.3 \text{ \AA}^{-1}$. These values differ not only from those observed experimentally but also from those stated above for $\beta S\alpha Ag$. This

suggests the packing of pigments within sheets consisting of the two different but similar dimer configurations differ significantly. Further investigation of this may provide insight into why the $\beta\text{S}\alpha\text{Au}$ dimer motif does not exhibit curvature in triple layer systems. Of the structures, the only simulations which had peaks in this region corresponding to those seen experimentally were $\alpha\text{S}\beta\text{A}_2$ and $\alpha\text{S}\beta\text{Ad}_2$ which both had a strong peak at $\sim 0.76 \text{ \AA}^{-1}$. Additionally, a peak at 0.54 \AA^{-1} was observed for $\alpha\text{S}\beta\text{A}_2$. The significance of this is not clear. Where peaks were observed in this region, they were less pronounced than those shown in Figure 4.22j. It should however be noted that prominent peaks are also absent in the X-ray scattering patterns for chlorosomes of certain species, i.e. *Chlorobaculum phaeobacteroides*.³⁸ Chlorosomes of these species typically exhibit greater disorder. Consequently, the lower prominence, and in some cases absence, of peaks in the predicted patterns could be indicative of greater disorder.

This discrepancy between predicted X-ray scattering for simulated structures and that observed experimentally can most likely be ascribed to the fact that calculated curves are based single layer structures whereas multilamellar structures are believed to exist within chlorosomes. Consequently, further X-ray scattering predictions are required for triple layer systems. The increase in the number of scattering centres for triple layer systems combined with the fact that the brute force algorithm employed here scales with the square of the system size, means this will likely necessitate the modification of the script to incorporate a Monte-Carlo sampling method.

All simulations except for those of $\alpha\text{A}\alpha\text{A}$ (Figure 4.22a) exhibited a peak at $\sim 1.6 \text{ \AA}^{-1}$ corresponding to a spacing of 3.9 \AA . This peak corresponds to the peak observed experimentally at 1.4 \AA^{-1} for dried chlorosomes. The smaller spacing observed for short range interactions the absence of solvent or additional components (e.g. inter-digitating carotenoid pigments) in simulated structures. The simulated peak is far sharper than that observed experimentally, indicating a smaller degree of disorder in simulated structures compared to chlorosomes. In addition, as the predicted X-ray scattering curves correspond to single layer systems. As a consequence, these sheets are not affected by tails of pigments from neighbouring sheets which are also

likely to increase the spacing between units as well as, due to their high flexibility, increasing disorder.

4.3 Multilamellar systems

Following the simulation of single sheet systems, triple layer systems were investigated. It was hoped that these simulations would more accurately represent the lamellar structure believed to be found within chlorosomes. Furthermore, by having a central sheet of pigments which was surrounded on both sides by another layer of pigments, it was hoped that conclusions could be drawn on the role of stabilising effects in *in vivo* and *in vitro* aggregates.

4.3.1 Structures from simulation

Figure 4.23 shows RMS pair-wise separation plots for Mg atoms in each simulation. As with the single layer structure, there is a sharp initial decrease in Mg atom spacing. This decrease is larger than that observed for single layers. This is likely due to individual layers moving together at the beginning of the unrestrained simulation. Another difference between these RMS pair-wise separation plots and those for single layer structures is the smaller variation in RMS pair-wise separation for a given dimer configuration. This may be explained by motion and available structures being more restricted in triple layer systems due to pigments having less space to move around. As with the single layer structures, a more detailed description of final simulation structures is given below.

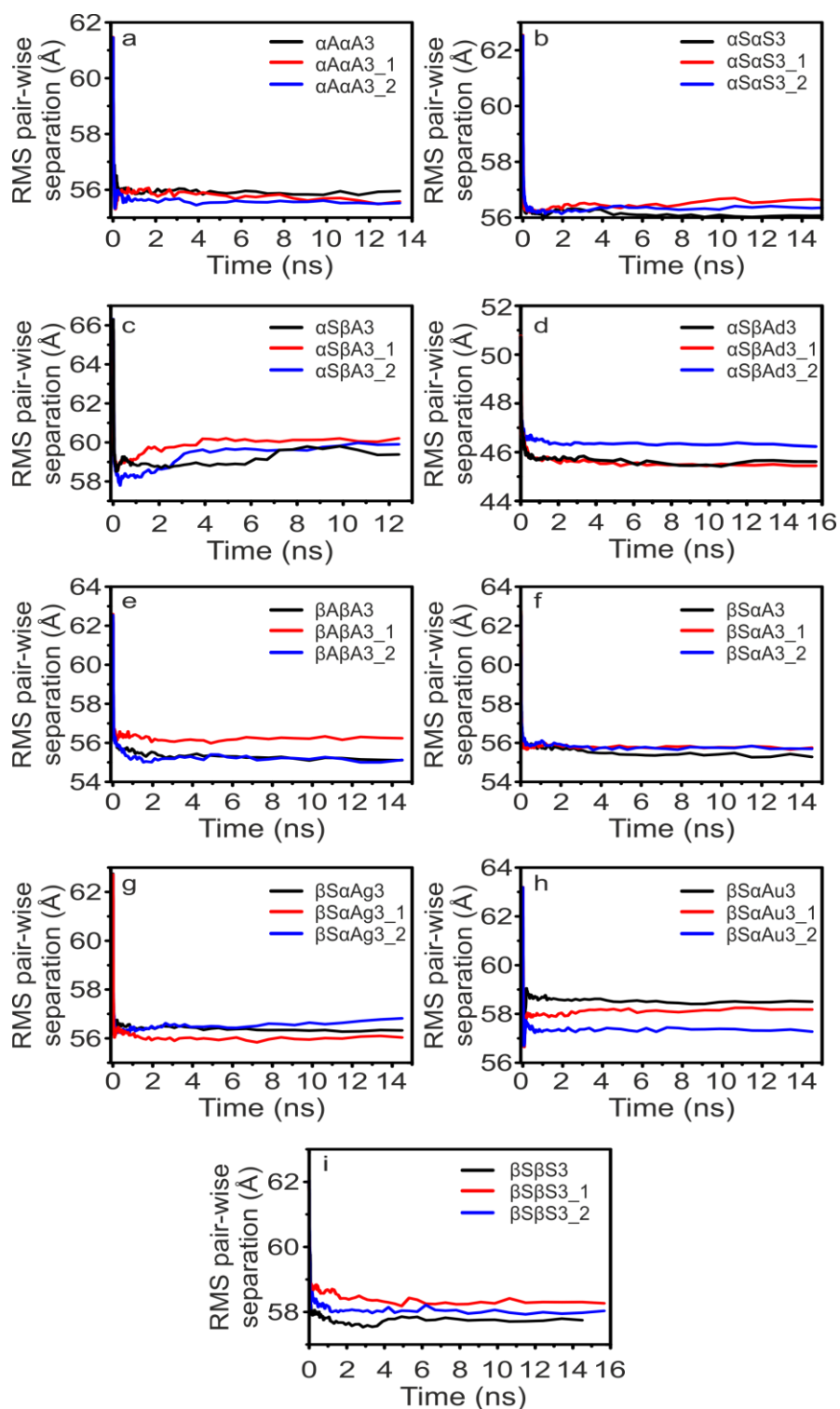


Figure 4.23 RMS pair-wise separation of Mg atoms for single layer pigment systems.

Change in RMS separation of Mg atoms with time for simulations based on (a) $\alpha A\alpha A$, (b) αSaS , (c) $\alpha S\beta A$, (d) $\alpha S\beta Ad$, (e) $\beta A\beta A$, (f) βSaA , (g) $\beta SaAg$, (h) $\beta SaAu$, and (i) $\beta S\beta S$ dimer configurations and their repeats.

$\alpha A\alpha A3$: Both $\alpha A\alpha A3$ and $\alpha A\alpha A3_2$ showed slight curvature whereas no discernible curvature was observed for $\alpha A\alpha A3_1$ (Figure 4.24). This contrasts with single layer simulations of the $\alpha A\alpha A$ dimer configuration in which two out of the three repeats curved substantially. A possible explanation is that the presence of additional layers reduced the amount of space each layer has to curve and suggests that curvature may take place on a single layer level rather than as a group of layers all curving together. In all cases, sheets, and the spaced between sheets, contracted substantially early in the simulation – consistent with observations for Mg atom RMS pair-wise separation. As with single layer simulations of this dimer configuration, a degree of disorder is present in the dipole moment plots (Figure 4.25).

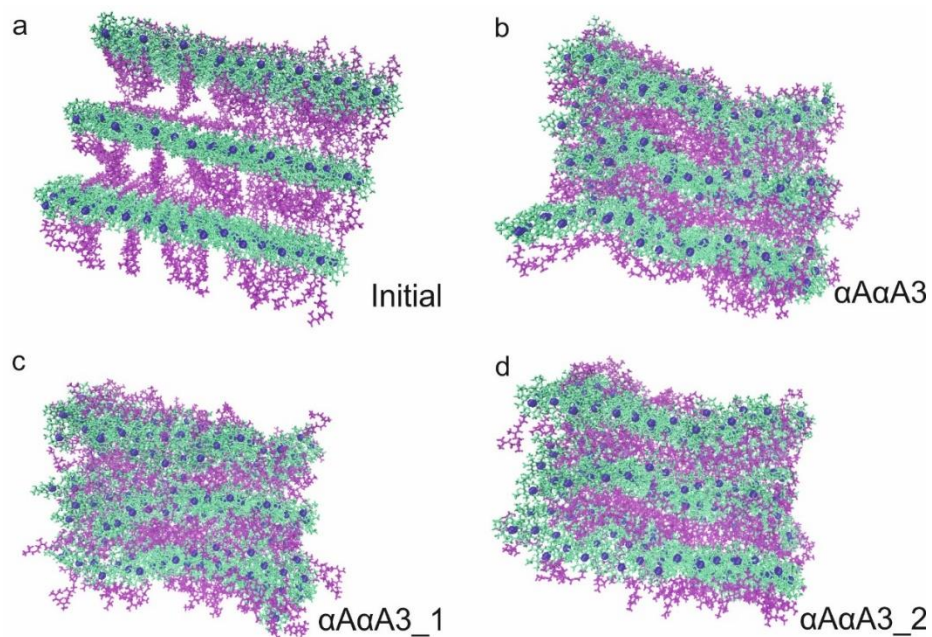


Figure 4.24 Initial and final structures for simulations on triple layer systems formed using the $\alpha A\alpha A$ dimer arrangement.

Edge-on views of (a) the initial starting structure along with the three simulation repeats (b) $\alpha A\alpha A3$, (c) $\alpha A\alpha A3_1$, and (d) $\alpha A\alpha A3_2$.

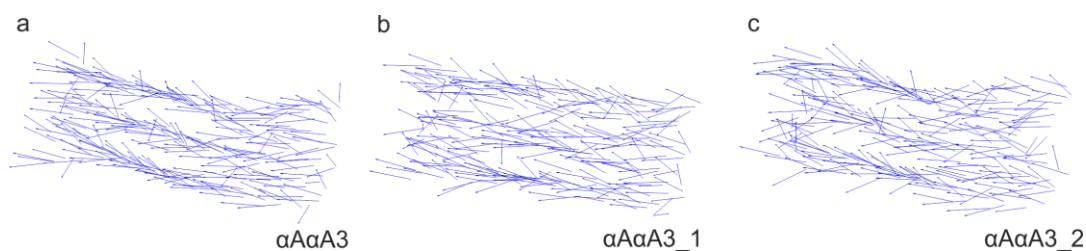


Figure 4.25 Q_y dipole moments for sheets formed using the $\alpha A\alpha A$ dimer arrangement.

Edge-on views of the arrangement of the Q_y dipole moments, shown as arrows, for the final structures of simulations (a) $\alpha A\alpha A3$, (b) $\alpha A\alpha A3_1$, and (c) $\alpha A\alpha A3_2$. Arrow indicates the direction of the dipole moment.

$\alpha S\alpha S3$: No curvature was observed for $\alpha S\alpha S3_1$ or $\alpha S\alpha S3_2$. Very slight curvature was observed for $\alpha S\alpha S3$ (Figure 4.26). The space between layers decreased rapidly at the beginning of the simulation however, the contraction of the individual pigment layers was less than that observed for $\alpha A\alpha A3$. Dipole moment plots (Figure 4.27) indicate a high level of order was maintained for this dimer configuration during simulation.

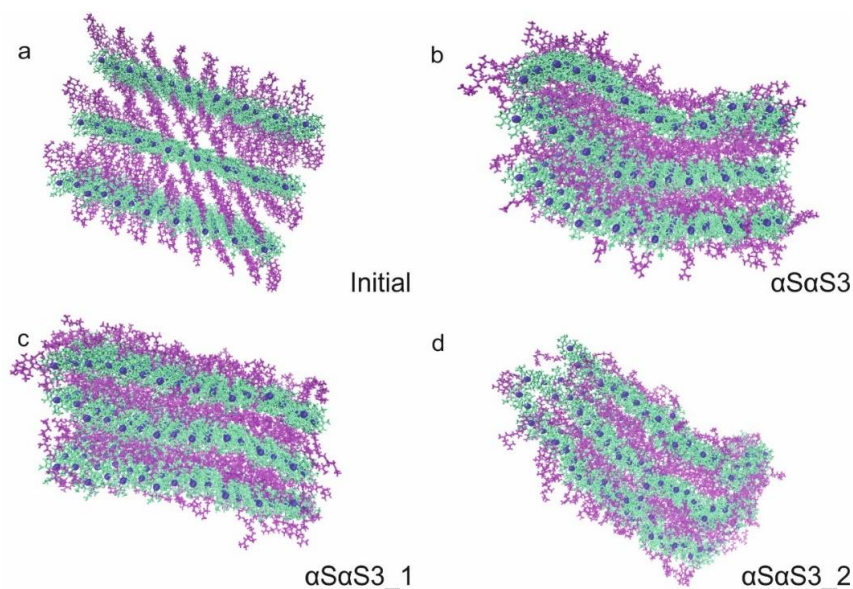


Figure 4.26 Initial and final structures for simulations on triple layer systems formed using the $\alpha S\alpha S$ dimer arrangement.

Edge-on views of (a) the initial starting structure along with the three simulation repeats (b) $\alpha S\alpha S3$, (c) $\alpha S\alpha S3_1$, and (d) $\alpha S\alpha S3_2$.

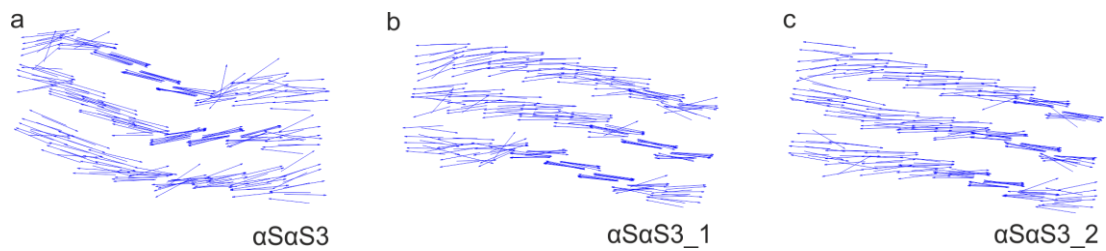


Figure 4.27 Q_y dipole moments for sheets formed using the $\alpha\text{S}\alpha\text{S}$ dimer arrangement.

Edge-on views of the arrangement of the Q_y dipole moments, shown as arrows, for the final structures of simulations (a) $\alpha\text{S}\alpha\text{S}$, (b) $\alpha\text{S}\alpha\text{S}_1$, and (c) $\alpha\text{S}\alpha\text{S}_2$. The direction of the arrow indicates the direction of the dipole moment.

$\alpha\text{S}\beta\text{A3}$: Initially, $\alpha\text{S}\beta\text{A3}$ developed slight curvature which persisted for some time before progressing into more distinct curvature. In the case of $\alpha\text{S}\beta\text{A3}_1$ and $\alpha\text{S}\beta\text{A3}_2$, the system only exhibited mild curvature (Figure 4.28). The existence of an intermediate less curved state for $\alpha\text{S}\beta\text{A}$ is consistent with the change in RMS pair-wise separation of Mg atoms observed for this simulation at ~ 7 ns. The dipole moment plots (Figure 4.29) suggest that initial order is maintained better for this simulation repeat than the other two. This adds further weight to the hypothesis that the preservation of order within the system is required for curvature - at least as far as the $\alpha\text{S}\beta\text{A}$ dimer motif is concerned.

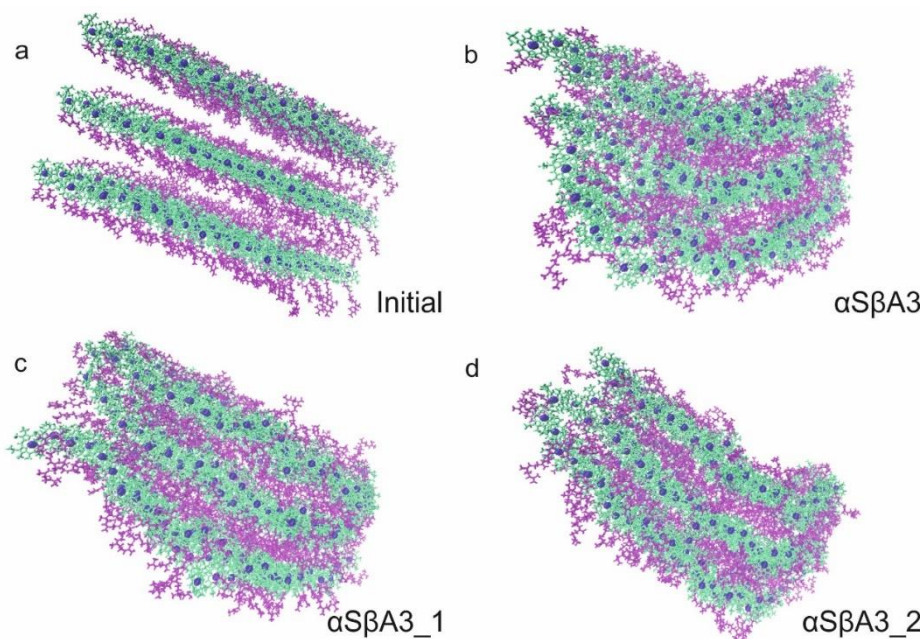


Figure 4.28 Initial and final structures for simulations on triple layer systems formed using the $\alpha\beta A$ dimer arrangement.

Edge-on views of (a) the initial starting structure along with the three simulation repeats (b) $\alpha\beta A_3$, (c) $\alpha\beta A_{3_1}$, and (d) $\alpha\beta A_{3_2}$.

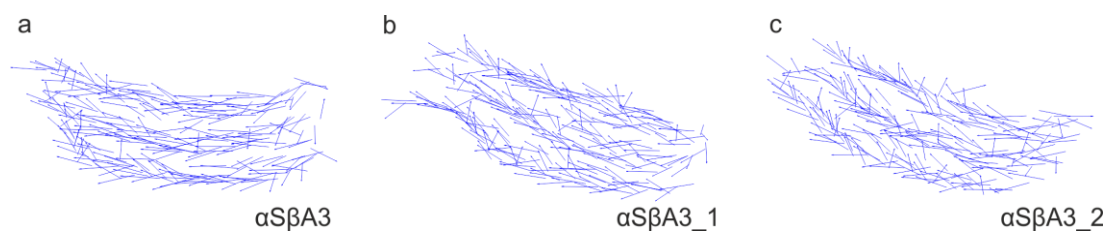


Figure 4.29 Q_y dipole moments for sheets formed using the $\alpha\beta A$ dimer arrangement.

Edge-on views of the arrangement of the Q_y dipole moments, shown as arrows, for the final structure of simulations (a) $\alpha\beta A$, (b) $\alpha\beta A_{3_1}$, and (c) $\alpha\beta A_{3_2}$. The direction of the arrow indicates the direction of the dipole moment.

$\alpha\beta\text{Ad3}$: Neither $\alpha\beta\text{Ad3_1}$ nor $\alpha\beta\text{Ad3_2}$ curved significantly, however $\beta\text{Ad3_1}$ showed a “defect” type anomaly on one layer with a highly local bend of approximately 90 degrees (Figure 4.30). In addition, $\alpha\beta\text{Ad3_2}$ showed some bending localised to sheet edges. These two observations may be ascribed to the highly anisotropic nature of the sheets which, unlike all other dimer configurations, resemble rhombuses rather than rectangles. $\alpha\beta\text{Ad3}$ showed significant curvature which none of the single layer simulations did. The reason for this remains unclear, however, the curved structure also appears to be the most ordered as shown in dipole moment plots (Figure 4.31).

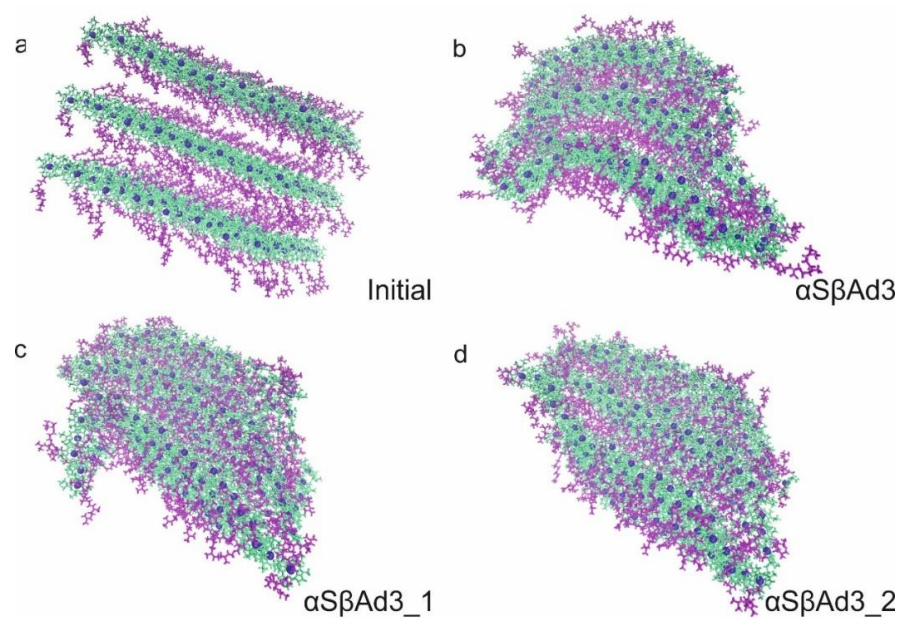


Figure 4.30 Initial and final structures for simulations on triple layer systems formed using the $\alpha\beta\text{Ad}$ dimer arrangement.

Edge-on views of (a) the initial starting structure along with the three simulation repeats (b) $\alpha\beta\text{Ad3}$, (c) $\alpha\beta\text{Ad3_1}$, and (d) $\alpha\beta\text{Ad3_2}$.



Figure 4.31 Q_y dipole moments for sheets formed using the $\alpha S\beta Ad3$ dimer arrangement.

Edge-on views of the arrangement of the Q_y dipole moments, shown as arrows, for the final structures of simulations (a) $\alpha S\beta Ad3$, (b) $\alpha S\beta Ad3_1$, and (c) $\alpha S\beta Ad3_2$. Arrow indicates the direction of the dipole moment.

$\beta A\beta A3$: In the case of $\beta A\beta A$, as with single layer simulations, curvature was observed for all three repeats (Figure 4.32). Curvature took place in the same direction for all repeats and corresponds to the direction of curvature observe for single sheets. As with $\beta A\beta A$ single layer systems, dipole moment plots for this structure look very different to those observed for other dimer configurations with dimers appearing to remain stacked and twist together as columns to provide curvature (Figure 4.33).

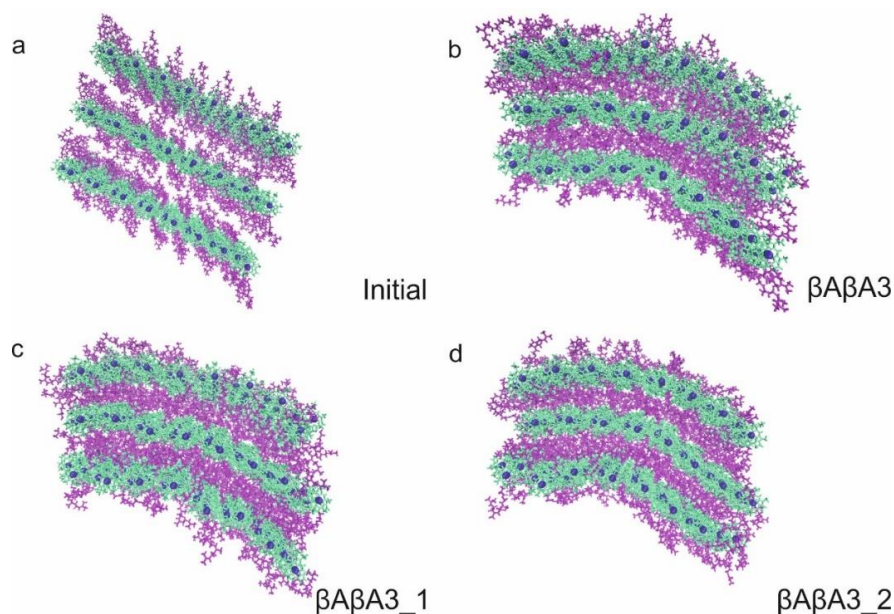


Figure 4.32 Initial and final structures for simulations on triple layer systems formed using the $\beta A \beta A$ dimer arrangement.

Edge-on views of (a) the initial starting structure along with the three simulation repeats (b) $\beta A \beta A_3$, (c) $\beta A \beta A_{3_1}$, and (d) $\beta A \beta A_{3_2}$.

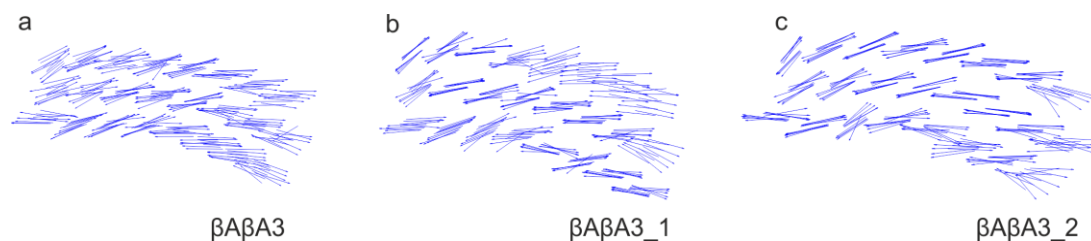


Figure 4.33 Q_y dipole moments for sheets formed using the $\beta A \beta A$ dimer arrangement.

Edge-on views of the arrangement of the Q_y dipole moments, shown as arrows, for the final structures of simulations (a) $\beta A \beta A_3$, (b) $\beta A \beta A_{3_1}$, and (c) $\beta A \beta A_{3_2}$. The direction of the arrow indicates the direction of the dipole moment.

β S α A3: For triple layers of the β S α A dimer system (Figure 4.34), all repeats exhibited unambiguous curvature in the same direction as that observed for single layer simulations on β S α A. In addition, a high level of order is apparent in the dipole moment plots (Figure 4.35).

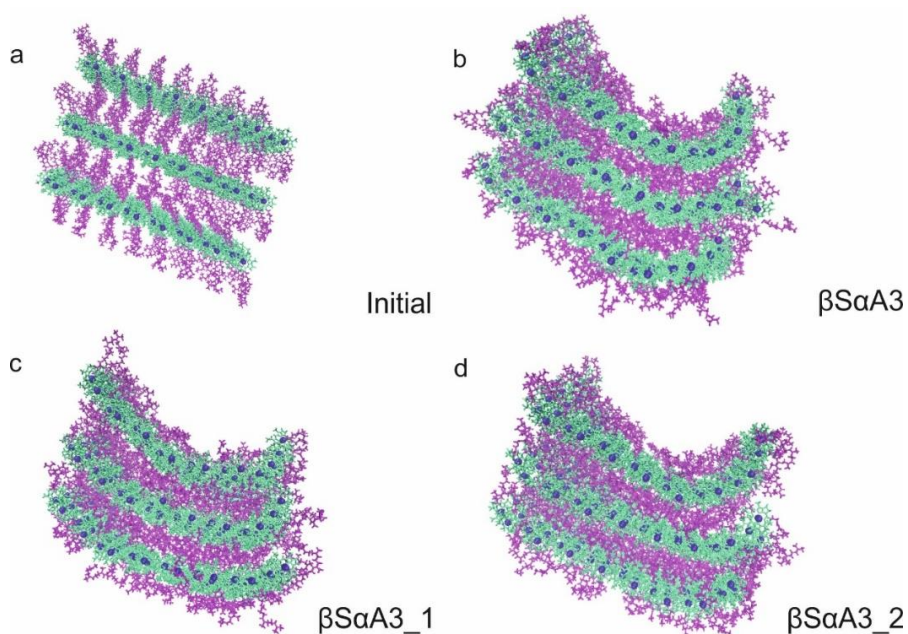


Figure 4.34 Initial and final structures for simulations on triple layer systems formed using the β S α A dimer arrangement.

Edge-on views of (a) the initial starting structure along with the three simulation repeats (b) β S α A3, (c) β S α A3_1, and (d) β S α A3_2.

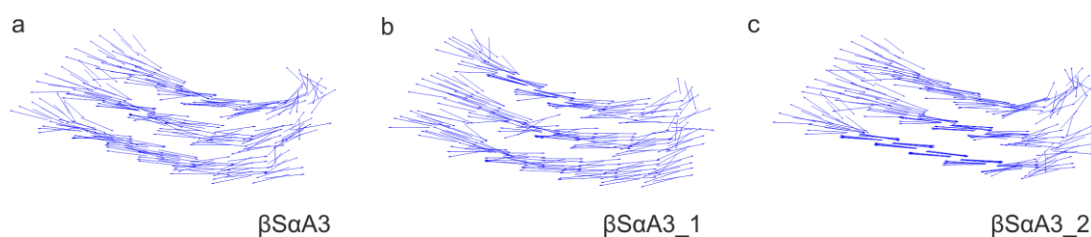


Figure 4.35 Q_y dipole moments for sheets formed using the β S α A dimer arrangement.

Edge-on views of the arrangement of the Q_y dipole moments, shown as arrows, for the final structures of simulations (a) β S α A3, (b) β S α A3_1, and (c) β S α A3_2. Arrow indicates the direction of the dipole moment.

β SaAg3: As with the β SaA systems, simulations on the Ganapthy³² optimised arrangement, β SaAg triple layers all lead to curved systems with curvature taking place in the same direction (Figure 4.36). In addition, some helical twisting of the sheets was apparent both in simulation movies and in the dipole moment plots (Figure 4.37).

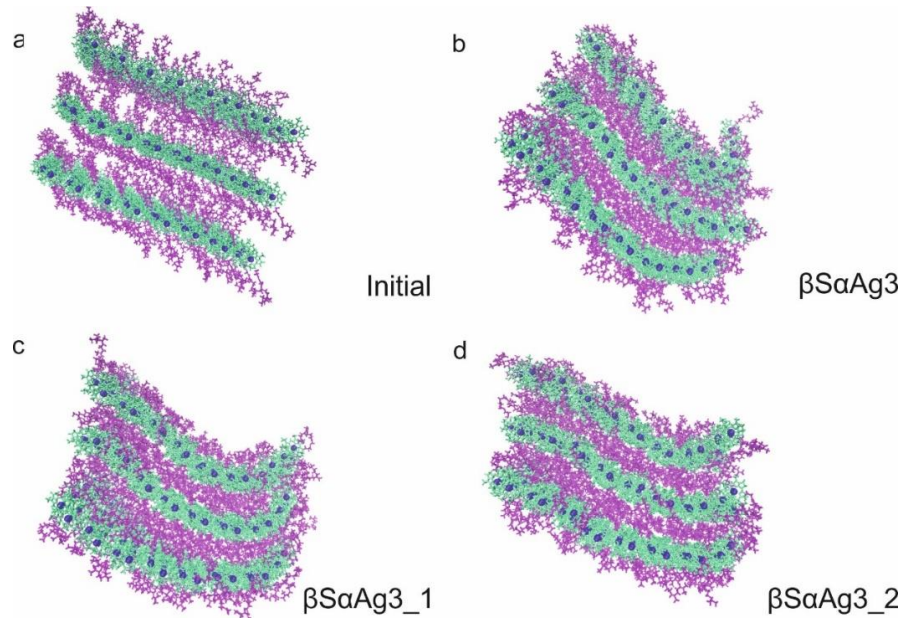


Figure 4.36 Initial and final structures for simulations on triple layer systems formed using the β SaAg dimer arrangement.

Edge-on views of (a) the initial starting structure along with the three simulation repeats (b) β SaAg3, (c) β SaAg3_1, and (d) β SaAg3_2.

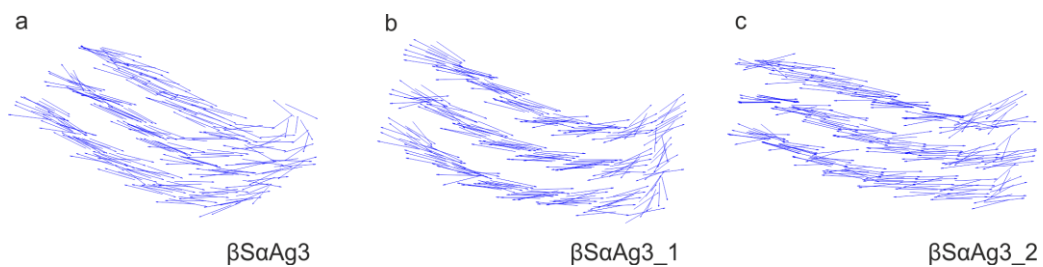


Figure 4.37 Q_y dipole moments for sheets formed using the β SaAg dimer arrangement.

Edge-on views of the arrangement of the Q_y dipole moments, shown as arrows, for the final structure of simulations (a) β SaAg3, (b) β SaAg3_1, and (c) β SaAg3_2. Arrow indicates the direction of the dipole moment.

β SaAu3: Little to no curvature was observed for triple layer systems composed of the X-ray optimised β SaAu dimer arrangement (Figure 4.38). However, some twisting of the sheets was observed. A reasonable degree of dipole moment disorder was apparent in these structures (Figure 4.39).

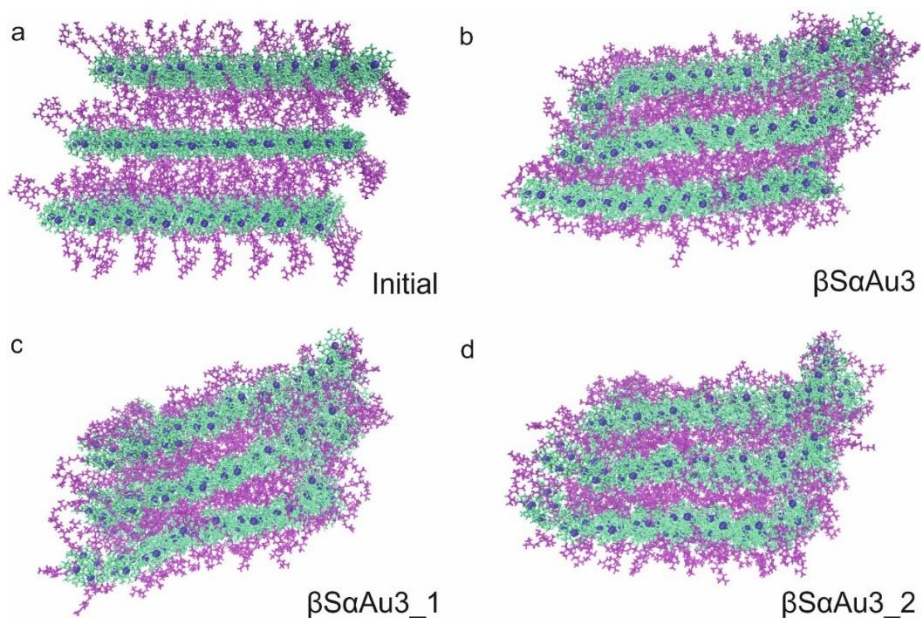


Figure 4.38 Initial and final structures for simulations on triple layer systems formed using the β SaAu dimer arrangement.

Edge-on views of (a) the initial starting structure along with the three simulation repeats (b) β SaAu3, (c) β SaAu3_1, and (d) β SaAu3_2.

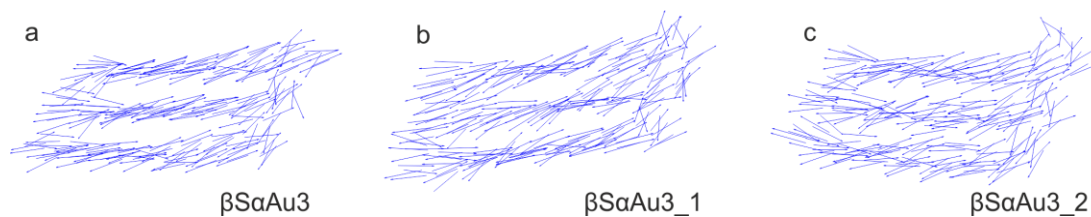


Figure 4.39 Q_y dipole moments for sheets formed using the β SaAu dimer arrangement.

Edge-on views of the arrangement of the Q_y dipole moments, shown as arrows, for the final structures of simulations (a) β SaAu3, (b) β SaAu3_1, and (c) β SaAu3_2. The direction of the arrow indicates the direction of the dipole moment.

$\beta S\beta S3$: Triple layer sheets formed of the $\beta S\beta S$ dimer arrangement (Figure 4.40) did not show any curvature however some slight twisting was observed – especially in the case of $\beta S\beta S3_1$. This can most easily be seen in the dipole moment plots (Figure 4.41). These plots also indicate that despite the lack of curvature, a high level of order is maintained during the simulation.

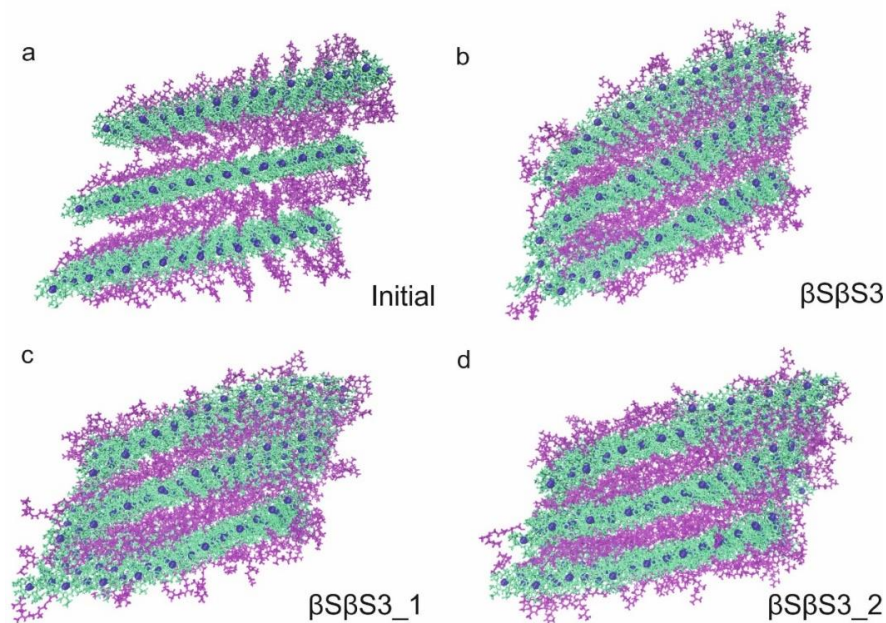


Figure 4.40 Initial and final structures for simulations on triple layer systems formed using the $\beta S\beta S$ dimer arrangement.

Edge-on views of (a) the initial starting structure along with the three simulation repeats (b) $\beta S\beta S3$, (c) $\beta S\beta S3_1$, and (d) $\beta S\beta S3_2$.

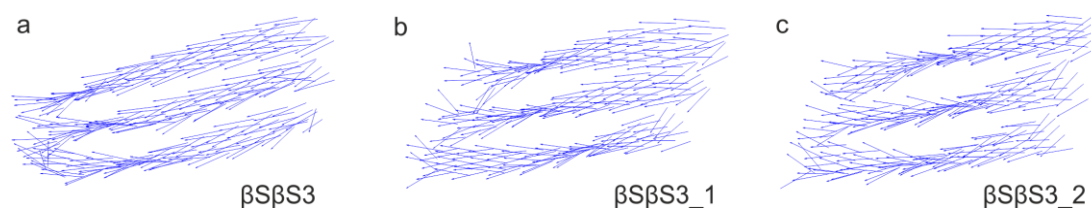


Figure 4.41 Q_y dipole moments for sheets formed using the $\beta S\beta S$ dimer arrangement.

Edge-on views of the arrangement of the Q_y dipole moments, shown as arrows, for the final structure of simulations (a) $\beta S\beta S3$, (b) $\beta S\beta S3_1$, and (c) $\beta S\beta S3_2$. Arrow indicates the direction of the dipole moment.

Summary of physical structures:

In all cases, curvature for triple layer systems was less than that observed for single layer systems. This is most likely due to reduced freedom of movement in larger more densely packed systems. As with the single layer systems, should a particular dimer unit structure exhibit curvature, this takes place always in the same direction for repeats of that configuration as well as that observed for the single layer variant. Providing further evidence that curvature may be dictated by an asymmetry of the dimer unit.

Additionally, there appears to be a link between dipole order and curvature with more curved systems exhibiting greater order. However, the case of $\beta S\beta S$ which shows a high level of disorder but no curvature suggest this may be necessary but not sufficient for curvature to form.

As with single layer simulations, the dipole moment plots for the $\beta A\beta A$ motif differ markedly to those observed for other repeats and appear to indicate either a different form or origin of curvature. The diversity within the dipole moment plots observed for single layers was similarly observed for triple layer systems. The significance of this being that different dipole configurations will lead to different absorbance and circular dichroism (CD) spectral properties which may help identify which of these structures – if any - are present in chlorosomes and *in vitro* aggregates.

4.3.2 Energy of simulated systems

The total system energy as a function of simulation time for simulations of triple layer systems in vacuum is show in Figure 4.42. As with the RMS pair-wise separation plots a rapid decrease in energy is shown at the start of the simulation. Again, as with the RMS pair-wise separation plots less diversity is observed compared with the single layer simulation and in the majority of cases, energy evolved similarly for all repeats of a given dimer configuration. Exceptions to this are for $\alpha S\beta Ad$, $\alpha S\beta Ad3$, and $\beta A\beta A3$ which are explained below.

$\alpha S\beta A3$: The energy trajectories for $\alpha S\beta A3_1$ and $\alpha S\beta A3_2$ remain close to each other throughout their evolution. In contrast total system energy of $\alpha S\beta A$

whilst initially decreasing almost identically to $\alpha\text{S}\beta\text{A3}_1$ and $\alpha\text{S}\beta\text{A3}_2$ spends an extended period in a higher energy state before eventually transition to a lower energy state. This is consistent with the observation of an intermediate slightly curved state which later transitions to a more curved final state. The timescale over which this takes place is consistent with both the observed simulation trajectories and the RMS pair-wise separation plots (Figure 4.23 c).

$\alpha\text{S}\beta\text{Ad3}$: For this dimer configuration, all repeats undergo a rapid decrease in energy, reaching equilibration quickly. However, the final energy of the $\alpha\text{S}\beta\text{Ad}$ repeat – the only one to exhibit curvature – is higher.

$\beta\text{A}\beta\text{A3}$: The energy trajectories for triple layers of this dimer arrangement follow similar trends however, the system energy for the most curved system ($\beta\text{A}\beta\text{A3}_2$) is slightly lower.

The apparent contradiction between the $\alpha\text{S}\beta\text{A}$ and $\beta\text{A}\beta\text{A}$ simulations in which the most curved sheet exhibit both the highest and lowest energy respectively suggest that that whilst curvature may be energetically favourable for a particular dimer arrangement, it may be unfavourable for another. This suggests that there may not necessarily be a straightforward connection between curvature and overall system energy.

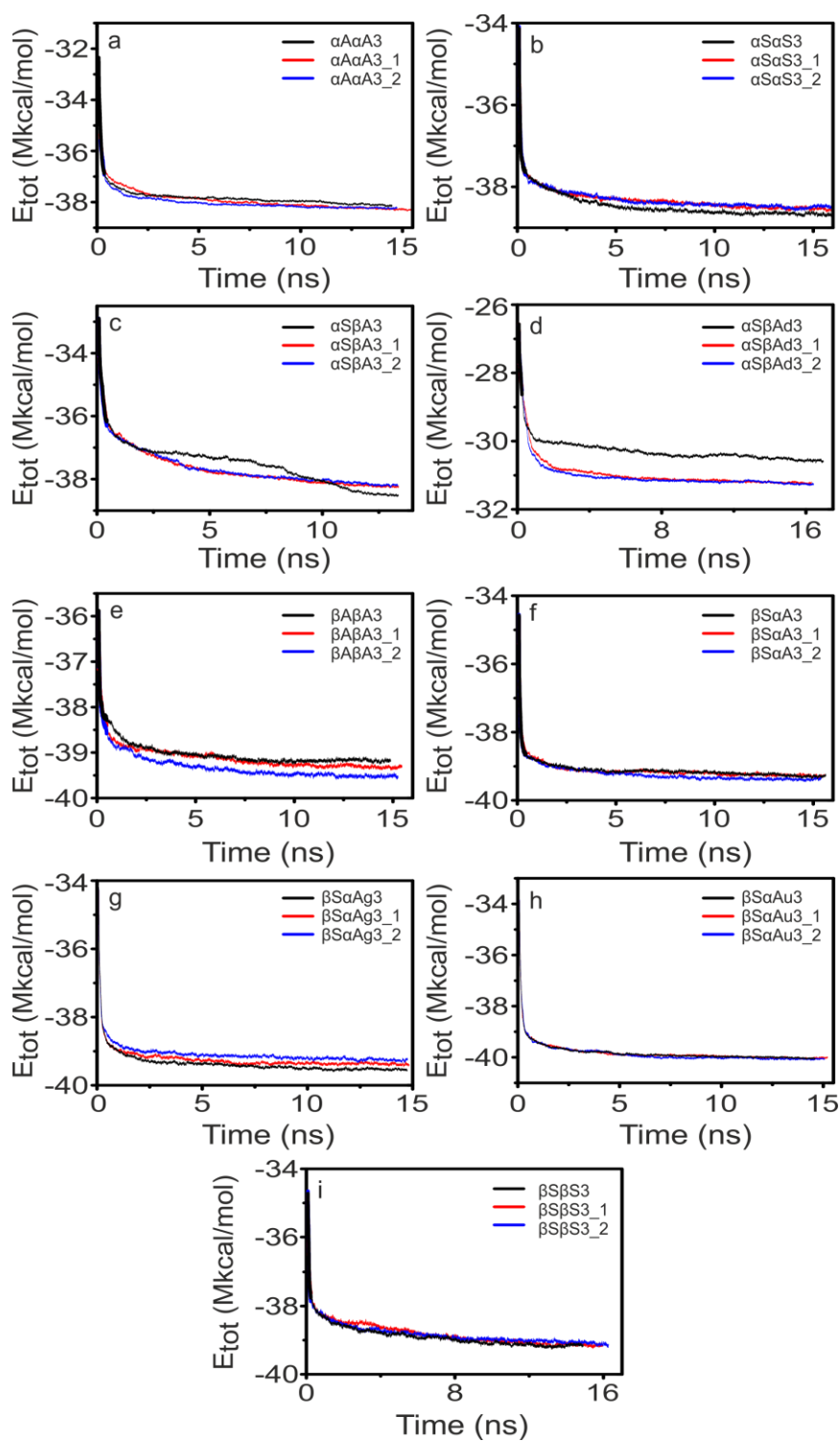


Figure 4.42 Energy evolution for the simulation of triple layer pigment systems.

Total system energy as a function of time for simulations of triple layers based on (a) $\alpha\text{A}\alpha\text{A}$, (b) $\alpha\text{S}\alpha\text{S}$, (c) $\alpha\text{S}\beta\text{A}$, (d) $\alpha\text{S}\beta\text{Ad}$, (e) $\beta\text{A}\beta\text{A}$, (f) $\beta\text{S}\alpha\text{A}$, (g) $\beta\text{S}\alpha\text{Ag}$, (h) $\beta\text{S}\alpha\text{Au}$, and (i) $\beta\text{S}\beta\text{S}$ dimer configurations and their repeats.

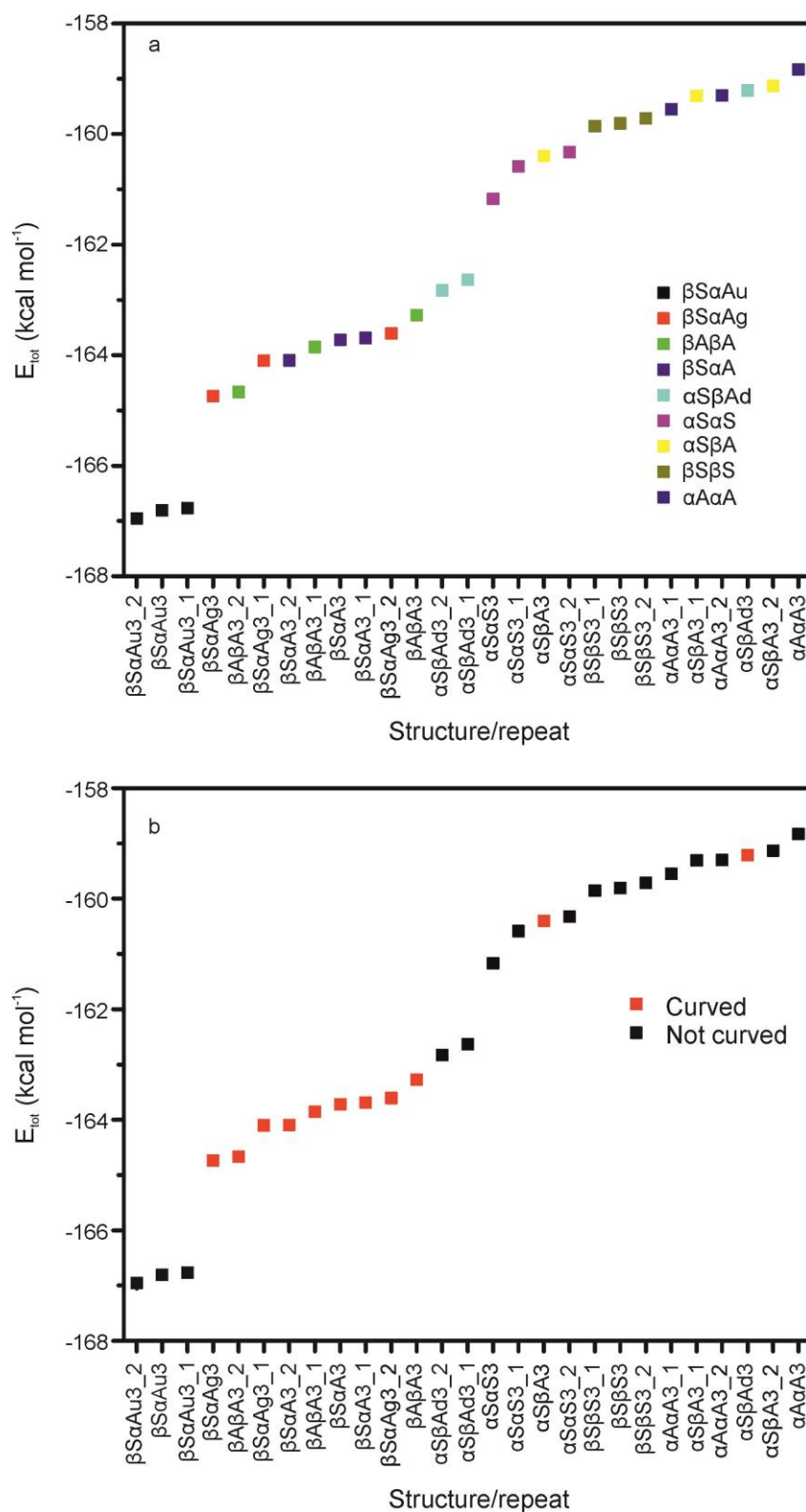


Figure 4.43 Final energy per dimer of triple layer systems.

Final E_{Tot} /dimer of multilamellar systems averaged over the last 1 ns colour coded according to (a) dimer arrangement and (b) curvature.

Figure 4.43a shows the final system energy averaged over the final 1 ns colour coded by dimer configuration. Again, energy is presented per dimer to allow comparison with the $\alpha\beta$ Ad sheets which contain a smaller number of dimers. As with the single sheet simulations, the antiparallel dimer arrangement appears to be the energetically favourable arrangement. It can be seen that of the majority lowest energy states, correspond to the $\beta\text{S}\alpha\text{A}$, $\beta\text{S}\alpha\text{Ag}$, and $\beta\text{S}\alpha\text{Au}$ dimer arrangements with the $\beta\text{S}\alpha\text{Au}$ arrangement, again, having the lowest energy.

Figure 4.43b shows the average final system energy colour coded according to curvature. Despite the inconsistency mentioned above, like the single layer simulations, the lowest energy triple layer systems generally exhibit curvature. The exception to this is the $\beta\text{S}\alpha\text{Au}$ motif which had the three lowest energies but did not curve.

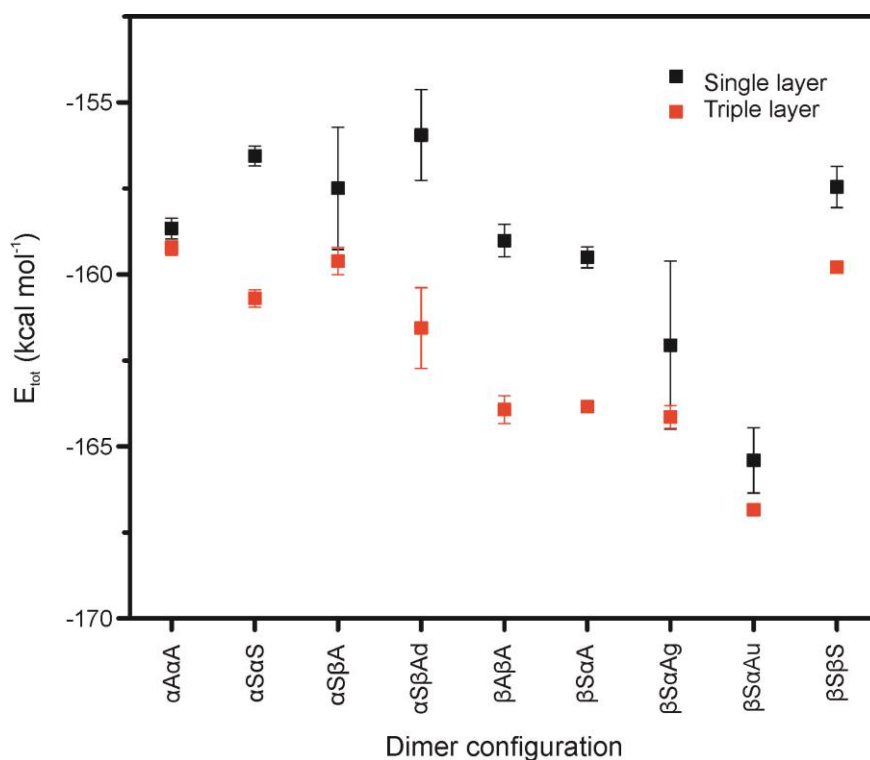


Figure 4.44 Energy stabilisation for triple layer systems.

Final E_{Tot} /dimer averages for each dimer configuration for single layer (black) and triple layer (red). Error bars = standard error.

Figure 4.44 shows final E_{Tot} averages over each dimer configuration for both single and triple layers. In all cases the energy for the triple layer systems is lower than for its single layer equivalent. This suggests that there is a stabilising effect from having additional layers/molecules. This effect was found to range between 0.56 ± 0.01 and 5.61 ± 0.06 kcal/mol depending on dimer configuration.

4.4 Conclusions and future directions

RMS pair-wise separation plots for Mg atom separation indicated that the prepared dimer sheets undergo rapid contraction and generally reach an equilibrium state within a couple of nanoseconds. In addition to investigating the displacement of Mg atoms, future work may investigate the separation of key groups within individual dimers, e.g. the length of the Mg-OH coordination bond. This may provide new information including whether or not initial spacings for optimised dimer units persist during simulation. This may be particularly relevant for the similar β SaA, β SaAg, and β SaAu arrangements where configurations differ from each other only in the separations of pigments and the molecular contacts within dimers.

For both single layer and triple layer systems, a variety of structures were observed. In some cases, different structures were seen for repeats of the same dimer configuration. In addition, for some dimer configurations simulations indicated the existence of long-lived intermediate states. A number of systems exhibited significant curvature with the β SaA and β SaAu configurations curving most strongly in both the single layer and triple layer simulations. In all cases, a higher degree of curvature was observed in single layer systems. The formation of wrapped helical-tube like structures together with overlapping and stacking of the dimers/dipole moments was only observed for single layer structures. The lower degree of curvature for multilamellar systems is most likely due to reduced freedom of movement in larger, more densely packed systems. This appears to contradict the observation of highly curved multilamellar structures in EM images in some chlorosomes. One possible explanation is a step-wise formation of curved

regions from single sheets with additional layers curving around the initial cylinder.

It was observed for both single and triple layer systems that, should a particular dimer unit structure exhibit curvature, this always takes place in the same direction for all repeats. As the chemical structure of pigments is the same in all simulated cases, this suggests that curvature may be dictated by an asymmetry of the dimer unit.

In this thesis, curvature has been assessed by visual means only. In order to draw more concrete conclusions about the role of curvature it will be necessary to find a means of mathematically describing and assessing the extent of this curvature.

A correlation between dipole order and curvature was observed with more curved systems exhibiting greater order. However, the case of $\beta S\beta S$ which shows a high level of disorder but no curvature suggest this may be necessary but not sufficient for curvature to form. The dipole moment plots for both the single and triple layer simulations on the $\beta A\beta A$ motif differ markedly to those observed for other repeats and appear to indicate either a different form or origin of curvature. It is expected that the large variation in the appearance of dipole moment arrangement presented here will lead to different CD and absorbance properties. Consequently, future work should include prediction of CD and absorbance properties for these simulation structures. This will offer an additional means of comparing simulation work to experimentally observed structures and may provide a means of determining which structures are likely to be present in chlorosomes and in *in vitro* aggregates.

Time resolved system energy plots for the simulations revealed an initial rapid decrease in energy on a time scale identical to that observed for the decrease in RMS pair-wise separation Mg atom separation. This suggests that the decrease in energy may be due to contraction of pigment assemblies into more favourable densely packed systems. Examination of the final energy per dimer of systems indicated that the X-ray unit cell optimised $\beta S\alpha Au$ dimer motif may be the most energetically favourable for both single and triple layer systems. This was followed by the similar $\beta S\alpha A$ and $\beta S\alpha Ag$ motifs.

In the majority of cases, the lowest energy systems generally exhibited curvature. The exception to this is the $\beta\text{S}\alpha\text{Au}$ motif which had the three lowest energies but did not curve. This apparent conflict could be explained by the existence of two phases within chlorosomes with $\beta\text{S}\alpha\text{Au}$ dimer motif forming the flat sections and $\beta\text{S}\alpha\text{Ag}$ forming the curved sections. Some evidence for the existence of both flat and curved regions has been seen in wild type chlorosomes.⁵

Further work is required to determine conclusively whether a link between lower energy states and curvature exists and if so, why the $\beta\text{S}\alpha\text{Au}$ dimer motif is an exception. In addition, it should be possible, by examining the evolution of individual energy components, including electrostatic and van der Waals contributions to gain a more comprehensive picture of the energetics of sheet curvature.

A significant energy stabilisation was observed for triple layer systems compared to their single layer counterparts. Again, a more comprehensive examination of individual energy components should shed light on the origins of this effect. In addition, it should be possible to decompose system energy into individual layers.

X-ray scattering predictions from single layer sheets failed to reproduce the peaks observed for dried chlorosomes. This is most likely due to the presence of a single sheet rather than the multilamellar structure believed to exist in chlorosomes.⁵ Therefore, future work should include the modification of the X-ray scattering script to use a Monte Carlo sampling method to allow the calculation of expected X-ray scattering behaviour for the simulation outputs from triple layer structures.

Finally, it should be noted that the exploratory study undertaken here has resulted in the generation of an extraordinarily large volume of data. The observation of unexpected dimer twisting for the $\beta\text{A}\beta\text{A}$ highlights the potential of data mining this large body of information to enable a more thorough understanding of BChl aggregation as well as to help set the direction of future study.

Chapter 5

Results and Discussion: Synthesis and characterisation of copper indium sulphide quantum dots

5.1 Introduction

This chapter contains results relating to the synthesis and characterisation of copper indium sulphide (CIS) nanoparticles (NPs). Section 5.2 deals with the structure and composition of the synthesised quantum dots (QDs) including size, composition, and crystal phase. Section 5.3 focuses on the optical properties of the quantum dots including: steady state absorbance measurements, steady state photoluminescence (PL) emission, photoluminescence quantum yield (PLQY) measurements, PL lifetime measurements, and transient absorption spectroscopy. In both sections, critical attention is played to the role of synthesis time and consequent nanoparticle size. Furthermore, care is taken to link optical properties of nanoparticles to their composition and structure. Finally, Section 5.4 provides an overview of results presented in this chapter and key conclusions.

5.2 Structure and composition

The dependence of QD size on synthesis time was followed using transmission electron microscopy (TEM). The crystal phase was determined using lattice spacing from high-resolution transmission electron microscope (HR-TEM) imaging and powder X-ray diffraction (XRD). Finally, detailed investigation of NP composition and its dependence on synthesis time was performed using energy dispersive analysis of X-rays (EDX) and X-ray photoelectron spectroscopy (XPS).

5.2.1 Quantum dot synthesis and cleaning

Figure 5.1 shows aliquots of quantum dots taken during synthesis. During synthesis a gradual colour change from colourless to red-orange (left to right), indicating particle nucleation and growth, was observed.

Quantum dots from different aliquots exhibited different levels of colloidal stability. Earlier aliquots were found to be far more stable than later ones which tended to flocculate more quickly. This may be explained by the number of available stabilising thiol ligands being insufficient to fully stabilise larger particles.

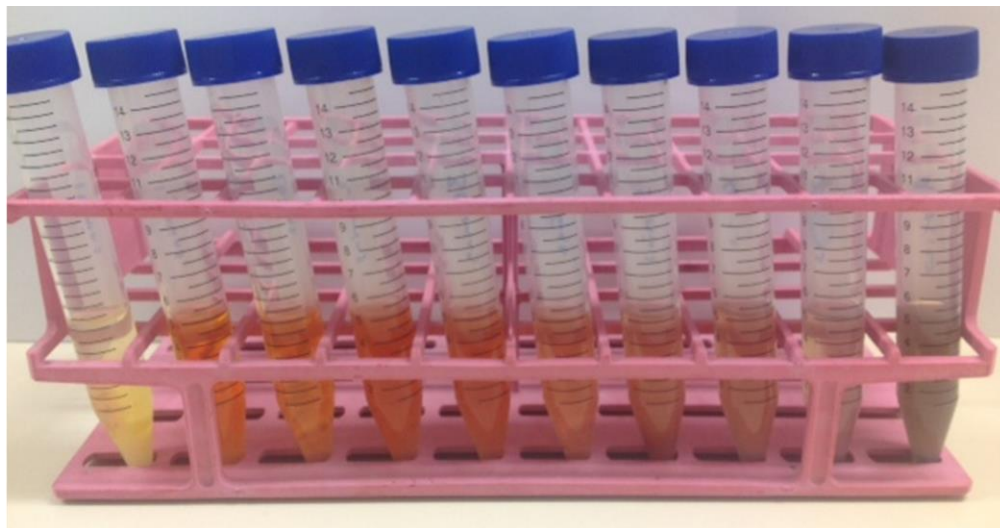


Figure 5.1 Aliquots of quantum dots taken at various synthesis times.

Aliquots of nanoparticles taken at (left to right) 10 min, 15 min, 20 min, 25 min, 30 min, 40 min, 50 min, 60 min, 75 min, and 90 min. A colour change, indicative of increasing nanoparticle size, is observed.

Quantum dots were cleaned using a diafiltration setup in which nanoparticles in methanol were pumped using a peristaltic pump through a dialysis membrane. For effective removal of unreacted product and free thiol with minimum loss of sample, the retentate containing the quantum dots should retain its strong initial colour whilst the permeate remains colourless. This was true for all but the shortest synthesis time aliquots, in which case the permeate was slightly coloured. This is likely due to smaller particles being able to cross the dialysis membrane in higher numbers than the other, larger particle containing aliquots. For synthesis times between 10 and 40 min, the turbidity of the samples decreased after cleaning suggesting the successful removal of unwanted components. For the later aliquots, this was not the case, suggesting the turbidity could be due to particle flocculation.

5.2.2 Transmission electron microscopy

HR-TEM was used to determine the size distribution (diameter) and morphology of nanoparticles. Well-dispersed nanoparticles were observed in low magnification TEM images (Figure 5.2).

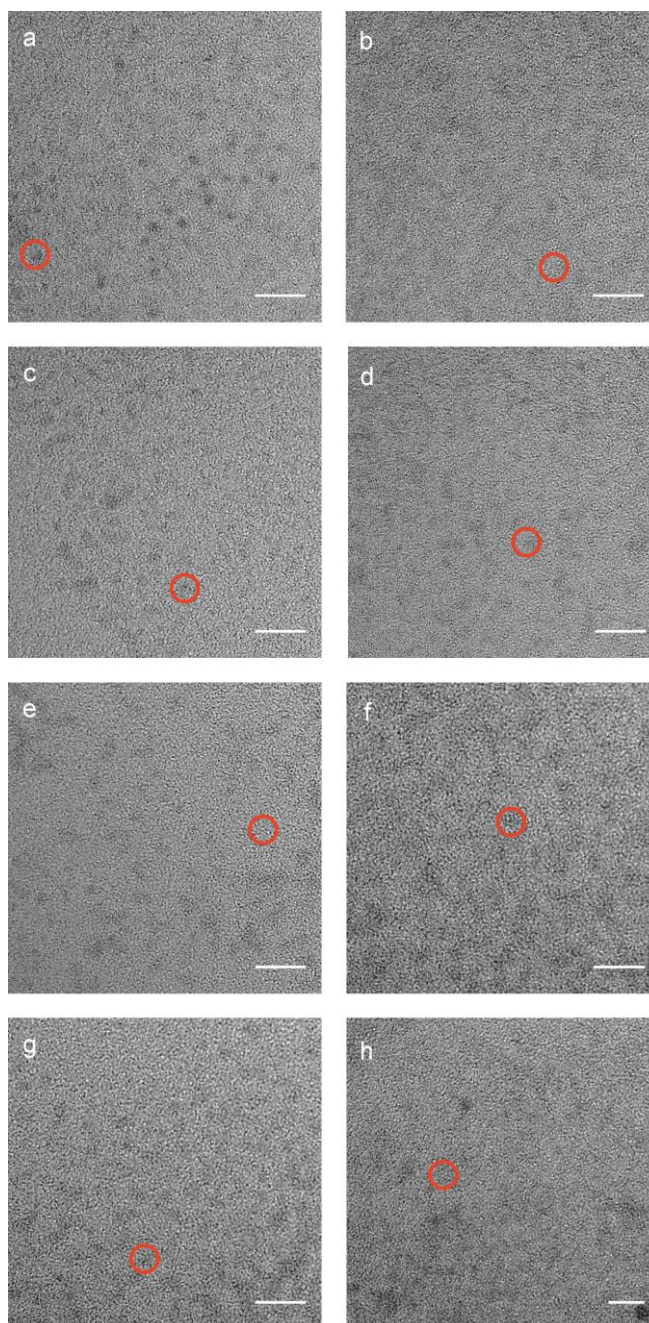


Figure 5.2 TEM images of CIS quantum dots (220 000x magnification).

TEM micrographs of QDs used for sizing of each aliquot (a) 10 min, (b) 15 min, (c) 20 min, (d) 25 min, (e) 30 min, (f) 40 min, (g) 50 min, (h) 60 min. Scale bar = 10 nm.

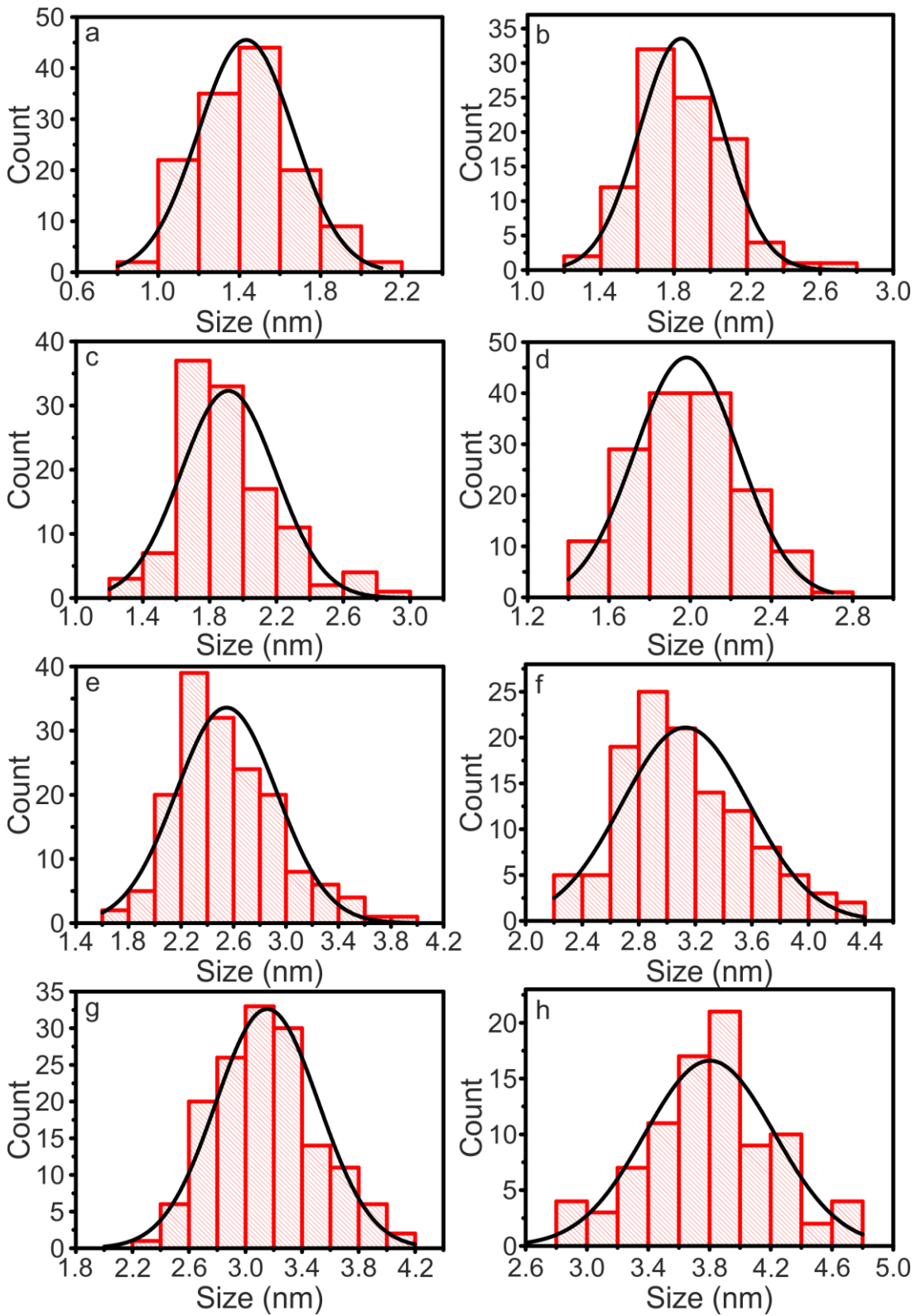


Figure 5.3 Size distribution histograms of quantum dots from TEM images.

Size-distribution histograms for synthesis times (a) 10 min, (b) 15 min, (c) 20 min, (d) 25 min, (e) 30 min, (f) 40 min, (g) 50 min, and (h) 60 min.

Size distributions for each synthesis time were fitted to normal distributions with widths ranging from 0.2 nm to 0.5 nm (Figure 5.3). Nanoparticle size increased with synthesis time from 1.4 ± 0.2 nm (10 min) to 3.8 ± 0.4 nm (60 min) (Figure 5.4 and Table 5.1). This is consistent with the colour change observed during synthesis. The increase in size with synthesis time shown in Figure 5.4 appears to be approximately linear and not of the form expected for Oswald ripening (see Chapter 1). This indicates growth may be taking place by a different mechanism.

Table 5.1 NP size as determined using TEM for each synthesis time.

Time (min)	Size (nm)
10 min	1.4 ± 0.2
15 min	1.8 ± 0.2
20 min	1.9 ± 0.3
25 min	2.0 ± 0.3
30 min	2.6 ± 0.4
40 min	3.1 ± 0.5
50 min	3.2 ± 0.4
60 min	3.8 ± 0.4

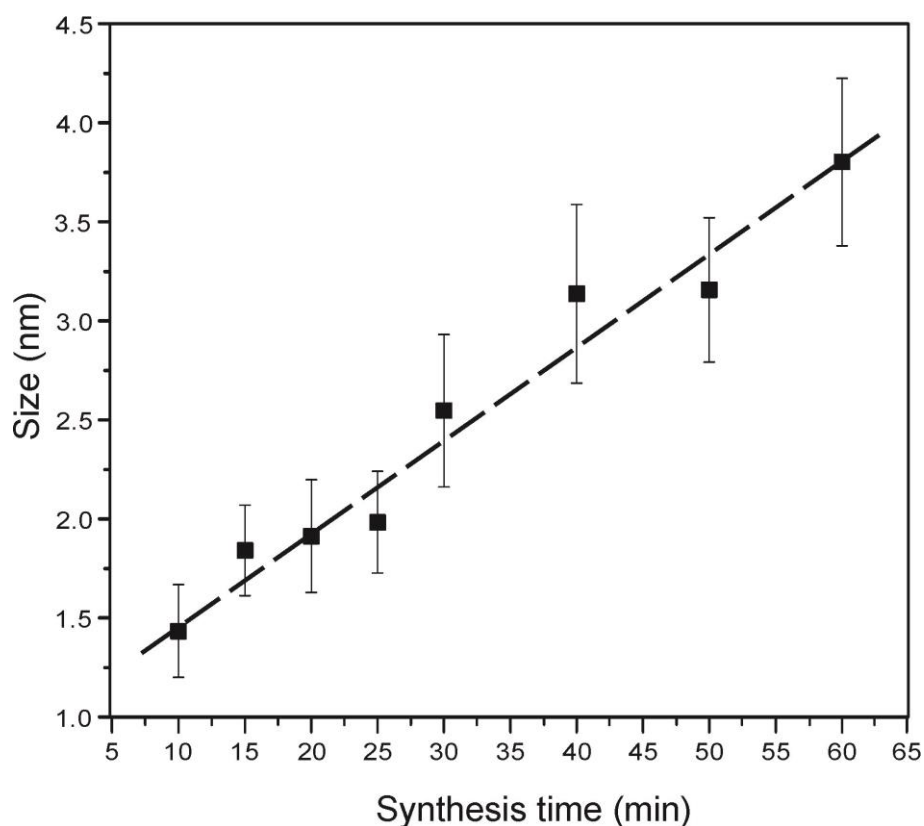


Figure 5.4 Dependence of quantum dot size on synthesis time.

The size of quantum dots increased with increasing synthesis time. Line added as a guide to the eye.

5.2.3 Lattice spacings from high resolution TEM

Higher magnification HR-TEM allowed the imaging of lattice fringes. These lattice fringes are clearly visible in Figure 5.5. Fringe separations determined by line fitting were 0.30 ± 0.01 nm. A Fast Fourier Transform (FFT) method was also used to determine lattice spacing of 0.3 ± 0.1 nm (inset Figure 5.5). These values are consistent with the 112 plane of chalcopyrite CIS.

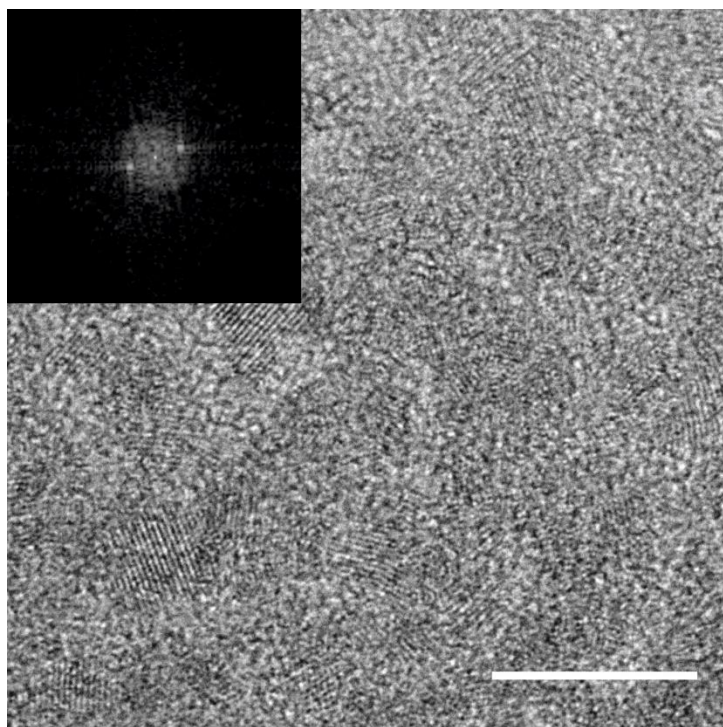


Figure 5.5 Lattice spacings from HR-TEM (690 000x magnification).

Lattice spacings were determined from HR-TEM images both using fringe separations determined from line spacing and using a FFT method applied to individual particles (insert). Scale bar = 5 nm.

5.2.4 X-ray diffraction

Powder XRD pattern (Figure 5.6) for the nanoparticles was consistent with reference data for the tetragonal chalcopyrite CIS phase. The Bragg peaks are consistent with the lattice spacing values obtained from TEM. Consequently, it can be assumed with some certainty that the quantum dots described here are of the same chalcopyrite crystal structure as those prepared using dodecanethiol as a solvent and sulphur source.²¹⁵

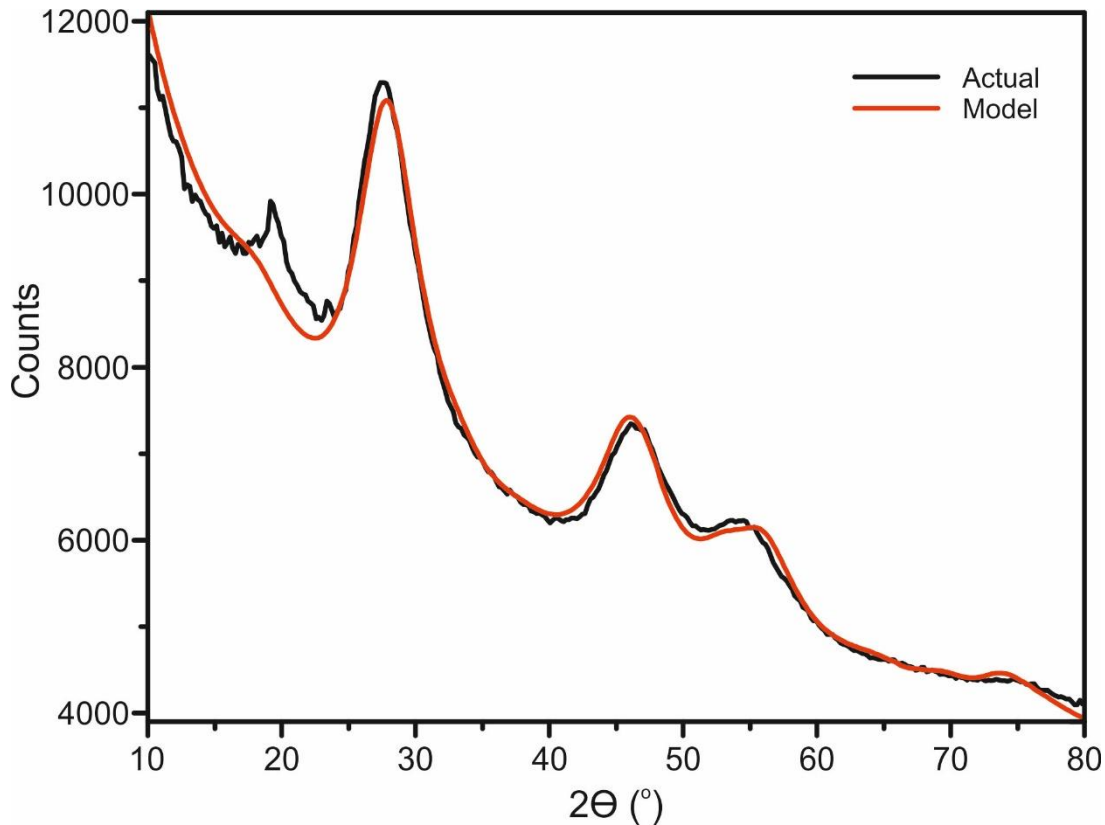


Figure 5.6 Powder XRD pattern of CIS nanoparticles.

XRD pattern for CIS NPs with a synthesis time of 20 min (black line) was in good agreement with reference data for CIS chalcopyrite (red line).

In the absence of strain, the line-broadening, β , of a diffraction peak at angle, θ , is related to the crystalline grain size, D .

$$D = \kappa\beta \cos \theta$$

where κ is a shape factor accounting for the shape of the crystallite. For a tetrahedron the value of κ is approximately 0.9. The wavelength, λ , of the incident X-rays was 0.154 nm. For the XRD data shown in Figure 5.6 the grain size was determined to be 1.8 ± 0.1 nm. This value is consistent (within error) with size determined from TEM for synthesis times of 20 min (1.9 ± 0.3 nm). This suggests that each QD is acting as a single diffracting domain (grain). Smaller grain sizes would indicate greater disorder.

5.2.5 Energy dispersive X-ray analysis

EDX analysis was performed on aliquots of nanoparticles taken between 10 and 60 min. The ratio of copper to indium was determined (Figure 5.7), with the proportion of copper decreasing with increasing size and synthesis time.

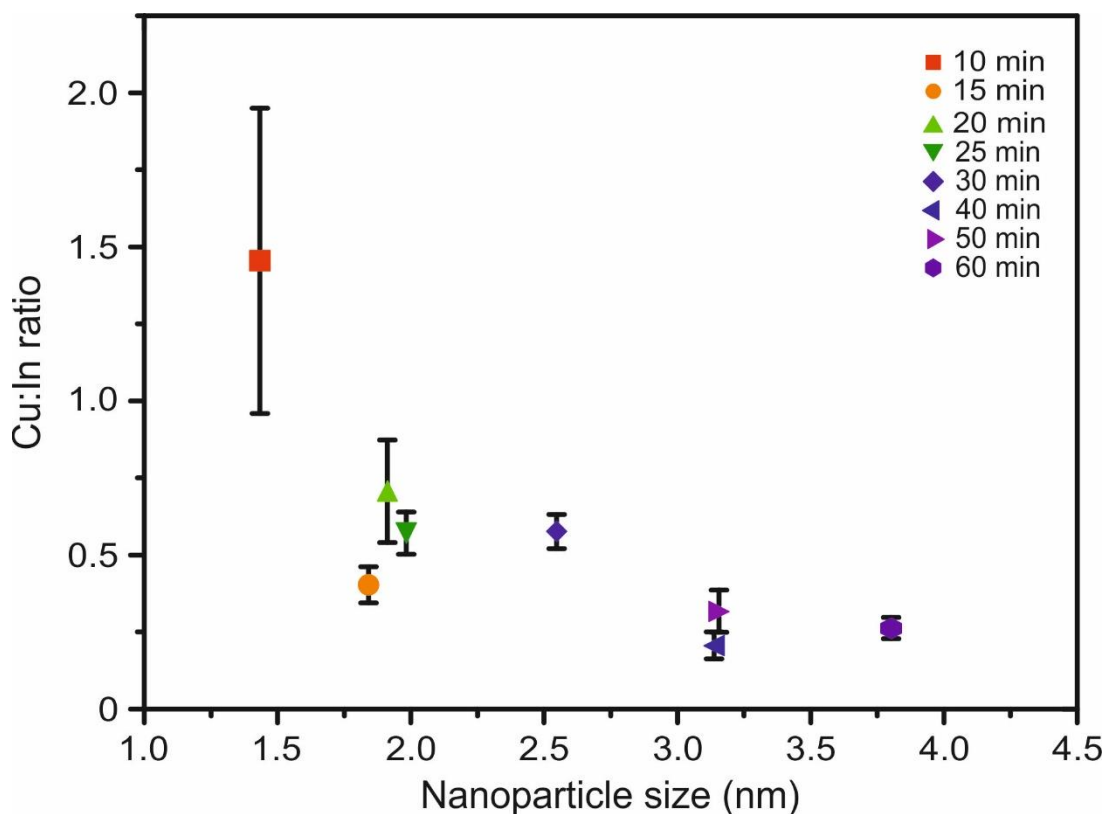


Figure 5.7 Dependence Cu:In ratio on nanoparticle size as determined by EDX analysis.

The ratio of copper to indium was found to decrease with increasing particle size. Despite issues with determining accurate ratios due to high background copper levels, a clear trend is nevertheless present.

5.2.6 X-ray photoelectron spectroscopy

XPS was performed on nanoparticles with synthesis times 10 min – 60 min. The surface sensitivity of XPS makes accurate composition determination difficult. The sampling depth for copper (at an electron energy of 1000 eV) is estimated to be >4.5 nm.²³³ As this is larger than the nanoparticles produced here, it is expected that this should not be too great an issue. Survey spectra

for all sizes are shown in Figure 5.8. The primary elements found were carbon, nitrogen, oxygen, copper, indium, sulphur, and gold. Whilst the presence of copper, indium, sulphur, carbon, oxygen, and nitrogen may be attributed to the CIS nanoparticles, it should be noted that carbon, oxygen, and nitrogen are also likely present as contaminants. The gold detected is from the gold layer on the coated microscope slide.

The individual Cu 2p, In 3d, and S 2p profiles of the CIS quantum dots are shown in Figure 5.9 for each size of nanoparticle. Atomic ratios of copper and indium are shown in Table 5.2. Figure 5.10 shows the dependence of Cu:In ratio on particle size. All particles were copper deficient with Cu:In <1. Additionally, the ratio of Cu to In increases with increasing particles size. This may be explained either by annealing of Cu vacancies with increasing synthesis time or alternatively by an increase in available copper or moderation of relative reactivities with higher temperatures. This is opposite to the trend was observed for EDX composition determination. Additionally, the Cu:In ratios determined by EDX were much higher. Both of these factors can be explained by the high and unstable copper background observed in these EDX measurements.

Table 5.2 Copper to indium ratio as determined using XPS for quantum dots of each size. Quantum dots were found to be increasingly copper deficient with increasing size.

Size (nm)	Cu:In ratio
1.4 \pm 0.2	0.15 \pm 0.01
1.8 \pm 0.2	0.18 \pm 0.01
1.9 \pm 0.3	0.22 \pm 0.02
2.0 \pm 0.3	0.19 \pm 0.01
2.6 \pm 0.4	0.32 \pm 0.02
3.1 \pm 0.5	0.30 \pm 0.02
3.2 \pm 0.4	0.34 \pm 0.02
3.8 \pm 0.4	0.37 \pm 0.03

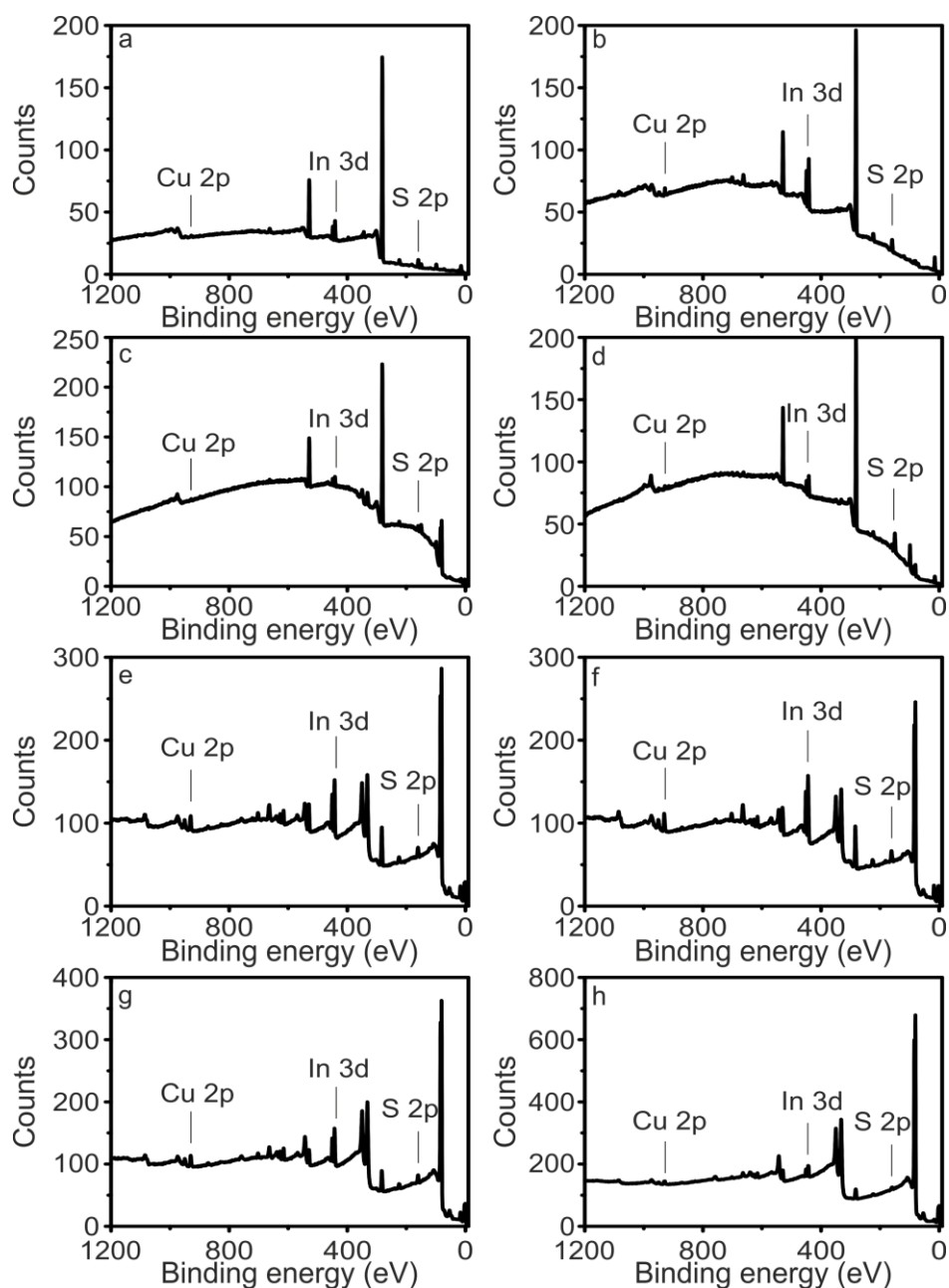


Figure 5.8 XPS survey spectra for CIS nanoparticles of various sizes.

XPS survey spectra for CIS nanoparticles of size (a) 1.4 ± 0.2 nm (10 min), (b) 1.8 ± 0.2 nm (15 min), (c) 1.9 ± 0.3 nm (20 min), (d) 2.0 ± 0.3 nm (25 min), (e) 2.6 ± 0.4 nm (30 min), (f) 3.1 ± 0.5 nm (40 min), (g) 3.2 ± 0.4 nm (50 min), and (h) 3.8 ± 0.4 nm (60 min).

Figure continued on adjacent page.

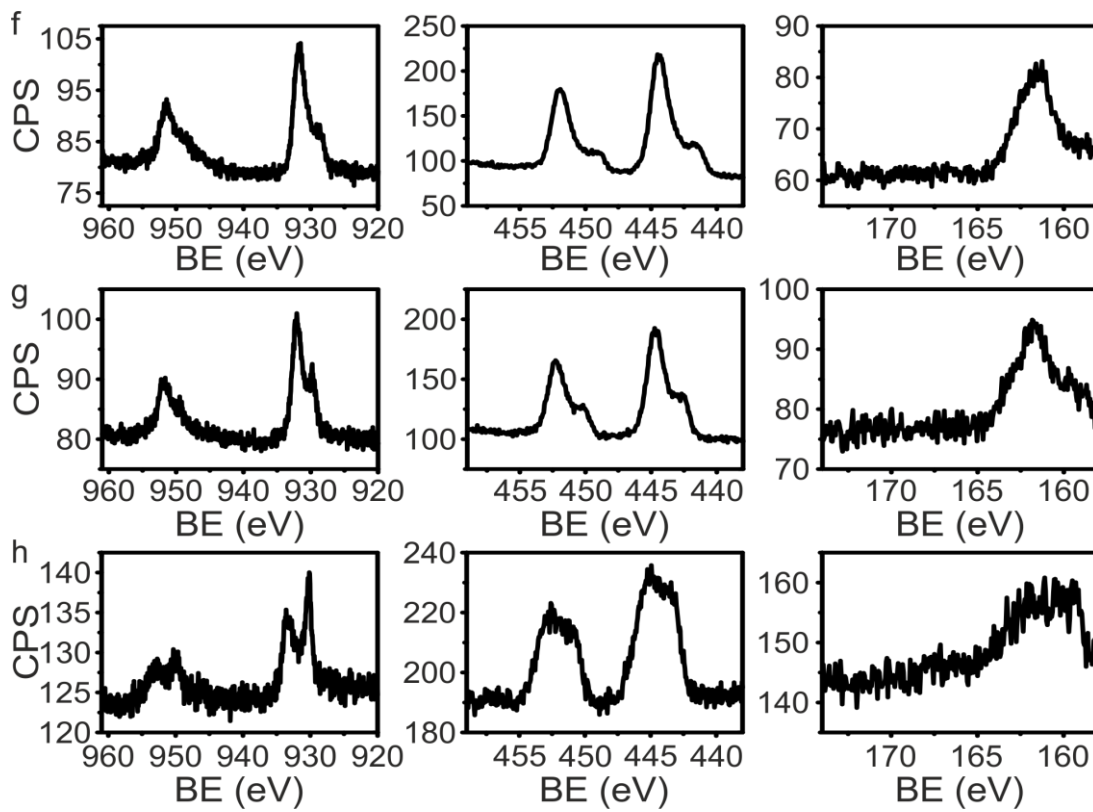


Figure 5.9 Detailed XPS spectra used for the determination of elemental ratios of Cu:In for various sizes of nanoparticles.

Cu 2p (left), In 3d (middle), and S 2p (right) XPS spectra used for the determination of nanoparticle composition are shown for nanoparticles of size (a) 1.4 ± 0.2 nm (10 min), (b) 1.8 ± 0.2 nm (15 min), (c) 1.9 ± 0.3 nm (20 min), (d) 2.0 ± 0.3 nm (25 min), (e) 2.6 ± 0.4 nm (30 min), (f) 3.1 ± 0.5 nm (40 min), (g) 3.2 ± 0.4 nm (50 min), and (h) 3.8 ± 0.4 nm (60 min).

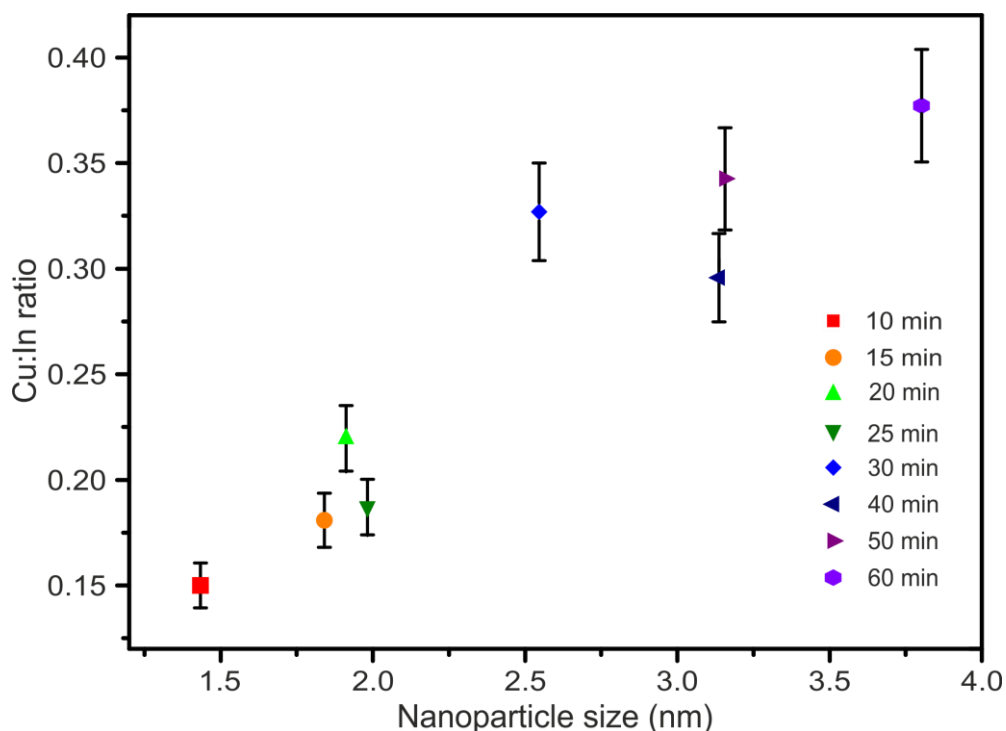


Figure 5.10 Composition: Dependence of copper-indium ratio on nanoparticle size as determined by XPS.

5.3 Optical properties

The size (and composition) dependent optical properties of the nanoparticles were investigated using steady state absorbance measurements, steady state PL emission, PLQY measurements, and PL lifetime measurements. In addition, transient absorption spectroscopy measurements were performed on nanoparticles of with a synthesis time of 20 min (size 1.9 ± 0.2 nm) in order to provide more information on energy levels and possible recombination pathways.

5.3.1 Absorbance measurements, determination of E_1 , E_x

Figure 5.11 shows UV-Visible (UV-Vis) absorbance spectra for each synthesis time. The UV-Vis absorbance spectra for the synthesized nanoparticles exhibit a broad shoulder and absorption edge corresponding to a single broad excitonic band. There is a marked red-shift in the absorbance spectra with increasing synthesis time and particle size (Figure 5.11), consistent with previous observations.^{154,182} In contrast with previously observed spectra, the

nanoparticles synthesised here exhibit more pronounced absorbance shoulder corresponding to the first excitation band (E_1). The shape and size dependent trend of these spectra are typical of all syntheses.

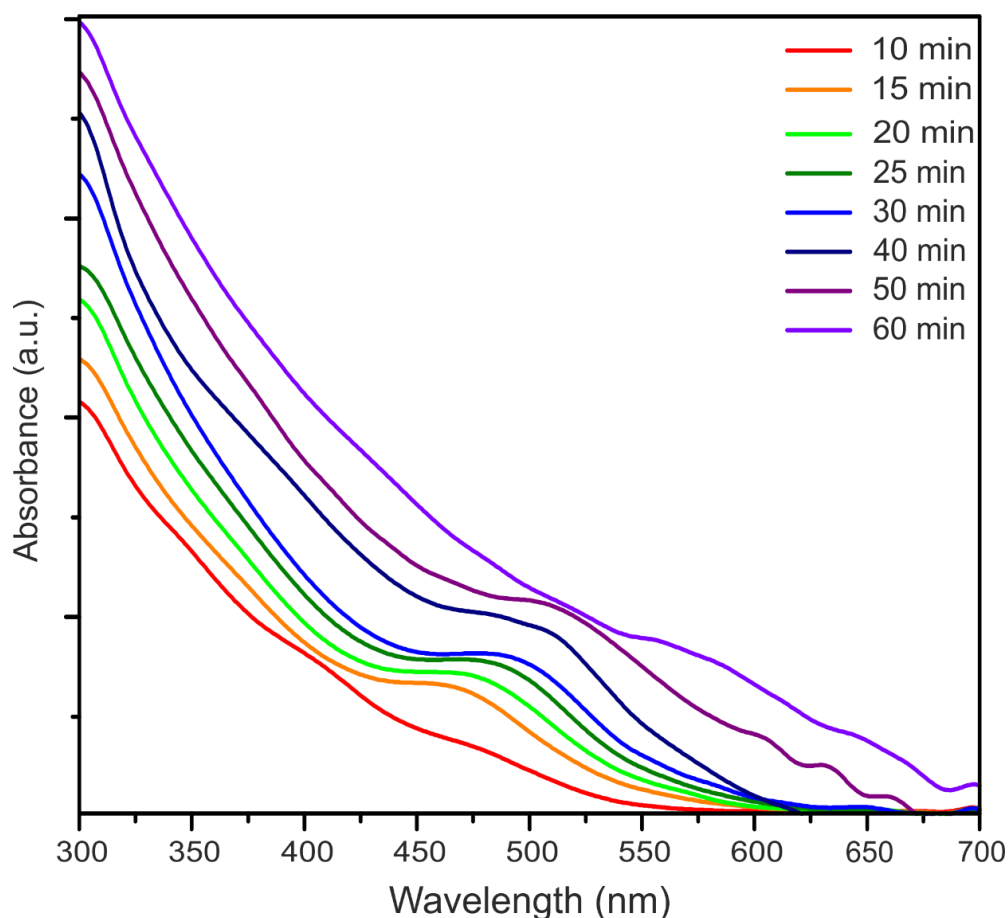


Figure 5.11 UV-Vis absorbance of quantum dots with various synthesis times.

Absorbance spectra for NPs with various synthesis times. The absorption feature is significantly red-shifted between 450 and 550 nm with increasing synthesis time.

Tauc plots were used for the determination of optical band-gaps, E_x , from absorbance data. Tauc plots corresponding to the quantum dots in Figure 5.11 are shown in Figure 5.12. The band-gap energy was found to decrease with increasing nanoparticle size owing to a decrease in quantum confinement, as expected. For the largest nanoparticles, the value of E_x is comparable to that for bulk CIS (~ 1.5 eV)¹⁵⁴ indicating weak/no quantum confinement. The decrease in band-gap energy with increasing particle size is shown in Figure 5.13. This decrease does not appear to follow the $\frac{1}{r^2}$ expected for quantum

confinement (Equation 1.18). This may be explained by defects and composition effecting the band-gap.

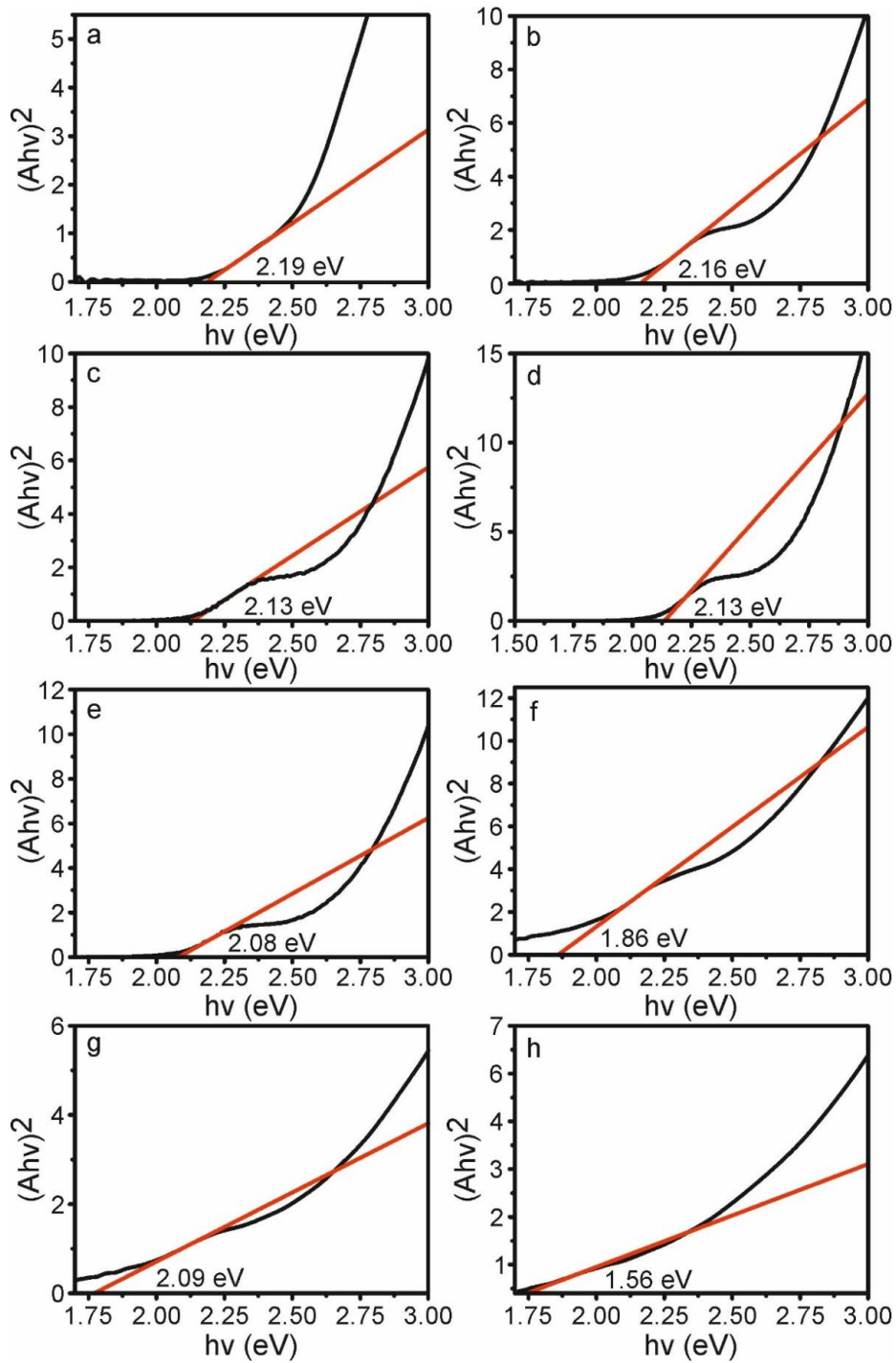


Figure 5.12 Tauc plots for determination of band-gap.

Tauc plots were used for the determination of band-gaps for each aliquot taken at (a) 10 min, (b) 15 min, (c) 20 min, (d) 25 min, (e) 30 min (f) 40 min, (g) 50 min, and (h) 60 min.

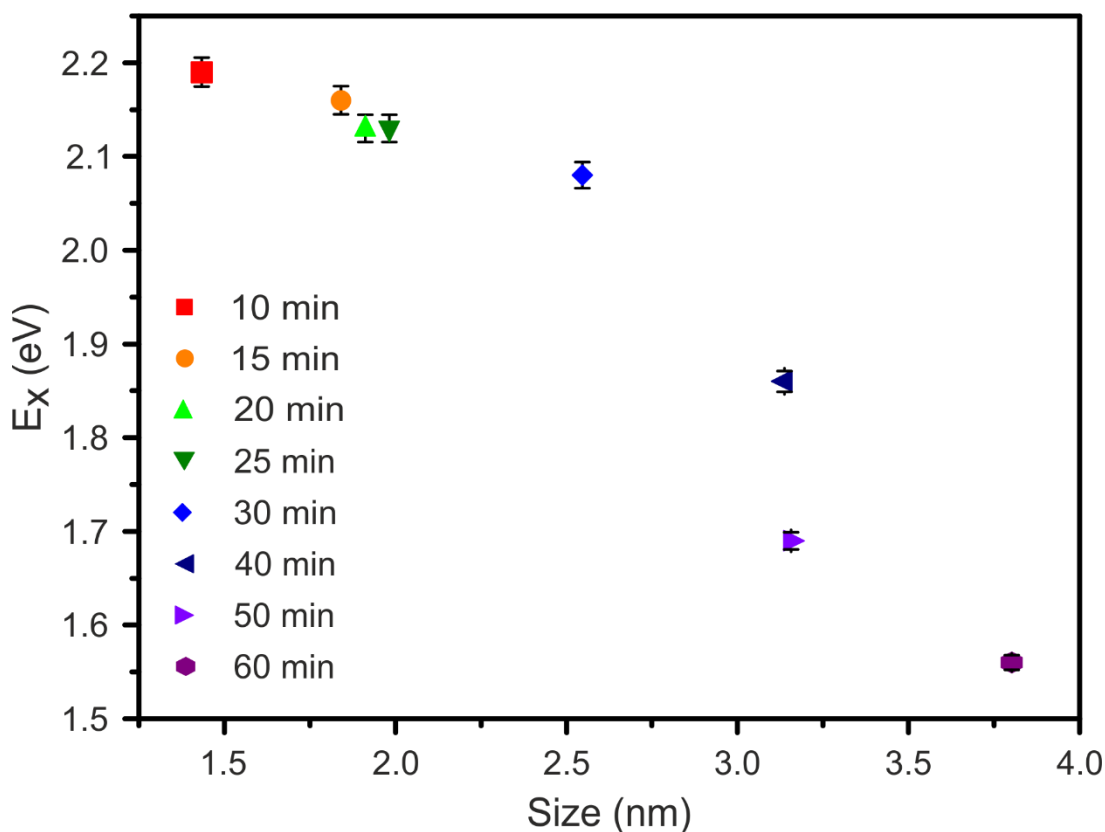


Figure 5.13 Band-gap of quantum dots as a function of size.

Optical band-gap energy, E_x , (as determined using Tauc plots shown in Figure 5.12) dependence on nanoparticle size.

In addition to calculating the optical band-gap energy, the energy of the first excitation was also determined. As the location of this feature can be difficult to determine in absorbance spectra, the local minimum of the second derivative of the absorbance with respect to wavelength was used. Generally, this feature was undetectable for those samples at the extremes of size e.g. those corresponding to synthesis times of 10 min or 60 min. Second derivatives of absorbance against wavelength for all other synthesis times are shown in Figure 5.14, together with the corresponding position of the first transition. Figure 5.15 shows the corresponding energy of the first transition plotted against synthesis time. In all cases, the energy of E_1 is greater than that of the optical band-gap, indicating that the energy of the first transition for which a solution to Schrodinger's equation exists is larger than the band-gap energy. (Figure 5.13).

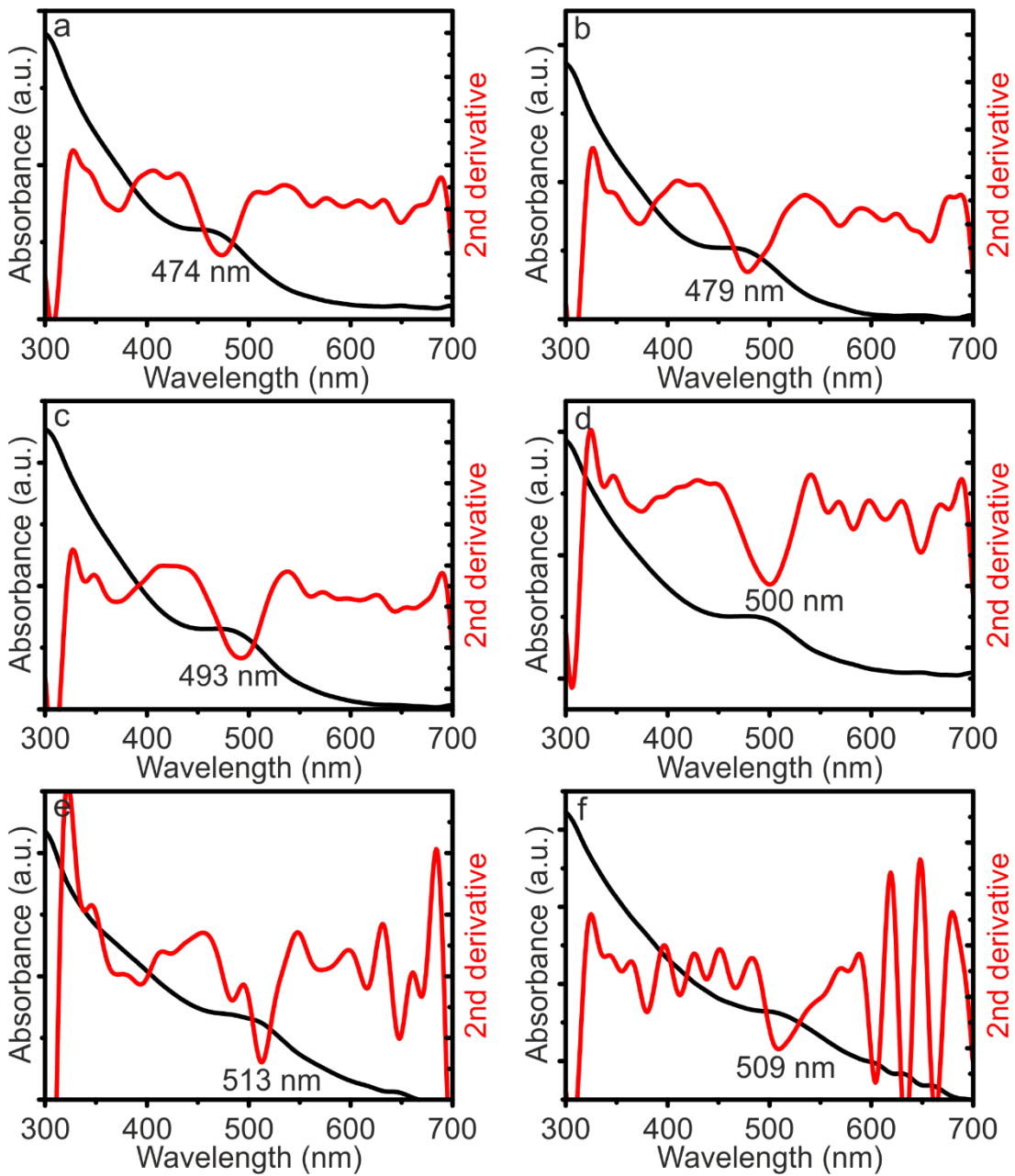


Figure 5.14 Second derivative of absorbance used for the determination of E_1 .

The local minimum of the second derivative of the absorbance with respect to wavelength was used to determine the position of the first excitation for aliquots taken at (a) 15 min, (b) 20 min, (c) 25 min, (d) 30 min, (e) 40 min, and (f) 50 min.

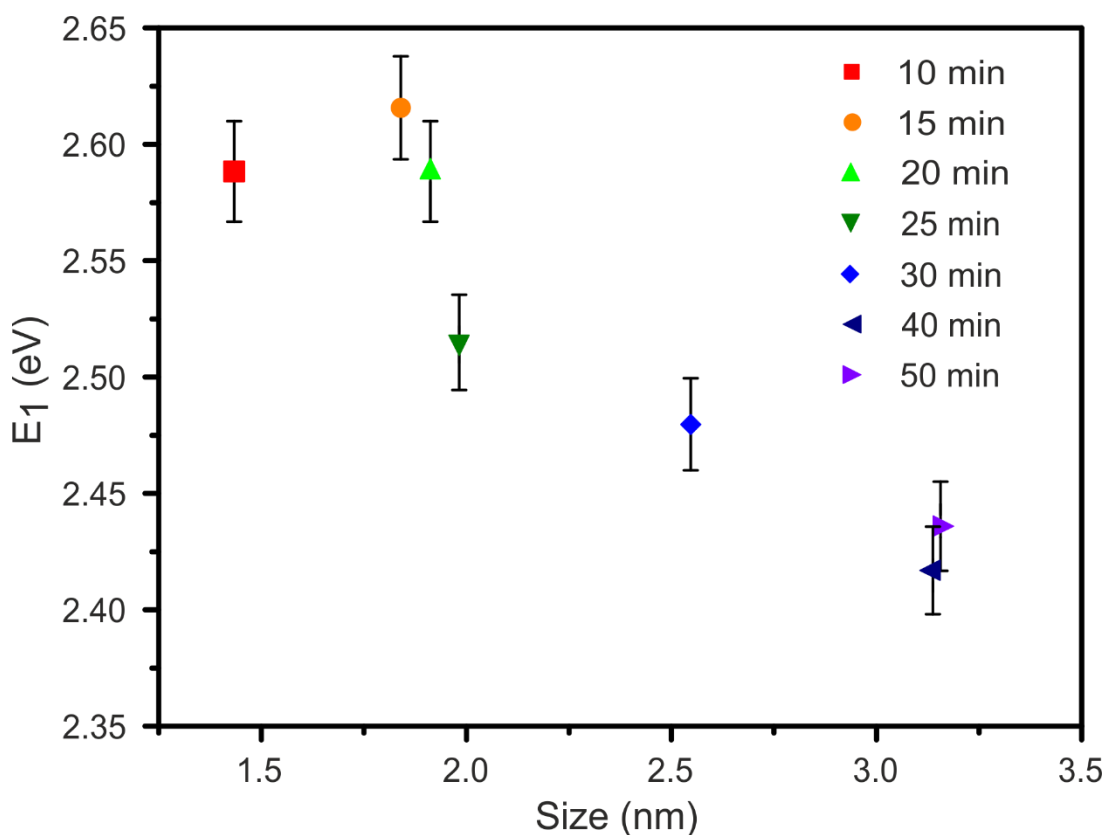


Figure 5.15 Position of first excitation of quantum dots as a function of size.

Size dependence of the first transition E_1 as determined from the second derivative as shown in Figure 5.14.

For both the optical band-gap and the energy of the first transition, the values and the overall trend was found to be reproducible across syntheses. Figure 5.16a and Figure 5.17b show values of E_1 and E_x respectively as determined for three different synthesis batches. This high level of consistency between batches indicates the synthesis method presented here allows for the reproducible synthesis of particles with well controlled properties.

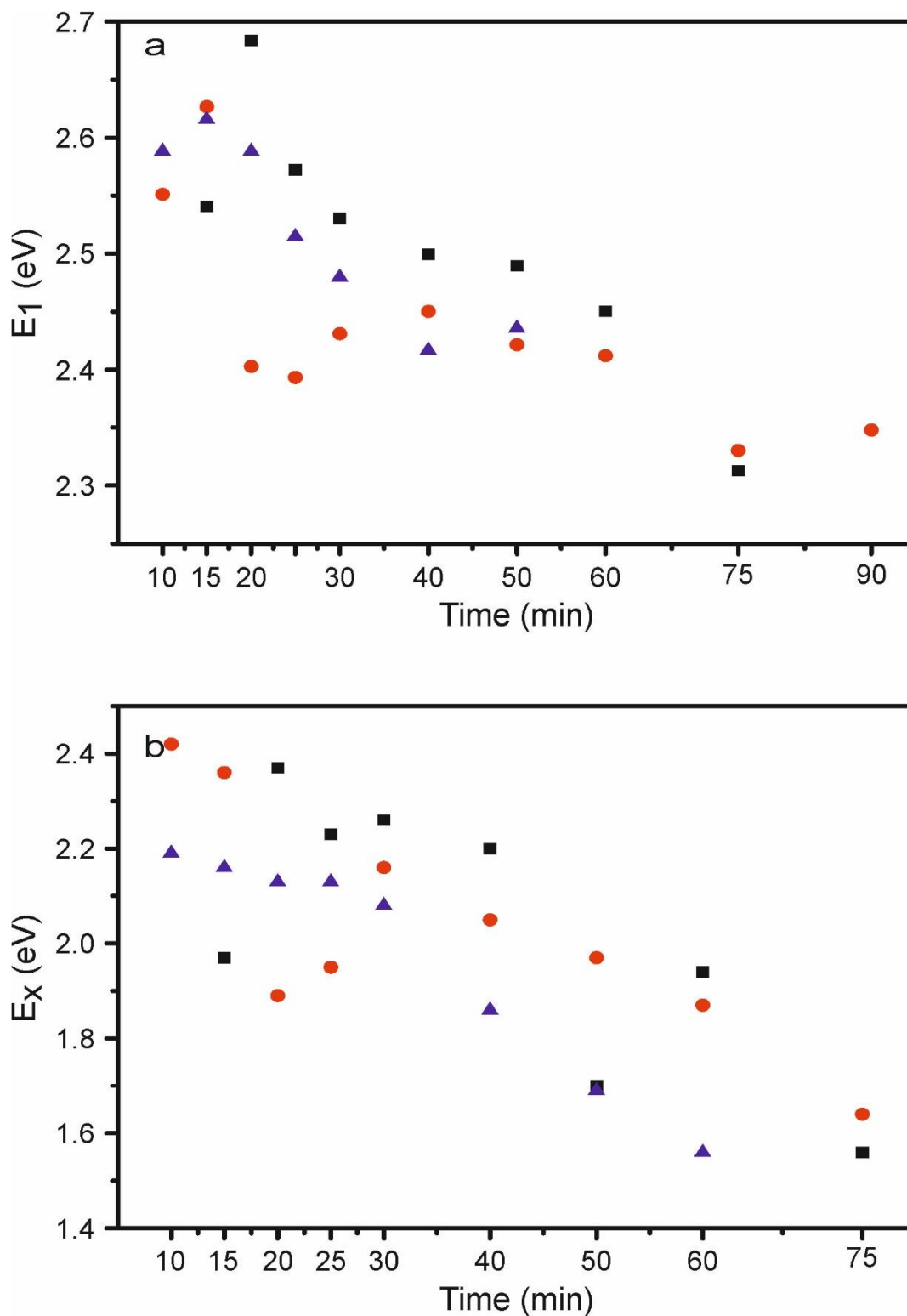


Figure 5.16 Reproducibility of E_x and E_1 between batches (different colours).

Both the optical band-gap and energy of the first transition was found to be reproducible between batches.

5.3.2 PL emission

PL emission spectra for sizes with measurable emission are shown in Figure 5.17. QD aliquots taken at 10 and 60 min did not exhibit fluorescence. In all cases the PL spectral peak is broad in nature due to the intra band-gap defect driven nature of emission. Peaks may be further broadened by the existence of a broad size distribution of particles. The energy of defect levels within the band-gap are highly sensitive to local properties of the crystal structure. Consequently, an ensemble of quantum dots of varying sizes should be expected to have a range of defect positions, leading to a broader spectral form. The position of the PL maximum is plotted against particle size in Figure 5.18. A clear size dependency of the peak position can be seen with its position increasing from 641 ± 1 nm to 695 ± 1 nm as nanoparticles increase in size from 1.8 ± 0.2 nm to 3.2 ± 0.4 nm. This trend is consistent with the expected decrease in band-gap with increasing quantum dot size. In addition to a pronounced red shift, peak broadening is also observed as synthesis time and consequently nanoparticle size increases.

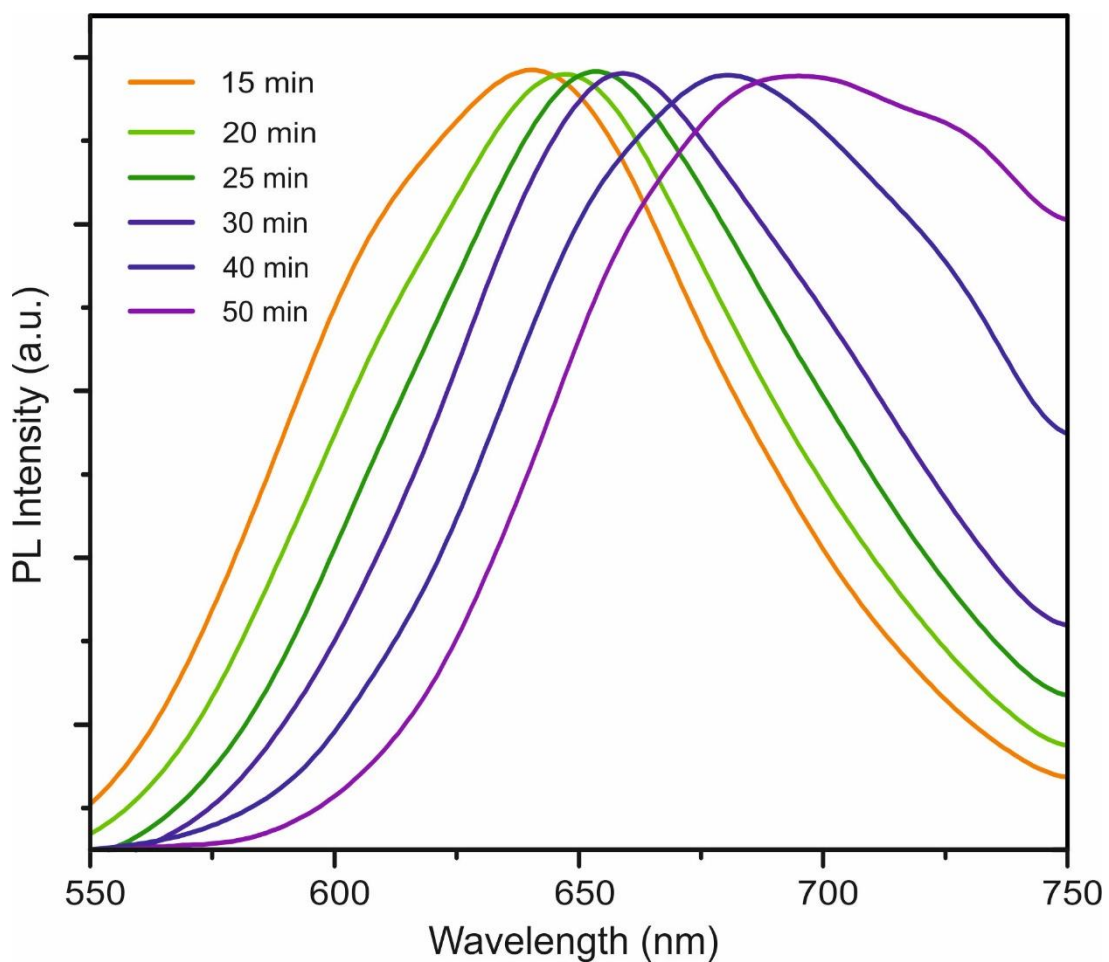


Figure 5.17 PL emission spectra for quantum dots with various synthesis times.

Representative PL emission spectra for synthesis time CIS quantum dots in methanol are shown.

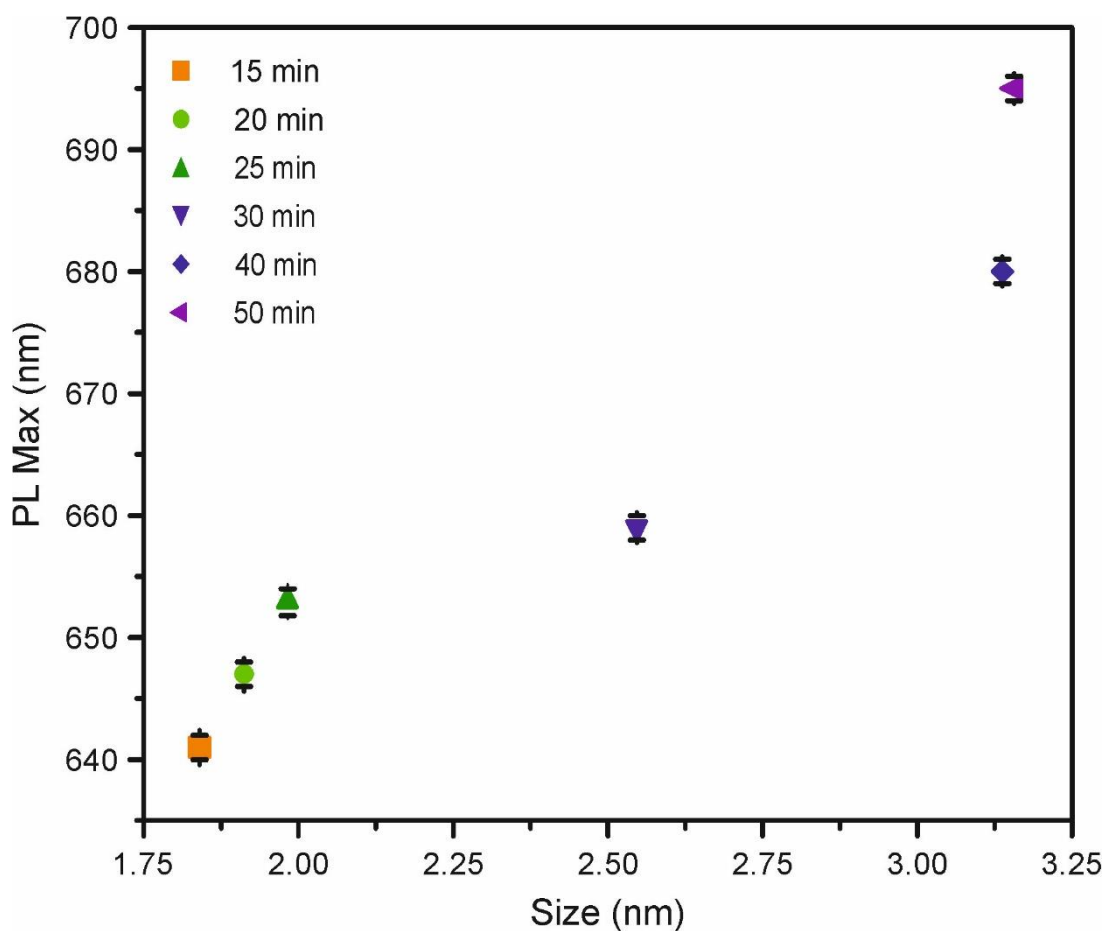


Figure 5.18 Dependence of PL peak position on NP synthesis time.

The strong dependence of the absorbance and emission properties on nanoparticle size and synthesis time, combined with the batch-to-batch reproducibility (Figure 5.19), demonstrates that the optical properties can be reliably tuned by varying synthesis time.

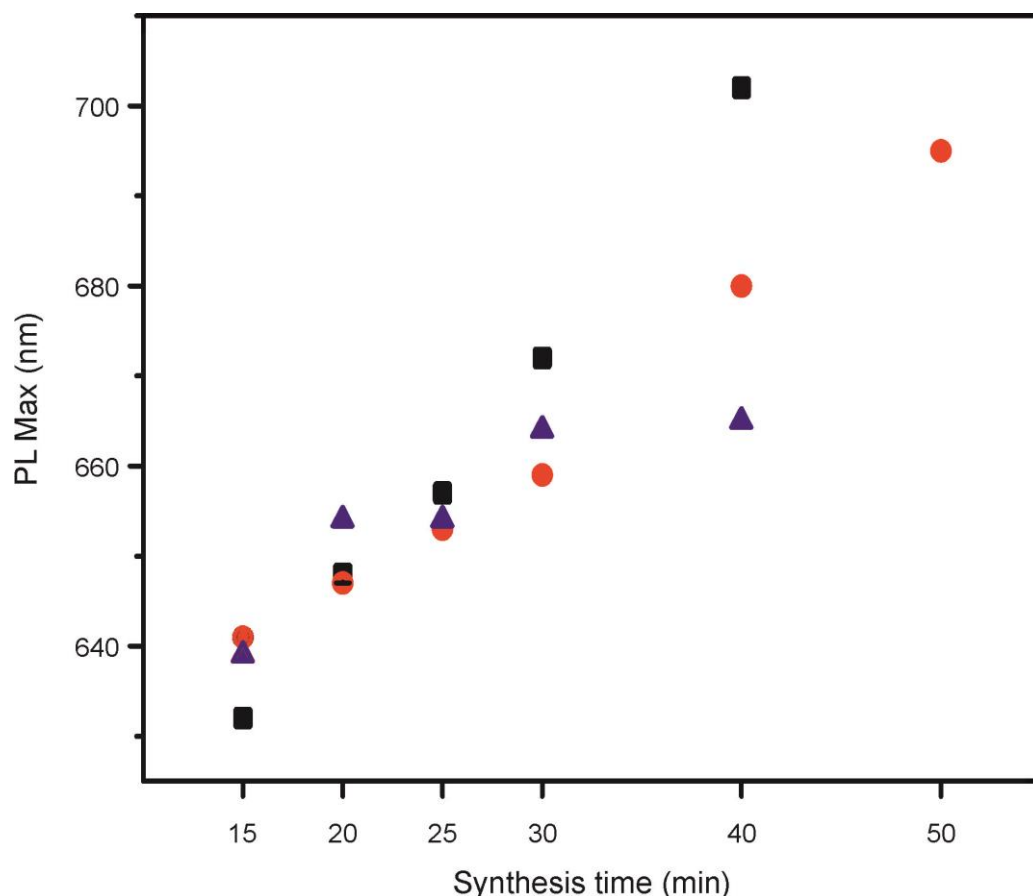


Figure 5.19 Reproducibility of PL emission between batches (different colours).

The size dependent shift in PL peak position was found to be consistent between batches.

Figure 5.20 below shows both the absorbance spectrum and the PL emission spectrum plotted together. As observed previously, there is a large energetic difference between the first excitonic feature in the absorbance spectrum and the PL emission peak. This difference, known as the Stokes shift, is typically attributed to the involvement of intra-gap states in PL emission. Table 5.3 contains calculated Stokes shifts for all nanoparticles for which PL emission was observable. The size of the Stokes shift was found to be independent of nanoparticle size.

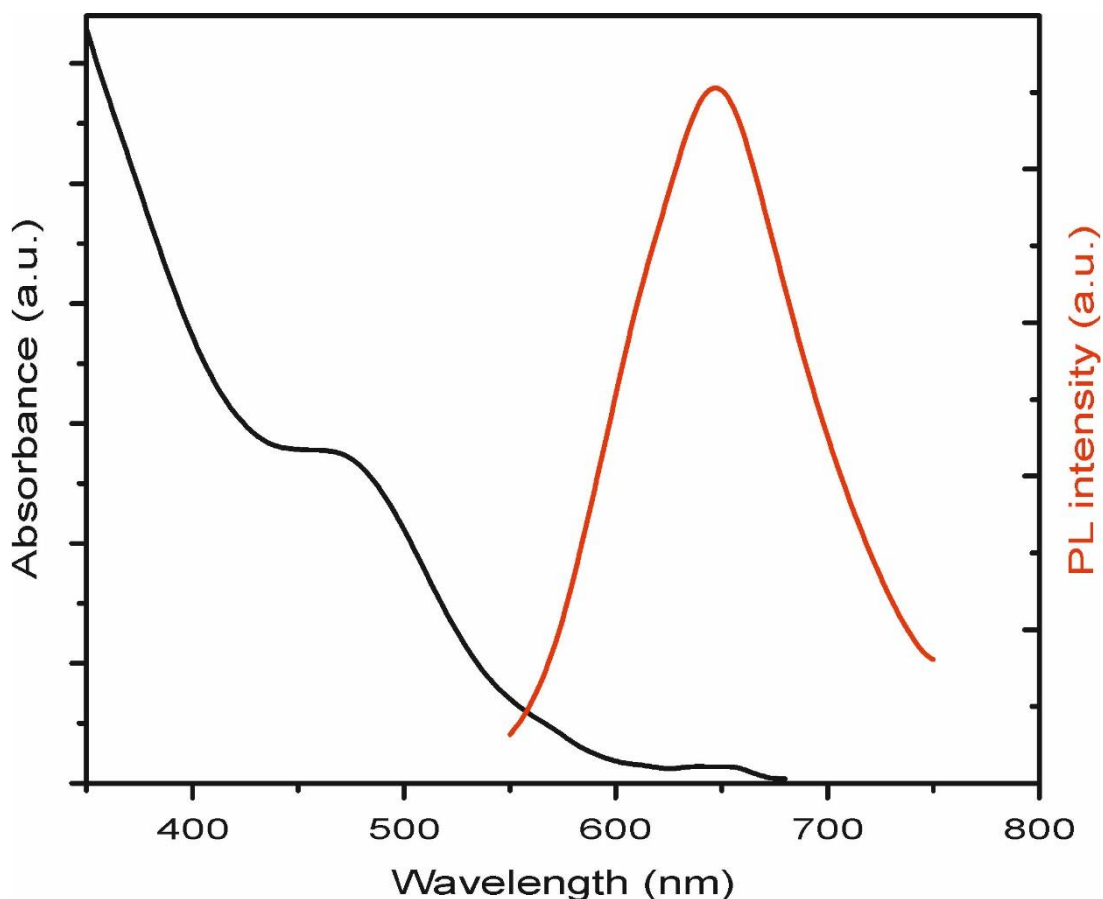


Figure 5.20 UV-vis and PL showing the Stokes shift for 1.9 ± 0.3 nm diameter nanoparticles.

The absorbance (black) and PL emission (red) spectra for 1.9 ± 0.3 nm diameter nanoparticles are overlaid.

Table 5.3 Stokes shifts calculated for nanoparticles of various sizes.

Size (nm)	Stokes shift (nm)
1.8 ± 0.2	167 ± 2
1.9 ± 0.3	168 ± 2
2.0 ± 0.3	160 ± 2
2.6 ± 0.4	159 ± 2
3.1 ± 0.5	167 ± 2
3.2 ± 0.4	186 ± 2

5.3.3 PLQY

PLQY measurements plotted against size, measured at various excitation energies, are shown in Figure 5.21 and Table 5.4. Values ranged from ~2-6%

comparable with previous best published values^{123,155,156,158,161,162,181–184} for core only CIS quantum dots. PLQY increased with increasing particle size while having slightly lower PLQY at higher excitation energies

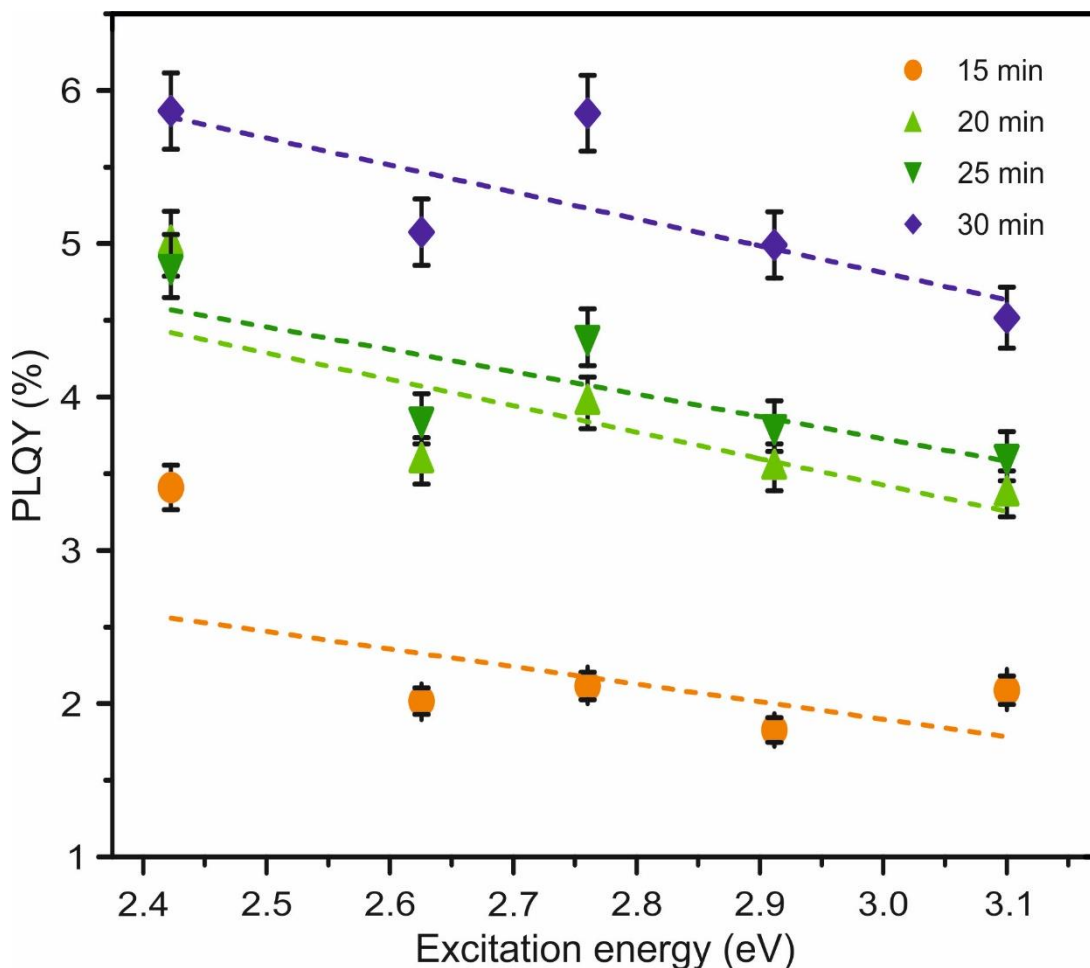


Figure 5.21 Dependence of PLQY on nanoparticle size and excitation energy.

The PLQY for nanoparticles between 1.8 ± 0.2 nm and 2.6 ± 0.4 nm is shown for excitation energies of 2.42 eV, 2.63 eV, 2.76 eV, 2.91 eV, and 3.1 eV.

Table 5.4 PLQY for nanoparticles between 1.8 ± 0.2 and 2.6 ± 0.4 nm at a range of excitation energies.

Size (nm)	PLQY (%) at 2.42 eV	PLQY (%) at 2.63 eV	PLQY (%) at 2.76 eV	PLQY (%) at 2.91 eV	PLQY (%) at 3.10 eV
1.8 ± 0.2	3.41 ± 0.14	2.02 ± 0.09	2.11 ± 0.09	1.83 ± 0.08	2.09 ± 0.09
1.9 ± 0.3	5.00 ± 0.21	3.58 ± 0.15	3.96 ± 0.17	3.54 ± 0.15	3.37 ± 0.15
2.0 ± 0.3	4.85 ± 0.21	3.86 ± 0.16	4.39 ± 0.19	3.81 ± 0.16	3.61 ± 0.16
2.6 ± 0.4	5.87 ± 0.25	5.08 ± 0.22	5.85 ± 0.25	4.99 ± 0.22	4.52 ± 0.20

5.3.3 Fluorescence lifetime measurements

Figure 5.22 shows a typical PL lifetime decay spectrum for nanoparticles with a synthesis time of 20 min. Spectra for samples with synthesis times of 15, 20, 25, and 30 min were all similar with a broad peak at ~ 596 nm (shifting to ~ 622 nm for larger nanoparticles), consistent with steady state PL measurements. A systematic blue shift of ~ 10 nm is observed in the PL emission, compared to steady state measurements, for all sizes. This can be explained either by the fact that steady state measurements are more sensitive to longer lived components which have a large PL max wavelength or via sample degradation with a decrease in the wavelength of maximum PL emission corresponding to particle shrinking. The PL emission peak shifts to longer wavelengths with increasing delay time before decaying to zero within ~ 1500 ns. This suggests the existence of a shorter lifetime component and a longer-lived red-shifted component as observed for stoichiometric CIS nanoparticles previously.¹⁸²

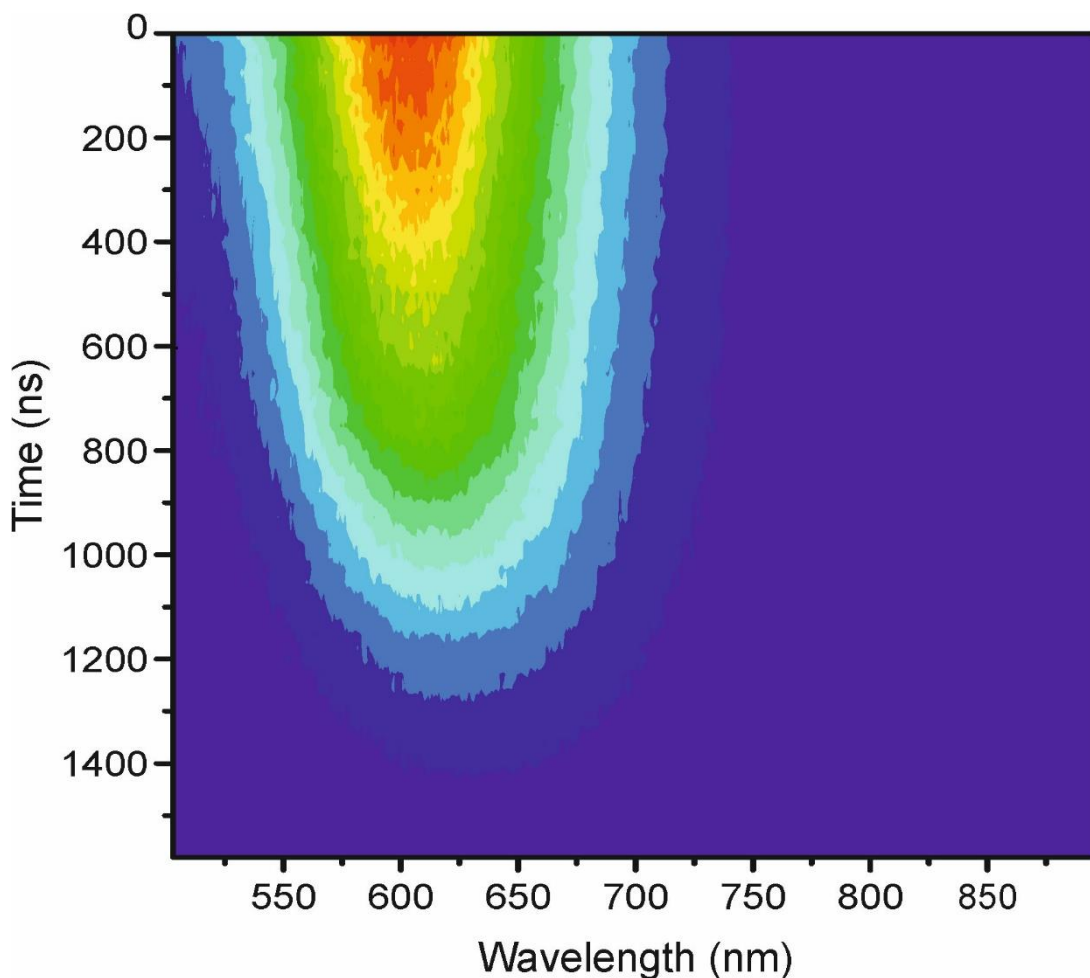


Figure 5.22 Contour plot of representative PL decay spectrum.

Representative data for 1.9 ± 0.3 nm (20 min synthesis time) nanoparticles taken over the first 1600 ns after excitation at 450 nm.

Global analysis fitting yielded three decay associated spectral components with different spectra: a short wavelength fast component with a lifetime of ~ 5 ns, a medium-lived component of ~ 35 ns and a long-lived component of ~ 245 ns (Figure 5.23). Three components were also identified by single value decomposition. Both the 35 ns peak and the 245 ns peak were red-shifted relative to the shortest lifetime component with the longest lifetime 245 ns lifetime peak exhibiting a significant shift. Based on both lifetimes and spectral peak positions, these components, consistent with previous literature,¹⁸² were attributed to band-gap emission, surface state emission, and defect-related emission respectively.

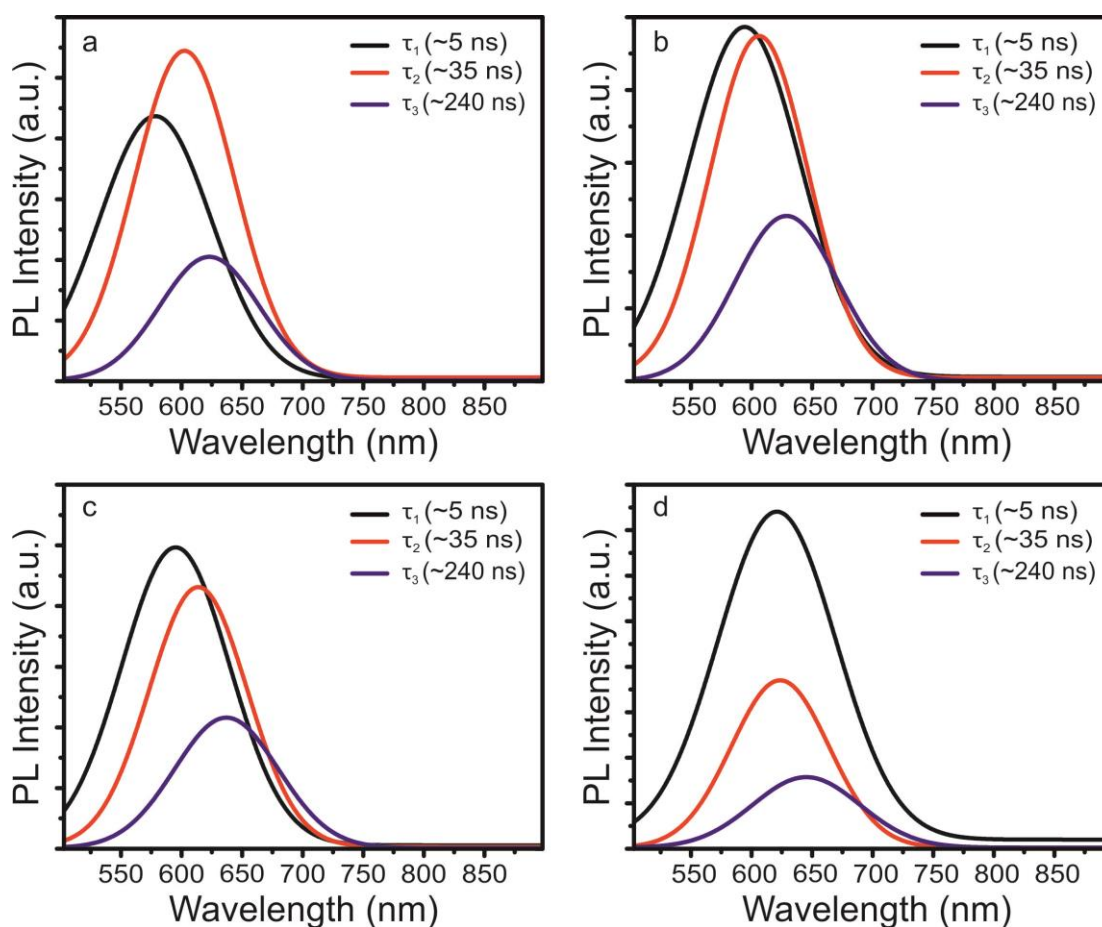


Figure 5.23 Decay associated spectra (DAS) obtained from global analysis fitting.

DAS obtained for nanoparticles of size (a) 1.8 ± 0.2 nm (15 min), (b) 1.9 ± 0.3 nm (20 min), (c) 2.0 ± 0.3 nm (25 min), (d) 2.6 ± 0.4 nm. In all case, optimal fitting was found for three components with $\tau_1 \sim 5$ ns (black), $\tau_2 \sim 35$ ns (red), and $\tau_3 \sim 240$ ns (blue). For each NP size, the amplitudes of peaks shown correspond to the relative spectral intensities determined by fitting.

The spectral position of all three components was found to be red-shifted with increasing nanoparticle size (Figure 5.24a). The increase in wavelength for the component corresponding to band-gap emission can be ascribed to a decrease in separation of the valence and conduction bands with increasing particle size owing to decreasing quantum confinement. The Stokes shift for

each of the three components was not found to vary significantly with nanoparticle size (Table 5.5).

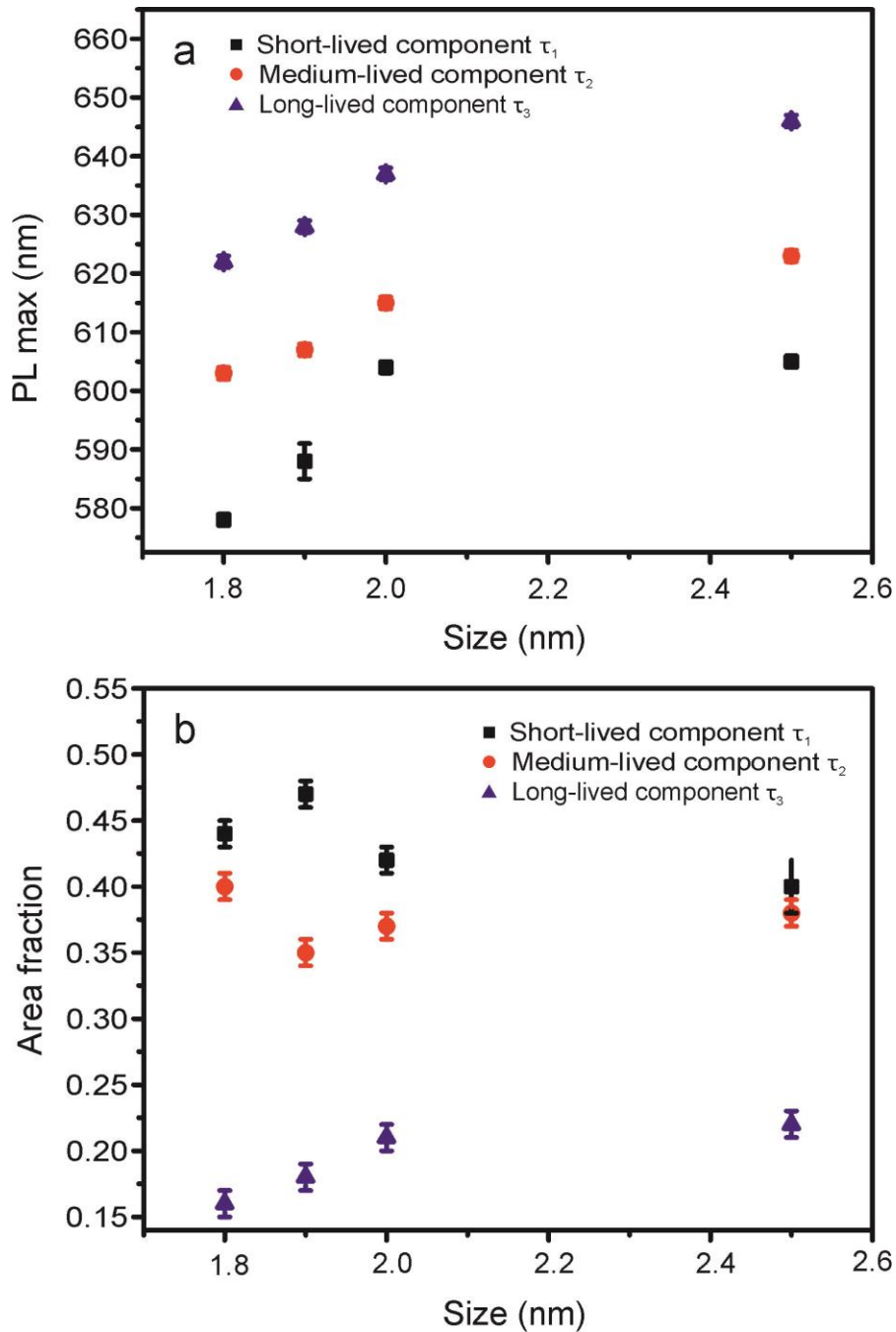


Figure 5.24 Size dependence of fitted peak positions and area fractions.

(a) Size dependence of fitted peak position for quantum dot size and each component. (b) Size dependence of area fraction determined for each DAS component.

Table 5.5 Stokes shift for each of the three fitted PL decay components. No significant dependence on nanoparticle size was observed.

Size (nm)	Stokes shift (nm) Short lifetime component	Stokes shift (nm) Medium lifetime component	Stokes shift (nm) Long lifetime component
1.8 \pm 0.2	4 \pm 2	29 \pm 2	48 \pm 2
1.9 \pm 0.3	9 \pm 2	23 \pm 2	46 \pm 2
2.0 \pm 0.3	22 \pm 2	33 \pm 2	55 \pm 2
2.6 \pm 0.4	11 \pm 2	27 \pm 2	49 \pm 2

It was assumed that peak area was proportional to the relative contribution of each type of recombination. The relative area of longest lifetime component increases with synthesis time whilst the relative area of the band-gap and surface state-related peaks decrease with nanoparticle size (Figure 5.24b).

Figure 5.25 shows a proposed recombination scheme based on the three pathways indicated by PL lifetime measurements and their size dependence.

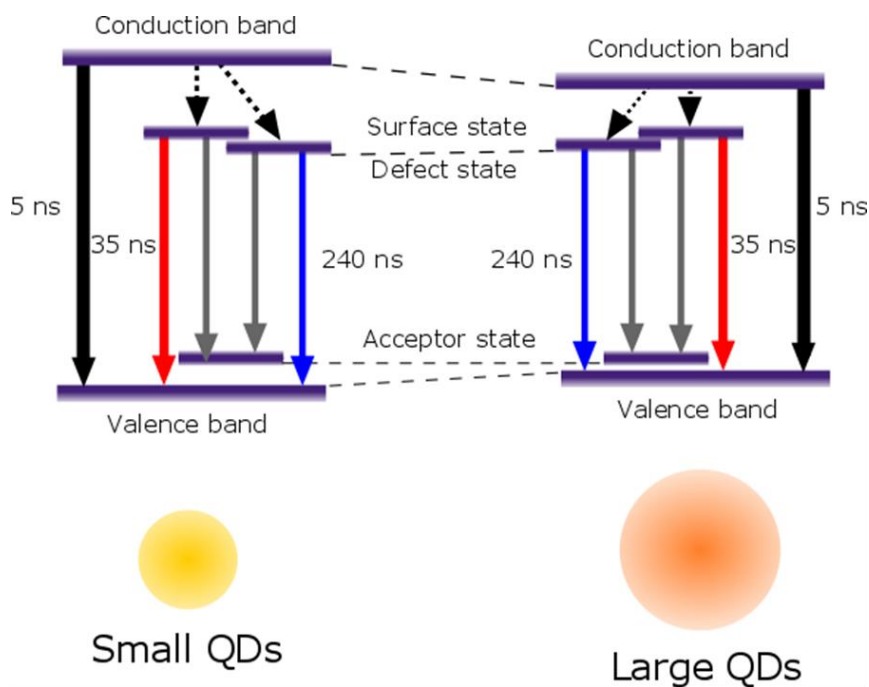


Figure 5.25 Effect of nanoparticle size on energy levels.

Schematic showing proposed changes to energy levels with increasing particle size. Arrow thickness is indicative of relative contribution of the component as indicated by DAS obtained from global analysis of PL lifetime data.

5.3.4 Transient absorption measurements

Figure 5.26a shows the transient absorption spectrum of evolution over 500 ns. This consists of a positive band at ~400nm, and two negative bands at ~500 nm and ~640 nm. A positive change in absorption, ΔA , is associated with excited state absorption (ESA). The strong negative ΔA centred at ~500 nm is associate with a ground state bleach (GSB) and thus the combination of the GSB and ESA bands correspond to the population of the ground and excited state. However, stimulated emission (SE) from the conduction band (CB) to the valance band (VB) will also cause a negative ΔA and this will be on the red-side of the GSB. It is therefore possible that the centre band at ~500 nm has contributions from GSB and SE. Stimulated emission often resembles the fluorescence spectrum. In this study, the dominant radiative pathway is consistent with donor to VB, and the third band is consistent with this wavelength position.

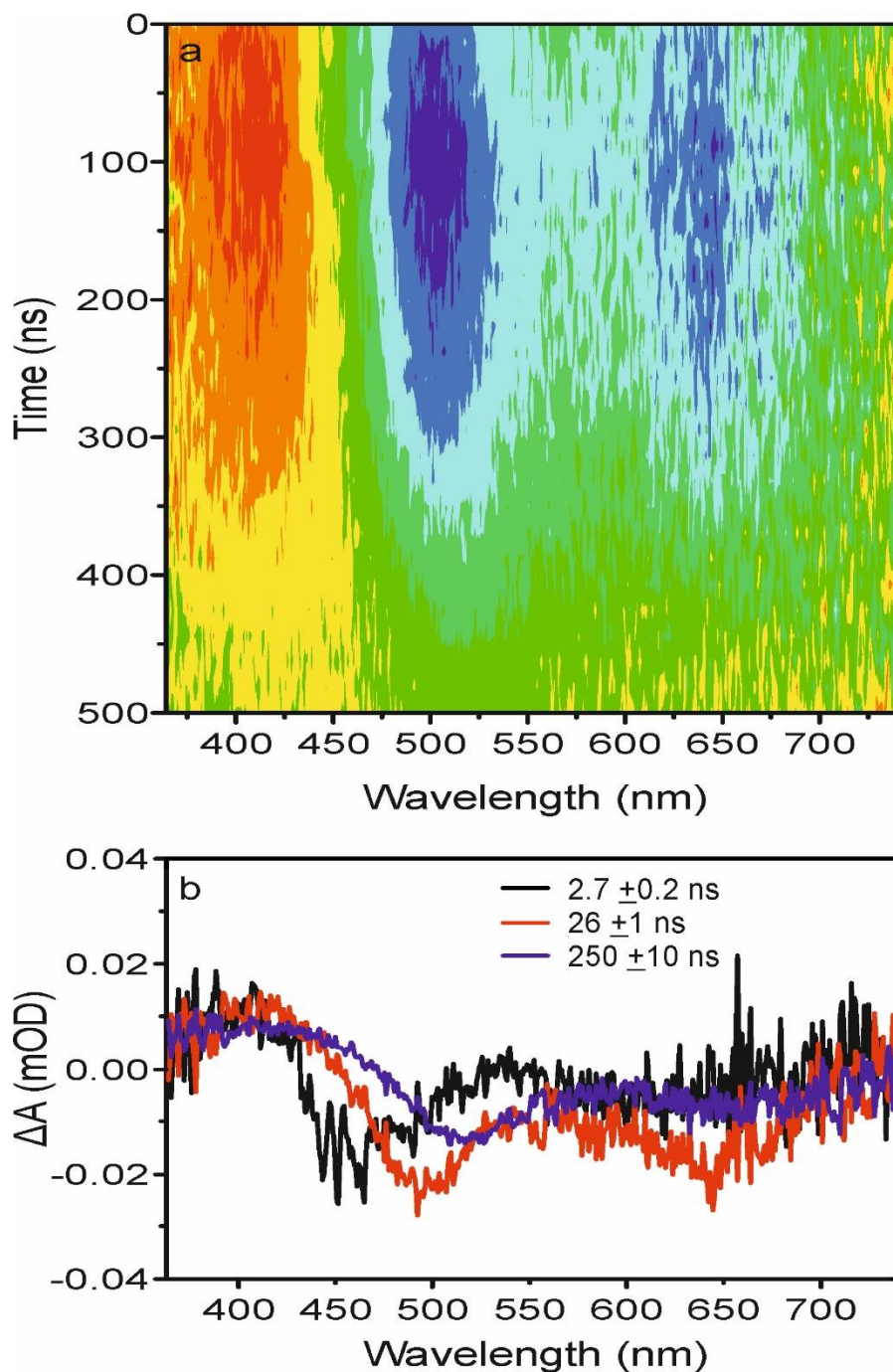


Figure 5.26 Transient absorption spectroscopy.

Transient absorption spectroscopy analysis of quantum dots of 1.91 nm (20 min synthesis time) (a) Transient absorption spectrum over the first 500 ns after excitation. (b) Fitted DAS showing three components with similar lifetimes to those observed for PL decay.

Global analysis fitting yielded three spectral components (shown in Figure 5.26b) with lifetimes similar to those observed from PL lifetime analysis. In

addition to the surface defect and core defect related energy levels observed in PL lifetime analysis, global analysis fitting suggests the existence of an acceptor level just above the valence band involved in stimulated emission from both defect levels as shown in Figure 5.25.

5.4 Conclusion

In conclusion, this chapter demonstrates a novel method for the direct synthesis of high quality hydrophilic nanoparticles with PLQY comparable to the best reported values for core CIS nanoparticles. Furthermore, this thesis presents the first known quantitative size dependent PLQY results for CIS nanoparticles. Consistent with previously published work,¹⁸² PL decay measurements suggest three key recombination pathways contributing to PL emission. Through careful control of nanoparticle size and synthesis of deliberately copper deficient nanoparticles with the degree of copper deficiency controlled by synthesis time, this thesis has shed new light on the role of size and composition on the relative contribution of band-gap recombination, core defect and surface defect emission. It is, however, difficult to conclusively separate what is a size dependent effect and what is a defect dependant effect. It is likely that further experimental and simulation work, including further study on the impact of composition variations for nanoparticles of a fixed size, will be needed to clarify this.

Chapter 6

Conclusions and future perspectives

This thesis concerns bacteriochlorophyll (BChl) pigments and copper indium sulphide (CIS) quantum dots (QDs) and how they may be combined for the production of novel photonic materials. The key aims of this thesis were:

- 1) Chemical modification of BChl pigments improve stability and facilitate coupling (Chapter 3).
- 2) Molecular dynamics simulations of BChl assemblies to investigate pigment aggregation and curvature (Chapter 4).
- 3) Synthesis and characterisation of Cu-deficient CIS QDs of various sizes (Chapter 5).

The key results for each of each chapter are summarised below (Section 6.1) with a discussion on the direction of future work on BChl pigment modification and QDs towards the production of hybrid BChl-QD nanostructures (Section 6.2). Proposals for the further study of pigment assemblies using molecular dynamics are also presented.

6.1 Conclusions

6.1.1 BChl and Zinc-(Bacterio)Pheophytin (Zn-(B)Phe) Preparation and Chemical Modification

Chapter 3 describes progress towards the production of chemically modified pigments suitable for coupling to QDs.

Bacteriochlorophylls and chlorophylls were successfully extracted with minimal sample degradation and pure samples obtained using high pressure liquid chromatography (HPLC). A facile and versatile method for conversion of (B)Chls to Zn-(B)Phe has also been developed and applied to Chl a, Chl b, BChl c, and BChl e, to produce zinc containing analogues. These pigments were spectrally characterised and a protocol for the purification of Zn-Phe a and Zn-BPhe c developed. Crucially, BChl pigments modified in this way

retained their ability to aggregate. This is significant as the ability of modified pigments to aggregate and retain their strong excitonic coupling and highly efficient energy transfer, is likely to be vital for their use in light harvesting or other photonic applications. Whilst evidence presented here is not conclusive, it is consistent with the successful incorporation of a thiol group for direct coupling to CIS quantum dots.

6.1.2 Simulations of BChl pigment assemblies

Chapter 4 presented the first molecular dynamics study on BChl pigment assemblies. This exploratory study led to a number of new observations on the behaviour of pigment sheets and their curvature as well as providing new evidence in support of the previously proposed syn-anti β S α A, β S α Ag and β S α Au dimer motifs.²⁶

A variety of structures were observed to form both within and between different dimer configurations with some simulations exhibiting long-lived intermediate states. In addition, a number of systems exhibited significant curvature with the β S α A and β S α Au configurations curving most strongly. Direction of curvature appears to be dictated by an asymmetry of the dimer unit. A higher degree of curvature was observed in single layer systems. The formation of wrapped helical tube like structures was only observed for single layer structures. The lower degree of curvature for multilamellar systems is most likely due to reduced freedom of movement in larger more densely packed systems. This appears to contradict the observation of highly curved multilamellar structures in electron microscopy (EM) images of certain chlorosomes. One possible explanation is the formation of curved regions from single sheets with additional layers curving around the initial cylinder.

The transition dipole moment plots for both the single and triple layer simulations on the β A β A motif differ markedly to those observed for other repeats and appear to indicate either a different form or origin of curvature. It is expected that the large variation in the appearance of dipole moment arrangement presented here will lead to different circular dichroism (CD) and absorbance properties.

Investigation of system energy showed a rapid decrease in energy which appears to be due contraction of pigment systems into more favourable densely packed systems. Examination of the final energy per dimer indicated that the X-ray unit cell optimised $\beta\text{S}\alpha\text{Au}$ dimer motif may be the most energetically favourable for both single and triple layer systems. This was followed by the similar $\beta\text{S}\alpha\text{A}$ and $\beta\text{S}\alpha\text{Ag}$ motifs.

In the majority of cases, the lowest energy systems generally exhibited curvature. The exception to this is the $\beta\text{S}\alpha\text{Au}$ motif which had the three lowest energies but did not curve in the triple sheet arrangement. This apparent conflict could be explained by the existence of two phases within chlorosomes, with $\beta\text{S}\alpha\text{Au}$ dimer motif forming the straight sections and $\beta\text{S}\alpha\text{Ag}$ forming the curved sections. Some evidence for the existence of both flat and curved regions has been seen in wild type chlorosomes.⁵ As well as providing a greater understanding of how pigment sheets curve in chlorosomes, investigation of curvature in these systems is likely to be important for the generation of hybrid systems containing aggregated BChls. In these structures it may be necessary to match curvature of aggregates to the radius of the quantum dots.

6.1.3 Synthesis and characterisation of CIS QDs

Chapter 5 describes a novel method for the direct synthesis of high quality hydrophilic CIS QDs and their extensive characterisation.

In this study, the dodecanethiol method of synthesizing CIS quantum dots²³⁴ was modified. Changing the solvent, surfactant and the sulphur source led to the synthesis of more hydrophilic nanoparticles. These nanoparticles had photoluminescence quantum yield (PLQY) comparable to the best reported values for core CIS nanoparticles. Furthermore, this thesis presents the first known quantitative size dependent PLQY results for CIS nanoparticles. Consistent with previously published work,¹⁸² photoluminescence (PL) decay measurements suggest three key recombination pathways contributing to PL emission. Through careful control of nanoparticle size and synthesis of deliberately copper deficient nanoparticles with the degree of copper deficiency controlled by synthesis time, this thesis has shed new light on the

role of size and composition on the relative contribution of band-gap recombination, core defect and surface defect emission. A detailed understating of the energy levels and recombination pathways of CIS quantum dots is essential for successful coupling of QDs to BChls and their aggregates.

6.2 Future work

6.2.1 Pigment modification and production of hybrid systems

Key to successful coupling of BChl pigments and QDs outlined in Chapter 1 lies in the successful chemical modification of BChl pigments to incorporate a trailing SH group to facilitate chemical linking of the two components. Therefore, further work should include the identification of a suitable purification method for the cysteamine treated pigments as well as further investigation to determine if chemically modification has been successful. It should then be possible, via ligand exchange to coat the QDs with Chl and BChl pigments.

The resulting hybrid material should then be extensively characterised to determine the extent and nature of coupling. This might use techniques such as: absorption measurements, PL emission, excitation, lifetime and transient absorption measurements. It is anticipated that transfer of energy between QDs and pigments will either take the form of Förster resonance energy transfer (FRET) or excitonic coupling. Direct excitonic coupling should lead to changes in peak positions and ratios of peaks in absorption, PL emission and PL excitation spectra distinct from those expected by simple superposition of their individual spectra. In the case of FRET only changes to PL and transient absorption (TA) lifetimes are expected due to the presence of additional energy levels and pathways within the system compared to bare QDs. Additionally, techniques such as dynamic light scattering (DLS) and fluorescence correlation spectroscopy (FCS) would allow changes to hydrodynamic radius to be investigated.

6.2.2 Simulations on pigment assemblies

The simulations on BChl pigment assemblies have highlighted a number of areas for future study.

Further work may investigate the separation of key groups within individual dimers, e.g. the length of the Mg-OH coordination bond. This may provide new information including whether or not initial spacings for optimised dimer units persist during simulation. This maybe particularly relevant for the similar β S α A, β S α Ag, and β S α Au arrangements.

In this thesis, curvature has been assessed by visual means only. In order to draw more concrete conclusions about the role of curvature it will be necessary to find a means of mathematically describing and assessing the extent of this curvature with respect to the direction of e.g. dipole moments.

Through additional simulations on different BChl c homologues and BChl d and e, it should be possible to correlate system curvature to chemical structure. In addition to providing insight on the behaviour of pigment assemblies in chlorosomes of different species, this may suggest ways in which pigments can be modified to alter curvature. Experimentally, this would allow fine tuning of pigment assemblies to increase the chances of successful coupling to quantum dots.

Future work should also include prediction of CD and absorbance properties for these simulation structures. This will offer an additional means of comparing simulation work to experimentally observed structures and may provide a means of determining structures are likely to be present in chlorosomes and *in vitro* aggregates.

Further work is required to determine conclusively whether a link between lower energy states and curvature exists and if so, why the β S α Au dimer motif is an exception. In addition, it should be possible, by examining the evolution of individual energy components, including electrostatic and van der Waals contributions to gain a more comprehensive picture of the energetics of sheet curvature. Again, a more comprehensive examination of individual energy components should shed light on the origins of the stabilisation effect observed for triple layers over their single layer counterparts. In addition, it should be possible to decompose system energy into individual layers.

X-ray scattering predictions from single layer sheets failed to reproduce the peaks observed for dried chlorosomes. This is most likely due to the presence

of a single sheet rather than the multilamellar structure believed to exist in chlorosomes.⁵ Therefore, future work should include the modification of the X-ray scattering script to use a Monte Carlo sampling method to allow the calculation of expected X-ray scattering behaviour for the simulation outputs from triple layer structures.

Finally, as mentioned previously, the exploratory study undertaken here has resulted in the generation of an extraordinarily large volume of data. Data mining this large body of information to enable a more thorough understanding of BChl aggregation as well as to help set the direction of future study.

6.2.3 Quantum dots

Further study on the impact of composition variations for nanoparticles of a fixed size may be useful to help separate which effects are size dependent and which are defect dependent. This could be combined with in-depth structural analysis using Electron energy loss spectroscopy (EELS) mapping in Super Scanning transmission electron microscopy (SuperSTEM) to enable a more detailed understanding of structure within Cu deficient CIS nanoparticles.²³⁵

Single particle spectroscopy could also be used to probe the properties of individual particles. Finally, total internal reflectance fluorescence microscopy (TIRFM) studies of fluorescence intermittency (FI) of quantum dots should be performed. FI is the observation of “on” and “off” periods for emitting QDs. Extensive characterisation of FI of CIS QDs has not yet been performed. This would likely provide additional information on the energy transfer pathways within CIS QDs. It is expected, as with PL and TA lifetimes, that in the case of FRET, the addition of BChl pigments may lead changes due to presence of additional energy levels and pathways.

List of Abbreviations

Acac – Acetylacetonate	Cryo-EM – Cryo-electron microscopy
AFM – Atomic force microscopy	CV – Cyclic voltammetry
ARC1 – Advanced research computer 1	DAP – Donor-acceptor pair
ARC2 – Advanced research computer 2	DDT – Dodecanethiol
ATR – Attenuated total reflectance	DLD – Delay-line detector
BChl – Bacteriochlorophyll	DLS – Dynamic light scattering
BChl c_F – Bacteriochlorophyll c esterified with farnesyl	EDTA - Ethylenediaminetetraacetic acid
BChlide – Bacteriochlorophyllide	EDX – Energy dispersive analysis of X-rays
CCD – Charge coupled device	EELS – Electron energy loss spectroscopy
BPhe – Bacteriopheophytin	EET – Exciton energy transfer
BPheide – Bacteriopheophorbide	EM – Electron microscopy
Chl – Chlorophyll	ESA – Excited state absorption
Chlide – Chlorophyllide	FCS – Fluorescence correlation spectroscopy
CB – Conduction band	FEG – Field emission gun
CCD – Charge coupled device	FFT – Fast Fourier transform
CD – Circular dichroism	FI – Fluoresce intermittency
Chl – Chlorophyll	FTIR – Fourier transform infra-red spectroscopy
Chlide – Chlorophyllide	FWHM – Full width at half maximum
CIS - Copper indium disulfide (CuInS ₂)	
CISE – Copper indium diselenide (CuInSe ₂)	

GAFF – General Amber Force Field

GSB – Ground state bleach

HAADF – High-angle annular dark field

HDA – Hexadecylamine

HPLC – High pressure liquid chromatography

HPLC-MS – High pressure liquid chromatography - mass spectrometry

HRTEM – High resolution transmission electron microscopy

ICCD – Intensified charge coupled device

IR – Infrared

IUPAC – International Union of Pure and Applied Chemistry

LC – Liquid chromatography

LD – Linear dichroism

LED - Light emitting diode

MCT – Mercury cadmium telluride

MD – Molecular dynamics

MeOH – Methanol

MGDG – Monogalactosyldiacylglycerol

MM – Molecular mechanics

mPES - modified Polyethersulfone

MUD – Mercaptoundecanol

NaOH – Sodium hydroxide

NC – Nanocrystal

NHS - N-hydroxysuccinimide

NIR – Near infra-red

NMR – Nuclear magnetic resonance

NP – Nanoparticle

OAc – Acetate

OD – Optical density

ODE – Octadecene

OLA – Oleylamine

OLAM – Oleylamine

OPO – Optical parametric oscillator

PEG – Polyethylene glycol

PBS – Phosphate buffered saline

Phe – Pheophytin

Pheide – Pheophorbide

PL – Photoluminescence

PLQY – Photoluminescence quantum yield

PME – Particle-mesh Ewald method

PTFE – Polytetrafluoroethylene

QD – Quantum dot

QM – Quantum Mechanical

RMS – Root-mean-squared

SDD - Silicon drift device

SE – Stimulated emission

SuperSTEM – Scanning
transmission electron microscopy

TA – Transient absorption

THF – Tetrahydrofuran

TEM – Transmission electron
microscopy

TFA – Trifluoroacetic acid

TFF – Tangential flow filtration

TIRF – Total internal reflectance
fluorescence

TOOP – Trioctylphosphite

TOPO – Trioclylphosphine

UV – Ultraviolet

UV-Vis – Ultraviolet-Visible

VB – Valence band

VMD – Virtual molecular dynamics

XPS – X-ray photoelectron
spectroscopy

XRD – X-ray diffraction

YAG - Yttrium aluminium garnet

Zn-BPhe – Zinc-
Bacteriopheophytin

Zn-BPheide – Zinc-
Bacteriopheophorbide

Zn-Phe – Zinc-Pheophytin

Zn-Pheide – Zinc-Pheophorbide

List of References

1. Cohen-bazire, G., Pfenning, N. & Kunisawa, R. The fine structure of green bacteria. *J. Cell Biol.* **22**, 207–225 (1964).
2. Bryant, D. A. *et al.* Candidatus Chloracidobacterium thermophilum: An Aerobic phototropic acidobacterium. *Science.* **317**, 523–526 (2007).
3. Eisen, J. *et al.* The complete genome sequence of Chlorobium tepidum TLS, a photosynthetic, anaerobic, green-sulfur bacterium. *Proc. Natl. Acad. Sci. U. S. A.* **99**, 9509–14 (2002).
4. Frigaard, N.-U. & Bryant, D. Seeing green bacteria in a new light: genomics-enabled studies of the photosynthetic apparatus in green sulfur bacteria and filamentous anoxygenic phototrophic bacteria. *Arch. Microbiol.* **182**, 265–76 (2004).
5. Psencík, J., Butcher, S. J. & Tuma, R. in *The Structural Basis of Biological Energy Generation, Advances in Photosynthesis and Respiration* (ed. Hohmann-Marriott, M.) 77–109 (Springer, 2014).
6. Martinez-Planells, A. *et al.* Determination of the topography and biometry of chlorosomes by atomic force microscopy. *Photosynth. Res.* **71**, 83–90 (2002).
7. Oostergetel, G. T., van Amerongen, H. & Boekema, E. J. The chlorosome: a prototype for efficient light harvesting in photosynthesis. *Photosynth. Res.* **104**, 245–55 (2010).
8. Bryant, D. & Frigaard, N.-U. Prokaryotic photosynthesis and phototrophy illuminated. *Trends Microbiol.* **14**, 488–96 (2006).
9. Blankenship, R. E. & Matsuura, K. in *Light-harvesting antennas in photosynthesis* (eds. Green, B. & Parsons, W.) 195–217 (Springer, 2003).
10. Staehelin, L., Golecki, J., Fuller, R. & Drews, G. Visualization of the supramolecular architecture of chlorosomes (Chlorobium type vesicles) in freeze-fractured cells of Chloroflexus aurantiacus. *Arch. Microbiol.* **119**, 269–277 (1978).
11. Staehelin, L. A., Golecki, J. & Drews, G. Supramolecular organization of chlorosomes (chlorobium vesicles) and of their membrane attachment sites in Chlorobium Limicola. *Biochim. Biophys. Acta* **589**, 30–45 (1980).
12. Sørensen, P. G., Cox, R. P. & Miller, M. Chlorosome lipids from Chlorobium tepidum: characterization and quantification of polar lipids and wax esters. *Photosynth. Res.* **95**, 191–6 (2008).
13. Buck, D. & Struve, W. Tubular exciton models for BChl c antennae in

- chlorosomes from green photosynthetic bacteria. *Photosynth. Res.* **48**, 367–377 (1996).
14. Blankenship, R. E., Olson, J. M. & Miller, M. in *Anoxygenic photosynthetic bacteria* (eds. Blankenship, R. E., Madigan, M. & Bauer, C.) 399–435 (Kluwer Academic Publishers, 1995).
 15. Ikonen, T. P. *et al.* X-ray scattering and electron cryomicroscopy study on the effect of carotenoid biosynthesis to the structure of *Chlorobium tepidum* chlorosomes. *Biophys. J.* **93**, 620–628 (2007).
 16. Arellano, J. B. *et al.* Hexanol-induced order-disorder transitions in lamellar self-assembling aggregates of bacteriochlorophyll c in *Chlorobium tepidum* chlorosomes. *Langmuir* **24**, 2035–2041 (2008).
 17. Pedersen, M. Ø., Linnanto, J., Frigaard, N.-U., Nielsen, N. C. & Miller, M. A model of the protein-pigment baseplate complex in chlorosomes of photosynthetic green bacteria. *Photosynth. Res.* **104**, 233–43 (2010).
 18. Arellano, J. B., Melø, T. B., Borrego, C. M., Garcia-Gil, J. & Naqvi, K. R. Nanosecond laser photolysis studies of chlorosomes and artificial aggregates containing bacteriochlorophyll e: evidence for the proximity of carotenoids and bacteriochlorophyll a in chlorosomes from *Chlorobium phaeobacteroides* strain CL1401. *Photochem. Photobiol.* **72**, 669–675 (2000).
 19. Olson, J. & Pedersen, J. Bacteriochlorophyll c monomers, dimers, and higher aggregates in dichloromethane, chloroform, and carbon tetrachloride. *Photosynth. Res.* **25**, 25–37 (1990).
 20. Tamiaki, H. *et al.* In vitro synthesis and characterization of bacteriochlorophyll-f and its absence in bacteriochlorophyll-e producing organisms. *Photosynth. Res.* **107**, 133–138 (2011).
 21. Harada, J., Mizoguchi, T., Tsukatani, Y., Noguchi, M. & Tamiaki, H. A seventh bacterial chlorophyll driving a large light-harvesting antenna. *Sci. Rep.* **2**, 671 (2012).
 22. Garcia Costas, A. M. *et al.* Identification of the bacteriochlorophylls, carotenoids, quinones, lipids, and hopanoids of ‘*Candidatus Chloracidobacterium thermophilum*’. *J. Bacteriol.* **194**, 1158–1168 (2012).
 23. Scheer, H. in *Chlorophylls and bacteriochlorophylls* (eds. Grimm, B., Porra, R., Rudiger, W. & Scheer, H.) 1–26 (Springer, 2006).
 24. Hildebrandt, P., Tamiaki, H., Holmarth, A. R. & Schaffner, K. Resonance Raman Spectroscopic Study of Metallochlorin Aggregates. Implications for the Supramolecular Structure in Chlorosomal BChl c Antennae of Green Bacteria. *J. Phys. Chem.* **98**, 2192–2197 (1994).

25. Jochum, T. *et al.* The supramolecular organization of self-assembling chlorosomal bacteriochlorophyll c, d, or e mimics. *Proc. Natl. Acad. Sci. U. S. A.* **105**, 12736–12741 (2008).
26. Alster, J., Kabeláč, M., Tuma, R., Pšenčík, J. & Burda, J. V. Computational study of short-range interactions in bacteriochlorophyll aggregates. *Comput. Theor. Chem.* **998**, 87–97 (2012).
27. van Rossum, B. J. *et al.* A refined model of the chlorosomal antennae of the green bacterium *Chlorobium tepidum* from proton chemical shift constraints obtained with high-field 2-D and 3-D MAS NMR dipolar correlation spectroscopy. *Biochemistry* **40**, 1587–1595 (2001).
28. Holzwarth, A. & Schaffner, K. On the structure of bacteriochlorophyll molecular aggregates in the chlorosomes of green bacteria. A molecular modelling study. *Photosynth. Res.* **41**, 225–233 (1994).
29. Egawa, A. *et al.* Structure of the light-harvesting bacteriochlorophyll c assembly in chlorosomes from *Chlorobium limicola* determined by solid-state NMR. *Proc. Natl. Acad. Sci. U. S. A.* **104**, 790–795 (2007).
30. Kakitani, Y. *et al.* Stacking of bacteriochlorophyll c macrocycles in chlorosome from *Chlorobium limicola* as revealed by intermolecular ¹³C magnetic-dipole correlation, X-ray diffraction, and quadrupole coupling in 25Mg NMR. *Biochemistry* **48**, 74–86 (2009).
31. Nozawa, T. *et al.* Structures of chlorosomes and aggregated BChlc in *Chlorobium tepidum* from solid state high resolution CP/MAS ¹³C NMR. *Photosynth. Res.* **41**, 211–223 (1994).
32. Ganapathy, S. *et al.* Alternating syn-anti bacteriochlorophylls form concentric helical nanotubes in chlorosomes. *Proc. Natl. Acad. Sci. U. S. A.* **106**, 8525–8530 (2009).
33. Klinger, P., Arellano, J. B., Vacha, F., Hala, J. & Psencik, J. Effect of Carotenoids and Monogalactosyl Diglyceride on Bacteriochlorophyll c Aggregates in Aqueous Buffer: Implications for the Self-assembly of Chlorosomes. *Photochem. Photobiol.* **80**, 572–578 (2004).
34. Psencík, J. *et al.* The lamellar spacing in self-assembling bacteriochlorophyll aggregates is proportional to the length of the esterifying alcohol. *Photosynth. Res.* **104**, 211–219 (2010).
35. Psencík, J. *et al.* Lamellar organization of pigments in chlorosomes, the light harvesting complexes of green photosynthetic bacteria. *Biophys. J.* **87**, 1165–72 (2004).
36. Oostergetel, G. T. *et al.* Long-range organization of bacteriochlorophyll in chlorosomes of *Chlorobium tepidum* investigated by cryo-electron microscopy. *FEBS Lett.* **581**, 5435–5439 (2007).

37. Psencik, J. *et al.* Structure of chlorosomes from the green filamentous bacterium *Chloroflexus aurantiacus*. *J. Bacteriol.* **191**, 6701–8 (2009).
38. Psencik, J. *et al.* Internal structure of chlorosomes from brown-colored chlorobium species and the role of carotenoids in their assembly. *Biophys. J.* **91**, 1433–1440 (2006).
39. Brune, D., Nozawa, T. & Blankenship, R. Antenna Organization in Green Photosynthetic Bacteria. 1. Oligomeric Bacteriochlorophyll c as a Model for the 740 nm Absorbing Bacteriochlorophyll c in *Chloroflexus aurantiacus* Chlorosomes. *Biochemistry* **26**, 8644–8652 (1987).
40. Shibata, Y., Tateishi, S., Nakabayashi, S., Itoh, S. & Tamiaki, H. Intensity borrowing via excitonic couplings among *soret* and *Q_y* transitions of bacteriochlorophylls in the pigment aggregates of chlorosomes, the light-harvesting antennae of green sulfur bacteria. *Biochemistry* **49**, 7504–7515 (2010).
41. Steensgaard, D., Wackerbarth, H., Hildebrandt, P. & Holzwarth, A. Diastereoselective control of bacteriochlorophyll e aggregation. 3 1-S-BChl e is essential for the formation of chlorosome-like aggregates. *J. Phys. Chem. B* **104**, 10379–10386 (2000).
42. Garcia Costas, A. M. *et al.* Ultrastructural analysis and identification of envelope proteins of 'Candidatus *Chloracidobacterium thermophilum*' chlorosomes. *J. Bacteriol.* **193**, 6701–6711 (2011).
43. Didraga, C., Klugkist, J. & Knoester, J. Optical Properties of Helical Cylindrical Molecular Aggregates: The Homogeneous Limit. *J. Phys. Chem. B* **106**, 11474–11486 (2002).
44. Frese, R. *et al.* The organization of bacteriochlorophyll c in chlorosomes from *Chloroflexus aurantiacus* and the structural role of carotenoids and protein An absorption , linear dichroism , circular dichroism and Stark spectroscopy study. *Photosynth. Res.* **54**, 115–126 (1997).
45. Griebenow, K., Holzwarth, A., van Mourik, F. & van Grondelle, R. Pigment organization and energy transfer in green bacteria. 2. Circular and linear dichroism spectra of protein-containing and protein-free chlorosomes isolated from *Chloroflexus aurantiacus* strain Ok-70-fl. *Biochem. Biophys. Acta* **1058**, 194–202 (1991).
46. Matsuura, K., Hirota, M., Shimada, K. & Mamoru, M. Spectral Forms and Orientation of Bacteriochlorophylls c and α in Chlorosomes of the Green Photosynthetic Bacterium *Chloroflexus aurantiacus*. *Photochem. Photobiol.* **57**, 92–97 (1993).
47. van Amerongen, H., Vasmel, H. & van Grondelle, R. Linear Dichroism of Chlorosomes from *Chloroflexus Aurantiacus* in Compressed Gels and Electric Fields. *Biophys. J.* **54**, 65–76 (1988).

48. van Amerongen, H., van Haeringen, B., van Gorp, M. & van Grondelle, R. Polarized fluorescence measurements on ordered photosynthetic antenna complexes. *Biophys. J.* **59**, 992–1001 (1991).
49. Arellano, J. B. *et al.* Effect of carotenoid biosynthesis inhibition on the chlorosome organization in *Chlorobium phaeobacteroides* strain CL1401. *Photochem. Photobiol.* **71**, 715–723 (2000).
50. Tamiaki, H., Tateishi, S., Nakabayashi, S., Shibata, Y. & Itoh, S. Linearly polarized light absorption spectra of chlorosomes, light-harvesting antennas of photosynthetic green sulfur bacteria. *Chem. Phys. Lett.* **484**, 333–337 (2010).
51. Saga, Y., Shibata, Y. & Tamiaki, H. Spectral properties of single light-harvesting complexes in bacterial photosynthesis. *J. Photochem. Photobiol. C Photochem. Rev.* **11**, 15–24 (2010).
52. Shibata, Y., Saga, Y., Tamiaki, H. & Itoh, S. Polarized fluorescence of aggregated bacteriochlorophyll c and baseplate bacteriochlorophyll a in single chlorosomes isolated from *Chloroflexus aurantiacus*. *Biochemistry* **46**, 7062–7068 (2007).
53. Shibata, Y., Saga, Y., Tamiaki, H. & Itoh, S. Anisotropic distribution of emitting transition dipoles in chlorosome from *Chlorobium tepidum*: fluorescence polarization anisotropy study of single chlorosomes. *Photosynth. Res.* **100**, 67–78 (2009).
54. Furumaki, S. *et al.* Absorption linear dichroism measured directly on a single light-harvesting system: the role of disorder in chlorosomes of green photosynthetic bacteria. *J. Am. Chem. Soc.* **133**, 6703–6710 (2011).
55. Linnanto, J. M. & Korppi-Tommola, J. E. I. Investigation on chlorosomal antenna geometries: tube, lamella and spiral-type self-aggregates. *Photosynth. Res.* **96**, 227–245 (2008).
56. Psencík, J., Ma, Y.-Z., Arellano, J. B., Hála, J. & Gillbro, T. Excitation energy transfer dynamics and excited-state structure in chlorosomes of *Chlorobium phaeobacteroides*. *Biophys. J.* **84**, 1161–1179 (2003).
57. Martiskainen, J., Linnanto, J., Kananavičius, R., Lehtovuori, V. & Korppi-Tommola, J. Excitation energy transfer in isolated chlorosomes from *Chloroflexus aurantiacus*. *Chem. Phys. Lett.* **477**, 216–220 (2009).
58. Savikhin, S., Zhu, Y., Blankenship, R. E. & Struve, W. Intraband energy transfers in the BChl c antenna of chlorosomes from the green photosynthetic bacterium *Chloroflexus aurantiacus*. *J. Phys. Chem.* **3654**, 17978–17980 (1996).
59. Dostál, J. *et al.* Two-dimensional electronic spectroscopy reveals ultrafast energy diffusion in chlorosomes. *J. Am. Chem. Soc.* **134**,

- 11611–11617 (2012).
60. Bystrova, M., Mal'gosheva, I. & Krasnovskii, A. Molecular mechanism of self-assembly of aggregated bacteriochlorophyll c. *Mol. Biol.* **13**, 582594 (1979).
 61. Smith, K. M. & Kehres, L. A. Aggregation of the Bacteriochlorophylls c, d, and e. Models for the Antenna Chlorophylls of Green and Brown Photosynthetic Bacteria. *J. Am. Chem. Soc.* **105**, 1387–1389 (1983).
 62. Chiefari, J. *et al.* Models for the Pigment Organization in the Chlorosomes of Photosynthetic Bacteria: Diastereoselective Control of in-vitro Bacteriochlorophyll cs Aggregation. *J. Phys. Chem.* **99**, 1357–1365 (1995).
 63. Nozawa, T., Ohtomo, K., Suzuki, M., Morishita, Y. & Madigan, M. Structure and Organization of Bacteriochlorophylls c's in Chlorosomes from a New Thermophilic Bacterium *Chlorobium tepidum*. *Bull. Chem. Soc. Jpn.* **66**, 231 – 237 (1993).
 64. Dudkowiak, A., Francke, C. & Amesz, J. Aggregation of 8, 12-diethyl farnesyl bacteriochlorophyll c at low temperature. *Photosynth. Res.* **46**, 427–433 (1995).
 65. Tamiaki, H. Supramolecular structure in extramembraneous antennae of green photosynthetic bacteria. *Coord. Chem. Rev.* **148**, 183–197 (1996).
 66. van Noort, P. I., Zhu, Y., LoBrutto, R. & Blankenship, R. E. Redox effects on the excited-state lifetime in chlorosomes and bacteriochlorophyll c oligomers. *Biophys. J.* **72**, 316–325 (1997).
 67. Balaban, T. & Leitich, J. Autocatalyzed self-aggregation of (3¹ R)-bacteriochlorophyll c F molecules in nonpolar solvents. Analysis of the kinetics. *J. Phys. Chem. B* **104**, 1362–1372 (2000).
 68. Mizoguchi, T., Hara, K., Nagae, H. & Koyama, Y. Structural transformation among the aggregate forms of bacteriochlorophyll c as determined by electronic-absorption and NMR spectroscopies: dependence on the stereoisomeric configuration and on the bulkiness of the 8-C side chain. *Photochem. Photobiol.* **71**, 596–609 (2000).
 69. Saga, Y., Matsuura, K. & Tamiaki, H. Spectroscopic Studies on Self-aggregation of Bacteriochlorophyll e in Nonpolar Organic Solvents: Effects of Stereoisomeric Configuration at the 3¹ Position and Alkyl Substituents at the 8¹ Position. *Photochem. Photobiol.* **74**, 72–80 (2001).
 70. Wang, Z., Kadota, T., Kobayashi, M., Kasuya, A. & Nozawa, T. NMR Relaxation Study of the Bacteriochlorophyll c in Solutions. *J. Phys. Chem. B* **108**, 15422–15428 (2004).

71. Uehara, K., Mimuro, M., Ozaki, Y. & Olson, J. The formation and characterization of the in vitro polymeric aggregates of bacteriochlorophyllc homologs from *Chlorobium limicola* in aqueous suspension in the presence of monogalactosyl diglyceride. *Photosynth. Res.* **41**, 235–243 (1994).
72. Miyatake, T. & Tamiaki, H. Self-aggregates of natural chlorophylls and their synthetic analogues in aqueous media for making light-harvesting systems. *Coord. Chem. Rev.* **254**, 2593–2602 (2010).
73. Miller, M., Gillbro, T. & Olson, J. Aqueous aggregates of bacteriochlorophyll c as a model for pigment organization in chlorosomes. *Photochem. Photobiol.* **57**, 98–102 (2008).
74. Hirota, M. *et al.* High degree of organization of bacteriochlorophyll c in chlorosome-like aggregates spontaneously assembled in aqueous solution. *Biochim. Biophys. Acta* **1099**, 271–274 (1992).
75. Ishii, T., Kimura, M., Yamamoto, T., Kirihata, M. & Uehara, K. The effects of epimerization at the 3¹-position of bacteriochlorophylls c on their aggregation in chlorosomes of green sulfur bacteria. Control of the ratio of 3¹ epimers by light intensity. *Photochem. Photobiol.* **71**, 567–573 (2000).
76. Kakitani, Y., Harada, K., Mizoguchi, T. & Koyama, Y. Isotopic replacement of pigments and a lipid in chlorosomes from *Chlorobium limicola*: characterization of the resultant chlorosomes. *Biochemistry* **46**, 6513–6524 (2007).
77. Balaban, T., Tamiaki, H. & Holzwarth, A. in *Supramolecular Dye Chemistry* (ed. Würthner, F.) 1–38 (Springer, 2005).
78. Tamiaki, H., Amakawa, Y., Tanikaga, R., Holzwarth, A. R. & Schaffner, K. Synthetic zinc and magnesium chlorin aggregates as models for supramolecular antenna complexes in chlorosomes of green photosynthetic bacteria. *Photochem. Photobiol.* **63**, 92–99 (1996).
79. Tamiaki, H., Holzwarth, A. R. & Schaffner, K. A synthetic zinc chlorin aggregate as a model for the supramolecular antenna complexes in the chlorosomes of green bacteria. *J. Photochem. Photobiol. B Biol.* **15**, 355–360 (1992).
80. Cheng, P., Liddell, P. a., Ma, S. X. C. & Blankenship, R. E. Properties of zinc and magnesium methyl bacteriopheophorbide d and their aggregates. *Photochem. Photobiol.* **58**, 290–295 (1993).
81. Wakao, N. *et al.* Discovery of natural photosynthesis using Zn-containing bacteriochlorophyll in an aerobic bacterium *Acidiphilium rubrum*. *Plant cell Physiol.* **37**, 889–893 (1996).
82. Tamiaki, H., Amakawa, M., Holzwarth, A. R. & Schaffner, K.

- Aggregation of synthetic metallochlorins in hexane. A model of chlorosomal bacteriochlorophyll self-assemblies in green bacteria. *Photosynth. Res.* **71**, 59–67 (2002).
83. Amakawa, M. & Tamiaki, H. Self-aggregates of a synthetic cadmium chlorin in solid film as a photosynthetic antenna model. *Bioorg. Med. Chem.* **7**, 1141–1144 (1999).
 84. Amakawa, M. & Tamiaki, H. Self-aggregation of synthetic cadmium chlorin. *J. Inorg. Biochem.* **S14**, 449 (1997).
 85. Balaban, T. S., Fromme, P., Holzwarth, A. R., Krauss, N. & Prokhorenko, V. I. Relevance of the diastereotopic ligation of magnesium atoms of chlorophylls in Photosystem I. *Photosynth. Res.* **86**, 197–207 (2002).
 86. Brus, L. E. Electron–electron and electron-hole interactions in small semiconductor crystallites: The size dependence of the lowest excited electronic state. *J. Chem. Phys.* **80**, 4403–4409 (1984).
 87. Wannier, G. H. The Structure of Electronic Excitation Levels in Insulating Crystals. *Phys. Rev.* **52**, 191–197 (1937).
 88. Frenkel, J. On the transformation of light into heat in solids. *Phys. Rev.* **37**, 17–44 (1931).
 89. Ekimov, A. I. *et al.* Absorption and intensity-dependent photoluminescence measurements on CdSe quantum dots: assignment of the first electronic transitions. *J. Opt. Soc. Am* **10**, 100–107 (1993).
 90. Weller, H. Colloidal Semiconductor Q-Particles: Chemistry in the Transition Region Between Solid State and Molecules. *Angew. Chemie Int. Ed. English* **32**, 41–53 (1993).
 91. Biju, V., Itoh, T. & Ishikawa, M. Delivering quantum dots to cells: bioconjugated quantum dots for targeted and nonspecific extracellular and intracellular imaging. *Chem. Soc. Rev.* **39**, 3031–3056 (2010).
 92. Murray, C. B., Norris, D. J. & Bawendi, M. G. Synthesis and Characterization of Nearly Monodisperse CdE (E = S, Se, Te) Semiconductor Nanocrystallites. *J. Am. Chem. Soc.* **115**, 8706–8715 (1993).
 93. Alivisatos, A. Perspectives on the physical chemistry of semiconductor nanocrystals. *J. Phys. Chem.* **3654**, 13226–13239 (1996).
 94. Klimov, V. *et al.* Optical Gain and Stimulated Emission in Nanocrystal Quantum Dots. *Science.* **290**, 314–317 (2000).
 95. Henini, M. Properties and applications of quantum dot heterostructures grown by molecular beam epitaxy. *Nanoscale Res. Lett.* **1**, 32–45 (2006).

96. Klimov, V. I. Mechanisms for Photogeneration and Recombination of Multiexcitons in Semiconductor. *J. Phys. Chem. B* **110**, 16827–16845 (2006).
97. Colvin, V., Schlamp, M. & Allvisatos, A. Light-emitting diodes made from cadmium selenide nanocrystals and a semiconducting polymer. *Nature* **370**, 354–357 (1994).
98. Shields, A. J. Semiconductor quantum light sources. *Nat. Photonics* **1**, 215–223 (2007).
99. Zhong, H., Bai, Z. & Zou, B. Tuning the Luminescence Properties of Colloidal I–III–VI Semiconductor Nanocrystals for Optoelectronics and Biotechnology Applications. *J. Phys. Chem. Lett.* **3**, 3167–3175 (2012).
100. Song, W.-S. & Yang, H. Efficient White-Light-Emitting Diodes Fabricated from Highly Fluorescent Copper Indium Sulfide Core/Shell Quantum Dots. *Chem. Mater.* **24**, 1961–1967 (2012).
101. Zhao, J. *et al.* Electroluminescence from isolated CdSe/ZnS quantum dots in multilayered light-emitting diodes. *J. Appl. Phys.* **96**, 3206–3210 (2004).
102. Yoon, H. C., Oh, J. H., Ko, M., Yoo, H. & Do, Y. R. Synthesis and Characterization of Green Zn–Ag–In–S and Red Zn–Cu–In–S Quantum Dots for Ultrahigh Color Quality of Down-Converted White LEDs. *ACS Appl. Mater. Interfaces* **7**, 7342–7350 (2015).
103. Kim, J. & Yang, H. All-solution-processed, multilayered CuInS₂/ZnS colloidal quantum-dot-based electroluminescent device. *Opt. Lett.* **39**, 5002–5005 (2014).
104. Yue, W. *et al.* CuInS₂ quantum dots synthesized by a solvothermal route and their application as effective electron acceptors for hybrid solar cells. *J. Mater. Chem.* **20**, 7570–7578 (2010).
105. Peng, Z., Liu, Y., Shu, W., Chen, K. & Chen, W. Synthesis of Various Sized CuInS₂ Quantum Dots and Their Photovoltaic Properties as Sensitizers for TiO₂ Photoanodes. *Eur. J. Inorg. Chem.* **2012**, 5239–5244 (2012).
106. Panthani, M. G. *et al.* Synthesis of CuInS₂, CuInSe₂, and Cu(In_xGa_{1-x})Se₂ (CIGS) Nanocrystal 'Inks' for Printable Photovoltaics. *J. Am. Chem. Soc.* **130**, 16770–16777 (2008).
107. Li, T.-L. & Teng, H. Solution synthesis of high-quality CuInS₂ quantum dots as sensitizers for TiO₂ photoelectrodes. *J. Mater. Chem.* **20**, 3656–3664 (2010).
108. Li, T.-L., Lee, Y.-L. & Teng, H. High-performance quantum dot-sensitized solar cells based on sensitization with CuInS₂ quantum

- dots/CdS heterostructure. *Energy Environ. Sci.* **5**, 5315–5324 (2012).
109. Li, L., Coates, N. & Moses, D. Solution-Processed Inorganic Solar Cell Based on in Situ Synthesis and Film Deposition of CuInS₂ Nanocrystals. *J. Am. Chem. Soc.* **132**, 22–23 (2010).
 110. Kamat, P. V. Quantum Dot Solar Cells. Semiconductor Nanocrystals as Light Harvesters. *J. Phys. Chem. C* **112**, 18737–18753 (2008).
 111. Karageorgopoulos, D., Stathatos, E. & Vitoratos, E. Thin ZnO nanocrystalline films for efficient quasi-solid state electrolyte quantum dot sensitized solar cells. *J. Power Sources* **219**, 9–15 (2012).
 112. Kida, T. *et al.* Visible-Light Sensitization and Photoenergy Storage in Quantum Dot/Polyoxometalate Systems. *Chemistry*. **21**, 7462–7469 (2015).
 113. Jung, S. W., Kim, J.-H., Kim, H., Choi, C.-J. & Ahn, K.-S. ZnS overlayer on in situ chemical bath deposited CdS quantum dot-assembled TiO₂ films for quantum dot-sensitized solar cells. *Curr. Appl. Phys.* **12**, 1459–1464 (2012).
 114. Jin, S., Son, H.-J., Farha, O. K., Wiederrecht, G. P. & Hupp, J. T. Energy transfer from quantum dots to metal-organic frameworks for enhanced light harvesting. *J. Am. Chem. Soc.* **135**, 955–958 (2013).
 115. Huang, W. *et al.* Solvothermal Synthesis of Zinblende and Wurtzite CuInS₂ Nanocrystals and Their Photovoltaic Application. *Langmuir* **28**, 8496–8501 (2012).
 116. Freitas, J. N., Gonçalves, A. S. & Nogueira, A. F. A comprehensive review of the application of chalcogenide nanoparticles in polymer solar cells. *Nanoscale* **6**, 6371–6397 (2014).
 117. Halpert, J. E. *et al.* Charge Dynamics in Solution-Processed Nanocrystalline CuInS₂ Solar Cells. *ACS Nano* **9**, 5857–5867 (2015).
 118. Klaer, J. *et al.* Efficient CuInS₂ thin-film solar cells prepared by a sequential process. *Semicond. Sci. Technol.* **13**, 1456–1458 (1998).
 119. Chan, W. C. & Nie, S. Quantum Dot Bioconjugates for Ultrasensitive Nonisotopic Detection. *Science*. **281**, 2016–2018 (1998).
 120. Bruchez Jr., M., Moronne, M., Gin, P., Weiss, S. & Alivisatos, A. Semiconductor Nanocrystals as Fluorescent Biological Labels. *Science*. **281**, 2013–2016 (1998).
 121. Pons, T. *et al.* Cadmium-free CuInS₂/ZnS quantum dots for sentinel lymph node imaging with reduced toxicity. *ACS Nano* **4**, 2531–2538 (2010).
 122. Deng, D. *et al.* High-Quality CuInS₂/ZnS Quantum Dots for In vitro and

- In vivo Bioimaging. *Chem. Mater.* **24**, 3029–3037 (2012).
123. Li, L. *et al.* Highly Luminescent CuInS₂/ZnS Core/Shell Nanocrystals: Cadmium-Free Quantum Dots for In Vivo Imaging. *Chem. Mater.* **21**, 2422–2429 (2009).
 124. Alivisatos, P. The use of nanocrystals in biological detection. *Nat. Biotechnol.* **22**, 47–52 (2004).
 125. Laurent, S. *et al.* Magnetic iron oxide nanoparticles: synthesis, stabilization, vectorization, physicochemical characterizations, and biological applications. *Chem. Rev.* **108**, 2064–2110 (2008).
 126. Zhang, P., He, Y., Ruan, Z., Chen, F. F. & Yang, J. Fabrication of quantum dots-encoded microbeads with a simple capillary fluidic device and their application for biomolecule detection. *J. Colloid Interface Sci.* **385**, 8–14 (2012).
 127. Parak, W. *et al.* Biological applications of colloidal nanocrystals. *Nanotechnology* **14**, R15–R27 (2003).
 128. Choi, H. S. *et al.* Highly luminescent, off-stoichiometric Cu_xIn_yS₂/ZnS quantum dots for near-infrared fluorescence bio-imaging. *RSC Adv.* **5**, 43449–43455 (2015).
 129. Yong, K.-T. *et al.* Synthesis of ternary CuInS₂/ZnS quantum dot bioconjugates and their applications for targeted cancer bioimaging. *Integr. Biol.* **2**, 121–129 (2010).
 130. Yong, K.-T. *et al.* Imaging pancreatic cancer using bioconjugated InP quantum dots. *ACS Nano* **3**, 502–510 (2009).
 131. Xie, R. & Peng, X. Synthesis of Cu-doped InP nanocrystals (d-dots) with ZnSe diffusion barrier as efficient and color-tunable NIR emitters. *J. Am. Chem. Soc.* **131**, 10645–10651 (2009).
 132. Smith, A. M., Duan, H., Mohs, A. M. & Nie, S. Bioconjugated quantum dots for in vivo molecular and cellular imaging. *Adv. Drug Deliv. Rev.* **60**, 1226–1240 (2008).
 133. Alivisatos, P., Gu, W. & Larabell, C. Quantum dots as cellular probes. *Annu. Rev. Biomed. Eng.* **7**, 55–76 (2005).
 134. Cassette, E. *et al.* Synthesis and Characterization of Near-Infrared Cu–In–Se/ZnS Core/Shell Quantum Dots for In vivo Imaging. *Chem. Mater.* **22**, 6117–6124 (2010).
 135. Derfus, A. M., Chan, W. C. W. & Bhatia, S. N. Probing the Cytotoxicity of Semiconductor Quantum Dots. *Nano Lett.* **4**, 11–18 (2004).
 136. Erogbogbo, F. *et al.* Biocompatible Luminescent Silicon. *ACS Nano* **2**, 873–878 (2008).

137. He, Y. *et al.* Ultrastable, highly fluorescent, and water-dispersed silicon-based nanospheres as cellular probes. *Angew. Chem. Int. Ed. Engl.* **48**, 128–132 (2009).
138. Kirchner, C. *et al.* Cytotoxicity of colloidal CdSe and CdSe/ZnS nanoparticles. *Nano Lett.* **5**, 331–338 (2005).
139. Michalet, X. *et al.* Quantum dots for live cells, in vivo imaging, and diagnostics. *Science.* **307**, 538–545 (2005).
140. Park, J. *et al.* CuInSe/ZnS core/shell NIR quantum dots for biomedical imaging. *Small* **7**, 3148–52 (2011).
141. Santori, C. *et al.* Photon correlation studies of single GaN quantum dots. *Appl. Phys. Lett.* **87**, 051916 (2005).
142. Lin, Y., Zhang, F. & Pan, D. A facile route to $(\text{ZnS})_x(\text{CuInS}_2)_{1-x}$ hierarchical microspheres with excellent water-splitting ability. *J. Mater. Chem.* **22**, 22619–22623 (2012).
143. Tsuji, I., Kato, H. & Kudo, A. Visible-light-induced H_2 evolution from an aqueous solution containing sulfide and sulfite over a ZnS-CuInS₂-AgInS₂ solid-solution photocatalyst. *Angew. Chem. Int. Ed. Engl.* **44**, 3565–3568 (2005).
144. Guo, Y. *et al.* Facile one-pot preparation of cadmium sulfide quantum dots with good photocatalytic activities under stabilization of polar amino acids. *Mater. Lett.* **86**, 146–149 (2012).
145. Ipe, B. I., Lehnig, M. & Niemeyer, C. M. On the generation of free radical species from quantum dots. *Small* **1**, 706–709 (2005).
146. Selvan, S. T., Tan, T. T. & Ying, J. Y. Robust, Non-Cytotoxic, Silica-Coated CdSe Quantum Dots with Efficient Photoluminescence. *Adv. Mater.* **17**, 1620–1625 (2005).
147. Ruddy, D. A., Johnson, J. C., Smith, E. R. & Neale, N. R. Size and Bandgap Control in the Solution-Phase Synthesis of Near-Infrared-Emitting Germanium Nanocrystals. *ACS Nano* **4**, 7459–7466 (2010).
148. Lee, D. C. *et al.* Colloidal synthesis of infrared-emitting germanium nanocrystals. *J. Am. Chem. Soc.* **131**, 3436–3437 (2009).
149. Lucey, D. W. *et al.* Monodispersed InP Quantum Dots Prepared by Colloidal Chemistry in a Noncoordinating Solvent. *Chem. Mater.* **17**, 3754–3762 (2005).
150. Pradhan, N., Goorskey, D., Thessing, J. & Peng, X. An Alternative of CdSe Nanocrystal Emitters: Pure and Tunable Impurity Emissions in ZnSe Nanocrystals. *J. Am. Chem. Soc.* **127**, 17586–17587 (2005).
151. Zhong, H. *et al.* A facile route to synthesize chalcopyrite CuInSe₂

- nanocrystals in non-coordinating solvent. *Nanotechnology* **18**, 025602 (2007).
152. Du, W., Qian, X., Yin, J. & Gong, Q. Shape- and phase-controlled synthesis of monodisperse, single-crystalline ternary chalcogenide colloids through a convenient solution synthesis strategy. *Chemistry*. **13**, 8840–8846 (2007).
 153. Torimoto, T. *et al.* Facile Synthesis of ZnS-AgInS₂ Solid Solution Nanoparticles for a colour-adjustable luminophore. *J. Am. Chem. Soc.* **129**, 12388–12389 (2007).
 154. Zhong, H. *et al.* Noninjection Gram-Scale Synthesis of Monodisperse Pyramidal CuInS₂ Nanocrystals and Their Size-Dependent Properties. *ACS Nano* **4**, 5253–5262 (2010).
 155. Li, L. *et al.* Efficient synthesis of highly luminescent copper indium sulfide-based core/shell nanocrystals with surprisingly long-lived emission. *J. Am. Chem. Soc.* **133**, 1176–1179 (2011).
 156. Xie, R., Rutherford, M. & Peng, X. Formation of high-quality I-III-VI semiconductor nanocrystals by tuning relative reactivity of cationic precursors. *J. Am. Chem. Soc.* **131**, 5691–5697 (2009).
 157. Kolny-Olesiak, J. & Weller, H. Synthesis and application of colloidal CuInS₂ semiconductor nanocrystals. *ACS Appl. Mater. Interfaces* **5**, 12221–12237 (2013).
 158. Liu, S., Zhang, H., Qiao, Y. & Su, X. One-pot synthesis of ternary CuInS₂ quantum dots with near-infrared fluorescence in aqueous solution. *RSC Adv.* **2**, 819–825 (2012).
 159. Qi, Y. *et al.* Synthesis and Characterization of Nanostructured Wurtzite CuInS₂: A New Cation Disordered Polymorph of CuInS₂. *J. Phys. Chem. C* **113**, 3939–3944 (2009).
 160. Jiang, Y. *et al.* Elemental solvothermal reaction to produce ternary semiconductor CuInE₂ (E= S, Se) nanorods. *Inorg. Chem.* **39**, 2964–2965 (2000).
 161. Nam, D.-E., Song, W.-S. & Yang, H. Noninjection, one-pot synthesis of Cu-deficient CuInS₂/ZnS core/shell quantum dots and their fluorescent properties. *J. Colloid Interface Sci.* **361**, 491–496 (2011).
 162. Nam, D.-E., Song, W.-S. & Yang, H. Facile, air-insensitive solvothermal synthesis of emission-tunable CuInS₂/ZnS quantum dots with high quantum yields. *J. Mater. Chem.* **21**, 18220–18226 (2011).
 163. Cui, Y., Ren, J., Chen, G., Qian, Y. & Xie, Y. A simple route to synthesize MInS₂ (M= Cu, Ag) nanorods from single-molecule precursors. *Chem. Lett.* **2**, 236–237 (2001).

164. Lu, Q. *et al.* Synthesis of nanocrystalline CuMS₂ (M = In or Ga) through a solvothermal process. *Inorg. Chem.* **39**, 1606–1607 (2000).
165. Liu, H.-T. *et al.* L-cystine-Assisted Growth and Mechanism of CuInS₂ Nanocrystallines via Solvothermal Process. *Chinese Phys. Lett.* **28**, 057702 (2011).
166. Kruszynska, M., Borchert, H., Parisi, J. & Kolny-Olesiak, J. Synthesis and shape control of CuInS₂ nanoparticles. *J. Am. Chem. Soc.* **132**, 15976–15986 (2010).
167. Norako, M. E., Franzman, M. a. & Brutchey, R. L. Growth Kinetics of Monodisperse Cu–In–S Nanocrystals Using a Dialkyl Disulfide Sulfur Source. *Chem. Mater.* **21**, 4299–4304 (2009).
168. Abdelhady, A. L., Malik, M. & O'Brien, P. iso-Propylthiobiuret-copper and indium complexes as novel precursors for colloidal synthesis of CuInS₂ nanoparticles. *J. Mater. Chem.* **22**, 3781–3785 (2012).
169. Pan, D. *et al.* Synthesis of Cu-In-S Ternary Nanocrystals with Tunable Structure and Composition. *J. Am. Chem. Soc.* **130**, 5620–5621 (2008).
170. Bao, N. *et al.* Facile thermolysis synthesis of CuInS₂ nanocrystals with tunable anisotropic shape and structure. *Chem. Commun.* **47**, 9441–9443 (2011).
171. Zhang, A. *et al.* Copper-indium sulfide hollow nanospheres synthesized by a facile solution-chemical method. *Cryst. Growth Des.* **8**, 2402–2405 (2008).
172. Czekelius, C. *et al.* A simple colloidal route to nanocrystalline ZnO/CuInS₂ bilayers. *Adv. Mater.* **11**, 643–646 (1999).
173. Sheng, X., Wang, L., Luo, Y. & Yang, D. Synthesis of hexagonal structured wurtzite and chalcopyrite CuInS₂ via a simple solution route. *Nanoscale Res. Lett.* **6**, 562 (2011).
174. Park, J. & Kim, S.-W. CuInS₂/ZnS core/shell quantum dots by cation exchange and their blue-shifted photoluminescence. *J. Mater. Chem.* **21**, 3745–3745 (2011).
175. Kruszynska, M., Borchert, H., Parisi, J. & Kolny-Olesiak, J. Investigations of solvents and various sulfur sources influence on the shape-controlled synthesis of CuInS₂ nanocrystals. *J. Nanoparticle Res.* **13**, 5815–5824 (2011).
176. Niezgodna, J. S., Harrison, M., McBride, J. R. & Rosenthal, S. J. Novel Synthesis of Chalcopyrite Cu_xIn_yS₂ Quantum Dots with Tunable Localized Surface Plasmon Resonances. *Chem. Mater.* **24**, 3294–3298 (2012).
177. Batabyal, S. K., Tian, L., Venkatram, N., Ji, W. & Vittal, J. J. Phase-

- Selective Synthesis of CuInS₂ Nanocrystals. *J. Phys. Chem. C* **113**, 15037–15042 (2009).
178. Koo, B., Patel, R. N. & Korgel, B. A. Wurtzite-Chalcopyrite Polytypism in CuInS₂ Nanodisks. *Chem. Mater.* **21**, 1962–1966 (2009).
179. Nose, K., Soma, Y., Omata, T. & Otsuka-Yao-Matsuo, S. Synthesis of Ternary CuInS₂ Nanocrystals; Phase Determination by Complex Ligand Species. *Chem. Mater.* **21**, 2607–2613 (2009).
180. Bera, P. & Seok, S. Facile synthesis of nanocrystalline wurtzite Cu–In–S by amine-assisted decomposition of precursors. *J. Solid State Chem.* **183**, 1872–1877 (2010).
181. Castro, S. L., Bailey, S. G., Raffaele, R. P., Banger, K. K. & Hepp, A. F. Synthesis and Characterization of Colloidal CuInS₂ Nanoparticles from a Molecular Single-Source Precursor. *J. Phys. Chem. B* **108**, 12429–12435 (2004).
182. Zhong, H. *et al.* Controlled Synthesis and Optical Properties of Colloidal Ternary Chalcogenide CuInS₂ Nanocrystals. *Chem. Mater.* **20**, 6434–6443 (2008).
183. Uehara, M., Watanabe, K., Tajiri, Y., Nakamura, H. & Maeda, H. Synthesis of CuInS₂ fluorescent nanocrystals and enhancement of fluorescence by controlling crystal defect. *J. Chem. Phys.* **129**, 134709 (2008).
184. Chen, B. *et al.* Highly Emissive and Color-Tunable CuInS₂-Based Colloidal Semiconductor Nanocrystals: Off-Stoichiometry Effects and Improved Electroluminescence Performance. *Adv. Funct. Mater.* **22**, 2081–2088 (2012).
185. Nakamura, H. *et al.* Tunable photoluminescence wavelength of chalcopyrite CuInS₂-based semiconductor nanocrystals synthesized in a colloidal system. *Chem. Mater.* **18**, 3330–3335 (2006).
186. Lu, X., Zhuang, Z., Peng, Q. & Li, Y. Controlled synthesis of wurtzite CuInS₂ nanocrystals and their side-by-side nanorod assemblies. *CrystEngComm* **13**, 4039–4045 (2011).
187. Pein, A. *et al.* Investigation of the formation of CuInS₂ nanoparticles by the oleylamine route: Comparison of microwave-assisted and conventional syntheses. *Inorg. Chem.* **50**, 193–200 (2011).
188. Tang, X., Cheng, W., Choo, E. S. G. & Xue, J. Synthesis of CuInS₂-ZnS alloyed nanocubes with high luminescence. *Chem. Commun.* **47**, 5217–5219 (2011).
189. Chang, J. & Waclawik, E. R. Controlled synthesis of CuInS₂, Cu₂SnS₃ and Cu₂ZnSnS₄ nano-structures: insight into the universal phase-

- selectivity mechanism. *Crystengcomm* **15**, 5612–5619 (2013).
190. Yao, R.-Y. *et al.* Surfactant-Free CuInS₂ Nanocrystals: An Alternative Counter-Electrode Material for Dye-Sensitized Solar Cells. *ACS Appl. Mater. Interfaces* **5**, 3143–3148 (2013).
 191. Yu, K. *et al.* Low-Temperature approach to highly emissive copper indium sulfide colloidal nanocrystals and their bioimaging applications. *ACS Appl. Mater. Interfaces* **5**, 2870–2880 (2013).
 192. Shi, L., Pei, C. & Li, Q. Ordered arrays of shape tunable CuInS₂ nanostructures, from nanotubes to nano test tubes and nanowires. *Nanoscale* **2**, 2126–2130 (2010).
 193. Chen, Y., Li, S., Huang, L. & Pan, D. Green and Facile Synthesis of Water-Soluble Cu-In-S/ZnS Core/Shell Quantum Dots. *Inorg. Chem.* **52**, 7819–7821 (2013).
 194. Dutta, D. P. & Sharma, G. A facile route to the synthesis of CuInS₂ nanoparticles. *Mater. Lett.* **60**, 2395–2398 (2006).
 195. Kino, T. *et al.* Synthesis of Chalcopyrite Nanoparticles via Thermal Decomposition of Metal-Thiolate. *Mater. Trans.* **49**, 435–438 (2008).
 196. Wang, D., Zheng, W., Hao, C., Peng, Q. & Li, Y. General synthesis of I-III-VI₂ ternary semiconductor nanocrystals. *Chem. Commun.* **2008**, 2556–2558 (2008).
 197. Connor, S. T., Hsu, C.-M., Weil, B. D., Aloni, S. & Cui, Y. Phase transformation of biphasic Cu₂S-CuInS₂ to monophasic CuInS₂ nanorods. *J. Am. Chem. Soc.* **131**, 4962–4966 (2009).
 198. Chiang, M., Chang, S., Chen, C.-Y., Yuan, F.-W. & Tuan, H. Quaternary CuIn(S_{1-x}Se_x)₂ Nanocrystals: Facile Heating-Up Synthesis, Band Gap Tuning, and Gram-Scale Production. *J. Phys. Chem. C* **115**, 1592–1599 (2011).
 199. Nairn, J. J. *et al.* Preparation of ultrafine chalcopyrite nanoparticles via the photochemical decomposition of molecular single-source precursors. *Nano Lett.* **6**, 1218–1223 (2006).
 200. Gardner, J. S. *et al.* Rapid synthesis and size control of CuInS₂ semiconductor nanoparticles using microwave irradiation. *J. Nanoparticle Res.* **10**, 633–641 (2008).
 201. Bensebaa, F. *et al.* A new green synthesis method of CuInS₂ and CuInSe₂ nanoparticles and their integration into thin films. *J. Nanoparticle Res.* **12**, 1897–1903 (2010).
 202. Sun, C. *et al.* Controlled stoichiometry for quaternary CuIn_xGa_{1-x}S₂ chalcopyrite nanoparticles from single-source precursors via microwave irradiation. *Chem. Mater.* **22**, 2699–2701 (2010).

203. Sun, C. *et al.* A High-Yield Synthesis of Chalcopyrite CuInS₂ Nanoparticles with Exceptional Size Control. *J. Nanomater.* **2009**, 1–7 (2009).
204. Omata, T., Nose, K. & Otsuka-Yao-Matsuo, S. Size dependent optical band gap of ternary I-III-VI₂ semiconductor nanocrystals. *J. Appl. Phys.* **105**, 073106 (2009).
205. Huxter, V. M., Mirkovic, T., Nair, P. S. & Scholes, G. D. Demonstration of Bulk Semiconductor Optical Properties in Processable Ag₂S and EuS Nanocrystalline Systems. *Adv. Mater.* **20**, 2439–2443 (2008).
206. Tell, B., Shay, J. & Kasper, H. Electrical Properties, Optical Properties, and Band Structure of CuGaS₂ and CuInS₂. *Phys. Rev. B* **4**, 2463–2471 (1971).
207. Jaffe, J. & Zunger, A. Theory of the band-gap anomaly in ABC₂ chalcopyrite semiconductors. *Phys. Rev. B* **29**, 1882–1906 (1984).
208. Chen, H., Wang, C. Y., Wang, J. T., Hu, X. P. & Zhou, S. X. First-principles study of point defects in solar cell semiconductor CuInS₂. *J. Appl. Phys.* **112**, 084513 (2012).
209. Huang, D. & Persson, C. Stability of the bandgap in Cu-poor CuInSe₂. *J. Phys. Condens. Matter* **24**, 455503 (2012).
210. Vidal, J., Botti, S., Olsson, P., Guillemales, J. F. & Reining, L. Strong interplay between structure and electronic properties in CuIn(S,Se)₂: A first-principles study. *Phys. Rev. Lett.* **104**, 1–4 (2010).
211. Booth, M., Brown, A. P., Evans, S. D. & Critchley, K. Determining the Concentration of CuInS₂ Quantum Dots from the Size-Dependent Molar Extinction Coefficient. *Chem. Mater.* **24**, 2064–2070 (2012).
212. Qin, L. *et al.* The determination of extinction coefficient of CuInS₂, and ZnCuInS₃ multinary nanocrystals. *Nanoscale* **4**, 6360–6364 (2012).
213. Li, J. J. *et al.* Large-scale synthesis of nearly monodisperse CdSe/CdS core/shell nanocrystals using air-stable reagents via successive ion layer adsorption and reaction. *J. Am. Chem. Soc.* **125**, 12567–12575 (2003).
214. Cumberland, S. L. *et al.* Inorganic Clusters as Single-Source Precursors for Preparation of CdSe, ZnSe, and CdSe/ZnS Nanomaterials. *Chem. Mater.* **14**, 1576–1584 (2002).
215. Kraatz, I., Booth, M., Whitaker, B., Nix, M. & Critchley, K. Bandgap Emission and Intraband Defect-Related Excited-State Dynamics in Colloidal CuInS₂/ZnS Quantum Dots Revealed by Femtosecond Pump–Dump–Probe. *J. Phys. Chem. C* **118**, 24102–24109 (2014).
216. Zhang, S. B., Wei, S.-H., Zunger, A. & Katayama-Yoshida, H. Defect

- physics of the CuInSe₂ chalcopyrite semiconductor. *Phys. Rev. B* **57**, 9642–9656 (1998).
217. Hofhuis, J., Schoonman, J. & Goossens, A. Elucidation of the Excited-State Dynamics in CuInS₂ Thin Films. *J. Phys. Chem. C* **112**, 15052–15059 (2008).
 218. Nanu, M., Boulch, F., Schoonman, J. & Goossens, A. Deep-level transient spectroscopy of TiO₂/CuInS₂ heterojunctions. *Appl. Phys. Lett.* **87**, 242103 (2005).
 219. Massé, G. Concerning lattice defects and defect levels in CuInSe₂ and the I-III-VI₂ compounds. *J. Appl. Phys.* **68**, 2206–2210 (1990).
 220. Wahlund, T., Woese, C., Castenholz, R. & Madigan, M. A thermophilic green sulfur bacterium from New Zealand hot springs, *Chlorobium tepidum* sp. nov. *Arch. Microbiol.* **156**, 81–90 (1991).
 221. Zhu, Y., Lin, S., Ramakrishna, B. L., Noort, P. I. Van & Blankenship, R. E. Self quenching of chlorosome chlorophylls in water and hexanol-saturated water. *Photosynth. Res.* **47**, 207–218 (1996).
 222. Stanier, R. & Smith, J. The chlorophylls of green bacteria. *Biochim. Biophys. Acta* **41**, 478–484 (1960).
 223. Borrego, C. M., Arellano, J. B., Abella, C. A. & Gillbro, T. The molar extinction coefficient of bacteriochlorophyll e and the pigment stoichiometry in *Chlorobium phaeobacteroides*. *Photosynth. Res.* **17**, 257–264 (1999).
 224. Craft, N. *Handbook of Food Analytical Chemistry*. (Wiley, 2000).
 225. McCammon, J. A., Gelin, B. R. & Karplus, M. Dynamics of folded proteins. *Nature* **267**, 585–90 (1977).
 226. Schlick, T., Collepardo-Guevara, R., Halvorsen, L. A., Jung, S. & Xiao, X. *Biomolecular modeling and simulation: a field coming of age. Quarterly Reviews of Biophysics* **44**, 119-228 (2011).
 227. Sweeney, S. F., Woehrlé, G. H. & Hutchison, J. E. Rapid purification and size separation of gold nanoparticles via diafiltration. *J. Am. Chem. Soc.* **128**, 3190–7 (2006).
 228. Valenta, J. Determination of absolute quantum yields of luminescing nanomaterials over a broad spectral range: from the integrating sphere theory to the correct methodology. *Nanosci. Methods* **3**, 11–27 (2014).
 229. Alster, J. Study of light-harvesting antennae based on bacteriochlorophyll aggregates (PhD Thesis). (Charles University Prague, 2011).
 230. Alster, J. *et al.* β -Carotene to bacteriochlorophyll c energy transfer in

- self-assembled aggregates mimicking chlorosomes. *Chem. Phys.* **373**, 90–97 (2010).
231. Gomez Maqueo Chew, A., Frigaard, N.-U. & Bryant, D. a. Bacteriochlorophyllide c C-8² and C-12¹ methyltransferases are essential for adaptation to low light in *Chlorobaculum tepidum*. *J. Bacteriol.* **189**, 6176–84 (2007).
 232. Saga, Y., Osumi, S., Higuchi, H. & Tamiaki, H. Bacteriochlorophyll-c homolog composition in green sulfur photosynthetic bacterium *Chlorobium vibrioforme* dependent on the concentration of sodium sulfide in liquid cultures. *Photosynth. Res.* **86**, 123–30 (2005).
 233. Moulder, J. F., Stickle, W. F., Sobol, P. E. & Bomben, K. D. *Handbook of X-ray Photoelectron Spectroscopy*. (Physical Electronics, Inc., 1992).
 234. Booth, M. *et al.* Amphipol-encapsulated CuInS₂/ZnS quantum dots with excellent colloidal stability. *RSC Adv.* **3**, 20559–20566 (2013).
 235. Harvie, A. J. *et al.* Observation of compositional domains within individual copper indium sulfide quantum dots. *Nanoscale* **5**, 43449–43455 (2016).
 236. Akdas, T. *et al.* The effects of post-processing on the surface and the optical properties of copper indium sulfide quantum dots. *J. Colloid Interface Sci.* **445**, 337–347 (2015).
 237. Deng, Z. & Mao, C. DNA-Templated Fabrication of 1D Parallel and 2D Crossed Metallic Nanowire Arrays. *Nano Lett.* **3**, 1545–1548 (2003).
 238. Gong, F., Tian, S., Liu, B., Xiong, D. & Zhao, X. Oleic acid assisted formation mechanism of CuInS₂ nanocrystals with tunable structures. *RSC Adv.* **4**, 36875–36881 (2014).
 239. Dierick, R. *et al.* Surface Chemistry of CuInS₂ Colloidal Nanocrystals, Tight Binding of L-Type Ligands. *Chem. Mater.* **26**, 5950–5957 (2014).
 240. Omata, T., Nose, K., Kurimoto, K. & Kita, M. Electronic transition responsible for size-dependent photoluminescence of colloidal CuInS₂ quantum dots. *J. Mater. Chem. C* **2**, 6867–6872 (2014).
 241. Sakamoto, M. *et al.* Photoinduced Carrier Dynamics of Nearly Stoichiometric Oleylamine-Protected Copper Indium Sulfide Nanoparticles and Nanodisks. *J. Phys. Chem. C* **119**, 11100–11105 (2015).
 242. Sun, C. *et al.* One-pot synthesis and characterization of chalcopyrite CuInS₂ nanoparticles. *J. Mater. Chem. A* **2**, 10629–10633 (2014).
 243. Tanaka, M., Critchley, K., Matsunaga, T., Evans, S. D. & Staniland, S. S. Fabrication of lipid tubules with embedded quantum dots by membrane tubulation protein. *Small* **8**, 1590–1595 (2012).

244. Venkatram, N., Batabyal, S. K., Tian, L., Vittal, J. J. & Ji, W. Shape-dependent nonlinear absorption and relaxation in CuInS₂ nanocrystals. *Appl. Phys. Lett.* **95**, 201109 (2009).
245. Wang, X. *et al.* A high efficient photoluminescence Zn–Cu–In–S/ZnS quantum dots with long lifetime. *J. Alloys Compd.* **640**, 134–140 (2015).
246. Xia, C. *et al.* One-step synthesis of near-infrared emitting and size tunable CuInS₂ semiconductor nanocrystals by adjusting kinetic variables. *CrystEngComm* **16**, 7469–7477 (2014).
247. Yin, Z. *et al.* One-pot controllable synthesis of wurtzite CuInS₂ nanoplates. *Appl. Surf. Sci.* **307**, 489–494 (2014).

Appendix A

Summary of “heat up” synthesis methods

Table A.1 Overview of experimental procedures for ‘heating up’ methods

Reagents/precursors	Method	NP properties (morphology, size, crystal phase)	Ref
Cu(SON(CNPr ₂) ₂) ₂ , In(SON(CNPr ₂) ₂) ₃ , OLAM, 1-DDT	200 – 280 °C, 1 h	10 nm, trigonal, quasi-spherical, hexagonal, conical, CP, WZ	Abdelhady et al. 2012 ¹⁶⁸
1-ODE, CuAc, In(OAc) ₃ , 1-DDT,	240 °C, 18 min	3 nm, tetragonal, CP	Akdas et al. 2015 ²³⁶
(Ph ₃ P)CuIn(SC{O}Ph) ₄ , 1-DDT, TOPO	350 °C	platelike, WZ, ZB	Batabyal et al. 2009 ¹⁷⁷
(Cu(SMDTC)Cl ₂), (In(SMDTC) ₂ Cl ₂)Cl, EN	120 °C, 1 h	anisotropic hexagonal, WZ	Bera et al. 2010 ¹⁸⁰
CuI, In(OAc) ₃ , 1-DDT	230 °C, 10 min to 1.5 h	2.5-5 nm, tetragonal, CP	Booth et al. 2012 ²¹¹
CuI, In(OAc) ₃ , 1-DDT	230 °C, 5 min to 1 h	~3 nm, tetragonal, CP	Booth et al. 2013 ²³⁴
(Ph ₃) ₂ CuIn(SET) ₄ , hexanethiol, dioctylphthalate	250/300 °C, 1 h	2-4 nm CP	Castro et al. 2004 ¹⁸¹
CuI, In(OAc) ₃ , 1-DDT, ODE CuI, In(OAc) ₃ , 1-DDT, OLAM	220 °C, overnight 190 °C, overnight	9 nm, 25 nm triangular pyramid, ZB hexagonal nanodisc, WZ	Chang et al. 2013 ¹⁸⁹
CuI, In(OAc) ₃ , 1-DDT, OA, ODE	210 °C, 60 min	5 nm, CP	Chen et al. 2012 ¹⁸⁴
CuCl, InCl ₃ , Na ₂ S, sodium citrate, thiourea, L-glutathion, H ₂ O	95 °C, 40 min	2.1 nm, ZB	Chen et al. 2013 ¹⁹³
CuCl, InCl ₃ , S, OLAM	265 °C, 1.5 h	15–17 nm, quasi-spherical, CP	Chiang et al. 2011 ¹⁹⁸
CuI, In(OAc) ₃ , DDT	180 °C, 10 h	3 nm, ZB	Choi et al. 2015 ¹²⁸
Cu-oleate, In-oleate, 1-DDT, OLAM	215 – 300 °C, 20 min	nanorods, WZ	Connor et al. 2009 ¹⁹⁷
Cu(OAc) ₂ , In(OAc) ₃ , 1-DDT, OA, ODE	215 – 280 °C	2.5 nm, ZB	Deng et al. 2012 ²³⁷

Cu(S ₂ COEt), In(S ₂ COEt) ₃ , EG	196 °C, 15 min to 4 h	3.6-3.8 nm, ~spherical, CP	Dutta et al. 2006 ¹⁹⁴
CuCl, InCl ₃ x 4H ₂ O, DDT, OA, ODE	200 °C, 30 min	tetragonal, ZB, hexagonal, WZ	Gong et al. 2014 ²³⁸
CuI, In(OAc) ₃ x H ₂ O, thiourea, OA	180 °C, 1 h	~10 nm, spheroidal, WZ	Halpert et al. 2015 ¹¹⁷
Cu(OAc) ₂ , In(OAc) ₃ , 1-DDT, Sn(OAc) ₂ Cl ₂	200 °C, 120 min	polygonal, CP	He et al. 2012 ¹²⁶
Cu(OAc) ₂ , In(OAc) ₃ , 1-DDT, tri-n-octylamine	230 °C	1.8–2.8 nm, quasi-spherical, CP	Kino et al. 2008 ¹⁹⁵
CuCl, InCl ₃ , thiourea, OLAM	240 °C, 1 h	13.4 × 5.7 nm, nanodiscs, CP/WZ	Koo et al. 2009 ¹⁷⁸
CuI, In(OAc) ₃ , 1-DDT	210 °C, 5 min – 1 h	3.4 nm tetragonal, CP	Kraatz et al. 2014 ²¹⁵
CuI, In(OAc) ₃ , 1-DDT, ODE	200–270 °C, 15–290 min	platelike, WZ, ZB	Li et al. 2009 ¹²³
CuI, In(OAc) ₃ , 1-DDT	230 °C, 5 min to 1 h	3–8 nm, triangular, CP	Li et al. 2011 ¹⁵⁵
Cu(NO ₃) ₂ , In(NO ₃) ₃ , 1-DDT, OLAM, OA	240 °C, 30 min	quasi-spherical, rods, WZ	Lu et al. 2011 ¹⁸⁶
Cu(acac) ₂ , In(acac) ₃ , S, OLAM, (ODAm, OLAm, ODE)/(OLAm, ODE)	241 °C, 1 h	7 nm, hexagonal tiles, CP	Martins et al. 2014 ²³⁹
CuI, InI ₃ , S, OLAM, TOP, ODE	160–180 °C, 60–300 s	3-6 nm, CP	Nakamura et al. 2006 ¹⁸⁵
CuI, InCl ₃ , S/triphenylphosphite, TOOP, HDA, ODE	200–240 °C, 2–10 min	5 nm, ZB, WZ	Nose et al. 2009 ¹⁷⁹
CuI, OLA, ODE, InBr ₃ , OLA, ODE, S, TPOP, TOOP	200 °C, 30 s - 30 min	2.9 - 4.1 nm, ~spherical, CP	Omata et al. 2014 ²⁴⁰
CuI, InCl ₃ , OLAM, S	120 °C 15 min - 20 h, 220 °C, 15 min - 80 min	3 - 10 nm, irregular shapes, CP	Pein et al. 2011 ¹⁸⁷
CuI, In(acac) ₃ , n-DDT, 1-ODE, OA	200 °C, 10-120 min	2 - 8 nm, CP	Peng et al. 2012 ¹⁰⁵
o-dichlorobenzene, OLAM, Cu(acac) ₂ , In(acac) ₃ , S	180 °C, 1 h	7.4 nm, spherical, CP	Sakamoto et al. 2015 ²⁴¹
Cu(acac) ₂ , In(acac) ₃ , S, OLAM, o-dichlorobenzene	180 °C, 1 h	20 × 200, nanotubes, CP	Shi et al. 2010 ¹⁹²
CuI, In(OAc) ₃ , 1-DDT	230 °C, 5 min	2 nm, CP	Song et al. 2012 ¹⁰⁰
Ph ₃ P, CuCl, benzyl acetate, InCl ₃ , NaSEt	150 - 190 °C, 3 h	1.8 - 5.2 nm, CP	Sun et al. 2014 ²⁴²

Cu(OAc) ₂ , In(OAc) ₃ , 1-DDT, OA, TOP, ODE	120 °C, 10 min	9–11.5 nm, cubic, CP	Tang et al. 2011 ¹⁸⁸
InAc, CuI, 1-NNT	200 °C, until desired colour	2-3 nm, CP	Tanaka et al. 2012 ²⁴³
CuI, InI, S, OLAM, DDT	160–240 °C	~4 nm, CP	Uehara et al. 2008 ¹⁸³
[(Ph ₃ P)CuIn(SC(O)Ph) ₄], DDT, TOPO	150, 250, 350 °C, 15 h	6.5 - 35 nm, WZ, ZB	Venkatram et al. 2009 ²⁴⁴
CuCl, In(NO ₃) ₃ , S, octadecylamine	120 °C, 10 min	7 nm ~spherical	Wang et al. 2008 ¹⁹⁶
CuCl, DDT, In(Ac) ₃	230 °C, 60 min	2.2 - 2.5 nm, CP	Wang et al. 2015 ²⁴⁵
CuI, In(Ac) ₃ , DDT, ODE	230 °C	Irregular nanorods, 2.9 nm CP	Xia et al. 2014 ²⁴⁶
In(OAc) ₃ , CuCl, 1-DDT, ODE	240 °C, 1 h	~7 nm, CP	Yao et al. 2013 ¹⁹⁰
Cu(acac) ₂ , InCl ₃ , DDT, ODE	220 °C, ~10s of min	Hexagonal nanoplates, 5.8 - 9.6 nm, WZ	Yin et al. 2014 ²⁴⁷
CuI, In(OAc) ₃ , 1-DDT, diphenylphosphine sulphide	50 – 160 °C	2.8–3.4 nm, quasi-spherical, CP	Yu et al. 2013 ¹⁹¹
CuAc, In(Ac) ₃ , DDT, ODE	240 °C, 1 - 360 min	Nanoparticles, 2 - 5 nm, nanorods w/ aspect ratios of 1 - 3, CP	Zhong et al. 2008 ¹⁸²
CuI, In(OAc) ₃ , DDT, ODE, OA	200 °C, 20 - 120 min	Pyrimidal, 3 - 8 nm, CP.	Zhong et al. 2010 ¹⁵⁴

Appendix B

Preparation of triple layer pigment systems for simulation

This section lists the c script (a modified version of a script provided by Roman Tuma) used to prepare triple layer pigment sheets from quantum mechanically optimised single layer pigment systems.

```
#include <stdio.h>
#include <math.h>
#include <fcntl.h>
#include <stdlib.h>
#include <string.h>
#define NP 120 /* max number of input coord pts */
#define NS 180
float x[NP], y[NP], z[NP]; // input coords of diffracting
points
float xr[NP], yr[NP], zr[NP]; // output coords of
diffracting points
char s1[NP][50],s2[NP][50],s3[NP][50], s4[NP][50],
s5[NP][50], s6[NP][50], s7[NP][50];
int main(int na, char *ars[])
{
    FILE *fp1, *fp2;
    int np; // nro of atoms in one structure
    int k,i,j,i1,i2,n,nr=1;
    char c, spc[10];
    int no,npo=1; // nro of output data pts
    float q1,q2, dil=1.0, phi=0, r;
    float xm, ym, zm, xm0, ym0, zm0,x0,y0,z0,x1,y1,z1;
    if(na==3)
        {
            printf("\n processing script file : %s  output
into file: %s \n", ars[1], ars[2]);
            fp1=fopen(ars[1],"r");fp2=fopen(ars[2],"w");
            if(fp2==NULL){printf("\n problem opening output
file\n");exit(-1);};
            if(fp1==NULL){printf("\n input file
missing\n");exit(-1);}else
```

```

    {
        fscanf(fp1,"%i", &n);fprintf(fp2,"%i\n",3*n);
        if(n>NP*NS){printf("\n out of memory: too
many points\n"); exit(-1);}
        fscanf(fp1,"%f, ",&q1);
        q1=0.05; fprintf(fp2,"%f\n",q1);
        fscanf(fp1,"%f, ",&q2);
        q2=2.5; fprintf(fp2,"%f\n",q2);
        fscanf(fp1,"%i,
",&no);fprintf(fp2,"%i\n",no);
        np=0;
        printf("np = %i \n",n);
        do
            {
                fscanf(fp1,"%s",&s1[np][0]);//printf("\n
>%s<",s1[np]);
                c=s1[np][0];
                while (c != 84 && c != 69)
                    {
                        fscanf(fp1,"%s",&s2[np][0]);
                        fscanf(fp1,"%s",&s3[np][0]);
                        fscanf(fp1,"%s",&s4[np][0]);
                        fscanf(fp1,"%s",&s5[np][0]);
                        fscanf(fp1,"%f", &x[np]);
                        fscanf(fp1,"%f", &y[np]);
                        fscanf(fp1,"%f", &z[np]);
                        fscanf(fp1,"%s",&s6[np][0]);
                    }
                if(s3[np][0]=='M'){xm=x[np];ym=y[np];zm=z[np]; };
                fscanf(fp1,"%s",&s7[np][0]);
                np++;
                fscanf(fp1,"%s",&s1[np][0]);
                c=s1[np][0]; //printf("\n np=%i >%s<
c=<%c>",np,s1[np],c);
            };
        // printf("Mg nro %i = %f %f %f\n", np,
xm, ym, zm);
        for(i=0;i<np;i++)
            {
                // transformation of coords starts

```

```
        xr[i]=x[i];
        yr[i]=y[i];
        zr[i]=z[i];
        spc[0]='\0';
        if(strlen(s3[i])==2){spc[0]='
';spc[1]=' ';spc[2]='\0';}
        if(strlen(s3[i])==3){spc[0]='
';spc[1]='\0';}
        fprintf(fp2,"%s %6i %s%s%4s%6i %
8.3f%8.3f% 8.3f %s\n",s1[i],npo,s3[i],spc, s4[i], nr,
xr[i],yr[i],zr[i],s6[i]);
        npo++;
    }
    nr++;
    fprintf(fp2,"%s\n",s1[np]);
    for(i=0;i<np;i++)
    {
// transformation of coords lamellar 1 starts
        xr[i]=x[i]+10;
        yr[i]=y[i]+30;
        zr[i]=z[i];
        spc[0]='\0';
        if(strlen(s3[i])==2){spc[0]='
';spc[1]=' ';spc[2]='\0';}
        if(strlen(s3[i])==3){spc[0]='
';spc[1]='\0';}
        fprintf(fp2,"%s %6i %s%s%4s%6i %
8.3f%8.3f% 8.3f %s\n",s1[i],npo,s3[i],spc, s4[i], nr,
xr[i],yr[i],zr[i],s6[i]);
        npo++;
    }
    nr++;
    fprintf(fp2,"%s\n",s1[np]);
    for(i=0;i<np;i++)
    {
// transformation of coords lamellar 2 starts
        xr[i]=x[i]+10;
        yr[i]=y[i]+60;
        zr[i]=z[i];
```

```
        spc[0]='\0';
        if(strlen(s3[i])==2){spc[0]='
';spc[1]=' ';spc[2]='\0';}
        if(strlen(s3[i])==3){spc[0]='
';spc[1]='\0';}

        fprintf(fp2,"%s %6i %s%s%4s%6i %
8.3f%8.3f% 8.3f %s\n",s1[i],npo,s3[i],spc, s4[i], nr,
xr[i],yr[i],zr[i],s6[i]);
        npo++;
    }
nr++;

    fprintf(fp2,"%s\n",s1[np]);
    np=0;
}while (c != 69);
fclose(fp1);fclose(fp2);
//for(i=0;i<20;i++)printf(">%f<>%f<>%f<
atom= %s \n",x[i],y[i],z[i], s3[i]);
    }
}
else printf("\n usage inputfile outputfile\n");
return 0;
}
```

Appendix C

Amber simulation scripts

This section lists the Amber simulation scripts used to perform the molecular dynamics simulations in Chapter 4. This includes the shell script used to run simulation (Section C.1), the four minimisation steps, min1-min4,(Section C.2-C.5) and the nine molecular dynamics steps, md1-md9, (Section C.6 – C.14).

C.1 equil.sh

```
#!/bin/bash
#$ -cwd -V
#$ -l h_rt=48:00:00
#$ -pe ib 16
module add amber
l=crd
f=min1
mpirun pmemd.MPI \
    -O -i $f.in -o FILE$f.out -inf FILE$f.inf \
    -c FILE.$l -ref FILE.$l -r FILE.$f \
    -p FILE.top -x FILE$f.x -e FILE$f.ene
l=min1
f=min2
mpirun pmemd.MPI \
    -O -i $f.in -o FILE$f.out -inf FILE$f.inf \
    -c FILE.$l -ref FILE.$l -r FILE.$f \
    -p FILE.top -x FILE$f.x -e FILE$f.ene
l=min2
f=min3
mpirun pmemd.MPI \
    -O -i $f.in -o FILE$f.out -inf FILE$f.inf \
    -c FILE.$l -ref FILE.$l -r FILE.$f \
    -p FILE.top -x FILE$f.x -e FILE$f.ene
l=min3
f=min4
mpirun pmemd.MPI \
    -O -i $f.in -o FILE$f.out -inf FILE$f.inf \
```

```
        -c FILE.$l -ref FILE.$l -r FILE.$f \  
        -p FILE.top -x FILE$f.x -e FILE$f.ene  
l=min4  
f=md1  
mpirun pmemd.MPI \  
        -O -i $f.in -o FILE$f.out -inf FILE$f.inf \  
        -c FILE.$l -ref FILE.$l -r FILE.$f \  
        -p FILE.top -x FILE$f.x -e FILE$f.ene  
l=md1  
f=md2  
mpirun pmemd.MPI \  
        -O -i $f.in -o FILE$f.out -inf FILE$f.inf \  
        -c FILE.$l -ref FILE.$l -r FILE.$f \  
        -p FILE.top -x FILE$f.x -e FILE$f.ene  
l=md2  
f=md3  
mpirun pmemd.MPI \  
        -O -i $f.in -o FILE$f.out -inf FILE$f.inf \  
        -c FILE.$l -ref FILE.$l -r FILE.$f \  
        -p FILE.top -x FILE$f.x -e FILE$f.ene3  
l=md3  
f=md4  
mpirun pmemd.MPI \  
        -O -i $f.in -o FILE$f.out -inf FILE$f.inf \  
        -c FILE.$l -ref FILE.$l -r FILE.$f \  
        -p FILE.top -x FILE$f.x -e FILE$f.ene  
l=md4  
f=md5  
mpirun pmemd.MPI \  
        -O -i $f.in -o FILE$f.out -inf FILE$f.inf \  
        -c FILE.$l -ref FILE.$l -r FILE.$f \  
        -p FILE.top -x FILE$f.x -e FILE$f.ene  
l=md5  
f=md6  
mpirun pmemd.MPI \  
        -O -i $f.in -o FILE$f.out -inf FILE$f.inf \  
        -c FILE.$l -ref FILE.$l -r FILE.$f \  
        -p FILE.top -x FILE$f.x -e FILE$f.ene
```

```
l=md6
f=md7
mpirun pmemd.MPI \
    -O -i $f.in -o FILE$f.out -inf FILE$f.inf \
    -c FILE.$l -ref FILE.$l -r FILE.$f \
    -p FILE.top -x FILE$f.x -e FILE$f.ene
l=md7
f=md8
mpirun pmemd.MPI \
    -O -i $f.in -o FILE$f.out -inf FILE$f.inf \
    -c FILE.$l -ref FILE.$l -r FILE.$f \
    -p FILE.top -x FILE$f.x -e FILE$f.ene
l=md8
f=md9
mpirun pmemd.MPI \
    -O -i $f.in -o FILE$f.out -inf FILE$f.inf \
    -c FILE.$l -ref FILE.$l -r FILE.$f \
    -p FILE.top -x FILE$f.x -e FILE$f.ene
```

C.2 min1.in

```
&cntrl
    imin=1, maxcyc=10000, ncyc=50, drms=0.5,
ibelly=1,
    ntb=1,
/
Atoms which are allowed to move in the min
RES 1 240
END
END
```

C.3 min2.in

```
&cntrl
    imin=1, maxcyc=10000, ncyc=50, drms=0.5, ntr=1,
    ntb=1,
&end
```

```
Restrain DNA
50.0
RES 1 304
END
END
```

C.4 min3.in

```
&cntrl
      imin=1, maxcyc=10000, ncyc=50, drms=0.5, ntr=1,
      ntb=1,
/
Restrain DNA
25.0
RES 1 304
END
END
```

C.5 min4.in

```
&cntrl
      imin=1, maxcyc=10000, ncyc=50, drms=0.2,
ibelly=0,
      ntb=1
/
```

C.6 md1.in

```
&cntrl
      irest=0, ntx=1,
      ntf=2, ntb=2, cut=9.0,
      ntr=1,
      nstlim=5000, dt=0.002,
      tempi=100.0 temp0=300.0, ntt=1,
      ntp=1,
      ntc=2,
/
Restrain DNA
100.0
```

```
RES 1 304  
END  
END
```

C.7 md2.in

```
&cntrl  
    irect=1, ntx=7,  
    ntf=2, ntb=2, cut=9.0,  
    ntr=1,  
    nstlim=5000, dt=0.002,  
    temp0=300.0, ntt=1,  
    ntp=1,  
    ntc=2,  
  
/  
Restrain DNA  
100.0  
RES 1 304  
END  
END
```

C.8 md3.in

```
&cntrl  
    irect=1, ntx=7,  
    ntf=2, ntb=2, cut=9.0,  
    ntr=1,  
    nstlim=5000, dt=0.002,  
    temp0=300.0, ntt=1,  
    ntp=1,  
    ntc=2,  
  
/  
Restrain DNA  
50.0  
RES 1 304  
END  
END
```

C.9 md4.in

```
&cntrl
    irect=1, ntx=7,
    ntf=2, ntb=2, cut=9.0,
    ntr=1,
    nstlim=5000, dt=0.002,
    temp0=300.0, ntt=1,
    ntp=1,
    ntc=2,

/
Restrain DNA
25.0
RES 1 304
END
END
```

C.10 md5.in

```
&cntrl
    irect=1, ntx=7,
    ntf=2, ntb=2, cut=9.0,
    ntr=1,
    nstlim=5000, dt=0.002,
    temp0=300.0, ntt=1,
    ntp=1,
    ntc=2,

/
Restrain DNA
10.0
RES 1 304
END
END
```

C.11 md6.in

```
MD on the water and Na about DNA
&cntrl
```

```
irest=1, ntx=7,  
ntf=2, ntb=2, cut=9.0,  
ntr=1,  
nstlim=5000, dt=0.002,  
temp0=300.0, ntt=1,  
ntp=1,  
ntc=2,  
  
/  
Restrain DNA  
5.0  
RES 1 304  
END  
END
```

C.12 md7.in

```
&cntrl  
  
irest=1, ntx=7,  
ntf=2, ntb=2, cut=9.0,  
ntr=1,  
nstlim=5000, dt=0.002,  
temp0=300.0, ntt=1,  
ntp=1,  
ntc=2,  
  
/  
Restrain DNA  
2.5  
RES 1 304  
END  
END
```

C.13 md8.in

```
&cntrl  
  
irest=1, ntx=7,  
ntf=2, ntb=2, cut=9.0,  
ntr=1,  
nstlim=5000, dt=0.002,
```

```
temp0=300.0, ntt=1,  
ntp=1,  
ntc=2,  
  
/  
Restrain DNA  
1.0  
RES 1 304  
END  
END
```

C.14 md9.in

```
&cntrl  
  irest=1, ntx=7,  
    ntf=2, ntb=2, cut=9.0,  
    nstlim=15000000, dt=0.002,  
    temp0=300.0, ntt=1,  
    ntp=1,  
    ntc=2,  
  ntwx=500,  
  /
```

Appendix D Molecular dynamics (MD) analysis scripts

D.1 Root-mean-squared (RMS) pair-wise separation

The Matlab script used to calculate root-mean-squared pair-wise separation of Mg atoms within a structure is listed below:

```
clear
tind=1;
h=1;
car=cputime;
num=1;
store=0;
y=logspace(0,5,150);
tcat=round(y);
%works out aprox log spaced set of points for a given
number of frames
for i=1:150
    if tcat(i)<30000
        if tcat(i)~=store;
            logsc(num)=tcat(i);
            store=tcat(i);
            num=num+1;
        end
    end
end
for t=1:1:(num-1)
    h=1;
    %Input filename
    fex=int2str(logsc(t));
    name='AAAAout.';
    fn=strcat(name, fex);
    %Opens file, ignores header line, reads in data from
file, x,y,z coords
    %are stored as doubles, closes file
    fid = fopen(fn);
```

```
fgetl(fid);
pdb = textscan(fid, '%s%s%s%s%s%f%f%f%s%s');
fclose(fid);
j=1;
%Reads N and Mg coords into an array
for i=66:119:9519
    Mgcoords(j,:)= [pdb{1,6}(i-65) pdb{1,7}(i-65)
pdb{1,8}(i-65)];
    j=j+1;
end
count=1;
for i=1:80
    %Copies norm values for each molecule into an
array, one column
    %for each time point read in
C(i,tind)={norm(count,1),norm(count,2),norm(count,3)};
    count=count+1;
    %Works out pairwise displacement and then
distance of Mg atoms
    for j=1:80
        if i~=j
            Mgdifffall(h,tind)={Mgcoords(i,:)-
Mgcoords(j,:)};
distances(h,tind)=sqrt(sum(Mgdifffall{h,tind}.*Mgdifffall{h
,tind}));
            %RMSD calc
RMSD(h,tind)=(distances(h,tind)*distances(h,tind));
            RMSD1(t)=sqrt(sum(RMSD)/57360);
            h=h+1;
        end
    end
end
h=1;
end
%for all mg atoms
tind=1;
figure()
plot(logsc,RMSD1)
axis tight;
xlabel('Time (frames)')
```

```
ylabel('RMSD (Angstroms)')
set(gca,'Title',text('String','RMSD - all Mg atoms'))
RMSD1=RMSD1';
logsc=logsc';
```

D.2 System energy analysis

The matlab script used for the extraction of total system energy, E_{Tot} , from Amber .out files. In addition to E_{Tot} a number of other parameters were also extracted. These included temperature, pressure and electrostatic and van der Waals contributions to energy.

```
names1 = dir('*.out');
    names1 = {names1.name};
    headings={'Nstep', 'Time (ps)', 'Temp (K)', 'Pres',
'Etot', 'Ektot', 'Eptot'};
    headings2={'deltaTemp', 'deltaPres', 'deltaEtot',
'deltaEktot', 'deltaEptot'};
for ii=1:length(names1)
    clearvars -except names1 headings headings2 ii
    fn=names1{ii};
    fid = fopen(fn);
    s= textscan(fid,'%s');
    fclose(fid);
    idx1=find(strcmp('NSTEP',s{1,1}));
for i=1:(numel(idx1));
    nstep(i)=str2num(s{1,1}{idx1(i)+2,1});
    time(i)=str2num(s{1,1}{idx1(i)+5,1});
    temp(i)=str2num(s{1,1}{idx1(i)+8,1});
    pres(i)=str2num(s{1,1}{idx1(i)+11,1});
    etot(i)=str2num(s{1,1}{idx1(i)+14,1});
    ektot(i)=str2num(s{1,1}{idx1(i)+17,1});
    eptot(i)=str2num(s{1,1}{idx1(i)+20,1});
end
nstep=nstep';
time=time';
temp=temp';
pres=pres';
etot=etot';
```

```
ektot=ektot';
eptot=eptot';
cell={nstep, time, temp, pres, etot, ektot, eptot};
ss=strread(names1{ii}, '%s', 'delimiter', '.')
fn1=strcat(ss{1}, 'prop.txt')
dlmwrite(fn1, cell);
deltatemp=temp(numel(idx1)-1)-temp(1);
deltapres=pres(numel(idx1)-1)-pres(1);
deltaetot=etot(numel(idx1)-1)-etot(1);
deltaektot=ektot(numel(idx1)-1)-ektot(1);
deltaeptot=eptot(numel(idx1)-1)-eptot(1);
cell1={deltatemp(1), deltapres(1), deltaetot(1),
deltaektot(1), deltaeptot(1)};
fn2=strcat(ss{1}, 'deltas.txt')
dlmwrite(fn2, cell1);
end
```

D.3 Dipole moment plots

The Matlab script used to produce dipole moment plots is listed below:

```
fex='30000';%frame number
name='AAAAout.';%root filename
fn=strcat(name, fex, '.pdb');
%Opens file, ignores header line, reads in data from
file, x,y,z coords
%are stored as doubles, closes file
fid = fopen(fn);
fgetl(fid);
pdb = textscan(fid, '%s%s%s%s%s%f%f%f%s%s');
fclose(fid);
j=1;
%Reads NB and ND coords into an array
figure()
for i=66:119:7615
    NBcoords(j, :)= [pdb{1,6}(i-14) pdb{1,7}(i-14)
pdb{1,8}(i-14)];
```

```
        NDcoords(j,:)=[pdb{1,6}(i-64)  pdb{1,7}(i-64)
pdb{1,8}(i-64)];
        dp=NBcoords(j,:)-NDcoords(j,:);

quiver3(NDcoords(j,1),NDcoords(j,2),NDcoords(j,3),dp(1),d
p(2),dp(3),4,'Linewidth',1,'Color','b')%draws arrows

        j=j+1;
        hold on
end
grid off
```

D.4 Parallelised Brute force X-ray scattering code

The modified c script parallelised, using OpenMP, to allow calculation of scattering from a greater number of structures is listed below. This script was based on an original script provided by Roman Tuma. This script was used for the calculation of all X-ray scattering in Chapter 4.

```
/* parallel distance distribution and debye formula
scattering brute force comp for pdb's from ptraj*/
#include <stdio.h>
#include <math.h>
#include <fcntl.h>
#include <stdlib.h>
#include <string.h>
#include <omp.h>
#define NP 57000 /* max number of input coord */
#define NO 500
#define NA 5 // nro of atom types
#define NA1 NA+1
float ** d;//[NP][NP];// pairwise distance matrix
float x[NP], y[NP], z[NP]; // input coords of diffracting
points
double s, ds[NO],dsa[NO];
double ** f;//[NP][NO];
int e1[NP], dsn[NO], nrmax; //index of atom H==0
float fs[NP]; // forward scattering power q=0 ~ Z
float dr;//=0.5; //histogram step A
```

```
int main(int na, char *ars[])
{
    float seconds;
    seconds=omp_get_wtime(); //start clock
    FILE *fp;
    int np; // nro of atoms in one structure
    int k,i,j,il,m,incre, inc;
    char
s1[30][200],s2[200],s3[200],filename[50],filename1[50],fi
lename2[50],sk[30][200];

    float a1[NA1],a2[NA1], a3[NA1], a4[NA1],b1[NA1],
b2[NA1],b3[NA1], b4[NA1], c[NA1]; // Cromer-Mann coeff
matrix
    int no; // nro of output data pts
    float dmax1, dm, q1,q2,dq;
    double Iq[NP],p, q[NO],qr,qk, di;
    float Iqm, dmin, dmax;
    if(na==8)
        #pragma omp parallel for private (m,incre, filename,
filename1,
filename2,a1,a2,a3,a4,c,j,i,b1,b2,b3,b4,fp,np,q1,q2,no,dr
,dq,e1,fs,s1,x,y,z,p,dmin,dmax,nrmax,dm,qk,il,di,qr,s,Iq,
Iqm,q,d,f)
        //crude parallelisation of script using parallel for
            for(m=0;m<1;++m){
                Iqm=100;
                np=atof(ars[3]);q1=atof(ars[4]);q2=atof(ars[5]);no=atof(
ars[6]);dr=atof(ars[7]); //sets values from input/usgage
                dmin=100;
                dmax=0;
                for(i=0;i<NP;++i){
                    Iq[i]=0;
                }
                //printf("IQ=%f",Iq);
                incre=atof(ars[2])+m;
                sprintf(filename,
"%s.%d.pdb",ars[1],incre); //sets input filename from
root given when program started
                sprintf(filename1,
"%sout%d.txt",ars[1],incre); //sets output filename from
root given when program started
                sprintf(filename2, "cm%d.asc",incre);
```

```
        fp=fopen("cm.asc","r"); //cm.asc is the Cromer
Man coefficient file

        for(i=0;i<NA;i++)

            {

                fscanf(fp,"%f %f %f %f %f %f %f %f
%f",&a1[i],&a2[i], &a3[i], &a4[i],&c[i], &b1[i],
&b2[i],&b3[i], &b4[i]); //reads in coeffs from file
assigns to variables

                //printf("\n %i %f %f %f %f %f %f %f %f
%f",i,a1[i],a2[i], a3[i], a4[i],c[i], b1[i], b2[i],b3[i],
b4[i]); for debug

            }

            a1[NA]=0;a2[NA]=0; a3[NA]=0; a4[NA]=0; c[NA]=0;
b1[NA]=0; b2[NA]=0; b3[NA]=0; b4[NA]=0;

            fclose(fp);

            //printf("\n processing script file : %s output
into file: %s \n", filename, filename1); for debug

            fp=fopen(filename,"r"); \\open input file, warn if
missing, if not assign memory for d and f arrays (the
large arrays)

            if(fp==NULL){printf("\n Input file %s
missing\n",filename);exit(-1);}else

                {

                    d=calloc( sizeof(float*),np);

                    if (d==NULL){

                        perror("d");

                        //return -1;

                    }

                    for (int cat=0;cat<np;cat++){

                        d[cat]=calloc(sizeof(float),np);

                        if (d[cat]==NULL){

                            perror("d");

                            //return -1;

                        }

                    }

                    f=calloc( sizeof(float*),np);

                    if (f==NULL){

                        perror("f");

                        //return -1;

                    }

                    for (int dog=0;dog<np;dog++){
```

```
        f[dog]=calloc(sizeof(float),np);
        if (f[dog]==NULL){
            perror("f");
            //return -1;
        }
    }
    dq=(q2-q1)/(no-1);
    for(i=0;i<np;i++)
    {
        e1[i]=0;fs[i]=0;
        fscanf(fp,"%s",&s1[0][0]);
        if (s1[0][0]=='T'){
fscanf(fp,"%s",&s1[0][0]); \\checks to see if line = TER
i.e. no atom info
            fscanf(fp,"%s",&s1[0][0]); i=i-1;}
        else if(s1[0][0]=='A'){
            \\for lines which do have atom
info, do the following
            fscanf(fp,"%s",&s1[0][0]); \\read atom
type
            fscanf(fp,"%s",&s1[0][0]);
            if(s1[0][0]=='H'){fs[i]=1;e1[i]=0;};
\\assign atom index and foward scattering power values
based on atom type
            if(s1[0][0]=='C'){fs[i]=6;e1[i]=1;};
            if(s1[0][0]=='N'){fs[i]=7;e1[i]=2;};
            if(s1[0][0]=='O'){fs[i]=8;e1[i]=3;};
            if(s1[0][0]=='M'){fs[i]=10;e1[i]=4;};
            fscanf(fp,"%s",&s1[0][0]); \\read and
ignore
            fscanf(fp,"%s",&s1[0][0]);
            fscanf(fp,"%f", &x[i]); \\read x
            fscanf(fp,"%f", &y[i]); \\read y
            fscanf(fp,"%f", &z[i]); \\read z
            fscanf(fp,"%s",&s1[0][0]); \\read and
ignore
            fscanf(fp,"%s",&s1[0][0]);
        }
    }
    fclose(fp);
```

```
        \\pairwise distance calc
        for(i=0;i<np-1;i++)
            {
                for(j=i+1;j<np;j++)
                    {
                        p=sqrt((x[i]-x[j])*(x[i]-x[j]) + (y[i]-
values      y[j])*(y[i]-y[j]) + (z[i]-z[j])*(z[i]-z[j]));
                        d[i][j]=p;
                        if (dmin>p) dmin=p; \\set max and min dist
                        if (dmax<p) dmax=p;
                    }
                }
                nrmax=floor((dmax-dmin)/dr)+1; \\binning
info          dm=(dmax-dmin)/(nrmax-1);
        for(i=0;i<np-1;i++) \\for every atom...
            {
                for(k=0;k<no;k++) \\and every value of k
                i.e. every value of q workout scattering intensity matrix
                using coefficients from cm.asc and particle data from
                inputfile
                    {
                        q[k]=q1+k*dq;
                        qk=q[k]/12.56637;
                        i1=e1[i];
                        f[i][k]=c[i1]+a1[i1]*exp(-
                b1[i1]*qk*qk)+a2[i1]*exp(-b2[i1]*qk*qk)+a3[i1]*exp(-
                b3[i1]*qk*qk)+a4[i1]*exp(-b4[i1]*qk*qk);
                    }
            }
        //Cromer Mann finished
        //Next section computes actual scattering data from
        scattering matrix and distance data and adds up
        contributions to scattering intensity at each value of k
        for(i=0;i<np-1;i++)
            {
                di=i/1000.0;
                di=di-floor(i/1000);
                for(j=i+1;j<np;j++)
                    {
```

```
        p=d[i][j];
        for(k=0;k<no;k++)
            {
                qr=p*q[k];
                s=f[i][k]*f[j][k];
                Iq[k]=Iq[k]+s*sin(qr)/qr;
            }
    }
    for(k=0;k<no;k++)
        {
            if(Iq[k]<Iqm) Iqm=Iq[k]; \\sets
minimum Iq value
        }
    fp=fopen(filename1, "w");
    for(i=0;i<no;i++)
        {
            fprintf(fp,"%f\t%f\n",q[i],Iq[i]-
Iqm+.1);
        } //write to output file
    fclose(fp);
    }
    for(i=0;i<np;++i){free(d[i]); free(f[i]);} \\free memory
    }
    else printf("\n usage inputfile_rootname
start_of_increment np q1 q2 no dr \n"); \\if incorrect
usage, remind user of correct usage
    seconds=omp_get_wtime()-seconds; \\get run time
    printf("elapsed wallclock time = %f",seconds); \\print
runtime to screen or on arc1/arc2 logfile
    return 0;
}
```

Appendix E Dipole moment plots from Chapter 4

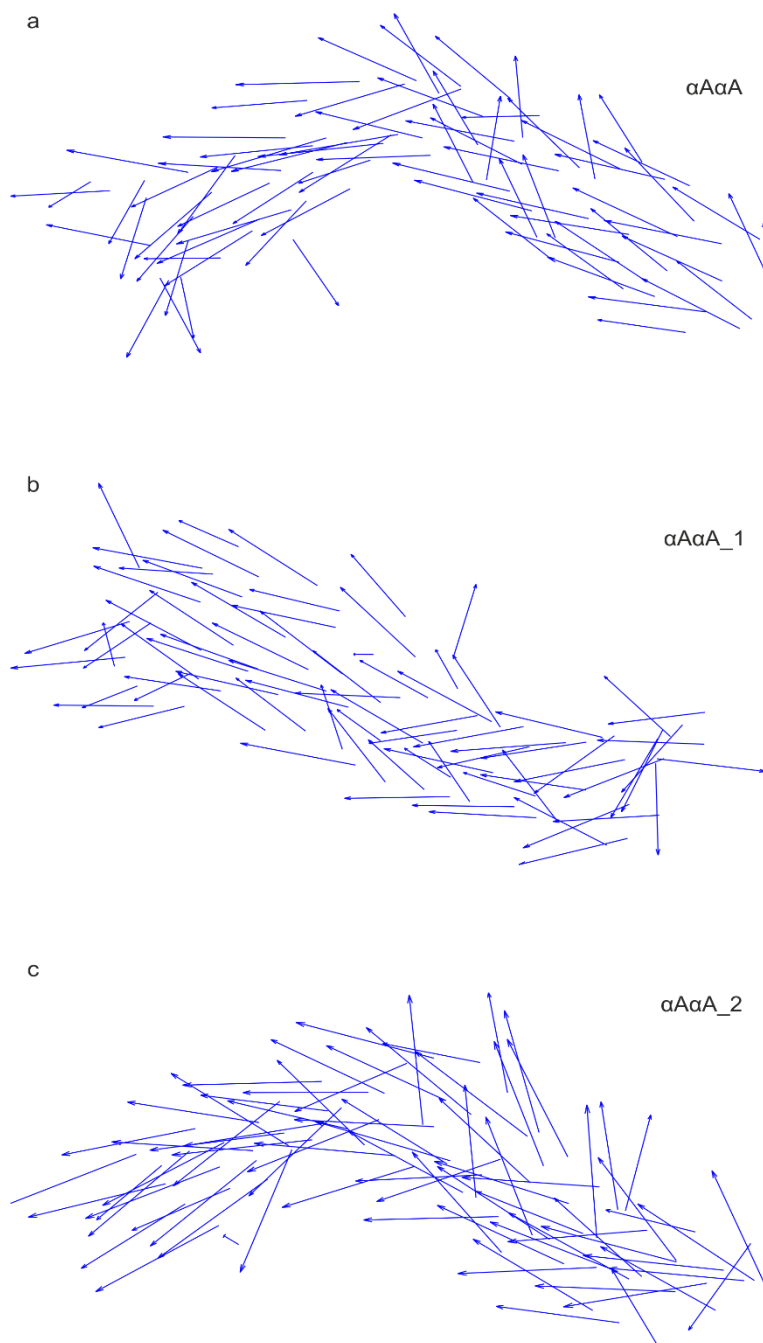


Figure E.1 Q_y dipole moments for sheets formed using the $\alpha A\alpha A$ dimer arrangement.

Q_y dipole moments, shown as arrows, for the final structures of simulations (a) $\alpha A\alpha A$, (b) $\alpha A\alpha A_1$, and (c) $\alpha A\alpha A_2$.

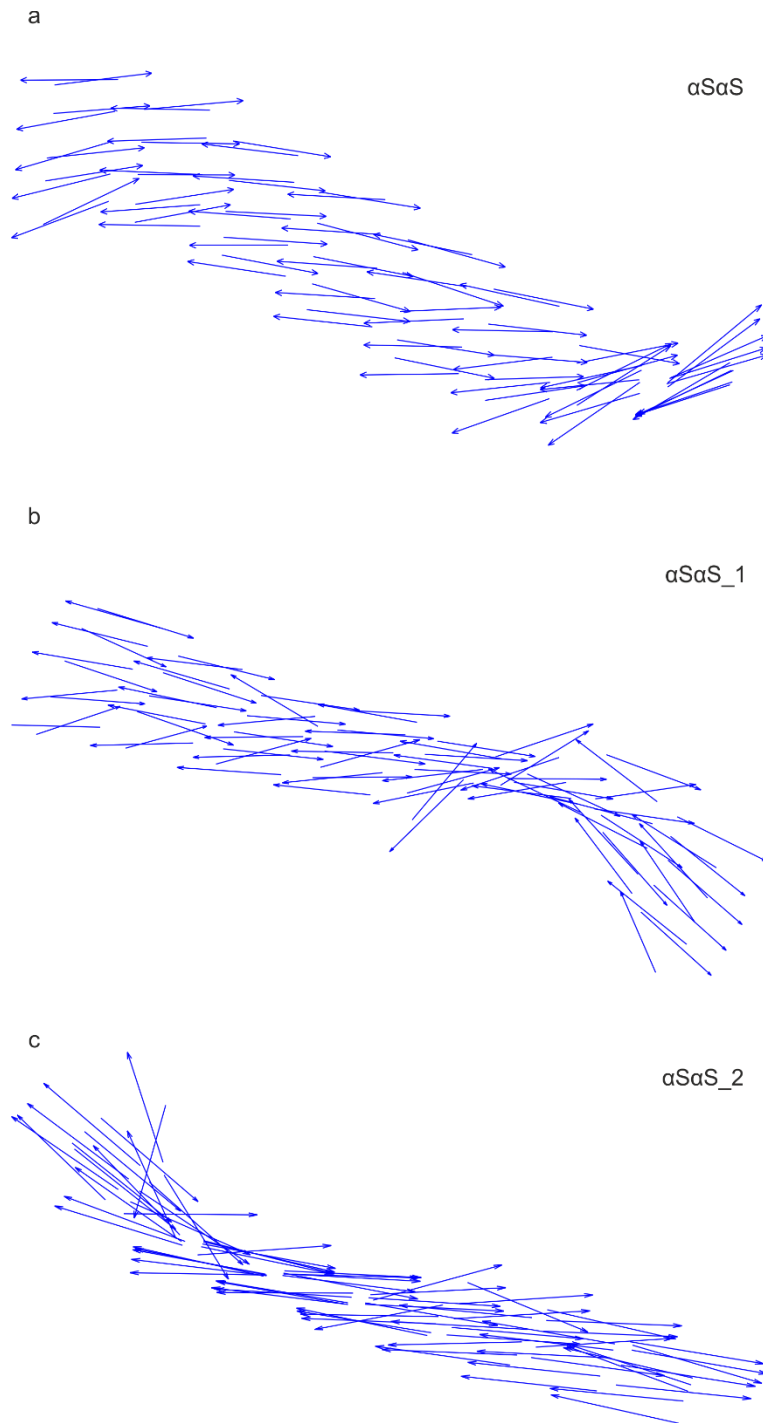


Figure E.2 Q_y dipole moments for sheets formed using the α SaS dimer arrangement.

Q_y dipole moments, shown as arrows, for the final structures of simulations (a) α SaS, (b) α SaS_1, and (c) α SaS_2.

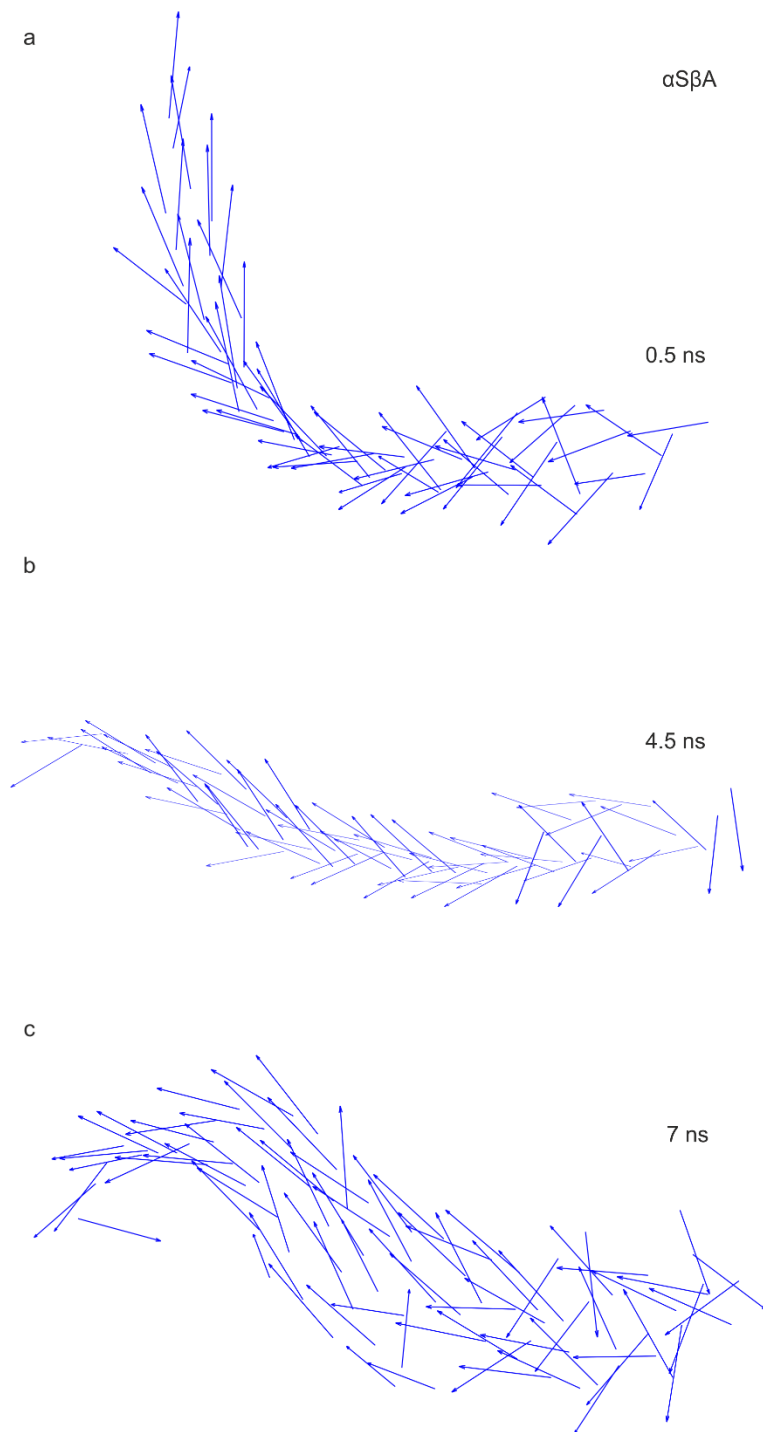


Figure E.3 Q_y dipole moments for sheets formed using the $\alpha\text{S}\beta\text{A}$ dimer arrangement (first repeat).

Q_y dipole moments, shown as arrows, for the final structures of simulations $\alpha\text{A}\alpha\text{A}$ at (a) 0.5 ns, (b) 4.5 ns, and (c) 7 ns.

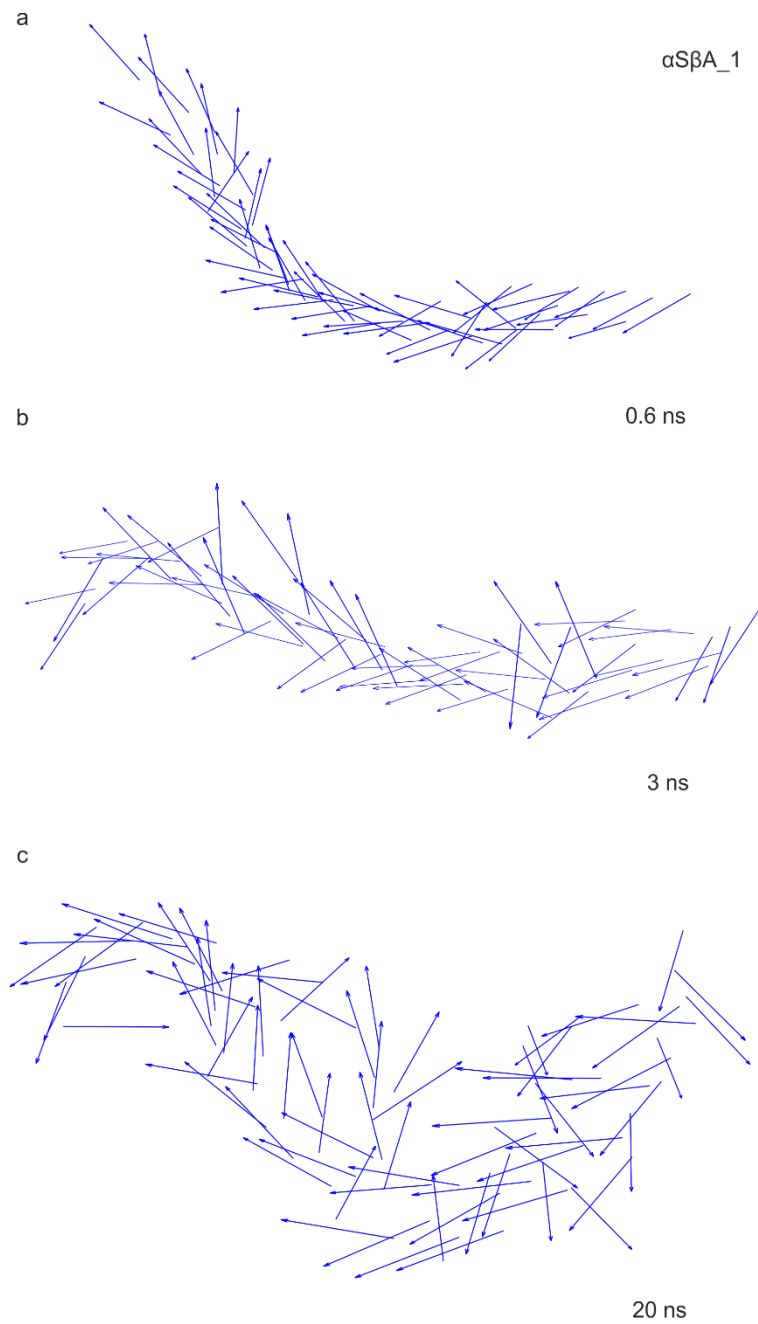


Figure E.4 Q_y dipole moments for sheets formed using the $\alpha\text{S}\beta\text{A}$ dimer arrangement (third repeat).

Q_y dipole moments, shown as arrows, for the final structures of simulations $\alpha\text{A}\alpha\text{A}$ at (a) 0.6 ns, (b) 3 ns, and (c) 20 ns.

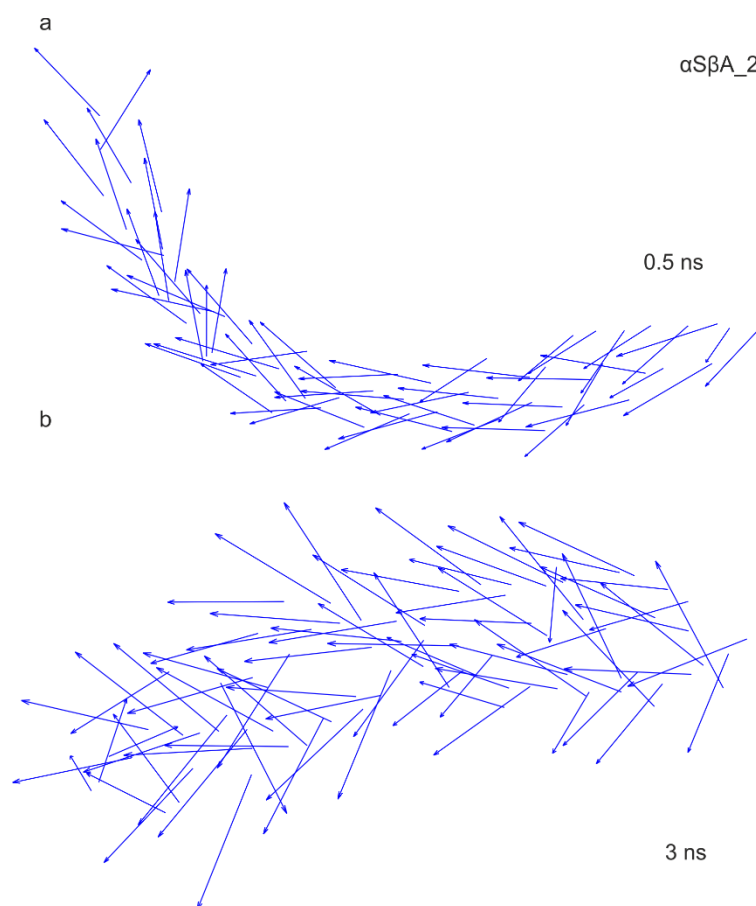


Figure E.5 Q_y dipole moments for sheets formed using the $\alpha S\beta A$ dimer arrangement (first repeat).

Q_y dipole moments, shown as arrows, for the final structures of simulations $\alpha A\alpha A$ at (a) 0.5 ns, and (b) 3 ns.

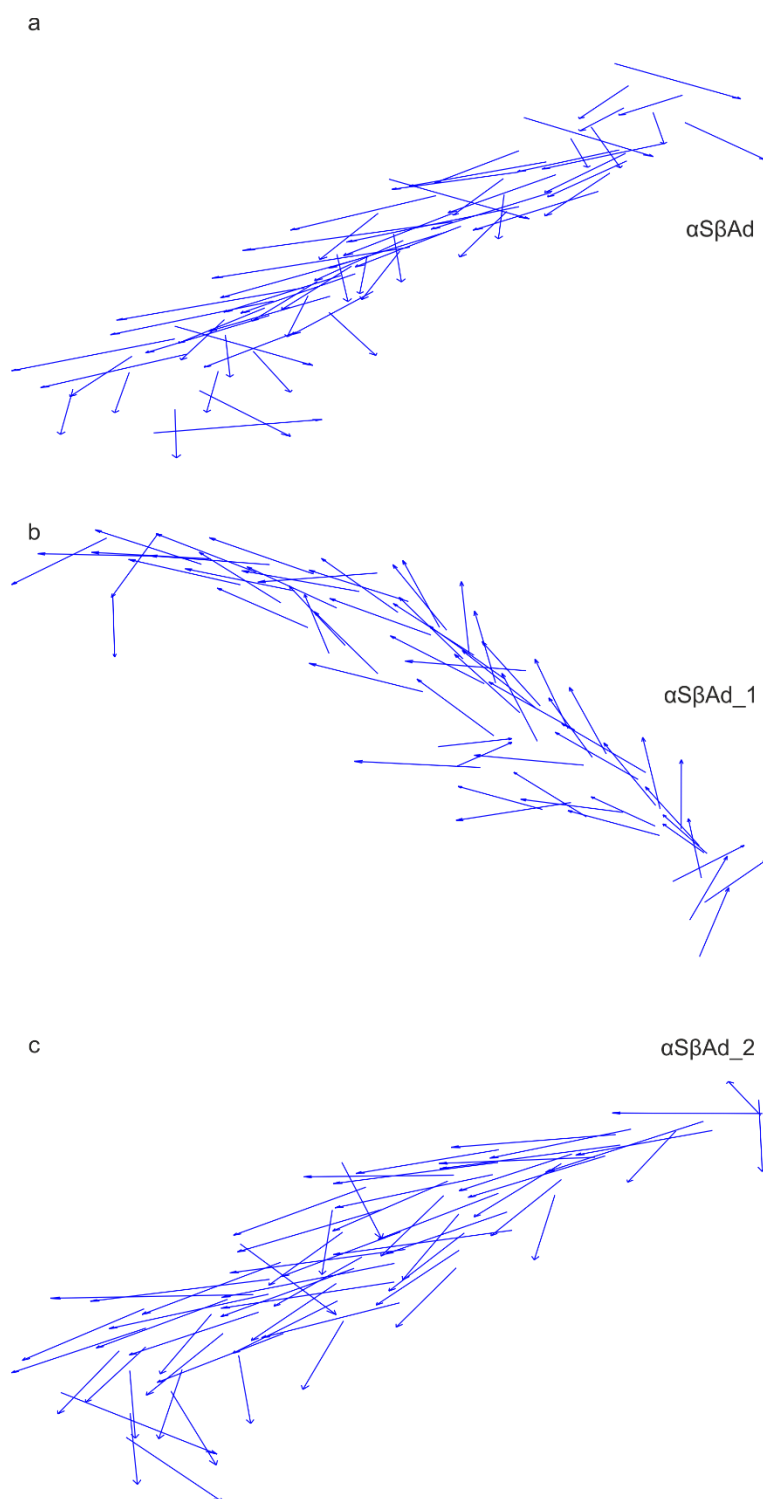


Figure E.6 Q_y dipole moments for sheets formed using the $\alpha\beta\text{Ad}$ dimer arrangement.

Q_y dipole moments, shown as arrows, for the final structures of simulations (a) $\alpha\beta\text{Ad}$, (b) $\alpha\beta\text{Ad}_1$, and (c) $\alpha\beta\text{Ad}_2$.

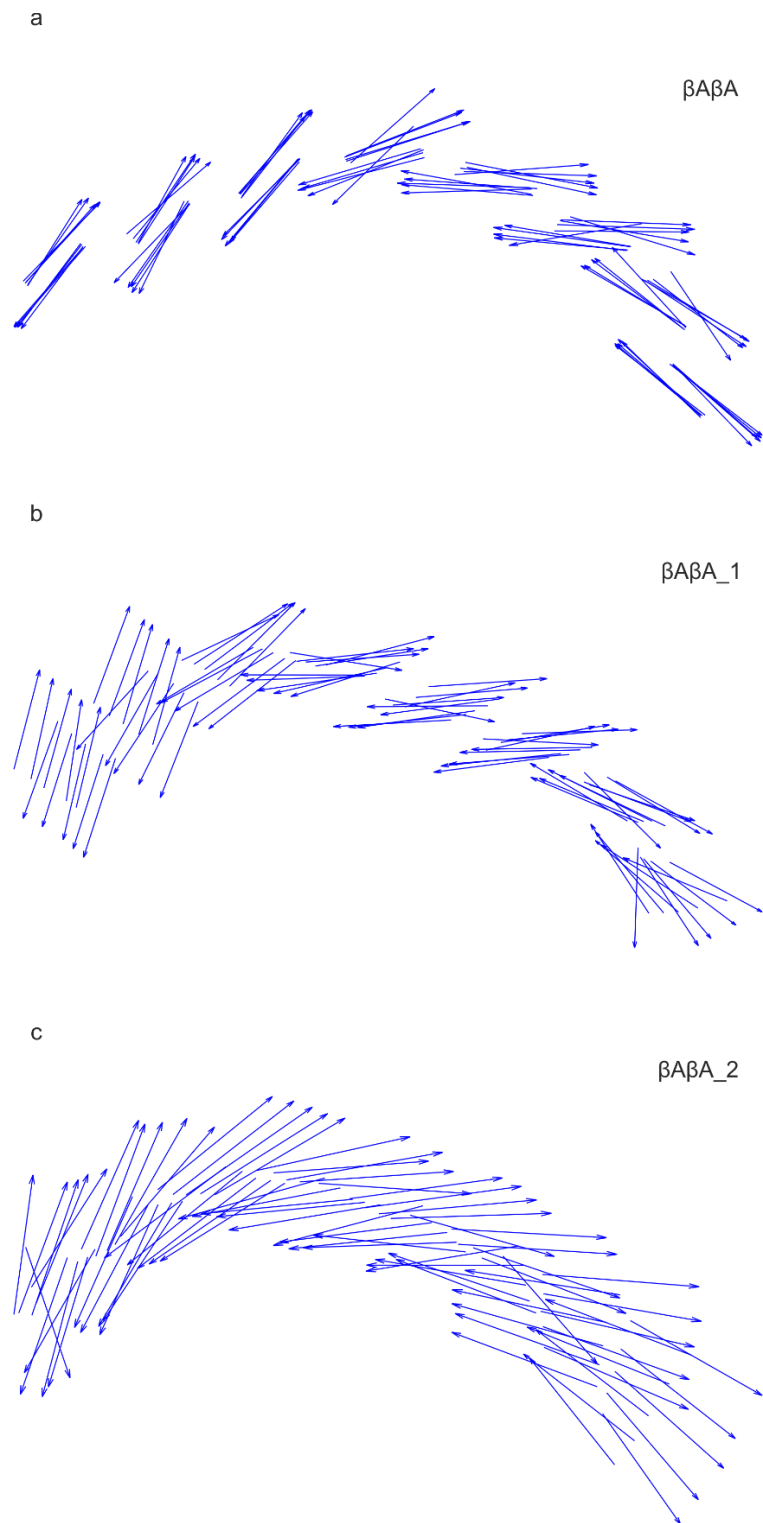


Figure E.7 Q_y dipole moments for sheets formed using the $\beta A \beta A$ dimer arrangement.

Q_y dipole moments, shown as arrows, for the final structures of simulations (a) $\beta A \beta A$, (b) $\beta A \beta A_1$, and (c) $\beta A \beta A_2$.

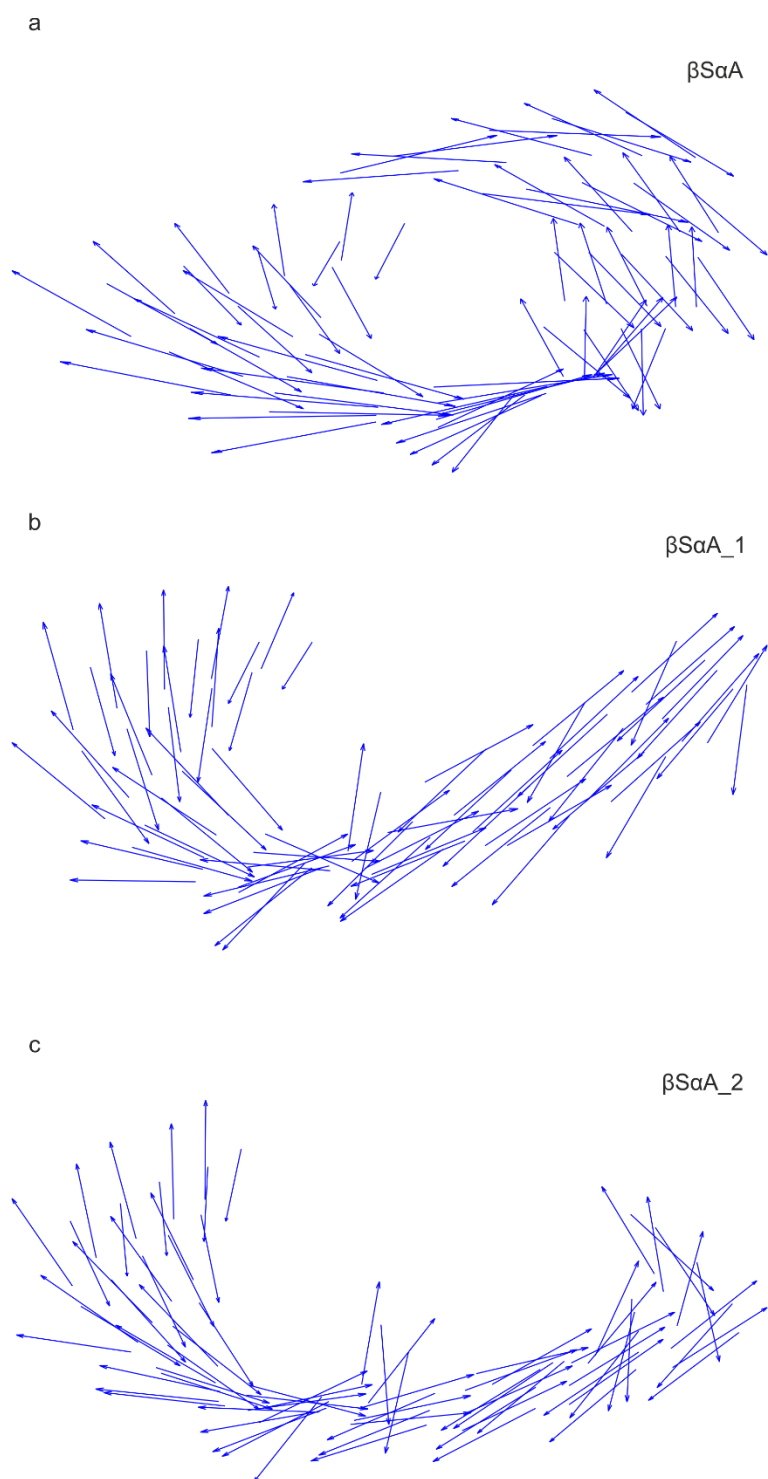


Figure E.8 Q_y dipole moments for sheets formed using the βSaA dimer arrangement.

Q_y dipole moments, shown as arrows, for the final structures of simulations (a) βSaA , (b) βSaA_1 , and (c) βSaA_2 .

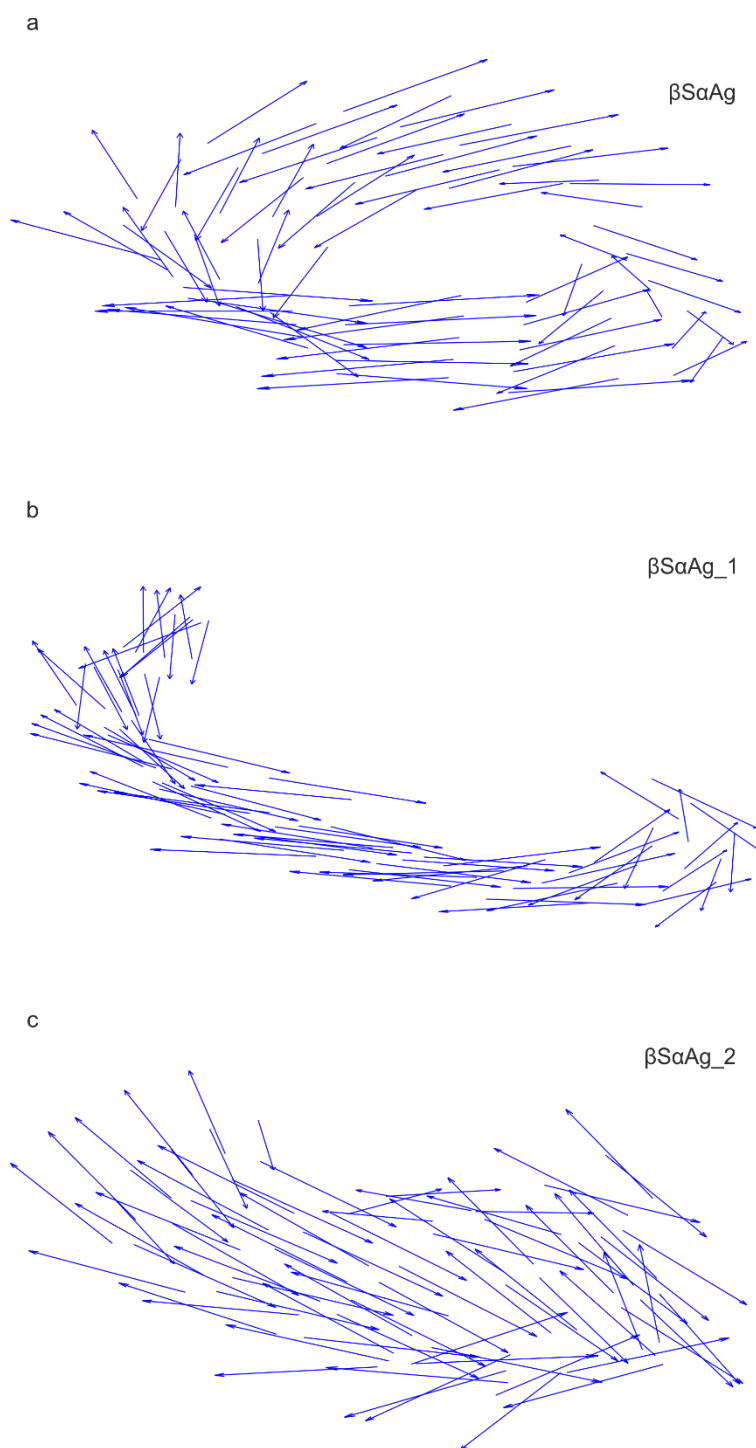


Figure E.9 Q_y dipole moments for sheets formed using the βSaAg dimer arrangement.

Q_y dipole moments, shown as arrows, for the final structures of simulations (a) βSaAg , (b) βSaAg_1 , and (c) βSaAg_2 .

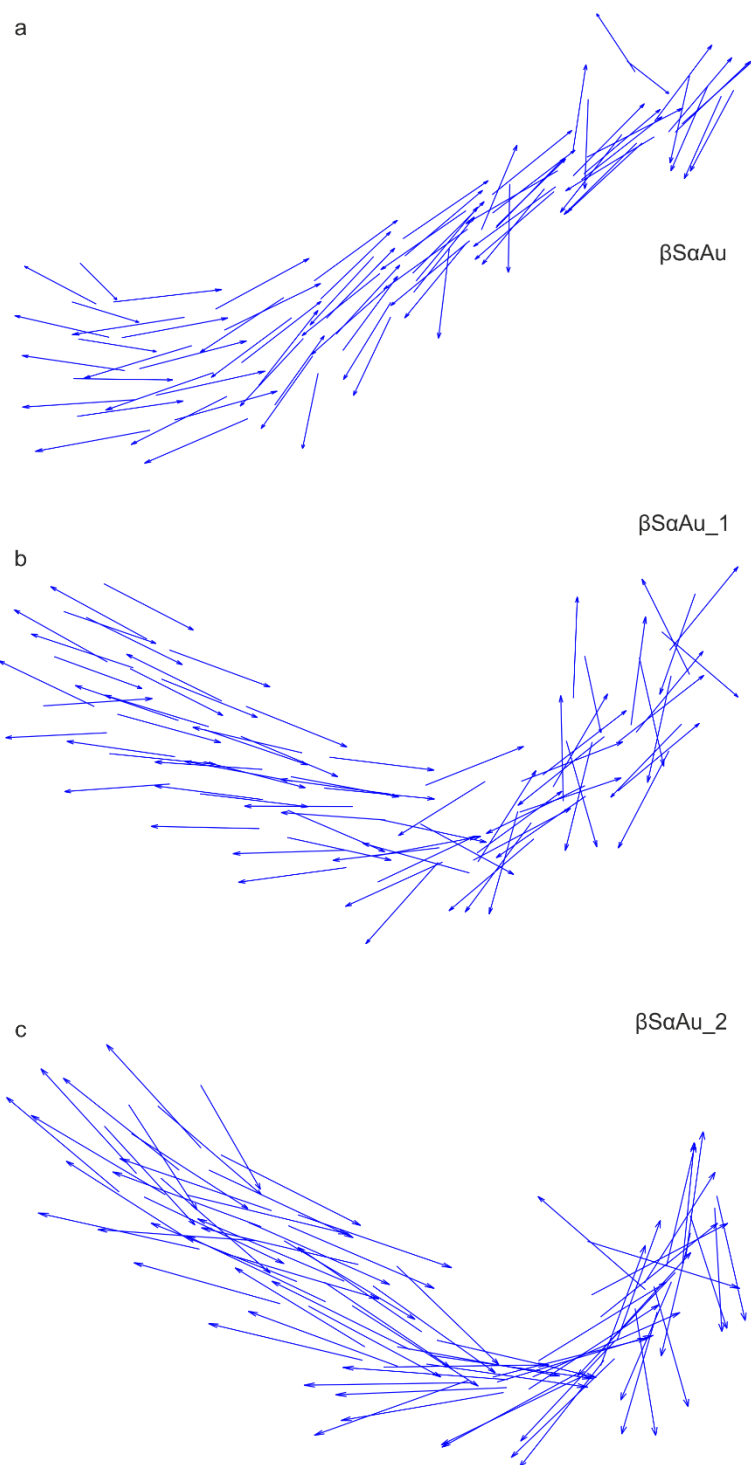


Figure E.10 Q_y dipole moments for sheets formed using the $\beta S\alpha Au$ dimer arrangement.

Q_y dipole moments, shown as arrows, for the final structures of simulations (a) $\beta S\alpha Au$, (b) $\beta S\alpha Au_1$, and (c) $\beta S\alpha Au_2$.

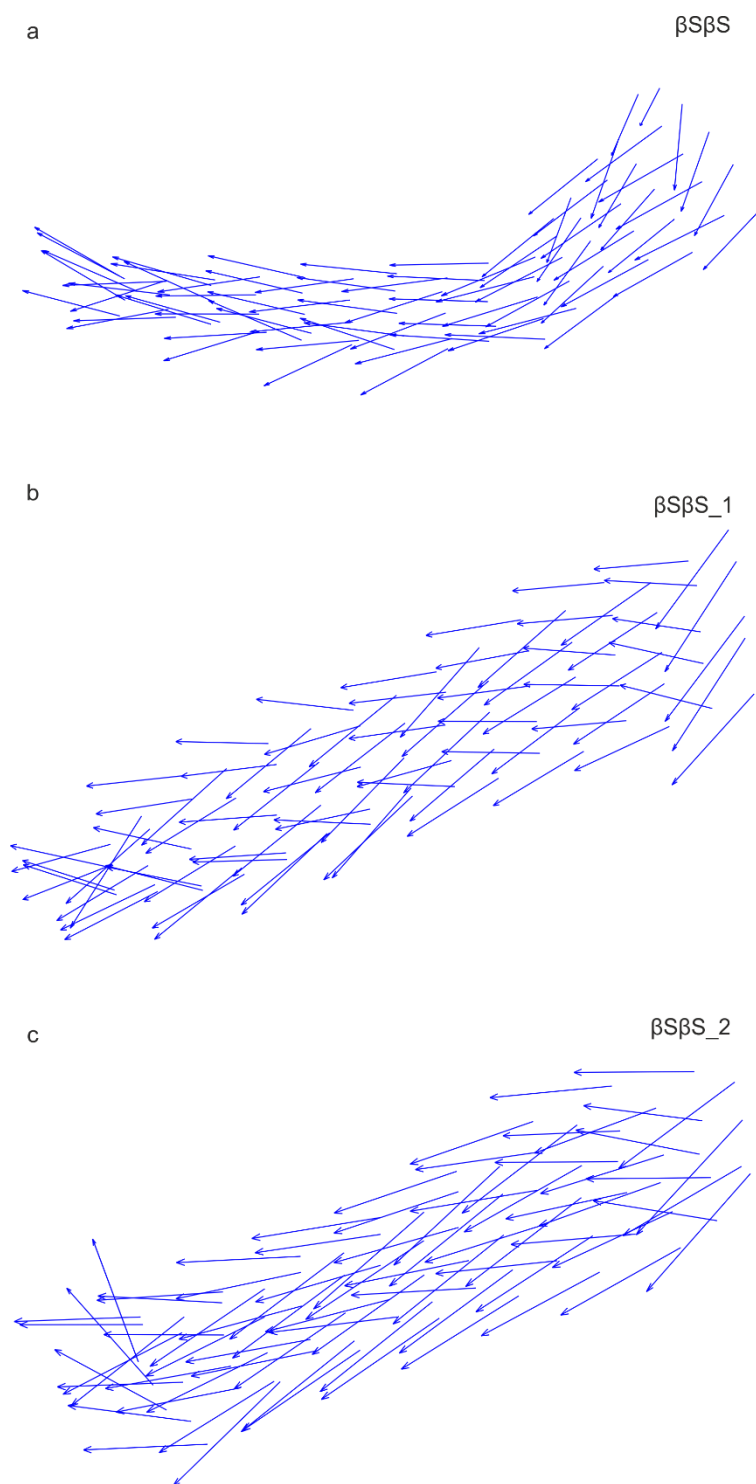


Figure E.11 Q_y dipole moments for sheets formed using the $\beta S\beta S$ dimer arrangement.

Q_y dipole moments, shown as arrows, for the final structures of simulations (a) $\beta S\beta S$, (b) $\beta S\beta S_1$, and (c) $\beta S\beta S_2$.

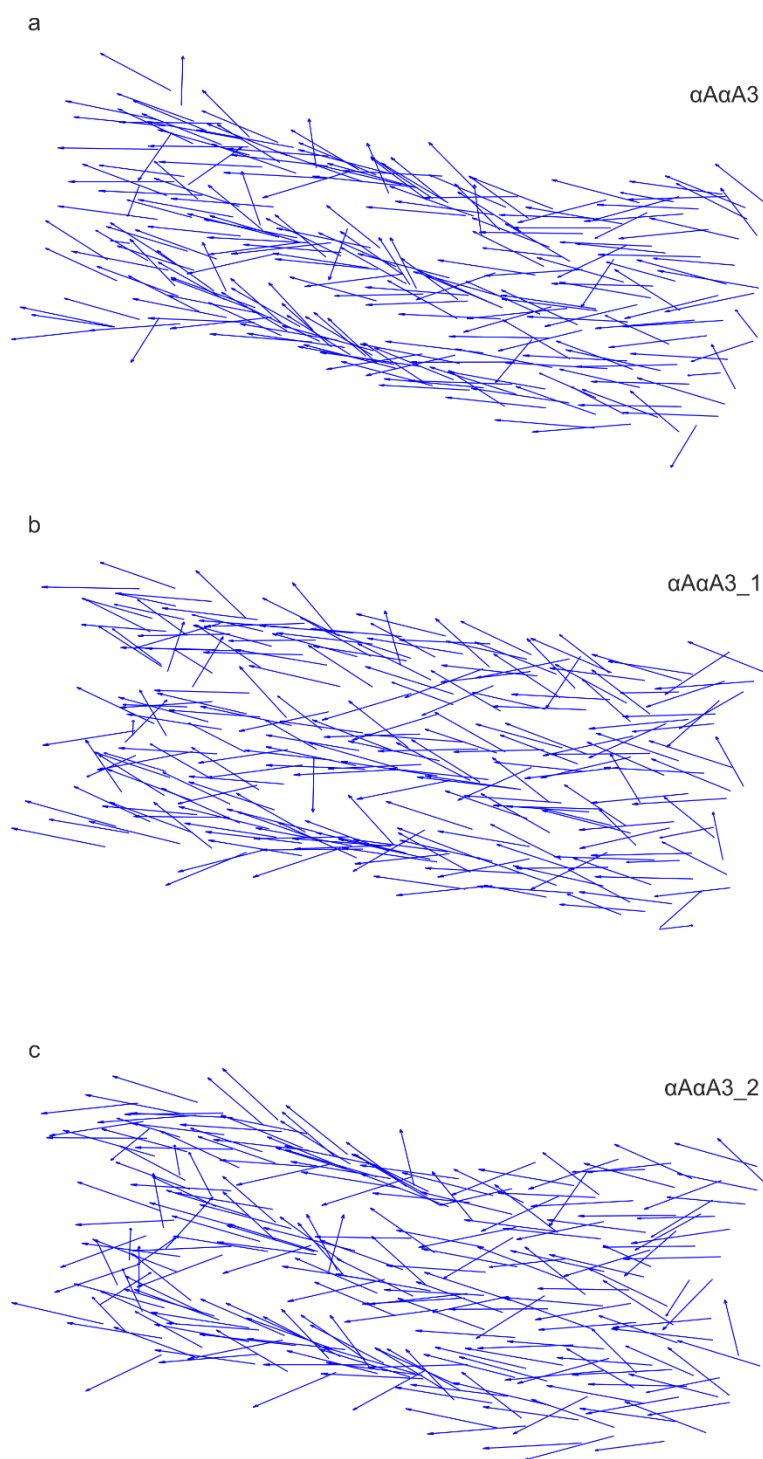


Figure E.12 Q_y dipole moments for triple layer sheets formed using the $\alpha A\alpha A$ dimer arrangement.

Q_y dipole moments, shown as arrows, for the final structures of simulations (a) $\alpha A\alpha A3$, (b) $\alpha A\alpha A3_1$, and (c) $\alpha A\alpha A3_2$.

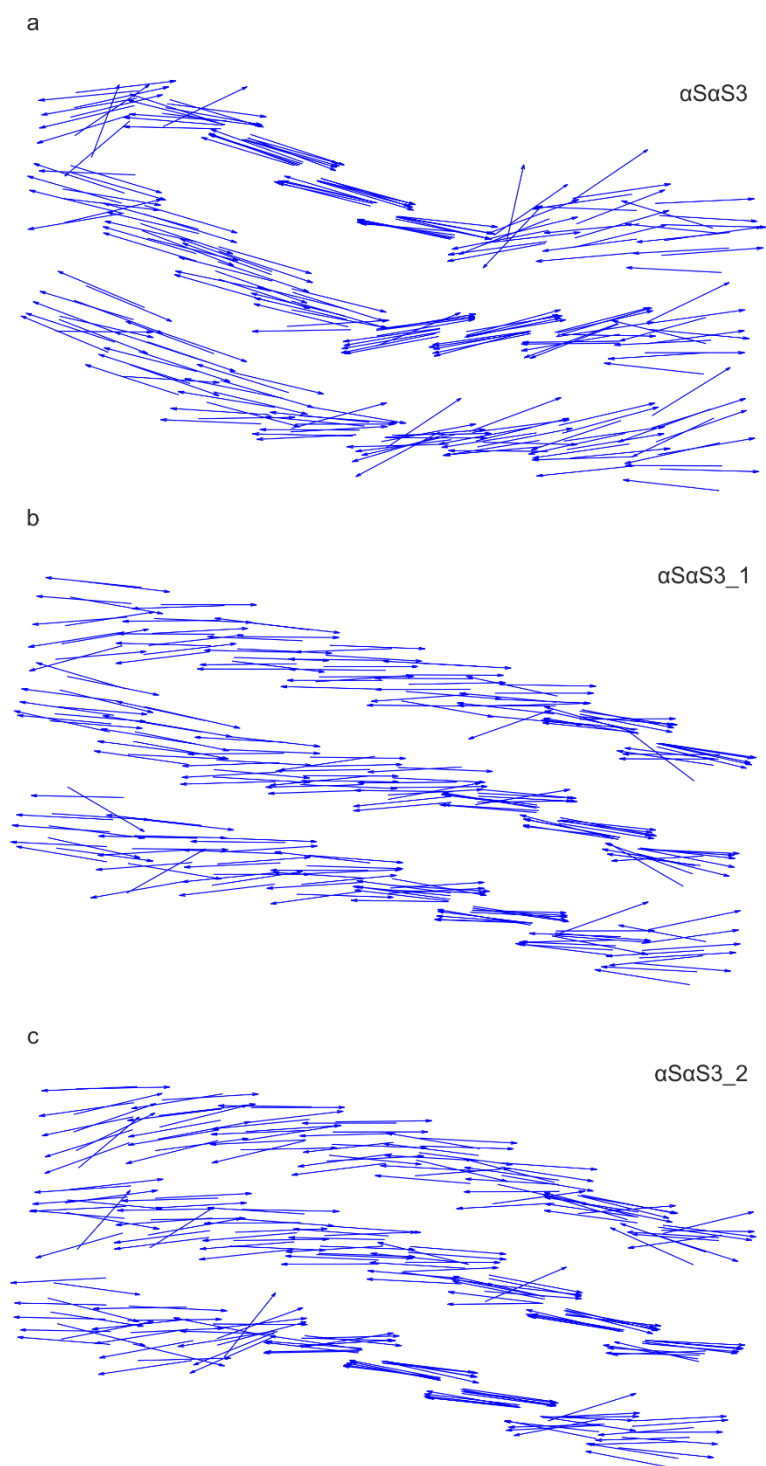


Figure E.13 Q_y dipole moments for triple layer sheets formed using the αSaS dimer arrangement.

Q_y dipole moments, shown as arrows, for the final structures of simulations (a) αSaS3 , (b) αSaS3_1 , and (c) αSaS3_2 .

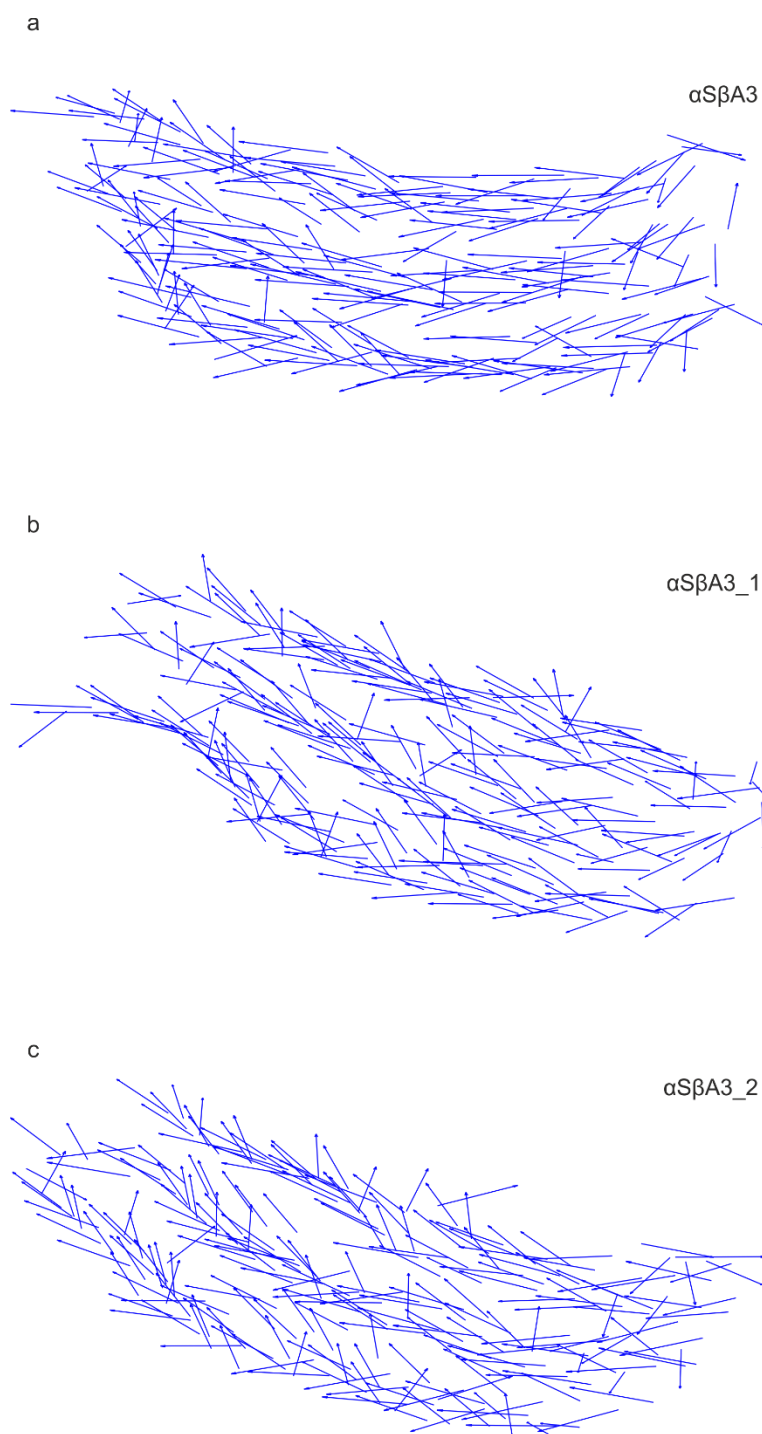


Figure E.14 Q_y dipole moments for triple layer sheets formed using the $\alpha\beta A$ dimer arrangement.

Q_y dipole moments, shown as arrows, for the final structures of simulations (a) $\alpha\beta A3$, (b) $\alpha\beta A3_1$, and (c) $\alpha\beta A3_2$.

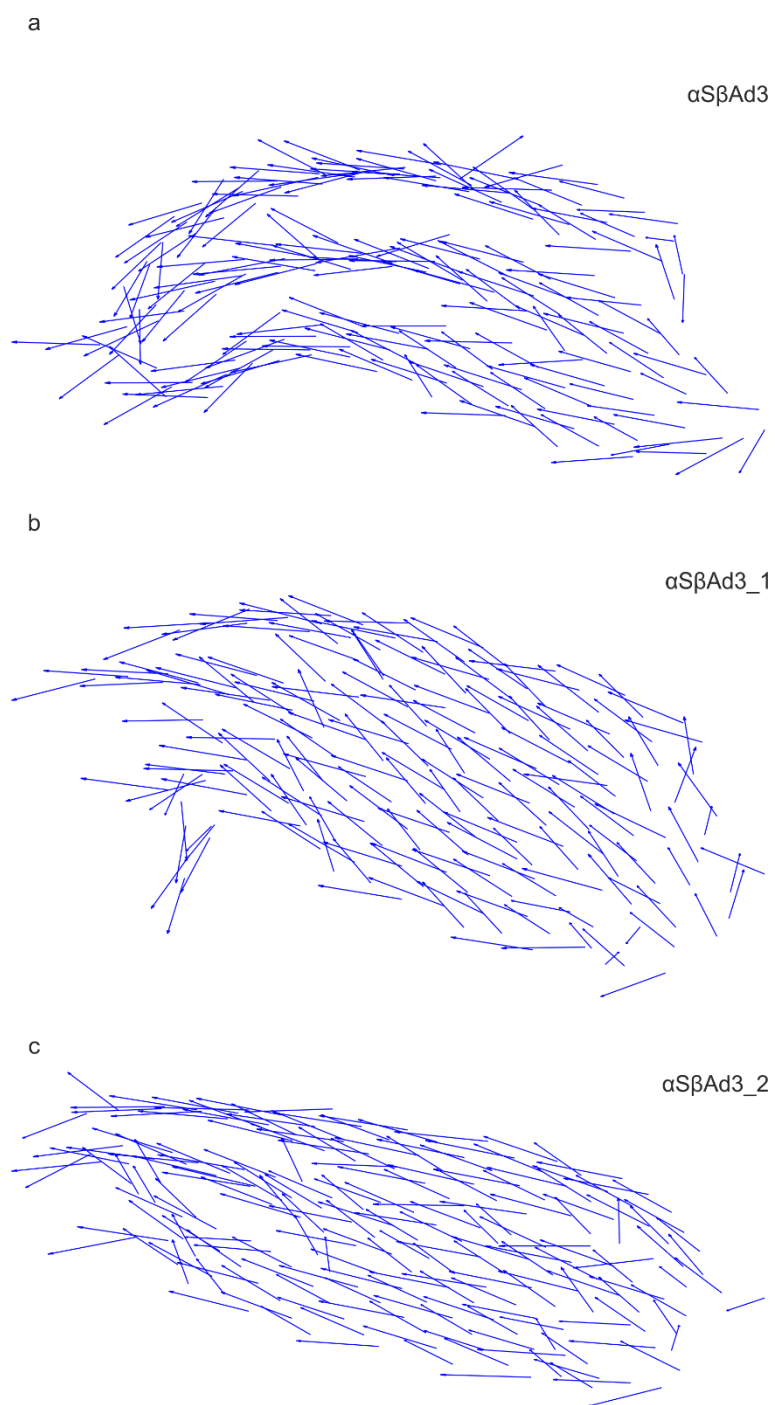


Figure E.15 Q_y dipole moments for triple layer sheets formed using the $\alpha\beta\text{Ad}$ dimer arrangement.

Q_y dipole moments, shown as arrows, for the final structures of simulations (a) $\alpha\beta\text{Ad3}$, (b) $\alpha\beta\text{Ad3}_1$, and (c) $\alpha\beta\text{Ad3}_2$.

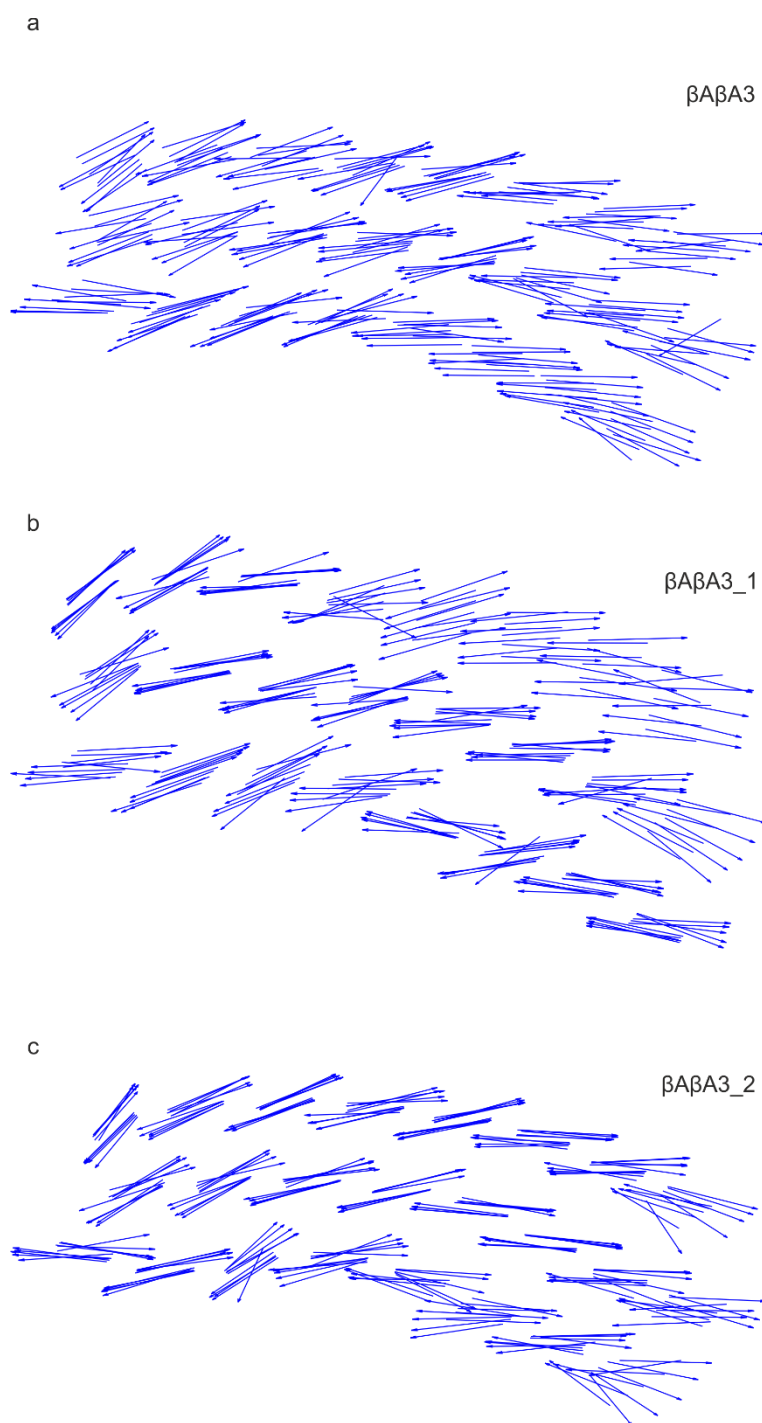


Figure E.16 Q_y dipole moments for triple layer sheets formed using the $\beta A \beta A$ dimer arrangement.

Q_y dipole moments, shown as arrows, for the final structures of simulations (a) $\beta A \beta A_3$, (b) $\beta A \beta A_3_1$, and (c) $\beta A \beta A_3_2$.

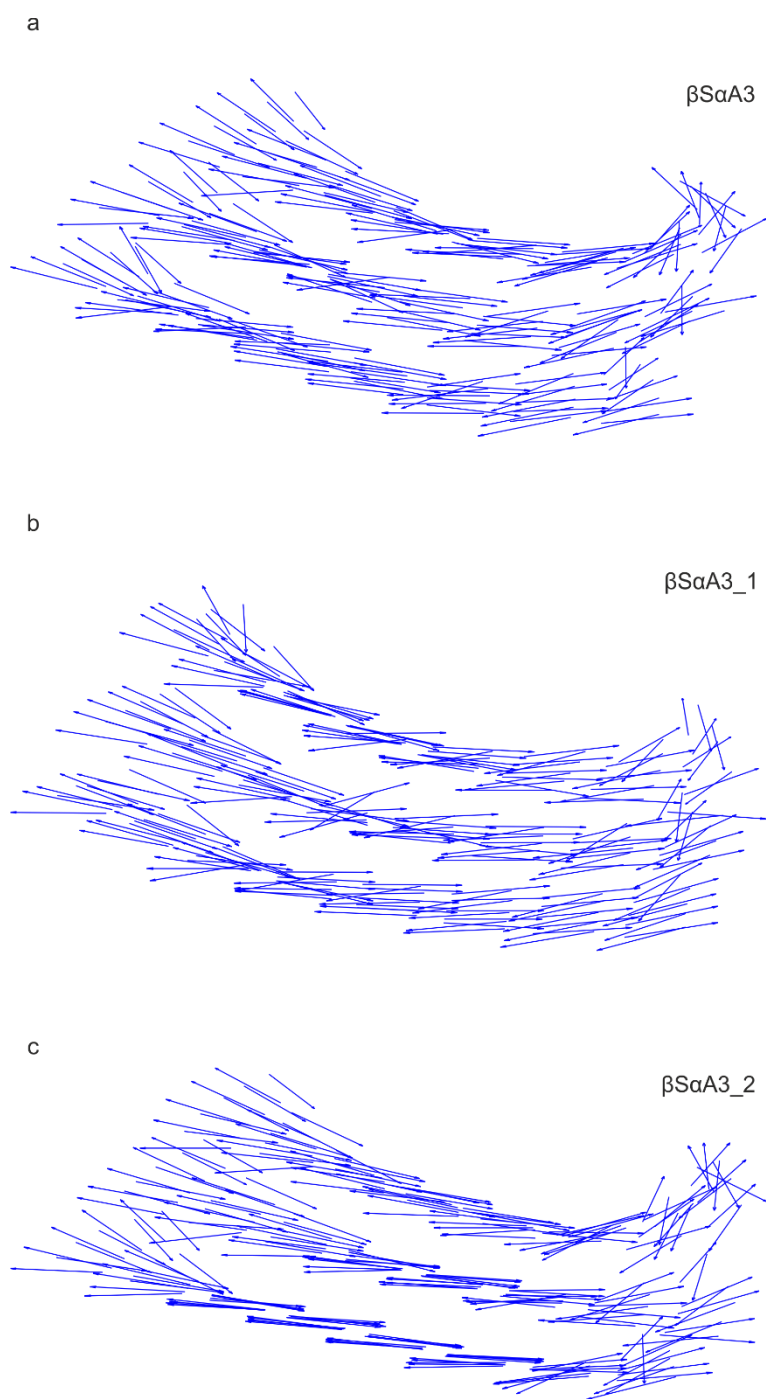


Figure E.17 Q_y dipole moments for triple layer sheets formed using the βSaA dimer arrangement.

Q_y dipole moments, shown as arrows, for the final structures of simulations (a) βSaA3 , (b) βSaA3_1 , and (c) βSaA3_2 .

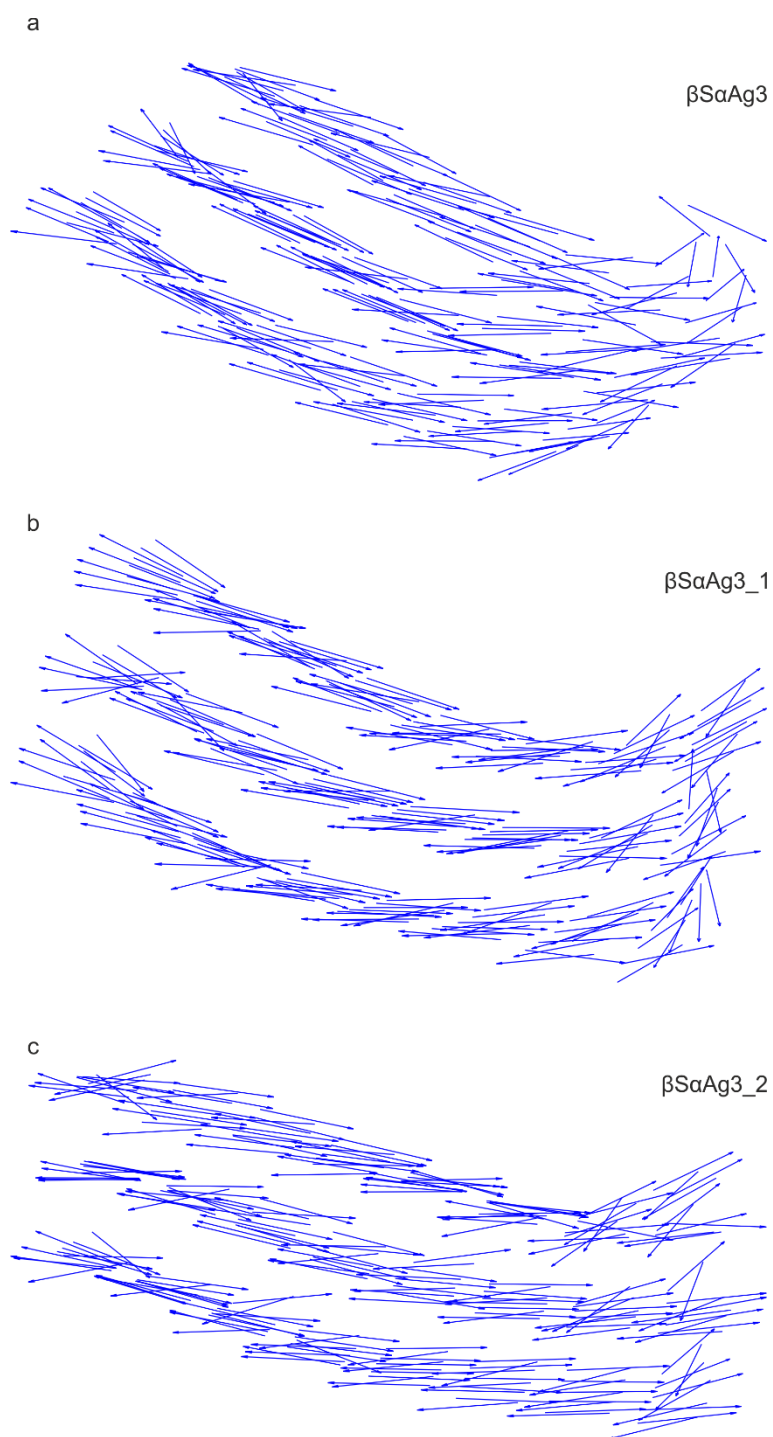


Figure E.18 Q_y dipole moments for triple layer sheets formed using the βSaAg dimer arrangement.

Q_y dipole moments, shown as arrows, for the final structures of simulations (a) βSaAg_3 , (b) βSaAg_3_1 , and (c) βSaAg_3_2 .

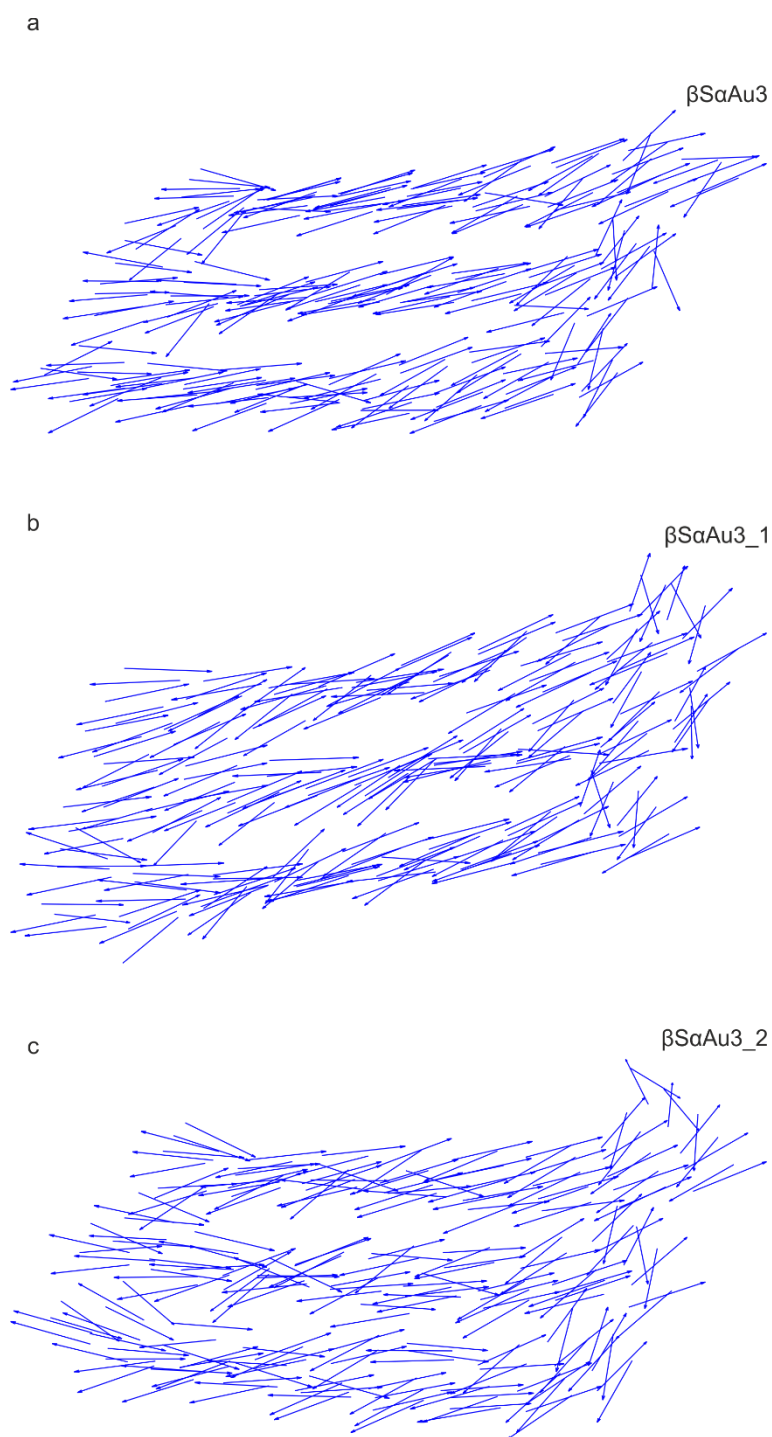


Figure E.19 Q_y dipole moments for triple layer sheets formed using the βScau dimer arrangement.

Q_y dipole moments, shown as arrows, for the final structures of simulations (a) βScau3 , (b) βScau3_1 , and (c) βScau3_2 .

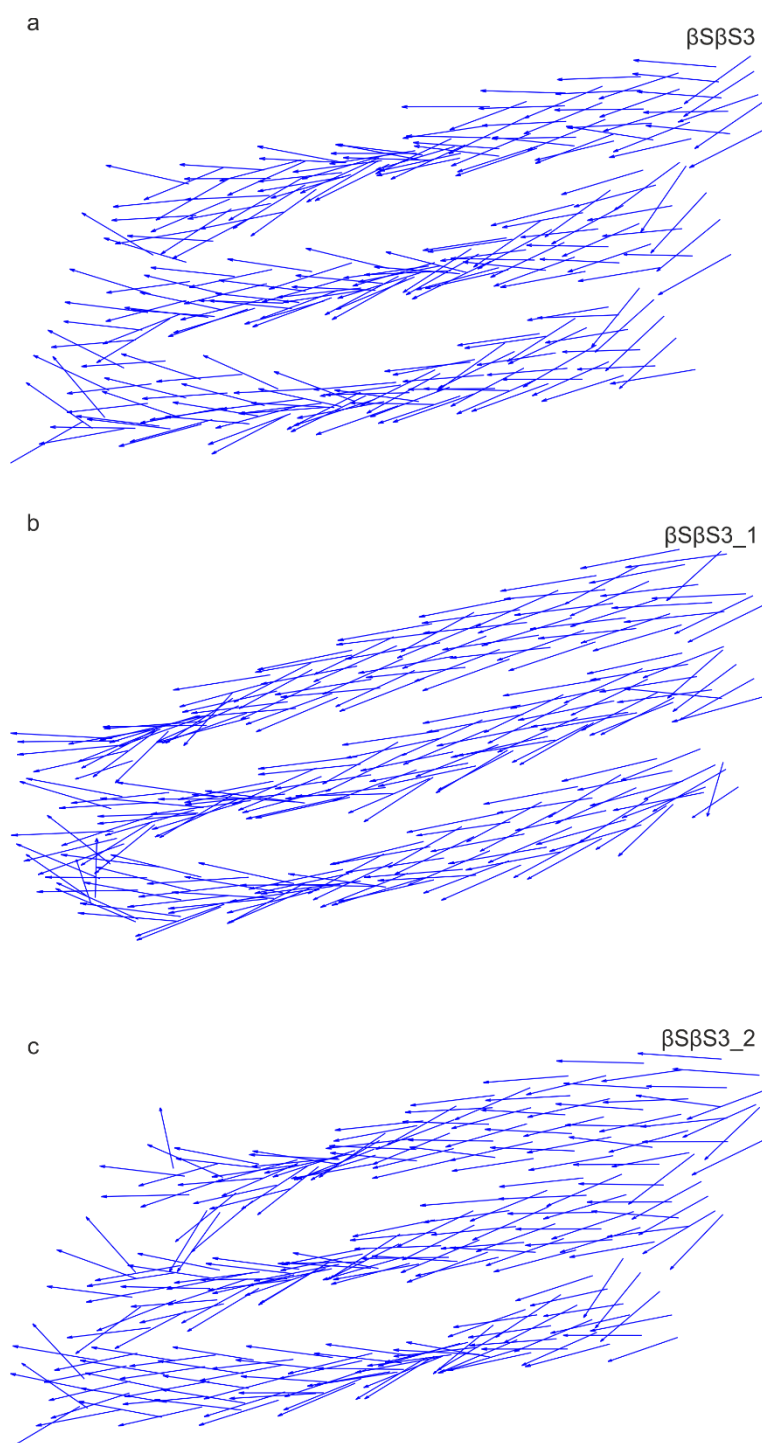


Figure E.20 Q_y dipole moments for triple layer sheets formed using the $\beta S\beta S$ dimer arrangement.

Q_y dipole moments, shown as arrows, for the final structures of simulations (a) $\beta S\beta S3$, (b) $\beta S\beta S3_1$, and (c) $\beta S\beta S3_2$.